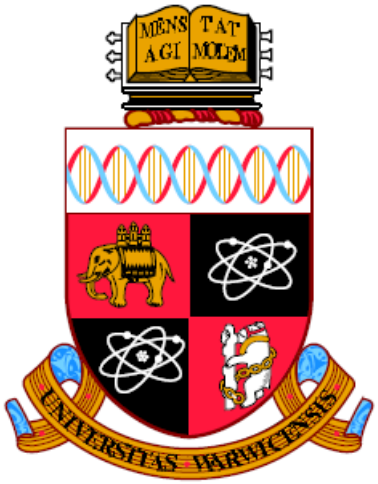

STARTLINK BUILDING SYSTEM AND CONNECTIONS FOR FIBRE REINFORCED POLYMER STRUCTURES

By

Behrouz Zafari

Thesis

Submitted to University of Warwick

for the degree of Doctor of Philosophy

THE UNIVERSITY OF WARWICK

School of Engineering

November 2012

To my beloved brother A. R. Zafari

and my friend B. Chakoshi

Contents

List of Tables

List of Figures

Acknowledgement

I would like to express my deepest gratitude to my supervisor, Prof. Toby Mottram, for his excellent guidance and patience. It is not often that one finds a supervisor who always finds the time for listening to the little problems and roadblocks that unavoidably crop up in the course of performing research. His technical and editorial advice was essential to the completion of this thesis.

I gratefully acknowledge the funding sources that made my PhD work possible. The work was funded by the Technology Strategy Board UK (TSB). Thanks also go to all members of the Startlink consortium, especially Dr John Hartely, Mark Singleton, John Hutchinson, David Kendall and Richard McWilliams.

I am also indebted to the members of civil engineering department with whom I have interacted during my PhD researches. Particularly, I would like to acknowledge Prof. Ian Guymer, Dr. Jawed Qureshi, Prof. Roger Johnson and Dr. Tony Price for their help to understand my study area better.

Special thanks should be given to skilled assistance from technical staff (Mr Colin Banks (civil engineering), Mr Rob Bromley (workshop) and Mr Graham Canham (photographer)), in the School of Engineering, is acknowledged as being invaluable to the quality and future impact of my research.

I would like to thank all my good friends, particularly, Dr. Sarvin Soltanieh, Mr Navroop Matharu, Dr. Reza Ghaffari, Mr Majd Khador and Ms Eyre Hover, and

other good colleagues in the office who, were always willing to help .Their support and care helped me overcome setbacks and stay focused on my graduate study. I greatly value their friendship.

Most importantly, none of this would have been possible without the love and support of my lovely family, who has been a constant source of motivation and inspiration for me.

Declaration

This thesis is presented in accordance with the regulations for the degree of doctor of philosophy. The work described in this thesis is entirely original and my own, except where otherwise indicated.

Behrouz Zafari
November 2012

Publications

- **Zafari, B. and Mottram, J. T.** (In Press) 'Effect of hot-wet aging on the pin-bearing strength of a pultruded material with polyester matrix,' *Journal of Composites for Construction*, 16 3, (2012), 340-352. ISSN 1090-0268 (on-line) doi:10.1061/(ASCE)CC.1943-5614.0000258
- **Mottram, J. T. and Zafari, B.** (In Press) Pin-Bearing Strengths for Design of Bolted Connections in Pultruded Structures. *Structures and Buildings*, 164, (2011), 291-305. Issue SB5
- **Zafari, B. and Mottram, J. T.** 'Effect of orientation on the pin-bearing strength for bolted connections in bolted joints',*in Proceedings 6th International Conference on FRP Composites in Civil Engineering (CICE 2012), 13th-15th June 2012*, Section 14: Codes and Design Guidelines, Paper 209, pp. 8 (CD-Rom)
- **Zafari, B. and Mottram, J. T.** (2011) Strength of Fibre Reinforced Polymer Dowel Connections for the Startlink House. In *Proceeding of the 5th International Conference on Advanced Composites in Construction (ACIC 2011)*, Coventry (Warwick University), 6-8 Sep, pp. 342-354.
- **Zafari, B. and Mottram, J. T.** (2010) Pin-Bearing Strengths for the Design of Bolted Connections with Pultruded Material. In *Proc. Fifth International Conference on FRP Composites in Civil Engineering (CICE 2010)*, Vol. 1., FRP for Future Structures, Advances in FRP Composites in Civil Engineering, Tsinghus University Press, pp. 99-102.

Abstract

The research presented in this thesis examines various aspects on connections and joints in Pultruded Fibre Reinforced Polymeric (PFRP) structures. The work is divided into two experimental investigations on the determination of pin-bearing strength and the characterisation of dowel connections and joint for the Startlink Lightweight Building System (SLBS).

To support the development of a strength formula for bearing resistance in bolted connections two pin-bearing strength test series were conducted to study the effects of load orientation and hot-wet conditioning. The limitations of existing standard test methods are exposed from a critical review to show that they do not specify the need for a clearance hole, the range of bolt diameters and PFRP thicknesses found in practice. Because the size of tension coupons is found to be too big to be cut from standard structural profiles an alternative test method, having a smaller coupon size, is needed for every pin-bearing strength to be quantified by testing. Reported in this thesis are test results using an in-house test method that requires a maximum blank coupon of 100 mm × 125 mm. Characteristic strength are determined using Annex D7 of Eurocode 0. Pin-bearing strengths for load orientations of 0, 5, 10, 20, 45 and 90^o, to the direction of pultrusion are obtained for a web material taken from a standard wide flange section of 9.53 mm thick. In the test matrix there were four sizes of pin diameter from 9.7 mm to 25.4 mm and a minimum clearance hole of 1.6 mm. The in-house test method is shown to satisfactorily determine pin-bearing strength. Another finding from this study is that the Hankinson formula cannot be applied to establish pin-bearing strength at any orientation on knowing the two characteristic strengths at 0^o and 90^o. To characterise the effect of hot-wet

conditioning 0, 45 and 90^{o} specimens were immersed under water for 3000 hours at 40° C. It is found that the average reduction in characteristic strength is in the range of 18 to 31%. The extent of strength reduction is found to be independent of pin size, except when the diameter is 25.4 mm.

The second experimental investigation is for fact finding strength tests towards the application of PFRP dowelling as a method of connection in SLBS. This innovative building system has been engineering for the execution of a FRP house that meets the requirements for code level 6. A series of static coupon-sized tests were conducted to determine the minimum resistance of dowel connections similar to those used in the Startlink house. These results were used to verify the structural engineering design calculations. Another sub-assembly test configuration was used to determine the moment-rotation characteristics of joint details for the portal frame in the SLBS house. Four different beam-to-column joints with dowel connections, and with and without adhesively bonded connections, were statically loaded so that their rotational stiffnesses and modes of failure could be determined. The main conclusions from this study are that:

- all joints had adequate strength against the design ULS moment;
- only when the joint had adhesive bonding between the overlapping beam and column members does the rotational stiffness approach the design rigid condition;
- when clearance holes are present the rotational stiffness is low and applying adhesive bonding around the dowels cannot remove this structural limitation.

Notation

d	Bolt diameter, mm
d_n	Hole diameter, mm
e_1	End distance, mm
e_2	Side distance, mm
k	Rate constant,
t	Constant thickness of FRP material, mm
w	Constant plate width for single bolted connection with $e_2 = w/2$, mm
A	Constant
E_a	Activation energy, kJ mol^{-1}
F_θ^{br}	Pin-bearing strength for the orientation of the resultant force at the bolt/FRP contact with respect to the direction of pultrusion, MPa
F_0^{br}	Pin-bearing strength in the longitudinal (0) direction of pultrusion, MPa
F_5^{br}	Pin-bearing strength in the longitudinal (5) direction of pultrusion, MPa
F_{10}^{br}	Pin-bearing strength in the longitudinal (10) direction of pultrusion, MPa
F_{20}^{br}	Pin-bearing strength in the longitudinal (20) direction of pultrusion, MPa
F_{45}^{br}	Pin-bearing strength in the longitudinal (45) direction of pultrusion, MPa
F_{90}^{br}	Pin-bearing strength in the longitudinal (90) direction of pultrusion, MPa
R_{br}	Pin-bearing strength (resistance) per bolt, kN
$R_{br,test}$	Compressive bearing force testing, kN
T	Absolute temperature, K
θ_1	Measured rotation taken from inclinometer positioned on the major axis of the column member at top of the joint (C1), mrad
θ_2	Measured rotation taken from inclinometer positioned at the centre of the joint (C2), mrad
θ_3	Measured rotation taken from inclinometer positioned on the major axis of the beam member at end of the beam (C3), mrad
$\emptyset$	Joint rotation, mrad
$\emptyset_j$	Rotation at the centre of joint obtained from relative rotation between the joint centre and the column member (i.e. θ_2- θ_1), mrad
$\emptyset_{j,int}$	Initial joint rotation, mrad

$\emptyset_{j,s}$ Joint rotation at Serviceability Limit State from $\emptyset_j$ response, mrad

$\emptyset_{j,U}$ Joint rotation at Ultimate Limit State from $\emptyset_j$ response, mrad

$\emptyset_{j,max}$ Central joint rotation at maximum linearity of M-$\emptyset_j$ response, mrad

$\emptyset_b$ Rotation at the end of the beam member obtained from relative rotation between the end of the beam member and the column member (i.e. θ_3- θ_1), mrad

$\emptyset_{b,int}$ End beam rotation at initial stage from $\emptyset_b$ response, mrad

$\emptyset_{b,s}$ End beam rotation at Serviceability Limit State from $\emptyset_b$ response, mrad

$\emptyset_{b,U}$ End beam rotation at Ultimate Limit State from $\emptyset_b$ response, mrad

$\emptyset_{b,max}$ Central joint rotation at maximum linearity of M-$\emptyset_b$ response, mrad

M Moment at joint, kNm

$M_{j,int}$ Central joint moment at initial stage, kNm

M_s Design moment of joint at Serviceability Limit State, kNm

M_U Design moment of joint at Ultimate Limit State, kNm

M_{max} Joint moment at maximum linearity of M-$\emptyset$ response, kNm

$M_{j,max}$ Joint moment at maximum linearity of M-$\emptyset_j$ response, kNm

$M_{b,max}$ Joint moment at maximum linearity of M-$\emptyset_b$ response, kNm

M_{fail} Joint moment at specimen failure, kNm

$M_{j,fail}$ Joint moment at specimen failure for $\emptyset_j$, kNm

$M_{b,fail}$ Joint moment at specimen failure for $\emptyset_b$, kNm

S Rotational stiffness at joint (secant stiffness, M / $\emptyset$), kNm/rad

$S_{j,int}$ Initial rotational stiffness at centre of joint from $M_{j,int}$ / $\emptyset_{j,int}$, kNm/rad

S_j Rotational stiffness of the joint at the centre of joint from $\emptyset_j$ rotational response, kNm/rad

$S_{j,s}$ Rotational stiffness (secant stiffness) of the joint at the centre of joint from M_s /$\emptyset_{j,s}$ rotational response at Serviceability Limit State, kNm/rad

$S_{j,U}$ Rotational stiffness of the joint at the centre of joint from M_U/$\emptyset_{j,U}$ rotational response at design Ultimate Limit State, kNm/rad

$S_{b,int}$ Initial rotational stiffness at end of the beam member from $M_{j,int}$ / $\emptyset_{b,int}$, kNm/rad

S_b Rotational stiffness at end of the beam member from $\emptyset_b$ rotational response, kNm/rad

$S_{b,s}$ Rotational stiffness at end of the beam from $M_s/\emptyset_{b,s}$ rotational response at design Serviceability Limit State, kNm/rad

$S_{b,U}$ Rotational stiffness at end of the beam from $\emptyset_{b,U}$ rotational response at design Ultimate Limit State, kNm/rad

L_b Span of the beam in the SLBS portal frame (from neutral axis to neutral axis of columns), mm

L_c Storey height in the SLBS portal frame, mm

K Non-dimensional joint stiffness obtained by dividing the joint's rotational stiffness of S to the flexural stiffness of beam (E_bI_b/L_b)

K_b Mean value of E_bI_b/L_b for all the beams at the top of that storey

$K_{j,ini}$ Non-dimensional joint stiffness at initial stage obtained by dividing the joint's rotational stiffness of $S_{j,ini}$ to the flexural stiffness of beam (E_bI_b/L_b)

$K_{j,s}$ Non-dimensional joint stiffness obtained by dividing the joint's rotational stiffness of $S_{j,s}$ to the flexural stiffness of beam (E_bI_b/L_b)

$K_{j,U}$ Non-dimensional joint stiffness obtained by dividing the joint's rotational stiffness of $S_{j,U}$ to the flexural stiffness of beam (E_bI_b/L_b)

$K_{b,ini}$ Non-dimensional stiffness at the end of the beam at initial stage obtained by dividing the joint's rotational stiffness of $S_{b,ini}$ to the flexural stiffness of beam (E_bI_b/L_b)

$K_{b,s}$ Non-dimensional stiffness at the end of the beam at design Serviceability Limit State obtained by dividing the joint's rotational stiffness of $S_{b,s}$ to the flexural stiffness of beam (E_bI_b/L_b)

$K_{b,U}$ Non-dimensional stiffness at the end of the beam at design Ultimate Limit State obtained by dividing the joint's rotational stiffness of $S_{b,U}$ to the flexural stiffness of beam (E_bI_b/L_b)

K_c Mean value of E_cI_c/L_c for all the beams at the top of that storey

E Modulus of elasticity, GPa

E_b Modulus of elasticity of the beam member in the SLBS portal frame joint, GPa

E_L Longitudinal modulus of the beam member in the SLBS portal frame joint, GPa

I_b Second moment of area of the SLBS beam member, mm^4

$I_{b,min}$ Second moment of at section where the beam flanges have been cut away, mm^4

l Vertical separation of transducers DTB and DBB, mm

lt Horizontal displacement measured by transducers DTB, mm

lb Horizontal displacement measured by transducers DBB, mm

Chapter 1

Introduction

Year on year there has been an increase in applications of Pultruded Fibre Reinforced Polymer (PFRP) shapes and systems in civil engineering projects (Bank, 2006), mainly due to benefits, such as their high strength-to-weight ratio, corrosion resistance and low maintenance (Anonymous, 2007). Future growth towards routine practice is hampered by the recognition that a lack of a design standard is a significant constraint. This problem will only be surmounted by the community at large conducting research and development work with the aim of preparing the required design provisions. It is recognised by everyone that the design of connections and joints is one of the most critical aspects when establishing that a primary load bearing structure, of any construction material, is going to be safe and reliable. This challenge is heightened when designing structures with PFRP shapes and systems as the stiffness and strength of their connections and joints is influenced by many parameters (Godwin and Matthews, 1980), including:

- Material parameters, such as fibre type, resin type, fibre orientation, thickness, etc.
- Fastener parameters, such as fastener type (bolt, screw, Unistrut connector, rivet), fastener size, clamping force, hole size, clearance hole, etc.
- Design parameters, such as joint type (single or double lap, moment resistant, etc.), geometry (edge distance, end distance, *etc*), load direction, static or dynamic load and failure criteria.

In 2012 the available design guidance does not have a level of maturity to identify every influence on stiffness and strength from the aforementioned parameters. For example with the method of connection bolting, the effect of changing bolt size, clearance hole and fiber orientation (or load direction) on the strength of plate-to-plate bolted connections has not received sufficient attention. Moreover, it is known that the modes of failure in the connections and joints will depend on geometrical parameters in the detailing (Mottram, 2009a). To support the preparation of a structural design standard there is a need to have standard (coupon) test methods to determine material (characteristic) strengths that are required in the strength formulae for the known distinct modes of failure (Mottram and Turvey, 2003). Available sources of information for the design of PFRP structures and their connections and joints includes the design manuals from pultruders, such as Creative Pultrusions Inc. (Anonymous, 2012a), Strongwell (Anonymous, 2012b) and Fiberline Composites A/S (Anonymous, 2012c), and from independent writers, such as the ASCE Structural Plastics Design Manual (ASCE, 1984), the EUROCOMP Design Code and Handbook (Clarke, 1996) and the Italian guidelines (Anonymous, 2008). The current situation is that design provisions are immature and to ensure safety the unknown uncertainties are accounted for by using a relative high 'factor of safety' on the resistance side.

Having mature, and verifiable guidance for the design of connection and joints will undoubtedly increase designers' confidence to execute PFRP structures with a more appropriate margin of safety, which will inherently use less pultruded material in more economical engineering solutions. In 2007 the American Society of Civil Engineers

(ASCE) and the American Composites Manufacturers Association (ACMA) signed a three-year agreement for a project to develop a pre-standard for the *Load and Resistance Factor Design (LRFD) of Pultruded Fiber-Reinforced Polymer (FRP) Structures*. When published this LRFD standard is expected to help structural engineers and architects use pultruded FRP composites (standard shapes) in building and transportation designs (Anonymous, 2007). In November 2010 this project delivered a pre-standard for the *Load and Resistance Factor Design of Pultruded Fiber-Reinforced Polymer Structures* (Anonymous, 2012d) and that is expected to be a standard by the end of 2013.

The work reported in this thesis is for two experimental studies to gain understanding and knowledge for connections and joints in PFRP structures. Because of the nature of the research it has been split into the following two topics:

1. Determination of pin-bearing strength for preparation of provisions for the design of bolted connections against this distinct failure mode.
2. Characterisation of dowel connection strengths and the moment-rotation response of frame joints (with the method of connection PFRP dowelling, with and without adhesive bonding), using shapes from the Startlink Lightweight Building System (SLBS).

In the first study fundamental material characterisation research is conducted towards the determination of the pin-bearing strength that is to be used with a simply design formula. The term ‘pin-bearing strength’ is for the average bearing stress (using the projected area of the bolt) when a single bolt in a plate-to-plate double lap-shear connection causes failure by the distinct mode of bearing. For the pin-

bearing situation there must be no lateral restraint provided by bolt tightening. In the series of tests for the work reported in Chapters 3 and 4 the steel bolt size and load direction with respect to the pultrusion orientation are the main variables. The research also involves a preliminary study on the influence of hot-wet aging on reducing the pin-bearing strength to a level that it might be during the service life of PFRP structures.

For the second study, the characterisation by testing of dowel connections and portal frame joints is specific to the bespoke geometries and assemblies in the Startlink house that is constructed using the SLBS. The purpose of beam-to-column joint research is to establish the moment-rotation characteristics to failure for four different joint details. The measured rotational stiffness can be used with appropriate frame analysis to develop an understanding of the stiffness and overall structural performance of the unbraced frame (two storeys and one bay) in the Startlink house.

The thesis consists of seven chapters. Presented in Chapter 2 is the literature review that scopes previous research concerning appropriate aspects to the determination of pin-bearing strength, and the reasons why modern methods of construction are looking to use FRP shapes and systems. To support the specific structural engineering research in the PhD work, the review provides general background information on FRP composite materials and the pultrusion composite processing method.

In the review the author highlights previous key research that has been conducted in order to ascertain the factors affecting the determination of pin-bearing strength. This

includes a summary on the various test methods and how the application of the test results can be used in design. Prominent investigations on strength variation with orientation and long-term durability with regards to the effect of hot-wet conditioning are presented. The research work reported in Chapters 3 and 4 was informed by an assessment of the previous work and understanding developed from this review.

The second part to Chapter 2 discusses the original concept to the SLBS and the steps taken within a TSB funded project by the consortium partners to develop a 'factory build' house that has its first (demonstration) unit constructed at Larkfleet Homes in Bourne, Lincolnshire.

Chapters 3 and 4 present two series of static load tests for the determination of pin-bearing strength. Chapter 3 first introduce the in-house test method before presenting and discussing measurements of pin-bearing strengths for a single PFRP material that has not be subjected to additional environmental aging. The test method used was developed specifically to overcome limitations with existing standard test methods so that the testing can cope with the range of detailing of bolted connections to be found in practice. One constant in the test matrix was a minimum clearance hole for the bolting of 1.6 mm. Given that the pultruded material has orthotropic (mechanical properties), the pin-bearing strength for the 9.5 mm thick material had to be measured in both the longitudinal (or pultrusion or 0^o) direction and in the transverse (or 90^o) direction. Published information to support the designer only gives these maximum (0^o) and minimum (90^o) strength values. To obtain knowledge on the variation of pin-bearing strength with orientation the testing was conducted

using the six material orientations of 0º, 5º, 10º, 15º, 30º, 45 º and 90º. Another test matrix variable was to have four bolt diameters in the range of 9.7 mm to 25.4 mm. Plotting of the normalized mean pin-bearing strengths against material orientation is used to compare the measured variation with that predicted by the simple Hankinson formula, which requires only the 0º and 90º strengths to be known. The non-aged test results are also evaluated with the aim of establishing how we can specify pin-bearing strength for the safe and reliable design of bolted connections.

Using the same PFRP material, same strength test method and same test matrix the effect of environmental conditioning on pin-bearing strength is examined by exposing, prior to testing, the blank coupon specimens to hot-wet conditioning of 3000 hours under water at 40^{o}C. The aim of this conditioning was to accelerate material aging in way that might start to represent what could occur when bolted connections are exposed to the weather over a service life of, say 50 years. To make an assessment of the level of strength reduction, the aged test results are compared with their equivalent pin-bearing strengths from the non-aged series of tests reported in Chapter 3. If we have knowledge of the degree of strength lost with aging it can be taken into account when designing bolted connections and joints.

Chapters 5 and 6 are concerned with reporting on the characterisation work for the determination of the structural properties of specific connections and joints in the Startlink house. Presented in Chapter 5 are factual strength results from a series of static tests to characterise the resistance of two PFRP shapes that make dowel-type connections with SLBS members in a number of sub-assemblies. The bearing

strengths are presented from a test series with five different load arrangements. An explanation is given for why there are five load arrangements, and the test results are analysed to provide pragmatic allowable loads for the purpose of conventional engineering design. Presented in Chapter 6 are a comprehensive set of results from a unique series of four full-size tests that have been conducted under static load to determine the moment-rotation characteristics of practical Startlink frame joints, between the floor beam and stud column at first floor level, and having FRP dowel connections. The specimens were prepared either with or without dowel hole clearance, and one specimen with hole clearance had adhesive bonding (bond connection) between common (mating) surfaces of the beam and column members. Using this novel and timely set of results an evaluation is made on the performance of the joints in the SLBS frames, which is required to have a rotational stiffness that classifies the joint as rigid.

Concluding remarks from the PhD research are given in Chapter 7, with possible avenues for further work in the field of connections and joints for structures of PFRP shapes and systems.

Chapter 2

Literature review

2.1 Introduction

Thousands of years have passed since the Mesolithic age, when humans beings first built permanent homes using animal skins and mammoth bones. Many centuries have gone by since the time when stone and mud-brick were the structural materials of houses for the first farmers. Although a quick glance through the history of construction by mankind shows that the technology of construction materials has consistently evolved through millenniums, the last two centuries are particularly noticeable for the sheer growth-rate of technological advancement in relation to the construction industry (Bank, 2006). These developments have enabled civil engineers to achieve impressive gains in the economy, and in the functionality of structures built to serve the common needs of today's society.

Despite rapid progress in the construction industry, devised to meet the demanding needs of improving living standards, an increasing number of new developments have suffered from a serious lack of attention with regard to quality, safety, energy efficiency, and environmental impact. Furthermore, building structures have been constructed from the same small selection of conventional materials for several hundreds of years: masonry, timber, steel and concrete. Conventional materials such as steel, concrete and wood have a number of advantages, not least of which is their

relatively low cost in construction. However, it is clear that conventional materials, in many cases, are either lacking in longevity, susceptible to rapid degradation, or are constrained by limitations such as dead load that restrict their design features. Moreover, hundreds of million tonnes of carbon dioxide is released each year from the production of conventional materials and the consumption of heat, light, and the way in which buildings are run. In all such cases, there is a critical need for the use of new and emerging materials and technologies, with the end goal of facilitating functionality and efficiency (Homes for future, 2007).

The construction material for this thesis is one of a class of structural materials that has been used in both the aerospace and marine industries since the 1940s. Only recently has the number of successful applications of Fibre Reinforced Polymer (FRP) in civil structures seen an increase. This may be primarily attributed to economic reasons and the low level of confidence designers have in employing FRPs with limited design guidance, in particular when compared with the competing conventional materials.

In the last two decades, due to FRPs' advantages such as high strength-to-weight ratios (which significantly exceed those of other materials), corrosion resistance and potential high durability, free form and tailorable design characteristics, the case for these new materials to meet higher public expectations in terms of functionality of building structures and other civil infrastructure has increased. Furthermore, several developments such as the pultrusion process have shown that technical efficiency in processing components can be achieved within competitive economical constraints. Moreover, replacing E-Glass fibres as a relatively cheaper reinforcement to those of

boron, carbon, and aramid, and a growth in research and demonstration projects funded by industries and governments, has meant that FRP materials are now finding wider acceptance in construction (Bakis *et al.*, 2002).

Since the materials used in all studies in this thesis are pultruded FRPs, the following sub-section provides a brief introduction to the pultrusion process and pultruded fibre-reinforced polymer materials, shapes and systems.

2.2 Pultruded Fibre Reinforced Polymer composites (PFRP)

Pultrusion is an automated industrialised process for the manufacture of fibre-reinforced polymer shapes and systems (Bank, 2006). Figure 2.1 illustrates the main stages of the pultrusion process schematically. In this figure it can be seen that the resin-coated fibre reinforcement is passed through guide plates; this is to ensure accurate alignment before the uncured FRP enters the heated die. It is here that the composite shape is cured and consolidated. The process draws continuous fibre reinforcement impregnated with a thermosetting resin through a heated die (say at 150^{o} C) to polymerise the material and form the profile shapes in a continuous process. The rate of pultrusion is about 1 m/min. The rate is lower the larger is the cross-section area and wall thicknesses. Pultrusion is the most cost-competitive method for producing high quality thin-walled FRP shapes for structural engineering applications (Bank, 2006). For a more comprehensive description and explanation of the pultrusion process the reader may consult Creative Pultrusions (Anonymous, 2012a) and Strongwell (Anonymous, 2012b).

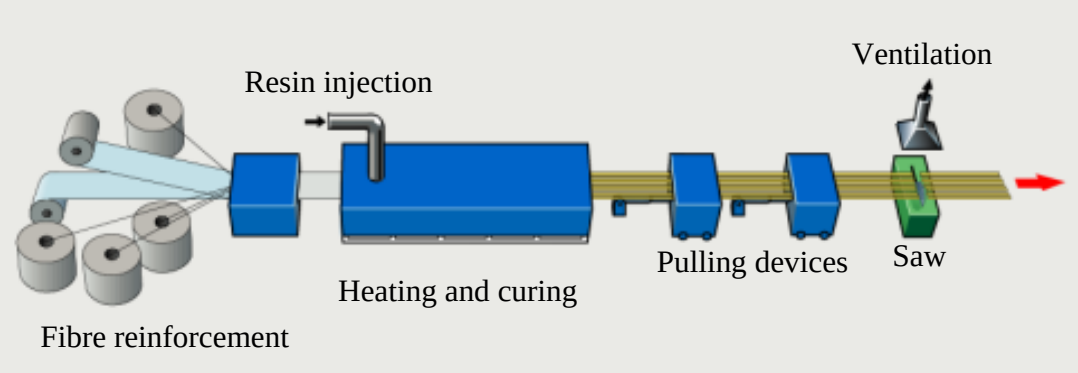

Figure 2.1 Details of the pultrusion process (reproduce from www.fiberline.com).

A pultruded shape can have either an open cross-section, such as a plate or a wide-flange section, or a single closed cross-section such as a hollow tube, or a multi-cellular cross-section, such as panel with internal webs. Although there is great flexibility in the shape, thickness variation, and size of the part cross-section, the cross-section must remain constant along its length. Pultrusion is used to manufacture two types of composite shapes:

- structural ‘standard profile’;
- ‘tailored’ (also known as ‘bespoke’).

The cross-sectional shape of structural standard profiles such as I, wide flange, channel, leg-angle profiles mimic steel sections, and so it is natural that construction follows what is seen in standard steelwork (Turvey, 2000; Bank, 2006; Anonymous, 2012a,b). In contrast, tailored (or bespoke) shapes have a non-standard shape chosen according to individual specifications or customers’ requirements, and often exploit the flexibility of the process to produce any cross-sectional shape. The scope of the first series of experimental investigations reported in Chapters 3 and 4 of this thesis is on a structural ‘standard profile’ but the work is equally valid for the both

'standard profile' and 'bespoke' sections, whereas the second series of physical investigations presented in Chapters 5 and 6 are with 'bespoke' shapes.

In the construction industry pultruded materials are reinforced with E-glass fibres (Turvey, 2000; Bank, 2006; Anonymous, 2012a,b) and possess a matrix based on a polyester or vinylester thermoset resin with fillers and additives. Figure 2.2 shows a PFRP shape with its reinforcement architecture. The outermost layer is a thin protective veil, which does not provide reinforcement. The first reinforcement layer is often of Continuous Filament (or Strand) Mat (CFM (or CSM)). This is followed by alternate layers of unidirectional (UD) rovings and CFM forming the material's core. Because each profile has its own layer construction, it is recognised that the directional elastic constants and material strengths will be varied accordingly (Bank, 2006; Anonymous, 2012a,b), and this poses a challenge when mean or characteristic properties are required for the preparation of strength formulae for bearing resistance of bolted connection. Another variable that makes the characterization of the strength and stiffness of PFRP materials more complicated is an elastic response which yields (ruptures) without significant ductility. These situations are considerably worse with regard to the behaviour of load-carrying joints in PFRPs since parameters related to the type of joint and its associated geometry must also be considered. Godwin and Matthews (1980) set out that these parameters can be subjectively divided into three groups: material parameters, fastener parameters, and design parameters. The mass of published information on mechanically fastened joints in PFRP materials is largely related to experimental results. Although there have been prominent computational and analytical models of pultruded FRP bolted joints (Hassan *et al*., 1996; Ireman, 1998; McCarthy *et al*., 2005), stress analysis through finite element methods proves

difficult due to the various complications mentioned and the local stress concentrations which are paramount to understanding the structural behaviour of the joints. The determination by testing of directional bearing strength for bolted connections in pultruded structures is the subject of Chapter 3.

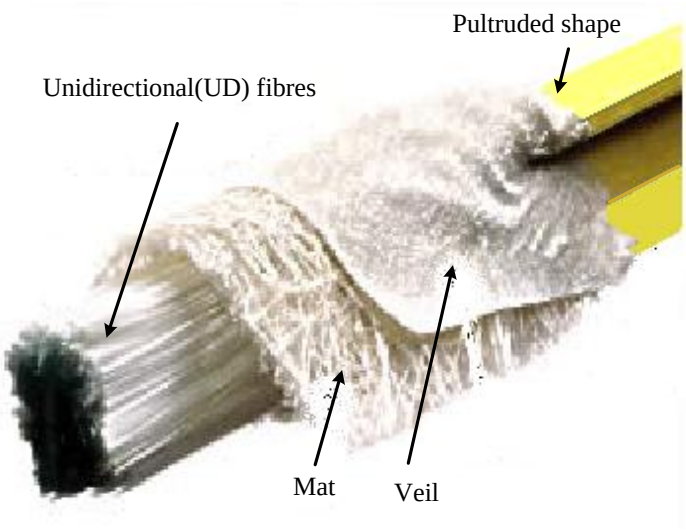

Figure2.2. PFRP shape with architecture of fibre reinforcement (reproduce from www.strongwell.com).

Table 2.1 shows some mechanical and physical properties of PFRP materials and a comparison between their properties and conventional materials.

Table 2.1. Comparison of material properties for conventional and PFRP materials.

Material	Tensile Strength: N/mm^2	Compressive Strength: N/mm^2	Young's Modulus: kN/mm^2	Density kg/m^3	Thermal conductivity: W/mK
Steel	430	430	205	7850	50
Concrete	9	35	20	2400	1.6
Glass FRP	50/400	100/300	7–35	1900	0.2–0.5

PFRP material used in the experimental work presented in Chapters 3 and 4 is from a 203× 203×9.53 mm WF standard shape having a filled isophthalic polyester polymer with E-glass fibres. According to the Creative Pultrusion Inc. (manufacturer) Design Manual (Anonymous, 2012a) the material has the compressive modulus and compressive strength of 20.7 kN/mm^2 and 231 N/mm^2 in longitudinal direction and 7 kN/mm^2 and 115 N/mm^2 in transverse direction, respectively. More details of the physical and mechanical properties for the material are given in Section 3.2.

Before starting a discussion specifically on the bearing resistance of bolted connections it is necessary to give a general review of the conventional methods of connections and joints with PFRP material.

The three conventional methods for connections are: mechanical fasteners (including bolts, screws, rivets and interlocks (or snap-fit)), adhesive bonding and hybrid connections that combine both methods. The type of connection used requires careful deliberation of all the relevant parameters affecting the performance of the structural joint. Bolting is commonly the preferred method of connection because of its familiarity, low cost and easy inspection. Bolted connections and joints are also easy to disassemble and have good quality control. The joint can transmit load immediately after assembly and failure can be progressive, giving a warning before ultimate failure. Adhesively bonded connections often need surface preparation and good on-site working conditions. Their advantage is that they are lightweight, low cost and there is no need to drill holes into the material which raises stress levels and stress concentrations around the hole (Camanho and Matthews, 1997).

2.3 Bolted Connections and Pin-bearing Strength in Pultruded Structures

To scope out the types of bolted connections and joints to be found in primary load-bearing structures, frame joints and plate-to-plate connections need to be considered. Frame joints, such as the web-cleated type shown in Figure 2.3, consist of plate-to-plate connections, such as there is for the beam's web and in each of the two legs for the web cleat shown in the figure.

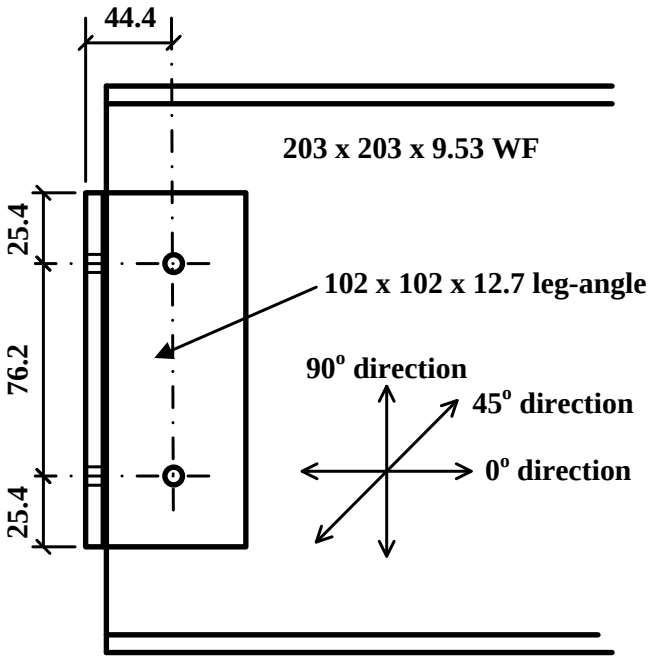

Figure 2.3. Typical beam-to-column bolted joint for steel bolts of diameters 9.53 mm (3/8 in) to 15.9 mm (5/8 in) based on engineering drawing on p. 19–6 of the Strongwell Design Manual (Anonymous, 2012b).

For the research reported in Chapters 3 and 4, the building block for bolted joints will now be considered. They consist of bolting with two or more thicknesses of PFRP. The discussion is restricted to plate-to-plate connections which have the double lap-shear configuration, and with in-plane loading. It is well-known that such

bolted connections of PFRP fail ultimately in one of a number of failure modes (e.g. bearing, shear-out, cleavage, net-tension and block shear). It is important to mention that the size of the steel bolting is such that failure by either bolt rupture or bolt pull-through should not occur (Mottram and Turvey, 2003). The sketches in Figure 2.4 show the simplified stress distribution and fracture paths for these distinct plate-to-plate modes of failure (for tension loading). Mix modes (e.g. when the connection force is off-axis with respect to the direction of pultrusion) are possible and block-shear is a mode when there are multiple rows of bolts (Mottram and Turvey, 2003).

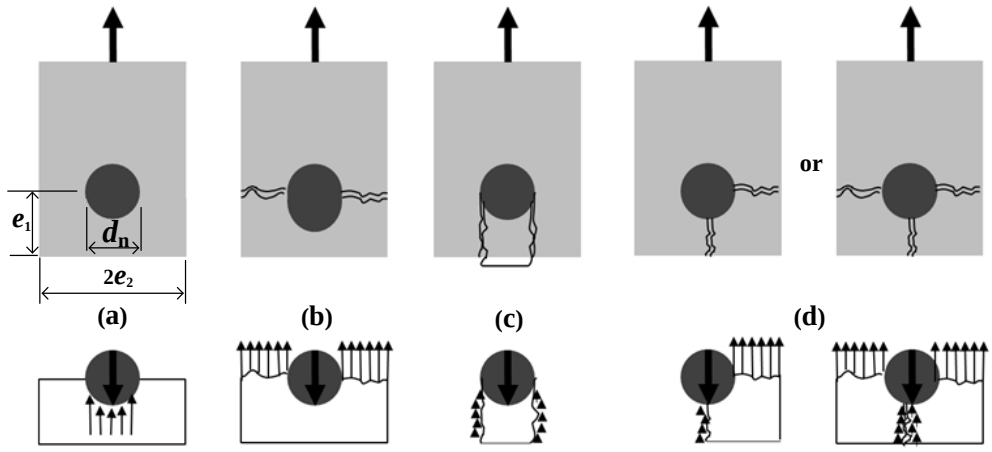

Figure 2.4. Plate-to-plate distinct modes of failure with a single steel bolt; (a) bearing; (b) net-tension; (c) shear-out; (d) cleavage.

The basic connection building block shown in Figure 2.4 is for the single-bolted situation (Mottram and Turvey, 2003). The plate is of constant thickness t and constant width w which, because the bolt is centrally placed, is twice the edge (or side) distance e_2. Other relevant geometric parameters are the hole diameter d_n, and the bolt diameter d, which due to a hole clearance is less than d_n. It is recognised from the series of double lap-shear single bolted test, introduced in Mottram and Turvey (2003), that, under constant environmental conditioning, the mode of failure

can be made to change by varying the geometric ratios e_1/d (or e_1/d_n) and w/d (or w/d_n), with $w = 2e_2$. To promote failure in the bearing mode these two ratios need to be at least four when the FRP material is pultruded.

The bearing mode shown in Figure 2.4(a) is the only one of the 'distinct' modes that does not always give a brittle failure response (Mottram and Turvey, 2003), and can be used to provide the bolted connection with a degree of damage tolerance; this is desirable in design because it imparts a degree of structural integrity (Mottram and Turvey, 2003; Thoppul *et al.*, 2009). It is also the mode with a strength formula (Bank, 2006) that requires its 'own' material strength property (F_θ^{br}), and the formula is

$$R_{br}=t\ d\ F_\theta^{br} \qquad (2.1)$$

The following is very similar to Mottram (2009b) to explain the pin-bearing strength by Equation 2.1. The bearing strength by Equation 2.1 is given by the projected area of the bolt bearing times the specified pin-bearing strength (F_θ^{br}) for the orientation (θ) of the resultant force at the bolt/FRP contact with respect to the direction of pultrusion. When designing a bolted connection, such as shown in Figure 2.3, bearing strength (in kN) is to be the sum of the appropriate R_{br}s (using Equation 2.1) times the number of bolts for each of the R_{br}s calculated using Equation 2.1 multiplied by the number of bolts for each of the different pin-bearing strengths per bolt. Clearly, if the bolt and hole sizes are constant then only a single R_{br} is to be calculated.

When the connection force is aligned with the longitudinal direction of pultrusion we have $\theta = 0^o$, and F_0^{br} is the highest pin-bearing strength. If $\theta = 90^o$ the force is

parallel to the transverse direction of pultrusion and F_{90}^{br} is the lowest pin-bearing strength. For the web connection in Figure 2.3 the bearing strength (resistance) is $2R_{\mathrm{br}}$, with $F_{\theta}^{\mathrm{br}}=F_{90}^{\mathrm{br}}$, t = 9.53 mm (3/8 in.) and d = 9.53 mm (3/8 in.), or 12.7 (1/2 in.) or 15.85 mm (5/8 in.).

By definition the pin-bearing strength (F_{θ}^{br}) is the mean stress at bearing failure, however the failure load is defined: there are several choices (Johnson and Matthews, 1979), as shown in Figure 2.5, when there is no lateral restraint (Mottram, 2009b). It is important to emphasise that for the bearing strength to be the pin value there must be no tightening of the bolting. It is well-known that bearing strength increases significantly on tightening because a torqued bolt provides stiffness to oppose the 'free' through-thickness deformation (Cooper and Turvey, 1995; Mottram, 2004). The beneficial effect of clamp-up on bearing strength (Cooper and Turvey, 1995) has to be off-set by its reduction from creep relaxation (Thoppul *et al*., 2009; Mottram, 2004) and from other possible influences to durability over the intended service life, which will be in tens of years. To ensure that a bolted connection should not fail prematurely it is deemed prudent for the bearing strength to be calculated using the 'minimum' strength that could be found in practice, and this has to be the pin-bearing measure (Mottram, 2009b). Other factors not already mentioned that influence the bearing strength are: the fibre reinforcement architecture and material thickness, the bolt-flexibility, the presence of thread over the bearing surface, the bolt diameter-to-thickness (d/t) ratio, the size of the clearance hole and the environmental conditioning.

Before a historical review of test methods, it is necessary to show that there is a lack of consistency in how pin-bearing strengths of pultruded materials have been measured.

2.3.1 Failure Load Criterion for Bearing Strength

The definition of the failure load in single bolted joints of PFRP is a difficult task but is mainly governed by the usefulness in design calculations. The problem can inherently be seen in the seven possible ways of defining the failure load from load/extension plots. Figure 2.5 shows the typical load/plot recorded during 1979 testing of single bolt E-glass/epoxy FRP plates (Johnson and Matthews, 1979). It must be noted that the load/extension response of a joint will be dependent on the specific detailing and environmental conditioning of the joint testing.

The failure load definition was noted as:

(a) The maximum load. Usually considerable damage will have occurred in reaching this load.

(b) The first peak in the load/extension plot. Damage sustained up to this load is not insignificant.

(c) The load corresponding to a specified amount of hole elongation; which has been specified at various percentages up to 4% (ASTM D 953-02, MIL-HDBK-17-3F, 2002, ASTM D5961-05, Thoppul *et at*., 2009)

(d) The load at which the load/extension curve first deviates from linearity. The point at which this occurs is usually difficult to establish.

(e) The load at which cracking first become audible. Specimens examined at this point would show visible cracks around the loaded side of the bolt hole.

(f) The load at which cracking is initiated. This load is probably quite low and very difficult to determine.

(g) The load at which cracks become visible outside the washers.

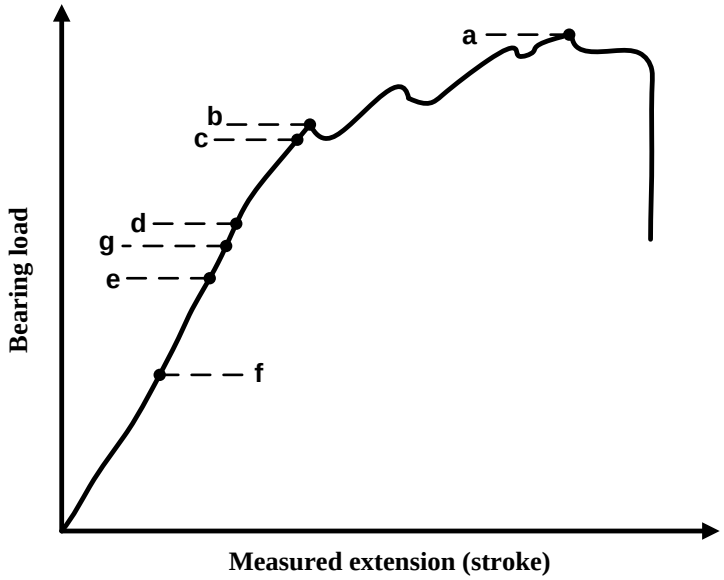

Figure 2.5. Bearing load with measured extension showing seven ways to define failure load, labelled (a) to (g), which can be used to determine a bearing strength (Johnson and Matthews, 1979).

Johnsons and Mathews stipulated that some of the aforementioned load definitions would be subject to variability and therefore they placed the measurement of bolt-hole deformation (definition (c)) as the most reliable approach. This method has often been concurrent in the aerospace industry and design standards including ASTM D953 (2002) which specifies a 4% hole diameter offset. Although this

standard has been used for the characterization of pultruded FRP materials, its scope actually lies within rigid plastics.

Vangrimde and Boukhili (2003) explained that the use of the 4% hole elongation was flawed as design parameters rely on bearing deformation which is dependent on a 'bearing' displacement and not hole elongation. This displacement is the point at which the stress concentrations have disappeared. This observation has been a contributing factor to why load/displacement plots cannot be readily compared (Mottram, 2009b). In addition, failure loads (d) to (g) have not been observed with pultruded materials when the test method is for the pin-bearing strength. Failure load (c) is dependent on the length of gauge used to measure hole elongation and at 4% the elongation can be too high for pultruded material. Previous testing for F_0^{br} always gives load-stroke plot curves without a failure load (b), and so by virtue of elimination the pin-bearing strengths for Equation (2.1) can be determined using failure load (a), the maximum load.

2.3.2 Historical Review of Test Methods for Pin-bearing Strength

Although historical bearing strengths have been reported in a number of sources (Lutz, 2005; Anonymous, 2012a,b) they are not always available in the public domain and can demonstrate significant differences in values; these variations can be explained by differences in PFRP materials and test parameters (Mottram, 2009b), as well as the seven possible ways of defining failure load from the load-stroke plot (see Figure 2.5) that has been recorded in testing (Johnson and Matthews, 1979).

The Pultrusion Industry Council (PIC) of USA recommends that bearing strengths be determined in accordance with ASTM D 953–02 (2002); ASTM standard was first published in 1948, again in 1995, and most recently in 2002. The scope of this ASTM standard is rigid plastics, in either sheet or moulded form, and is therefore not necessarily suitable for the testing of PFRPs.

This test method, and its testing Procedure A (fixture for the double lap-shear loading is shown in Figure 2.6), uses a hardened steel pin (with no lateral constraint) of nominal diameter 6.352 mm (d) and a maximum hole diameter of $d_n = 1.012d$. This geometry has a maximum hole clearance of only $0.012d_n$, many times smaller than that which can be found in practice. According to the American pre-standard for the *Load and Resistance Factor Design (LRFD) of Pultruded Fiber-Reinforced Polymer (FRP) Structures* (Anonymous, 2012d), a minimum clearance of 1.6 mm is required. Testing is conducted under stroke control at a displacement rate to make the loading static. Test specimen (No. 6 in Figure 2.6) thickness is specified at 6.4 mm, the edge distance ratio is 3 (e_1/d) and side distance (e_2) is $1.85d$. The length of material behind the hole with the bearing pin (No. 5 in Figure 2.6) is 100 mm (part of this length is used for load transfer gripping). The extensometer span (No. 4 in Figure 2.6) is the length of the straight-sided coupon used to measure the deformation that gives the load for the pin-bearing strength when the hole is deformed by 4% of its diameter (see Figure 2.6). This strength (Mottram and Turvey, 2003; Anonymous, 2012b; Thoppul *et al*., 2009) is known as the 4% hole deformation bearing strength and there is a doubt about its reliability (Mottram, 2009b). Back calculation using Equation (2.1); it is this procedure that the author uses in Chapter 3 and Chapter 4 to obtain pin-bearing strengths from a series of tests.

D 953 has been adopted by the American pultruders and its application provides the bearing strengths reported in their design manuals (Anonymous, 2012a,b).

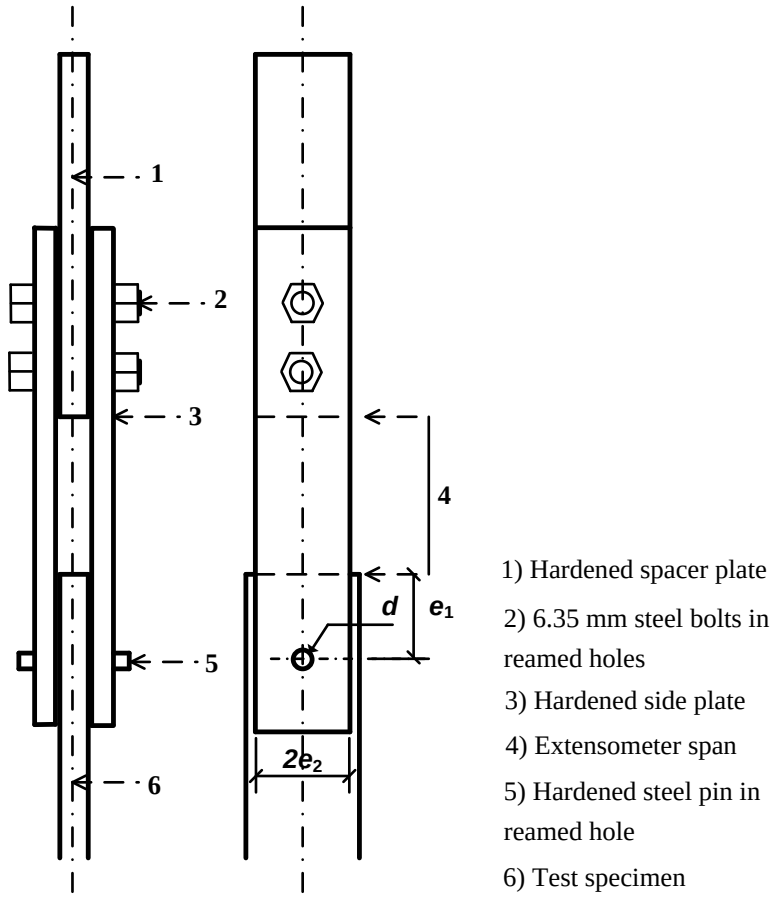

Figure 2.6. Steel tension loading fixture and FRP test specimen for ASTM D 953–02 (2002).

A second ASTM standard for bearing strength is ASTM D 5961-05 (2005). As its title suggests, it was written to be used with laminated FRP composites, commonly found in non-construction applications and is therefore consistent with the recommendations in MIL-HDBK-17 (2002); the test requirements also correspond to the way in which aircraft bolted connections with composite laminates are fabricated. It has provisions for coupon testing with both the double and single lap-shear configuration. Specified specimen geometry and fastener diameter are not too

different from D 953-02, with e_1/d = 3, w/d = 6 and laminate thickness t between 3 and 5 mm. Bearing load is normally applied through a close-tolerance, lightly torqued (2.2-3.4 N.m (20-30 lbf-in.)) metallic fastener of diameter 6 mm. The ultimate bearing strength of the material is determined from the maximum load: there is also provision for determining an offset bearing strength. As this standard is to be used with materials for which the laminate is balanced and symmetric with respect to the load direction, the bearing mode is most likely to occur with $e_1 = 3d$; for the bearing mode to govern with pultruded materials a larger end distance ratio is usually required (MIL-HDBK-17, 2002).

Since 2002 there has been a European EN in three parts for *Reinforced Plastics Composites - Specification of Pultruded Profiles*, with Annex E in Part 2 (BS EN 13706-2:2002) describing a tensile test procedure for pin-bearing strength. This double lap-shear test method (the same as that shown in Figure 2.6) does not define failure by a percentage of hole deformation, and requires only the determination of the maximum stress from the maximum load (see (a) in Figure 2.5, which is similar to D 5961-05). BS EN 13706-2 requires a similar specimen to Procedure A in D 953-02, but with the geometrical ratio e_1/d_n doubled, at 6, and e_2/d_n increased to 3. The hole diameter is to be 6±0.2 mm; the diameter of pin (i.e. a bolt without any lateral constraint) is actually not specified, but is believed to have a nominal diameter of 6 mm for a close fit. The absence of a clearance hole from standard test methods is a major deviation from what we can find in practice. The test results presented in Chapter 3 will highlight the importance of having the clearance hole when determining characteristic F_θ^{br}s for Equation (2.1).

The two American and the single European standard recommend a sample size of five to determine a characteristic value; this is not large given that a statistical analysis ASTM D 7290-06 (2006) requires a minimum of ten specimens per batch. It is worth mentioning that the procedure in Annex D of Eurocode 0 is not limited by the batch size. A characteristic value for a material (or product) property is the value having a prescribed probability of not being attained in a hypothetical unlimited test series. This value generally corresponds to a specified fractile of the assumed statistical distribution (two are used in this thesis) of the particular property of the material (or product). When a low value of material property is unfavourable, as is the situation for strength, their characteristic values should be defined as the 5% fractile, i.e. a value that will be exceeded in 95% of all tests. Because the three test methods were not written concurrently with the drafting of a structural standard for the design of PFRP structures their specifications ensure that some required bearing strengths cannot be measured, and when they can be, they may not be acceptable for F_{θ}^{br} in Equation (2.1). The reasons for this will further be developed and discussed Chapter 3.

2.4 Pin-bearing Strength Variation with Material Orientation

The structural performance of a joint in pultruded FRP material can be greatly affected by the geometric parameters associated with the joint, such as orientation of fibre reinforcement with respect to the direction of pultrusion. Various studies have investigated variables such as: type of loading; materials (bolts and PFRP); plate thicknesses, orientations and joint geometries; the bolt arrangements; and interface conditions (washer, torque and clearance hole) (Mottram and Turvey, 2003).

Prominent investigations on strength variation with orientation are presented and discussed below. Some of the first testing of PFRP materials and the aforementioned variables was conducted by Rosner and Rizkalla (1995). The investigation included a series of 102 single bolt tension tests on EXTREN™ 500 series (polyester matrix with E-glass fibres) flat sheet material of thicknesses 9.53, 12.7 and 19.05 mm. The testing included varying of load orientation of 0, 45 and 90° to the direction of pultrusion. The study concluded that the measured material strength decreased as the fibre orientation varied from 0° to 90° and this decrease was more predominant than the decrease in ultimate load capacity of the connection.

The need for additional test data when the pultrusion and tension axes do not coincide was identified by Turvey (1998), and as a result a series of 54 single bolt connection tests in tension were conducted. The study looked at the angle, θ, between the aforementioned axes at 90, 45 and 30° for EXTREN 500 series 6.4 mm PFRP plate material. The results of the research showed that the load capacity of the joint increases as the off-axis angle, θ, decreases. The failure modes observed within the 30 and 45° orientations showed that cracks propagate along the rovings which may be viewed (negatively) as zones of weakness, or alternatively (positively) as crack guides and/or arresters. Ascione *et al.* (2009) supported these findings by testing a glass fibre/epoxy plate laminate of 10 mm thickness. Their plate was made from eight equal orientation plies of GFRP of continuous strand mat (CSM) and unidirectional (UD) rovings in the 0º direction (with respect to direction of pultrusion) using a vacuum moulding process. In this independent testing for the variation of pin-bearing strength with material orientation, the nominal hole and pin diameters are 21 and 20 mm, respectively. Ascione, Feo and Maceri employed their

own test method, as described in their paper, and measurements were made at the 16 material orientations of 0, 1, 3, 5, 7, 10, 15, 20, 25, 30, 35, 40, 45, 60, 75 and 90^{o}. They showed that a significant decrease in bearing failure load occurred when the material orientation (θ) increases from 0º to 90º. The reduction of mean pin-bearing strength for 5 ^{o}, 10, 20, 45 and 90º was 10, 15, 21, 26 and 32%, respectively. Figure 2.7 shows the curve with the normalized mean pin-bearing strength that, at all orientations, has been reproduced using the test results of Ascione *et al*. From a survey of various bolted connection tests Mottram (2009b) noted that the 0°/90° pin-bearing strength ratio can be between 1.2 and 1.5, depending on how orthotropic the FRP material is.

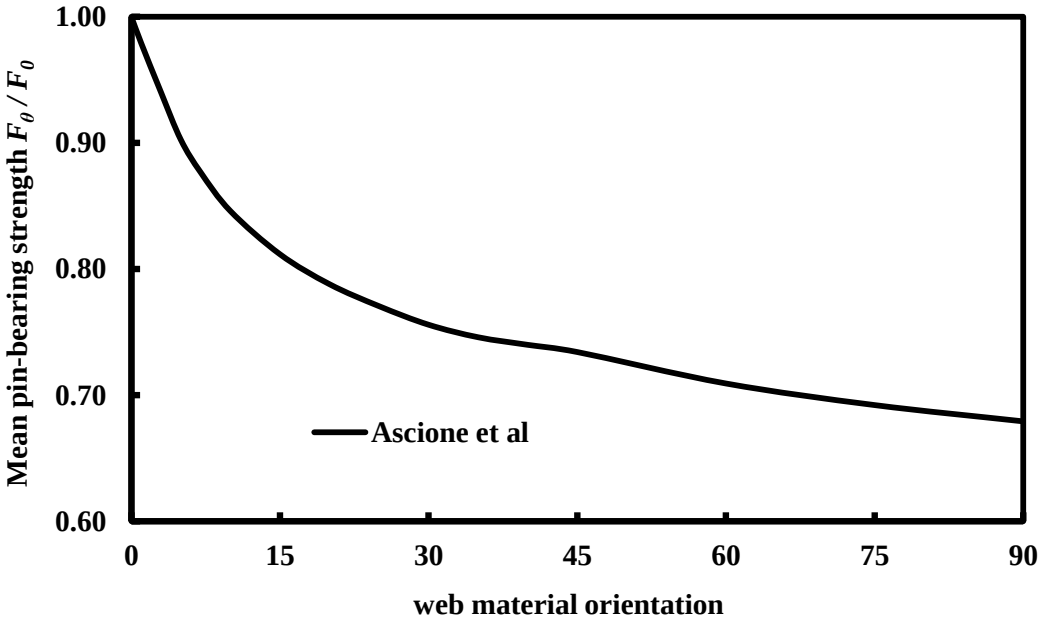

Figure 2.7. Normalized pin-bearing strength curve for 0º to 90º reproduced from Ascione *et al.* test results.

2.5 Long–term Durability of FRPs and Accelerated Aging

One of the key factors that affects the performance of pultruded materials is their durability and resilience against environmental conditions. The civil engineering

communities and construction industry are expected to create building structures with long service life, as contrasted with the use of FRP composites in the aerospace industry and with conventional construction materials. Since the PFRP materials are relatively unknown to designers and practicing engineers, there are heightened concerns about their durability (Karbahri *et al*., 2003). It should be noted that there is some evidence of rapid degradation of specific types of FRP composites exposed to certain environmental conditions found in civil engineering application environments (Karbahri *et al*., 2003). Various research has been conducted with FRP material exposed to aggressive conditions for extended periods of time, with results indicating a significant loss in mechanical properties (Sridharan *et al*.,1998) and material degradation (Ghorbel and Valentin, 1993). It was noted that there are 7 key environmental conditions that can lead to material degradation: thermal effects; an alkaline environment; material creep relaxation; moisture or solution ingress; fatigue; UV exposure (Karbhari, 2007).

Prior to discussing the background on the effect of hot-wet aging on pin-bearing strength in support of Chapter 4, it is necessary to review what is accelerated aging and why it is required for the property characterization (Karbhari, 2007). FRP materials have a property portfolio that make them ideal candidates to contribute to achieving sustainable construction, and pultruded materials are known to be resistant to many chemicals (Anonymous, 2012a,b). One obstacle preventing the exploitation of PFRP shapes and systems is the lack of long-term durability and performance data. This weakness manifests itself in design by the need for severe knock-down factors to make allowances for material degradation. As there is a lack of reliable and relevant test results available, these factors are best estimates; this weakness in

design means that there is an urgent need to develop a test methodology to estimate how strengths and stiffnesses reduce with time due to long-term durability effects. In what follows, the author presents a review of previous durability research to explain why, today, we still cannot make reliable service life predictions for the strength of PFRP members and connections.

Research with FRP materials exposed to aggressive conditions for prolonged periods of time has demonstrated that they can experience a significant loss in mechanical properties (Apicella *et al*., 1983; Bradley and Grant, 1995; Liao *et al*., 1998; Sridharan *et al*., 1998; Phifer *et al*., 2000) and marked material degradation (Ghorbel and Valentin, 1993; Chin *et al*., 1997; Prian and Barkatt, 1999). Many of the aging conditions applied by these researchers could realistically be expected when structures of pultruded shapes (having bolted connections) are exposed to the vagaries of the weather in North America or elsewhere, and with required service lives of tens of years.

The use of accelerated aging testing to simulate field conditions is very common when we want to know the change of a property over time (measured in years). Such tests are conducted to determine residual mechanical property data that can be used to predict the loss after longer times in the field than the aging duration. Accelerated aging subjects the material to an acceleration factor that, when multiplied by the actual aging time, gives the expected life time when the measured property is taken to exist. Time acceleration is often achieved by increasing the temperature, according to the Arrhenius law (Karbhari, 2007). What is essential to know is that this law assumes that the chemical degradation mechanism is the same at the

elevated aging temperature as at the mean service temperature, and that a single mechanism controls the degradation process throughout (BS EN ISO 2578:1999; Bank *et al*., 2003).

The Arrhenius equation defines a function linking temperature to the rate of reaction, and it is

$$k = Ae^{-E_a / RT} \qquad (2.2)$$

In Equation (2.2), k is the rate constant (also accelerated factor or acceleration factor), A is a constant, E_a is the activation energy, R is the universal gas constant, and T is the absolute temperature in Kelvin. Thus, the effect of service lives may be simulated by increasing the temperature and keeping it constant for a shorter period of time, dependent on the value of the acceleration factor.

Since 1994 researchers have addressed the effects of simulated environmental conditioning on properties of PFRP from various manufacturers with various fiber architectures and matrix compositions. Preliminary studies presented by Schutte (1994), Bank *et al*. (1995), Chin *et al*. (1997), Gentry *et al*. (1998), Kellogg *et al*. (1999), Liao *et al*. (1999), Van Den Abeele *et al*. (2001), Nishizaki and Meiarashi (2002), Karbhari and Zhang (2003) and Robert *et al*. (2010) have involved the measurement of one or more property of flexural and tensile moduli and strengths, and fatigue resistance. Each study used a different accelerated aging condition, with a constant temperature in the range -50°C to 80°C, and immersion in water, or salt solution, or acetic acid, or ammonia, for a period of time from 12 hours up to 2 years. From these unconnected studies, an overall finding from the reported test results (for several properties) is that they are differently reduced by their

environmental conditioning. In other words, the level of property change with aging remains to be quantified.

It is instructive in preparation for the work reported in Chapter 4 to briefly summarize the contributions from a number of previous papers. In the work by Liao *et al*. (1999) rectangular specimens of a vinyl ester matrix material were subjected to four-point-bending fatigue. Cyclic loading was set from zero to 30% of the dry flexural strength. After first immersing the pultruded specimens in water at 75°C water for 2400 hours the fatigue test results showed a 40% reduction in the flexural strength. This high temperature aging over a time period (less than that used in this study) demonstrates how large a reduction in a material strength can occur.

The study by Nishizaki and Meiarashi (2002) is of particular relevance to the author's work as their exposure conditions included soaking coupons in water at the elevated temperatures of 40^{o}C, 50^{o}C and 60^{o}C. The pultruded material had a matrix with a vinyl ester resin, which is known (Anonymous, 2012a, b) to possess a greater resistance to chemical agents and temperature than when the matrix resin is a filled isophthalic polyester which is specific to the author study presented in Chapter 4. The measurement of weight change (gain, which can be followed by a loss) and characterization of the material using chemical analysis methods showed how the material was degrading with time. Strength loss was established by flexural testing and this showed that when the temperature is 40^{o}C there was a loss in strength of 20% after soaking for 9120 hours. When giving their study's conclusions, Nishizaki and Meiarashi wrote:

> "although it is hard to imagine that deterioration of glass FRP materials exposed in construction applications would be as rapid as that found for the specimens in the deterioration experiment exposure conditions, still, water and moisture levels are clearly factors contributing to the long-term deterioration of materials exposed to water".

Robert, Wang, Cousin, and Benmokrane (2010) observed that many previous researchers were selecting high temperatures (up to 80°C) relative to the polymer resin's glass transition temperature (T_g) to get the maximum rate of aging (the highest possible acceleration factor from Equation (2.2)). The weakness with this approach, for the evaluation of the durability of a FRP reinforced with glass fibres, is that too high a temperature can cause additional material degradation (that could not be experienced in the field) because the chemical degradation mechanism had changed. Knowing of this weakness, it can be observed that the outcome of forcing a high acceleration factor, by selecting a too-high aging temperature, is to underestimate the actual durability.

Robert *et al*. (2010) also worked with a pultruded material having a vinyl ester based matrix. They observed that after conditioning in distilled water (a more aggressive solution than tap water) for 2880 hours at constant temperatures of 40°C, 60°C and 80°C, the loss in flexural strength is 11%, 19% and 46%, respectively, of the average flexural strength at 23°C (room temperature). These researchers used their study to conclude that the effect of temperature is the most important aging factor, with time and/or sustained loading of secondary importance.

Bank *et al*. (2003) outline a material specification with Procedure B for the determination of long-term properties for material qualification. Their accelerated

testing has the maximum aging temperature taken to be 0.8 of the (nominal) glass transition temperature (T_g) that can be based on data provided by Chateauminois *et al*. (1995). It is noteworthy that for the purpose of design, it has been recommended by Karbhari, Chin, Hunston, Behnmokrane, Juska, Morgan, Lesko, Sorathia, and Reynaud (2003) that the FRP material is to be chosen to have a T_g at least 30^{o}C above the maximum expected service temperature. This upper bound on T_g is without aging in water, which is shown by Chateauminois *et al*. (1995) to reduce the glass transition temperature.

Turvey and Wang (2007) have reported the effect of hot-wet aging on the strength of single-bolt tension joints. The material was EXTREN® 500 series pultruded flat sheet with a polyester resin matrix. Strongwell (Anonymous, 2012a) recommended that their 500 series material should not be used at temperatures above 65^{o}C. They choose the joint geometries (see Figure 2.4 for geometric ratios w/d, e_1/d) to ensure that for the tension loading the mode of failure in the double lap-shear tests was one of the distinct modes of bearing or net-tension. They found that the failure loads for the 'bearing' joints are almost independent of the water immersion time under ambient temperature conditioning. After aging at constant temperatures of 60°C and 80°C in water for about 1100 hours, joint strength (measured with the material at the aging temperature) was found to decrease by about 63% and 86% of the ambient temperature failure load. After another 1000 hours of immersion they found a further decrease of 7% and 3%. This finding suggests that there might be a limit to the loss in residual strength due to the long-term degradation of this pultruded material.

Like other researchers, Turvey and Wang (2007) recognized that any choice of conditioning for accelerated aging cannot exactly replicate the long-term material

degradation that FRP structures could probably experience in the field over their service lives. This fact informs us that a good measure of sound engineering judgment will be required when reduced mechanical properties are, for example, used in strength calculations for the design of FRP structures.

Presented in Figure 2.8 is a plot reproduced from Figure 10 of Robert *et al*. (2010) for the accelerated factor (0 to 140) as a function of temperature (0 to 100^{o}C). Multiplying the aged time by this factor gives the service time. Note that the term 'accelerated factor' is commonly written as 'acceleration factor', and it is the latter terminology that the authors use. The paper does not say how the values in the Arrhenius equation curve (Equation (2.3)) were established, and it may be assumed that they are specific to the PFRP bar material, having a vinyl ester matrix.

$$Accelerated\ factor = 0.66e^{0.068(Temperature\ in\ oC)} \qquad (2.3)$$

Robert *et al*. (2010) do, however, provide the following cautionary observations on the application of the Arrhenius equation curve given by Equation (2.3):

> "It has to be noted that in regions of large temperature variations such as Canada, one-year aging at an average temperature is not equivalent to one-year aging at temperatures varying around this median temperature. In fact, for two areas having the same average temperature, the material degradation will be lower in the region having the lowest temperature variation because, as the Arrhenius equation (Equation (2.2)) shows material degradation is not linearly proportional to the temperature but increases exponentially."

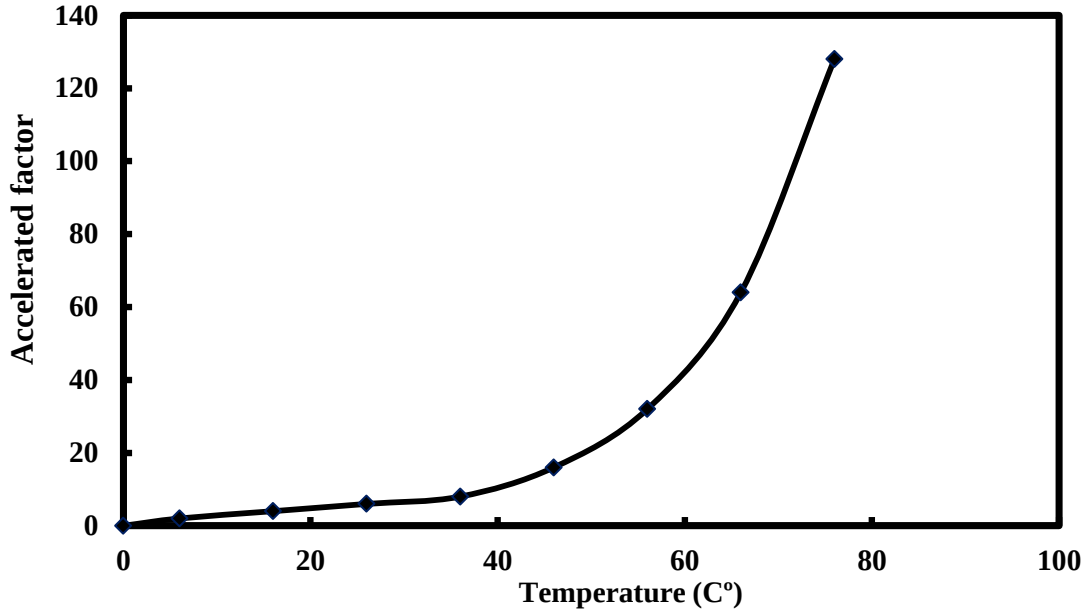

Figure 2.8. Accelerating factor as a function of temperature.

Beddows *et al*. (2002) use Equation (2.2) as the basis of presenting a model that allows lifetime predictions for hot water accelerated aging of FRPs. To explain how the model can be used to predict service lives, a small amount of data was collected from flexural strength testing of aged pultruded material, which is from the same 1525 series Wide Flange shape (Anonymous, 2012a) being used for the pin-bearing strength characterization presented in Chapters 3 and 4. Although the data sets in Beddows *et al*. (2002) are far too small to give reliability, the analysis gave the 1525 series material an activation energy (E_a) of 39000 $Jmol^{-1}$. The paper also reports the mean annual temperature is 10.4^{o}C in the UK. SaECaNet has an interactive web-page (www.saecanet.com/calculation_page/000376_000505_accelerating_factor.php) for *Calculation of Acceleration factor by Arrhenius equation*. To use this calculator, the activation energy (E_a) has to be in units of eV. To change units from $Jmol^{-1}$ to eV the activation energy, taken from Beddows *et al*. (2002), is multiplied by 1.036×10^{-5}

$eVJ^{-1}mol$, which is the ratio of the Boltzmann constant (8.617×10^{-5} eVK^{-1}) and the universal gas constant (R is 8.314 $Jmol^{-1}K^{-1}$). Activation energy 39000 $Jmol^{-1}$ for 1525 series material is therefore 0.404 eV.

2.6 Startlink Lightweight Building System

2.6.1 Modern Methods of Construction with FRPs Components and Systems

Hundreds of million tonnes of carbon dioxide is released each year from the production of conventional construction materials and through the consumption of heat, light, and the overall energy usage of buildings. As the UK strives for a low carbon economy, there is a critical need for new materials and technologies which facilitate functionality and efficiency (Homes for future, 2007).

In addition to these issues, for many years in the UK the supply of new homes has not kept up with rising demand. In 2004, Barker (ODPM) highlighted to the government the demands that an ever-growing population would have on housing construction in the UK, and recommended an additional 120, 000 houses per annum on top of the annual building plan of 160, 000.

As a result of the Barker report, the UK government has a strategy for three million new homes by 2020, with two million by 2016 (Homes for future, 2007). To meet this target, the UK government and local authorities have embraced off-site pre-assembly, which is associated with the concepts embedded in Modern Methods of Construction (MMC) (Post, 2003). The realisation that executing units with reduced carbon emissions in line with the UK Code for Sustainable Homes (2007) creates a

market advantage has been one of the motivating factors behind recent innovation in housing technologies, resulting in the emergence of low- and zero-carbon/energy housing systems designed around using MMC and conventional construction materials (Rogatzki, 2007; Stanfield, 2006).

FRP materials are advantageous as they have mechanical properties that will support lower carbon usage and with the maturity of composite material processing and application technologies in current buildings, it is now a good time to begin using these materials in the construction of houses. Component shapes and mechanical properties of FRP materials depend not only on the fibre reinforcement arrangement, but are also directly linked to the processing method itself. There are several methods capable of producing components suitable for application in the construction industry.

Prior to introducing the Startlink Lightweight Building System, a summary of MMC is first necessary in order to outline how and these might impact upon the research and development of new FRP building components. According to Gibb and Goodier (2005) there are four techniques which fall under this broad heading:

(a) Modular construction.

(b) Volumetric pre-assembly.

(c) Non-volumetric pre-assembly.

(d) Component manufacture and sub-assembly.

The term pre-assembly refers to the manufacture and assembly (usually off-site) of dwellings, or parts thereof, prior to being constructed on site, which is followed by their subsequent site installation and execution. Since the review by Gibb and

Goodier reports in the 1990s, during the last decade there has been a move towards more use of MMC; alongside this, we have witnessed the birth of an increased desire to reduce energy consumption, a factor which led to the UK Code for Sustainable Homes (2007). FRPs can contribute to these changes as they have lower thermal conductivities and adequate strength and stiffness properties, as shown in Table 2.1, to provide scope for house superstructures to make significant life-time energy savings as compared to construction using older technologies and materials.

According to the survey by Pan *et al*. (2005) of the top 100 UK house builders, the use of volumetric units for bathrooms and kitchens represents the greatest MMC growth potential. Pan *et al.* also identified the same potential for the exploitation of complete modular buildings. These researchers recognised that the most significant barriers to growth are high capital investment, lack of standardisation between different systems, and the inability to alter a design as the build progresses.

To introduce the historical background to FRP housing there is the paper by Evernden and Mottram (2012). The first reference to a dwelling of FRP is adeptly titled Prefabricated Plastic House (Kaiser, 1945). Designed by the Henry Kaiser Housing Company in 1945, this single-storey panel based structure (for, 90 m) is similar to the prefabricated timber systems, appearing at that time in the USA. In the 60 years from this first 'plastic house,' FRP components are to be found in many applications, as secondary load bearing structures (Bank, 2006) and architectural features, such as cladding and canopies (Leggart, 1984; Parkyn, 1970). As the historical review by Evernden and Mottram continues to show, the use of FRPs in

complete dwellings has been limited to a handful of prototype and showcase structures.

Called the ‘House of the Future’ the American resin company Monsanto (Parkyn, 1970) executed a FRP dwelling in 1957 that was a tourist attraction at Disneyland Anaheim, California until 1967. This was another early FRP house that ‘paved the way for an upsurge of interest in the possibility of using FRPs for structural application’ (Parkyn, 1970). There is evidence of cladding and modular bathroom units being used, but not in high volumes, together with non-structural window frames, tanks, pipes and ducts. According to Parkyn (1970) the restraining factors in the 1970s for a wider use of FRPs were said to be the lack of a ‘code of practice’ and, more importantly, a lack of robust information on their behaviour in fire.

These concerns have been somewhat overcome with the publication of the Eurocomp design handbook (Clarke, 1996) but gaps remain in understanding the durability and behaviour of FRP components when exposed to fire (Karbhari *et al.*, 2003). This continues to limit the use of FRP components as critical structural components in buildings.

In recent years, researchers have progressed further in understanding the benefits of FRPs in structural engineering applications. The following is very similar to Evernden and Mottram (2012) to provide a historical review on exploiting the applications of FRPs in structural engineering. Between the 1970s and the late 1980s there was no significant progress in the exploitation of FRPs in structural engineering applications (Hollaway and Head, 2001; Leggart, 1984), but government

review reports of the 1990s, along with the advent of our need to find engineering solutions to maintain existing structures, by retrofitting or strengthening or protecting from the environment, gave a renewed impetus (Bakis *et al*., 2002; Head, 1994) to using FRPs. During this period, continuous processing methods, and in particular pultrusion (Bank, 2006; Hollaway and Head, 2001), also became the most cost effective manufacturing methods able to produce high quality components (Bakis *et al.*, 2002), further contributing to the impetus for FRP application.

FRP composites have numerous potential advantages in house building construction including the following:

- Offsite fabrication and modular construction
    - ability to automate and mechanise production
    - faster build times
    - better quality control
- Reduced mass
    - geometrically more efficient solutions
    - easier and more economic installation - smaller cranes required
    - reduction in size and cost of supporting structure, foundations etc
- Superior durability
    - resistant to atmospheric degradation
    - reduction in through-life costs and possibility of recycling.
- Improved thermal insulation and lack of cold bridging
    - reduction in carbon emissions and running costs
    - sustainability
    - low embodied energy

From this research, it can be clearly stated that PFRP profiles are competitive engineering components that are ideally suited to a large number of building construction applications, and are especially well suited to house building.

FRPs do have a number of technical factors that are less than satisfactory, as with all building materials: the lack of stress redistribution associated with material ductility, the engineering of connection joints with structural integrity, and the relatively low modulus-to-density ratios that make FRP structures sensitive to dynamic actions. These can all add to project costs, thus making FRPs a less desirable option. The long-standing performance concerns about the durability and fire performance over the working life of the structure also remain. Much more understanding and know-how for the behaviour of FRPs in construction is available in Bank (2006), and this should enable these shortcomings to be satisfactorily engineered out.

Figures 2.9 to 2.11 show some previous FRP building systems. In Figure 2.9 a 'volumetric and modular' FRP system of 1968 is shown: this early FRP 'Futuro House' was designed by Finnish architect Matti Suuronen as a weekend chalet. It was constructed as a single shell-type structure, of 8m diameter and floor area of $25m^2$; the lightweight, self-contained structure was easily transportable by helicopter (Parkyn, 1970). The SpaceBox, shown in Figure 2.10, provides a further example of volumetric and modular construction. Developed by Holland Composites Industrials (see www.hollandcomposites.nl) and designed by De Vijfi, this represents a unique concept in modern-day residential buildings: the style exemplifies the building-block approach combined with the advantages of FRP materials in sandwich construction to provide individual self-contained, lightweight living modules. SpaceBox modules

can be stacked to three storeys, to create a small communal dwelling without the need for special foundations. Each individual module is completely prefabricated, plumbed, wired, furbished and finished off-site, such that modules may be inhabited within hours of deployment. An early client was Delft University Student Housing Service in 2004.

Figure 2.9. Weekend chalet of 36 GRP sections of double-skinned sandwich construction (via http://www.worldarchitecturemap.org).

Figure 2.10. The SpaceBox volumetric and modular system (courtesy of www.spacebox.nl)

One shortcoming of the ‘volumetric and modular’ approach is the lack of flexibility in building and room size, although this is less acute with ‘elements and panels’ systems, and in the ‘open-building’ system (Evernden and Mottram, 2012) form. Moreover, latter systems which have a higher number of smaller components give a greater degree of flexibility in design. A well-designed ‘open-building’ system allows for a wide range of buildings, each with a high degree of component repetition, to be created.

The Eyecatcher building shown in Figure 2.11 is the tallest residential/office building with a primary PFRP load bearing structure. This ‘Elemental and panel system’ (Evernden and Mottram, 2012) five-storey building was built for the 1999 Swissbau exhibition and was constructed using Fiberline Composite (Anonymous, 2012c) pultruded standard profiles. With steel-bolted connections that apply steelwork practice, the whole PFRP frame could be disassembled at the exhibition site and transported to Basel to be reassembled for office accommodation (Daniel, 2003). However, these buildings are limited by the component repetition and the paucity of integrated cladding systems to be attached to a PFRP frame.

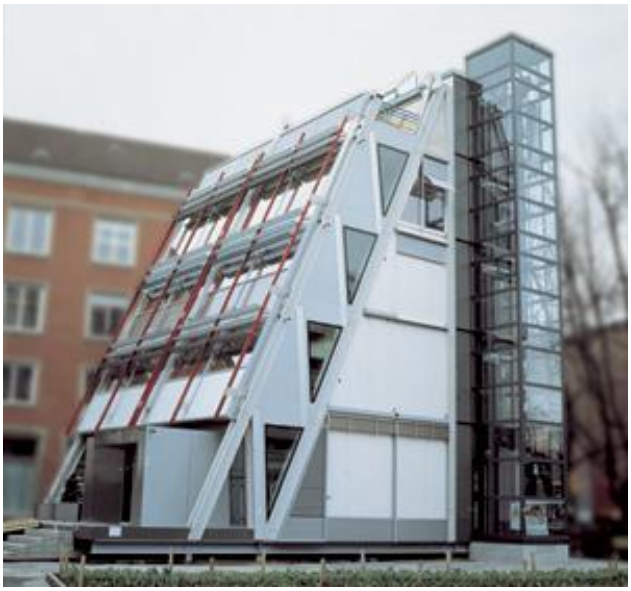

Figure 2.11. The five-storey Eyecatcher building with a hight of 15 m (courtesy of Fiberline Composite).

The first successful modular building system was the Advanced Composite Construction System (ACCS), created by Head (1994, 1995) in the 1980s, while at Maunsell Structural Plastics, UK. It has been used to execute many world firsts and flagship PFRP structures (Evernden and Mottram, 2012). Figure 2.12 shows the first ACCS building at the site of the Severn Crossing Visitors' Centre, a rapidly erected temporary structure which illustrates the merits of the innovative approach. After its original function as Maunsell's site office came to an end in 1998 the structure was used as a visitor's centre. Although it was never intended to be permanent, the site office provided a premier example of the potential for modular PFRP systems in future residential units until its demolition in April 2009. Gates *et al.* (2011) reported a study on the 'long-term' durability of the Severn Crossing Visitors' Centre building for assessing the characteristics of environmentally aged PFRP materials. The results reported by Gates *et al.* indicated that after 17 years of naturally aging (exposure condition), the mechanical properties of the building's components have not significantly diminished.

Although ‘open-building’ systems (Evernden and Mottram, 2012) provide a high degree of designer flexibility, the use of these systems is restricted by the initial high start-up costs that are inherent in designs with a large number of bespoke components. As an alternative, both standard and bespoke components may be used in combination to provide the designer with a high degree of flexibility without such prohibitive high costs. Open-building systems of this kind are likely to become a competitive choice in a number of other construction applications such as industrial application and emergency housing, allowing for versatility and flexibility along with the other benefits of FRP construction.

Figure 2.12. Severn Crossing road bridge site office and later visitor information centre constructed with the ACCS (courtesy of Sharon Loxton).

2.6.2 Startlink House

The original concept of Startlink Lightweight Building System (SLBS) proposed by Singleton (2004) was based on a range of 15 open and closed pultruded bespoke and standard shapes. These shapes are shown in Figure 2.13. This aimed at constructing a modular house system using ‘snap-fit’ connections with rubber weather seals, and solid and hollow dowel joint methods to fabricate house with component’s weight

less than 50 kg to allow fast-build with semi-skilled labour. Figure 2.14 shows the features of wall component and hollow dowel joint methods to a preliminary design concept for the Startlink house.

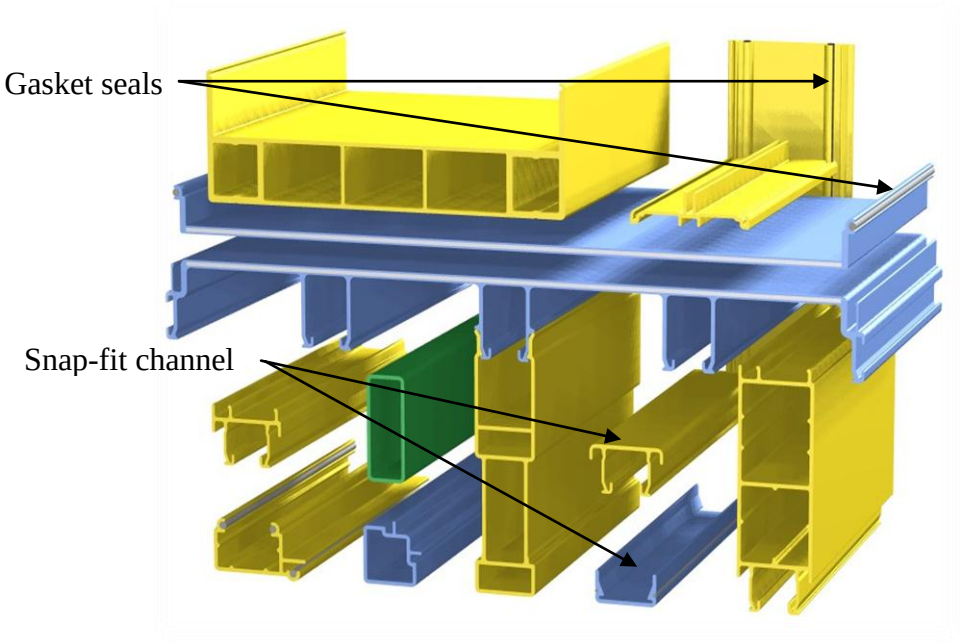

Figure 2.13. Range of 15 open and closed pultruded sections proposed by Singleton for ‘snap-fit’ connections in Startlink system (Startlink Systems Ltd).

Figure 2.14. Assembly of the Startlink system for low-cost housing (Startlink Systems Ltd).

Singleton and Hutchinson (2007) estimated that the use of such a lightweight PFRP housing system can reduce the quantity of materials bought to the site from approximately 80 to 90 tonnes of conventional materials to 8 tonnes of PFRP materials for a typical two-storey three-bedroom house. This reduction in transportation and assembly costs can offset the material costs, giving overall build costs of £550/m^2 compared to a minimum of £600/m^2 for conventional construction materials using both traditional and MMC. Analysis of the Startlink pultruded profiles required to build a 75m², two storey house based on profile costing in 2007, suggested a total pultrusion cost of £25,000. The demonstrator house that was constructed at Bourne has pultrusions costing about doubled. Pultrusion costs are governed by raw material costs, set-up time and machine speed, but pultrusion costs can be lowered by reducing expensive material with thinner or core-filled profiles, increasing machine speed and using longer production runs.

In June 2008 the Technology Strategy Board (TSB) announced investment in an innovative new R&D project to transform the Startlink Lightweight Building System (SLBS) from concept (Singleton, 2004) to reality. As a Low Impact Buildings Innovation Platform (2008) project it has the aim of helping the UK construction industry deliver buildings with a much lower environmental impact. The UK construction market is worth over £100 billion per year, and there is growing pressure from customers and regulators for more environmentally friendly buildings, creating new growth opportunities for innovative businesses (Technology Strategy Board UK, 2008). The SLBS was developed by the work of a partnership of six companies as a consortium, led by EXEL Composites UK, together with the University of Warwick. Based on the geometries of a similar original concept to the

Startlink house, this was developed so that an engineered family of pultruded shapes could be assembled off-site for panels in a house's superstructure that, with integrated energy management, meets the UK Government's requirements for Code Level 6. Legalisation from 2016 (Homes for future, 2007) requires all new-built dwellings to be carbon neutral over their service life which is over than 50 years, and the innovative SLBS alternative has been designed specifically to meet this very demanding challenge.

The house has been designed as a 'factory build', with modular panels fabricated in advance of transportation and on-site assembly; the fabrication and assembling drawing and Method Statements were prepared as part of the TSB project. The new features of the Startlink house were designed for energy efficiency, low cost, fire resistant, innovative joints and connections, etc; further information is presented by Hutchinson and Hartley (2011).

Startlink's bespoke shapes, processed during 2011, use thin and core-filled profiles and to enable long production runs in house construction. This offers the prospect of both environmentally friendly and cheap production. Figures 2.15(a) to 2.15(e) show the photographs of five main shapes that form the Startlink building system.

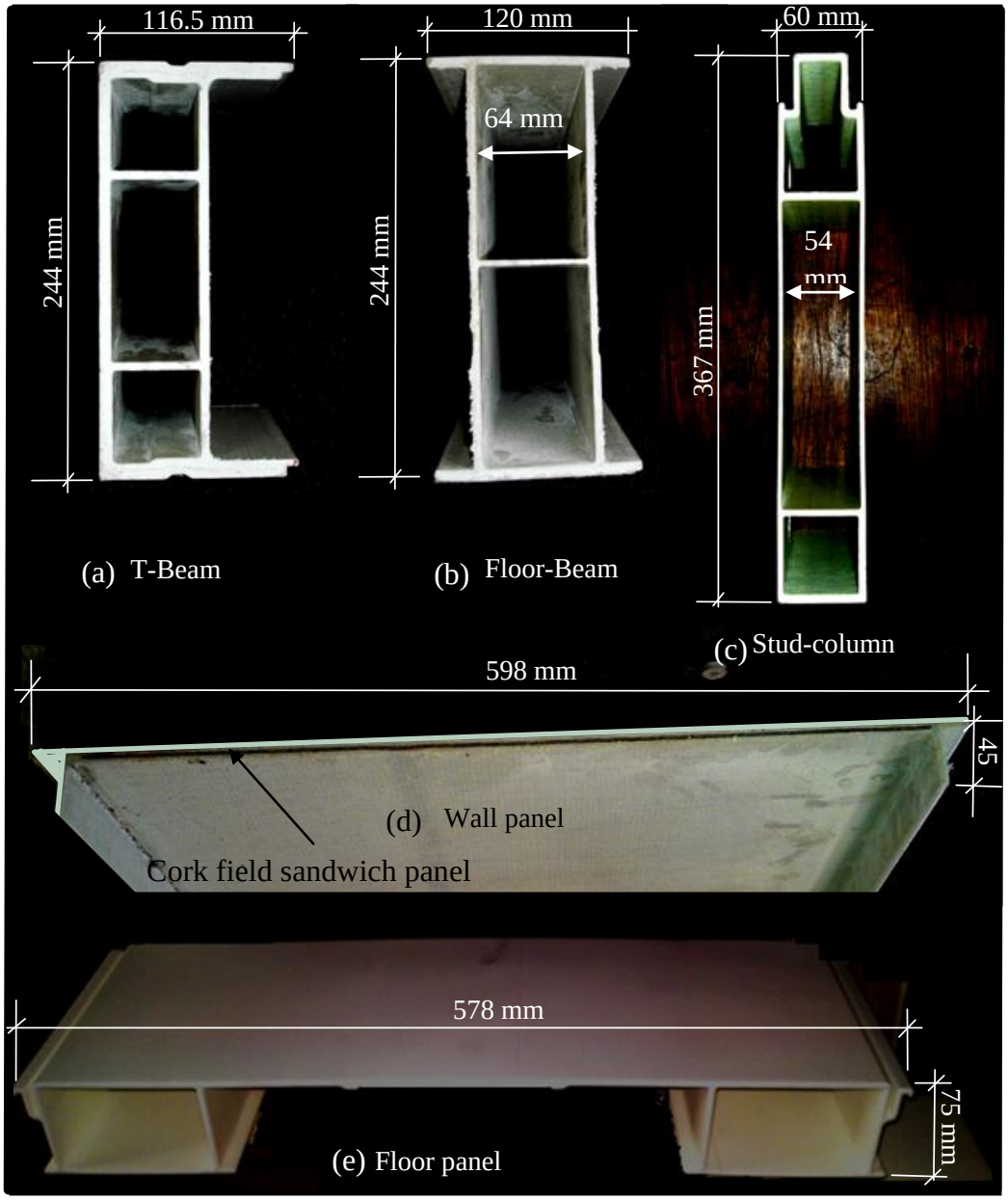

Figure 2.15. Five key pultruded tailored shapes in the Startlink house structure.

The bespoke shapes are the floor panel (overall dimensions are 578×75 mm), wall panel (598×45 mm), Toby-beam or T-beam (244×116.5 mm), floor beam (244×120 mm) and stud column (367×60 mm). The wall panel of 8 mm thickness has a cork core of 3 mm thickness to form a lightweight structural sandwich with lower thermal conductivity and improved noise absorption performance. Cork is a low-impact material adding to the low carbon credentials. Although the preliminary concept for

the Startlink house was based on component's weighing less than 50 kg, the required off-site fabrication meant that the panels weighed up to 500 kg. The house structure consists of the following primary elements:

- ground base frame (see Figure 2.16),
- floor and wall sub-assembly panels (see Figure 2.17),
- floor support square box and tube sections (see Figure 2.18),
- two storey, single bay portal frame (see Figure 2.17).

Figure 2.16 shows a stiff rectangular ring frame which is set-out to be in the horizontal plane for erection of the panels to construct the house superstructure. The photograph of the ground frame was taken during June 2012 at the construction site at Bourne, Lincolnshire. This ring beam frame of 9.9 m by 5.1 m was fabricated of two T-Beams with PFRP sheeting bonded top and bottom to form a large box section frame. The ground beam is supported by 10 FRP screw piles, as shown schematically in Figure 2.19.

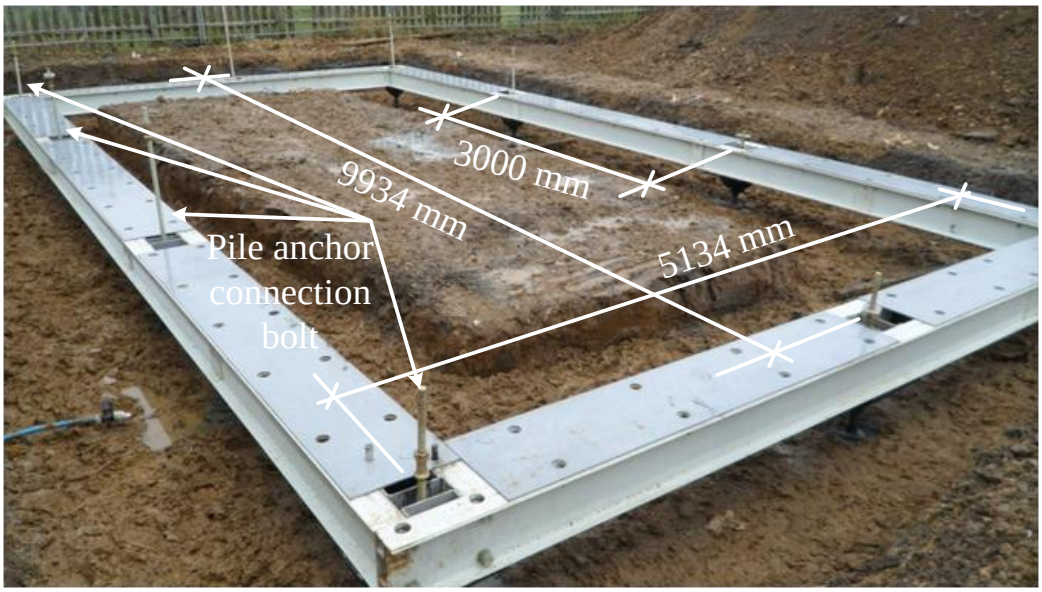

Figure 2.16. Ground frame on the composite pile system.

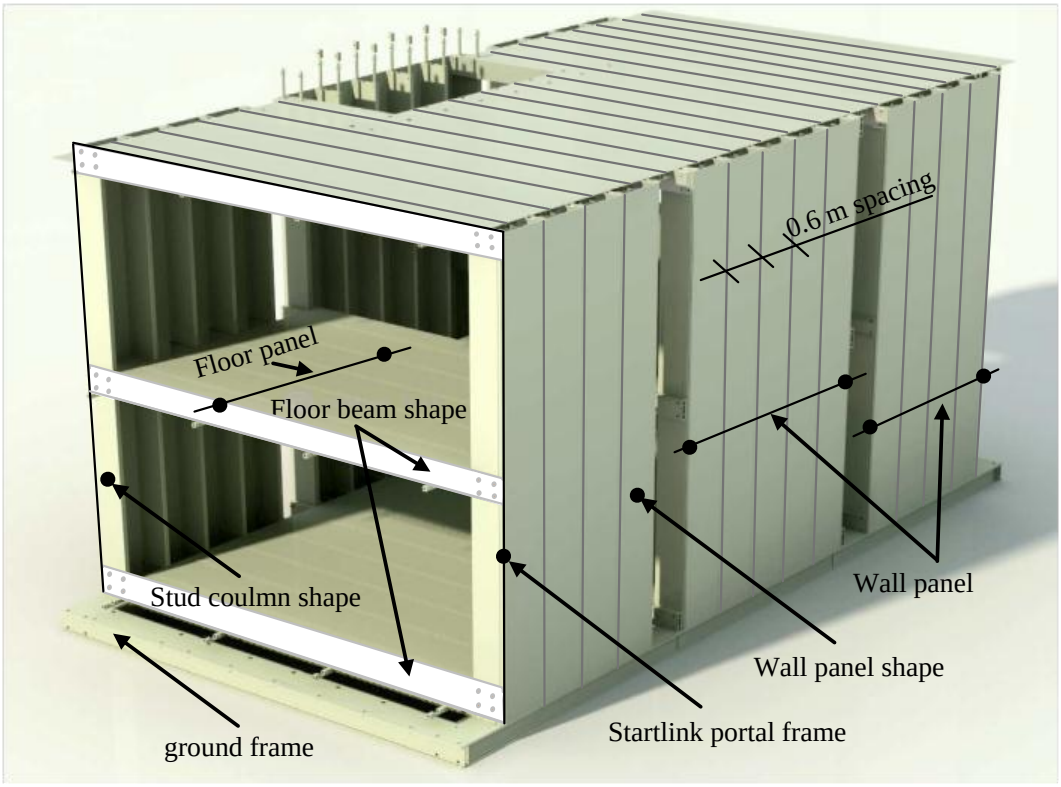

Figure 2.17. Floor and wall sub-assembly panels and two storey, single bay portal frame.

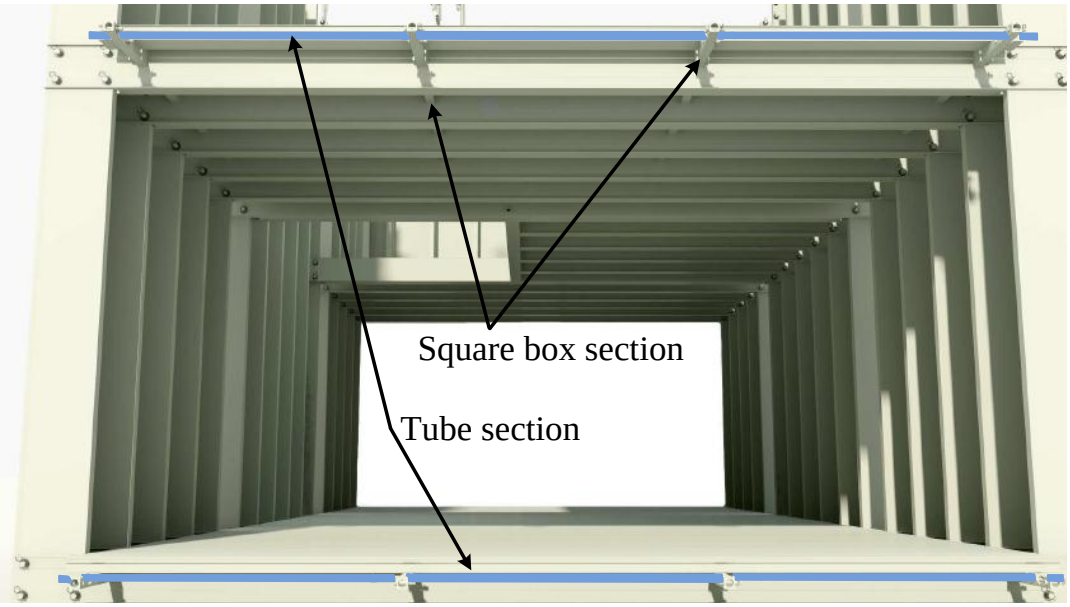

Figure 2.18. Floor panel support square box and tube sections

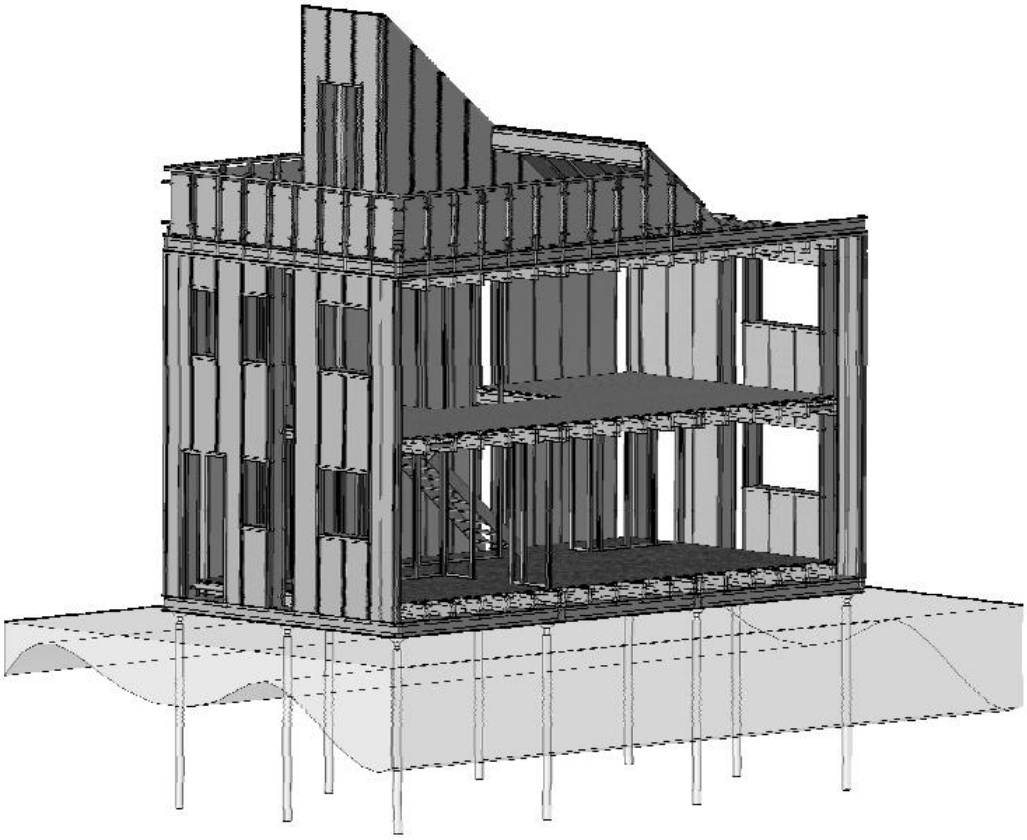

Figure 2.19. Startlink house on ten composites pile system.

It was an original aim of Singleton (2004) for the structural load-bearing members to be joined using snap-fit connections. During the early stages of the detailed design an analysis for the snap-fit joint showed that its bespoke shapes would require tight dimensional tolerances, which may not be possible with pultrusion processing technology. Several alternative snap-fit configurations were investigated by Kendall (2010) to develop the initial concept design in addition to other joining methodologies (Hutchinson and Singleton, 2007). These design calculations showed the Startlink house needed more resistance and stiffness to satisfy several design load cases, and in particularly for the lateral wind loading. There were also concerns that the snap-fit joints may allow small relative movements, resulting in flexibility in the house structure, and possible squeaks and noises as the structure is subjected to wind

and live loads. The structural system in the Startlink house was progressed to have portal frames for the primary load bearing structure. The methods of connection were dowelling and adhesive bonding. Figure 2.17 shows that there is a portal frame, wall and floor panels, every 0.6 m. This sub-assembly is to provide the house with adequate vertical and lateral stiffness. Based on the design analysis by Kendall (2010) the house superstructure is to have rigid frame action to provide adequate lateral stiffness to limit the lateral deflection from wind loading.

Figure 2.18 schematically shows how the floor panels are to be supported between the floor beams by square box sections passing through the floor beams. The box sections are continuous within each floor sub-assembly. Where there are site joints between floor assemblies the tubes may cantilever from the adjacent floor beam, assuming that the tube continues into other floor beams within the floor sub-assembly. From Figure 2.18, it can be seen that there is a horizontal tube on the outer side that makes dowel connections with the vertical stud columns in wall panel sub-assembly. By way of further dowel connections, the secondary tube member passes through box-sections to join the stud columns to either a floor or roof assembly. Figure 2.20 shows the demonstrator house that was constructed at Bourne, Lincolnshire during June to August 2012.

Figure 2.20. Startlink demonstrator house; Bourne, Lincolnshire.

Chapter 3

Effect of Orientation on Pin-bearing Strength

3.1 Introduction

The fibre architecture of PFRP can be varied, in particular, with regard to the proportion of UD rovings that will be used in the direction of pultrusion. Due to this anisotropic property there is strength variation with material orientation. This variation has to be considered when the aim is to design a bolted connection for a PFRP structures.

Considered in this chapter is the strength of plate-to-plate connections when its strength is to be determined by the distinct mode of failure known as bearing (see Section 2.3). Bearing is a failure mode with a strength formula that requires its 'own' material strength property (F_θ^{br}) and the formula is Equation (2.1). It is important to recognize that F_θ^{br} is a directional strength, specific to the bearing load situation, and depending on the orientation (θ) of the connection force with respect to the direction of pultrusion. It is noteworthy to mention that the pin-bearing value is the lower bound strength because there is no through-thickness constraint that is known (Mottram and Turvey, 2003) to significantly increase the connection force prior to bearing failure.

Figures 3.1(a) and 3.1(b) show a web-cleated type joint and a gusset type joint in two primary load bearing structures. With respecting to the pultrusion direction, the shear force from the beam member into the web-cleats is oriented in the transverse (90º) material orientation. For the purpose of design the bearing strength is therefore F_{90}^{br}. For the column member in Figure 3.1(a) the same shear force is directed along the length of the member and therefore, the bearing strength, F_{0}^{br}, is in longitudinal (0º) direction. In Figure 3.1(b) the bracing members are in either the tension or compression and have their resultant axial force aligned in the 0º direction. From Figure 3.1(b) it can also be seen that resultant forces at the bolts in the gusset plate are neither aligned with the 0º nor 90º material directions. Now the structural engineer designing for the resistance of the bolted connections needs to know how the bearing strength varies with θ.

In Section 2.3 the author explained what requirements are needed to make bearing failure the most likely mode, at room temperature, (Mottram and Turvey, 2003). Figures 3.2(a) and 3.2(b) show a specimen from the test series presented in this chapter with the side and top views. Figure 3.2(a) is labelled for the hole diameter d_{n} and the bolt diameter d, which due to a hole clearance is less than d_{n}. The plate is of constant thickness t and constant width w. The form of the pin-bearing failure mode is seen in Figure 3.2(b). The failure mechanism consists of delamination (i.e. splitting) between the layers of the fiber reinforcement, in the through-thickness direction, and in the vicinity of the hole.

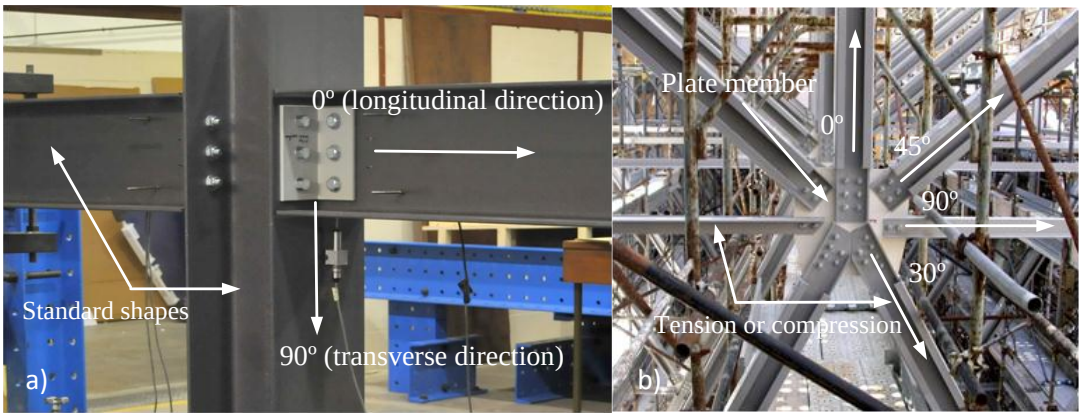

Figure 3.1. Bolted connections and joints: a) frame joint (courtesy of Qureshi, Warwick University); b) plate-to-plate connections (courtesy of Russo, IUAV University).

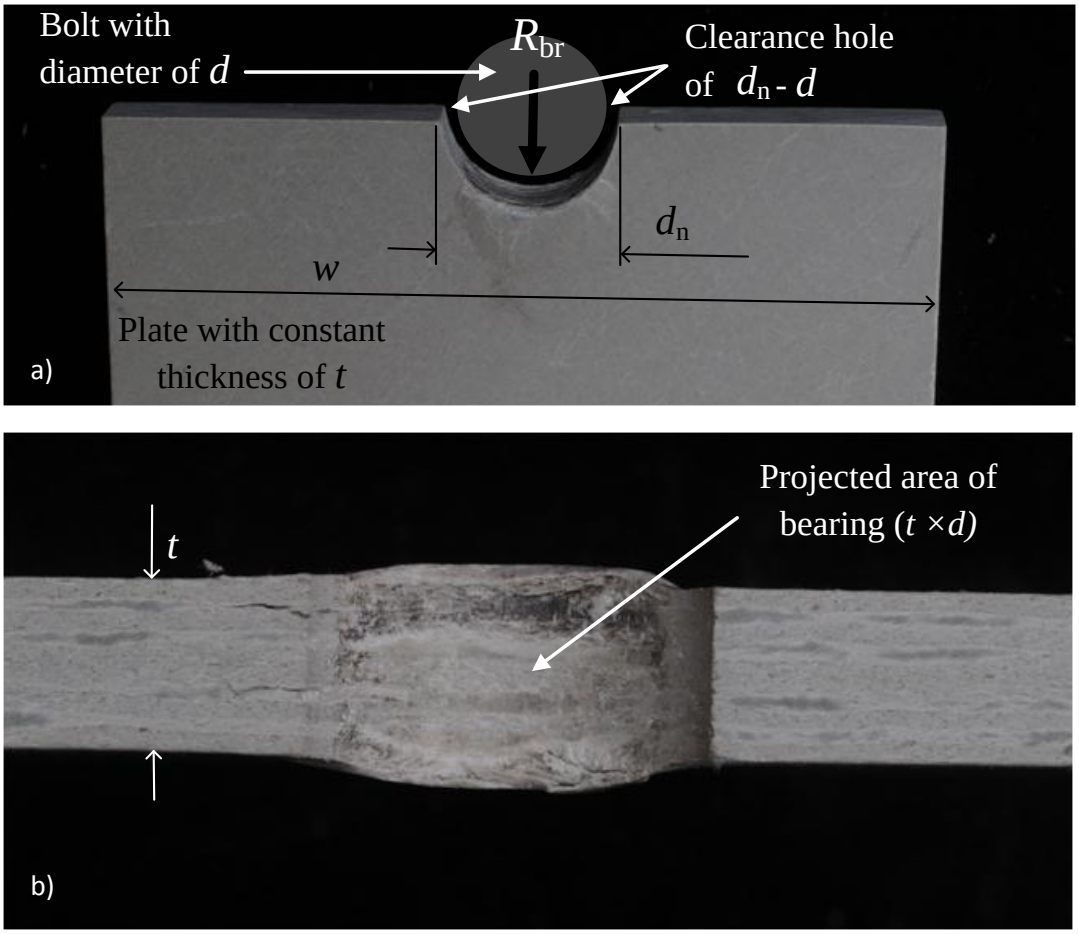

Figure 3.2: a) bearing failure for a specimen using the University of Warwick (UoW) test method; b) projeted bearing area.

For the purpose of design calculations, Equation (2.1) requires the characteristic value of F_{θ}^{br} per bolt. It has been recommended in the LRFD pre-standard (Anonymous, 2012d) that for θ between 0^{o} and 90^{o} the pin-bearing strength be the 0^{o} value when $0^{o} < \theta < 5^{o}$, and that it is the 90^{o} value for $\theta > 5^{o}$. One of the objectives of the work presented in this chapter is to check this mandatory guidance. This requires the determination of characteristic strengths for different orientations that can allow the profile from 0 to 90^{o} to be obtained from curve fitting.

Another purpose of this study is look at the Hankinson's equation (1921), which is in a normalised form is:

$$\frac{F_{\theta}^{\mathrm{br}}}{F_{0}^{\mathrm{br}}} = \frac{F_{90}^{\mathrm{br}}}{\sin^{2}\theta + \frac{F_{90}^{\mathrm{br}}}{F_{0}^{\mathrm{br}}}\cos^{2}\theta} \qquad (3.1)$$

Equation (3.1) is a mathematical relationship that has successfully been used to predict the off-axis (with respect to wood grain orientation) dowel or pin-bearing strength of timber. It is for this reason that it is given for the dowel strength in the American design standard (ASCE-16-95) for engineered wood construction (ASCE, 1995). It exisitence might suggest application with FRP materials. As it can be seen the equation is based on only needing to know the 0^{o} (timber grain orientation) 90^{o} strengths and the angle of orientation θ.

This chapter presents test results to examine the effect of load orientation on the pin-bearing strength of the web material of a Wide Flange (WF) standard shape to be introduce in Section 3.2. Using a non-standard test method a series of tests have been

conducted to characterize the web material and recommendations have been given on how pin-bearing strengths are to be determined so that they will match the geometries of bolted connections found in practice. Prominent test results are determined for pin-bearing strengths when load is oriented at 0, 5, 10, 20, 45 and 90^o to the direction of pultrusion. To complate the text matrix there are four steel 'pin' diameter from 9.7 mm to 25.4 mm. Comparing test results for the six orientations, an evaluation of the data, with varying pin diameter-to-thickness ratio, is made with the aim of establishing how we can specify strength with θ for the safe and reliable design of bolted connections.

3.2 Material and specimens

Specimens were cut from a 203 × 203 × 9.53 mm WF standard shape. Figure 3.3 shows the cross-section of this wide flange shape having a web depth of 180 mm. The web has a mean thickness (t) of 9.2 mm (see column (4) in Tables 3.1 to 3.6). The Creative Pultrusions Inc. (Anonymous, 2012a) product is from the 1525 series having a filled isophthalic polyester polymer. E-glass reinforcement is in the form of alternative layers, but not necessarily continuous or of constant thickness, of unidirectional (UD) rovings and continuous strand mats (Anonymous, 2012a; Bank, 2006). According to the Creative Pultrusion Inc. Design Manual the material has the following mechanical properties (Anon, 2012a):

- in the longitudinal (LenghtWise) direction - compressive modulus (D695) = 20.7 kN/mm^2; compression strength (D 695) = 231 N/mm^2; maximum bearing strength, F_0^{br} (D 953) = 207 N/mm^2.

- in the transverse (CrossWise) direction - compressive modulus (D695) = 7.0 kN/mm^2; compression strength (D 695) = 115 N/mm^2; maximum bearing strength, F_{90}^{br} (D 953) = 126 N/mm^2.

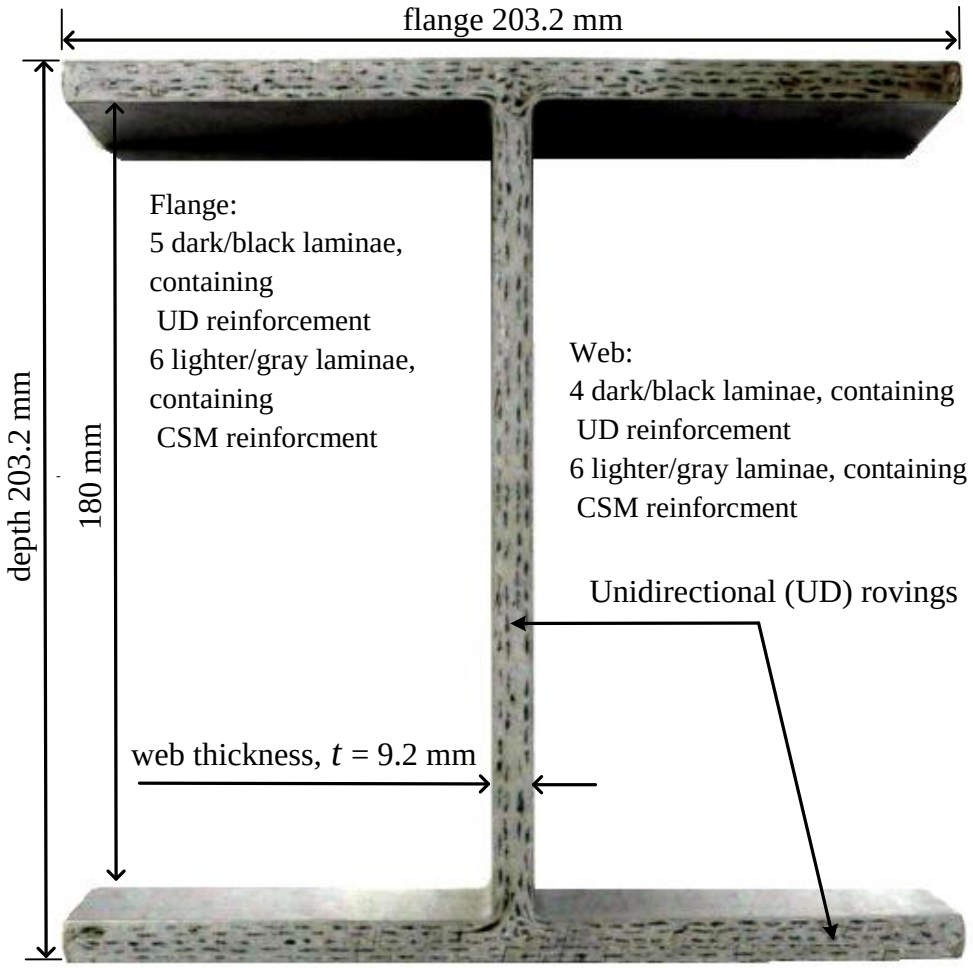

Figure 3.3. Cross-section of Wide-flange standard 203×203× 9.53 I-section with nominal dimension.

These mechanical properties are over a number of years minimum coupon values based on random sampling and testing of production lots (Anonymous., 2012a). It is of interest to note here that if we assume the material is from a standard shape classified as Grade 23, the CEN standard BS EN 13706-3:2002 states that the minimum longitudinal

(F_0^{br}) and transverse (F_{90}^{br}) pin-bearing strengths are 150 and 90 N/mm^2, respectively. The Creative Pultrusion Inc. values of 207 N/mm^2 and 126 N/mm^2 are higher. One reason for the difference is that they had been obtained in-house in accordance with test method D 953 and a failure load for a 4% hole elongation (see Section 2.3.1 and Figure 2.5).

Because bearing failure is most likely to occur when the end distance (e_1) and the width (w) is 4d (see Figure 2.4, Mottram and Turvey (2003)) the specimen height and width are set at 100 mm (for maximum pin diameter of 25 mm); The blank coupon is therefore 125 mm long to accommodate drilling for the 28 mm diameter hole. It is noteworthy that the 90^o coupon blanks of size 125 by 100 mm can readily be cut from the 180 mm deep web in the 203 × 203 × 9.53 wide flange shape. Figure 3.4 and 3.5 show the cutting patterns for having blanks for specimens with the direction of pultrusion at 0^o and 90^o, respectively.

For each of the six orientations of 0, 5, 10, 20, 45 and 90^o there are four batches, comprising the following pairs of nominal hole diameters (d_n) and pin diameters (d): 12 mm and 9.7 mm; 15 mm and 12.2 mm; 21 mm and 18.8 mm and 28 mm and 25.4 mm. The pins represent the smooth shafts of (black grade) steel bolts of diameters 3/8 in., 1/2 in., 3/4 in. and 1 in., respectively. Figure 3.6 shows the overall specimen size in scale of 1:1, having nominal dimensions of 100 × 100 mm. The diameter dimension d_n in the figure defines the four hole sizes required.

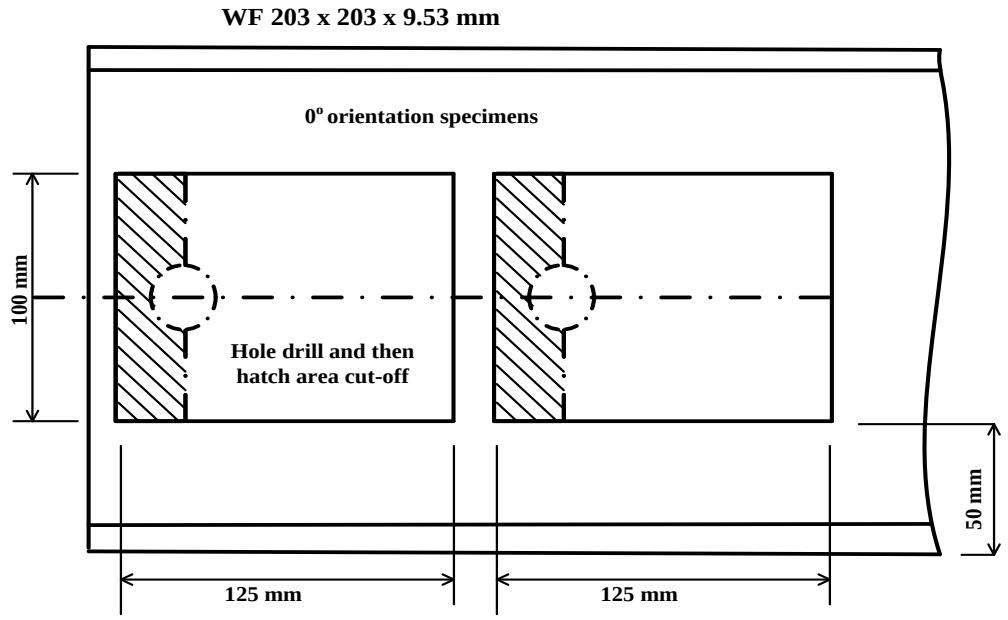

Figure 3.4. Blanks specimens and cutting pattern for the 0^o specimens.

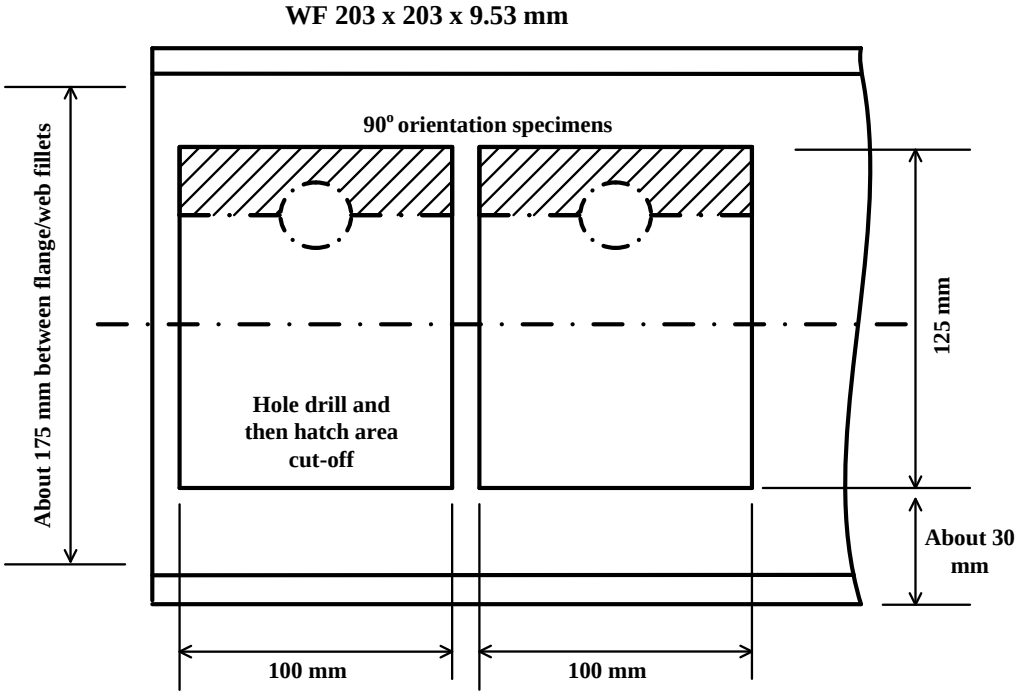

Figure 3.5. Blanks specimens and cutting pattern for the 90^o specimens.

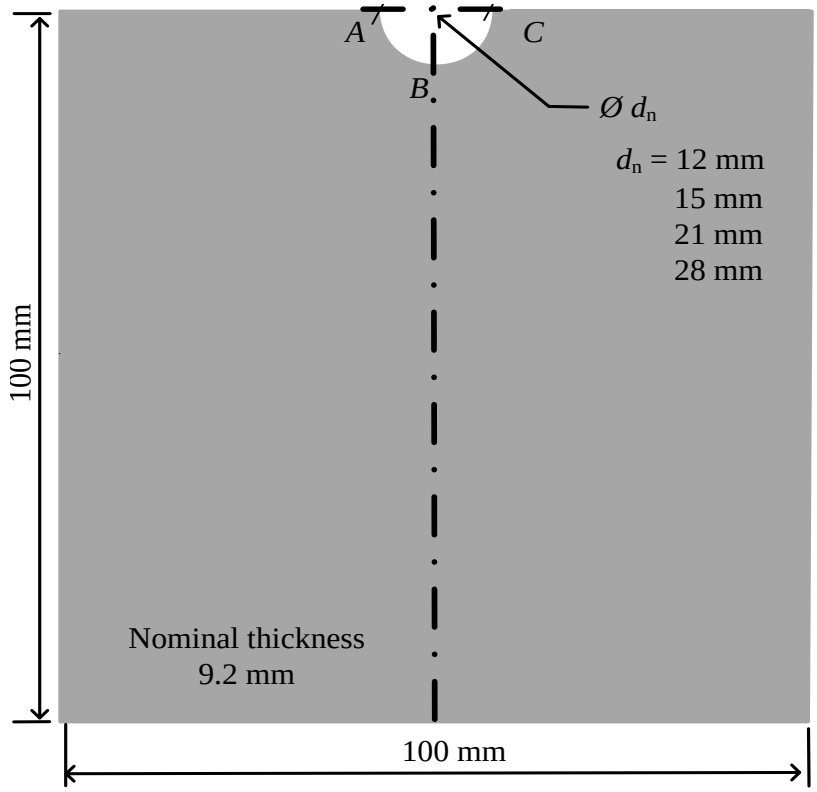

Figure 3.6. Plan of pin-bearing specimen size constant at 100×100 mm (Scale 1:1).

The 24 batches (six orientation × four pin sizes) were labelled with a scheme for the orientations of material, followed by the diameter of semi-circular notch (d_n), and next the number of specimen in the batch. For example, 0-21-06 is for the specimen having 0º orientation material, a nominal hole diameter of 21 mm and number of 6 in the batch.

Presented in Tables 3.1 to 3.6 are the measured thickness, semi-notch diameter and clearance hole per specimen in mm for all 24 batches of nominally identical specimens. In these tables column (1) and (2) are for the specimens labelling. Column (1) is for the material orientation and diameter of hole and Column (2) gives

the specimen number. Reported in Column (3) are measured thickness at three points of *A*, *B* and *C*, shown in Figure 3.6, to the nearest 0.05 mm with an outside micrometer, and *t* is found to have an average in the range of 8.88 to 9.40 mm. Average thickness (*t*) per specimen is given in Column (4). In Column (5) are measured notch diameters (d_n) and in the last column are hole clearances obtained using $d_n - d$. For each batch there are mean values of average thickness (*t*), notch diameter (d_n) and hole clearance, which are reported in the row immediately after the end of batch information. Number of nominally identical specimens per batch for the orientations of 0, 5, 10 and 20^o is from 10 to 13. This was reduced to six for the orientation of 45^o and 90^o and this batch property is reported in Tables 3.1 to 3.6. In total pin-bearing strength orientation tests have been carried out with 230 coupon specimens.

Table 3.1. Measured thickness, notch diameter and hole clearance for specimens with longitudinal (0º) material orientation.

Specimen		Measured thicknesses (t,mm)			Average (t,mm)	Notch (d_n,mm)	Clearance hole (mm)	Specimen		Measured thicknesses (t,mm)			Average (t,mm)	Notch (d_n,mm)	Clearance hole (mm)
(1)	(2)	(3)			(4)	(5)	(6)	(1)	(2)	(3)			(4)	(5)	(6)
	01	9.11	9.11	9.15	9.12	11.8	2.1		01	9.13	9.10	9.10	9.11	20.9	2.0
	02	9.13	9.15	9.13	9.14	11.8	2.1		02	9.10	9.07	9.08	9.08	20.8	2.0
	03	9.18	9.16	9.18	9.17	11.8	2.1		03	9.08	9.06	9.12	9.09	20.8	2.0
	04	9.25	9.16	9.22	9.21	11.8	2.1		04	9.12	9.08	9.06	9.09	20.8	2.0
	05	9.17	9.15	9.17	9.16	11.8	2.1		05	9.11	9.14	9.17	9.11	21.0	2.2
0-12	06	9.20	9.20	9.22	9.21	11.8	2.1	**0-21**	06	9.08	9.08	9.17	9.11	21.0	2.2
	07	9.12	9.13	9.14	9.13	11.8	2.1		07	9.21	9.13	9.13	9.16	20.9	2.1
	08	9.23	9.23	9.25	9.24	11.8	2.1		08	9.08	9.07	9.07	9.07	20.9	2.1
	09	9.11	9.11	9.09	9.10	11.8	2.1		09	9.20	9.11	9.11	9.14	20.8	2.0
	10	9.11	9.12	9.14	9.12	11.9	2.2		10	9.20	9.15	9.08	9.14	20.8	2.0
	11	9.10	9.15	9.11	9.12	11.8	2.1		11	9. 15	9.15	9.20	9.17	20.9	2.1
				Mean	**9.16**	**11.8**	**2.1**					**Mean**	**9.12**	**20.9**	**2.1**
	01	9.09	9.12	9.15	9.12	14.8	2.6		01	9.12	9.11	9.16	9.13	27.9	2.5
	02	9.12	9.07	9.07	9.09	14.8	2.6		02	9.17	9.08	9.04	9.09	27.9	2.5
	03	9.15	9.13	9.13	9.14	14.8	2.6		03	9.21	9.13	9.09	9.14	27.8	2.4
	04	9.08	9.12	9.12	9.11	14.8	2.6		04	9.20	9.16	9.11	9.16	27.8	2.4
	05	9.15	9.10	9.10	9.12	14.9	2.7		05	9.10	9.14	9.13	9.12	27.9	2.5
0-15	06	9.13	9.13	9.12	9.13	14.8	2.6	**0-28**	06	9.13	9.14	9.20	9.16	27.9	2.5
	07	9.13	9.13	9.10	9.12	14.9	2.7		07	9.12	9.16	9.13	9.14	27.9	2.5
	08	9.15	9.12	9.09	9.12	14.9	2.7		08	9.10	9.10	9.23	9.14	27.9	2.5
	09	9.22	9.20	9.23	9.22	14.8	2.6		09	9.22	9.17	9.11	9.17	27.9	2.5
	10	9.11	9.14	9.07	9.11	14.8	2.6		10	9.10	9.12	9.22	9.15	27.9	2.5
	11	9. 27	9.16	9.25	9.23	14.8	2.6		11	9. 21	9.13	9.10	9.15	27.9	2.5
				Mean	**9.14**	**14.8**	**2.6**					**Mean**	**9.14**	**27.9**	**2.5**

Table 3.2. Measured thickness, notch diameter and hole clearance for specimens with 5º material orientation.

Specimen		Measured thicknesses (t,mm)			Average (t,mm)	Notch (d_n,mm)	Clearance hole (mm)	Specimen		Measured thicknesses (t,mm)			Average (t,mm)	Notch (d_n,mm)	Clearance hole (mm)
(1)	(2)	(3)			(4)	(5)	(6)	(1)	(2)	(3)			(4)	(5)	(6)
5-12	01	9.15	9.20	9.15	9.17	12.0	2.3	**5-21**	01	9.21	9.31	9.34	9.29	21.0	2.2
	02	9.21	9.21	9.23	9.22	12.0	2.3		02	9.17	9.30	9.19	9.22	20.9	2.1
	03	9.18	9.18	9.14	9.17	12.0	2.3		03	9.18	9.22	9.29	9.23	21.2	2.4
	04	9.18	9.18	9.16	9.17	12.0	2.3		04	9.20	9.24	9.18	9.21	21.2	2.4
	05	9.17	9.19	9.17	9.18	12.0	2.3		05	9.16	9.20	9.21	9.19	21.2	2.4
	06	9.21	9.19	9.27	9.22	12.0	2.3		06	9.12	9.29	9.23	9.21	20.9	2.1
	07	9.16	9.17	9.17	9.17	12.0	2.3		07	9.23	9.20	9.20	9.21	21.0	2.2
	08	9.15	9.17	9.16	9.16	11.9	2.2		08	9.18	9.33	9.28	9.26	21.3	2.5
	09	9.10	9.13	9.07	9.10	12.0	2.3		09	9.13	9.19	9.13	9.15	21.2	2.4
	10	9.24	9.23	9.26	9.24	12.0	2.3		10	9.15	9.26	9.25	9.22	21.2	2.4
									11	9.10	9.13	9.09	9.11	21.3	2.5
				Mean	**9.18**	**12.0**	**2.3**					**Mean**	**9.21**	**21.1**	**2.3**
5-15	01	9.24	9.18	9.21	9.21	14.8	2.6	**5-28**	01	9.20	9.20	9.24	9.21	27.8	2.4
	02	9.14	9.18	9.14	9.15	14.7	2.5		02	9.15	9.38	9.32	9.28	27.9	2.5
	03	9.07	9.12	9.09	9.09	14.8	2.6		03	9.21	9.19	9.22	9.21	27.9	2.5
	04	9.22	9.24	9.22	9.23	14.8	2.6		04	9.17	9.19	9.19	9.18	27.7	2.3
	05	9.12	9.20	9.13	9.15	14.8	2.6		05	9.28	9.18	9.17	9.21	27.8	2.4
	06	9.24	9.24	9.24	9.24	14.9	2.7		06	9.21	9.25	9.36	9.27	27.9	2.5
	07	9.16	9.12	9.22	9.17	14.8	2.6		07	9.21	9.14	9.21	9.19	27.7	2.3
	08	9.30	9.20	9.22	9.24	14.7	2.5		08	9.25	9.11	9.18	9.18	27.9	2.5
	09	9.18	9.20	9.22	9.20	14.8	2.6		09	9.18	9.38	9.28	9.28	27.8	2.4
	10	9.15	9.26	9.21	9.21	14.8	2.6		10	9.21	9.19	9.17	9.19	27.8	2.4
	11	9.14	9.12	9.09	9.12	14.8	2.6		11	9.18	9.23	9.22	9.21	27.8	2.4
	12	9.21	9.17	9.24	9.21	14.8	2.6								
				Mean	**9.18**	**14.8**	**2.6**					**Mean**	**9.22**	**27.8**	**2.4**

Table 3.3. Measured thickness, notch diameter and hole clearance for specimens with 10º material orientation.

Specimen		Measured thicknesses (t,mm)			Average (t,mm)	Notch (d_n,mm)	Clearance hole (mm)	Specimen		Measured thicknesses (t,mm)			Average (t,mm)	Notch (d_n,mm)	Clearance hole (mm)
(1)	(2)	(3)			(4)	(5)	(6)	(1)	(2)	(3)			(4)	(5)	(6)
	01	9.25	9.20	9.18	9.21	11.9	2.2		01	9.21	9.30	9.22	9.24	21.1	2.3
	02	9.18	9.14	9.21	9.18	11.9	2.2		02	9.36	9.19	9.21	9.25	21.1	2.3
	03	9.15	9.11	9.12	9.13	11.9	2.2		03	9.21	9.32	9.13	9.22	20.9	2.1
	04	9.17	9.18	9.22	9.19	12.0	2.3		04	9.21	9.21	9.16	9.19	21.1	2.3
	05	9.27	9.24	9.25	9.25	11.8	2.1		05	9.16	9.20	9.18	9.18	21.0	2.2
10-12	06	9.28	9.18	9.20	9.22	11.9	2.2	**10-21**	06	9.24	9.16	9.09	9.16	21.0	2.2
	07	9.15	9.13	9.16	9.15	11.9	2.2		07	9.23	9.33	9.18	9.25	21.2	2.4
	08	9.15	9.13	9.16	9.15	11.9	2.2		08	9.15	9.26	9.15	9.19	21.3	2.5
	09	9.19	9.19	9.12	9.17	11.9	2.2		09	9.25	9.20	9.18	9.21	21.1	2.3
	10	9.24	9.17	9.27	9.23	12.0	2.3		10	9.22	9.17	9.12	9.17	21.1	2.3
	11	9.19	9.16	9.15	9.17	11.9	2.2		11	9.14	9.30	9.11	9.18	21.2	2.4
				Mean	**9.18**	**11.9**	**2.2**					**Mean**	**9.20**	**21.1**	**2.3**
	01	9.18	9.20	9.22	9.20	14.9	2.7		01	9.20	9.49	9.21	9.30	27.9	2.5
	02	9.24	9.18	9.18	9.20	14.9	2.7		02	9.11	9.36	9.17	9.21	27.8	2.4
	03	9.29	9.16	9.17	9.21	14.9	2.7		03	9.21	9.19	9.14	9.18	27.8	2.4
	04	9.25	9.16	9.16	9.19	14.9	2.7		04	9.25	9.20	9.18	9.21	27.8	2.4
	05	9.25	9.22	9.14	9.20	14.9	2.7		05	9.16	9.21	9.14	9.17	27.9	2.5
10-15	06	9.28	9.19	9.23	9.23	14.9	2.7	**10-28**	06	9.14	9.43	9.21	9.26	27.8	2.5
	07	9.12	9.16	9.19	9.16	14.9	2.7		07	9.23	9.22	9.24	9.23	27.8	2.4
	08	9.16	9.23	9.21	9.20	14.9	2.7		08	9.30	9.28	9.22	9.27	27.8	2.4
	09	9.16	9.17	9.21	9.18	14.9	2.7		09	9.29	9.21	9.24	9.25	27.9	2.5
	10	9.16	9.23	9.16	9.18	14.9	2.7		10	9.12	9.26	9.27	9.22	27.9	2.5
	11	9.24	9.16	9.26	9.22	14.9	2.7		11	9.26	9.37	9.25	9.29	27.9	2.5
				Mean	**9.20**	**14.9**	**2.7**					**Mean**	**9.24**	**27.8**	**2.4**

Table 3.4. Measured thickness, notch diameter and hole clearance for specimens with 20º material orientation.

Specimen		Measured thicknesses (t,mm)			Average (t,mm)	Notch (d_n,mm)	Clearance hole (mm)	Specimen		Measured thicknesses (t,mm)			Average (t,mm)	Notch (d_n,mm)	Clearance hole (mm)
(1)	(2)	(3)			(4)	(5)	(6)	(1)	(2)	(3)			(4)	(5)	(6)
	01	9.27	9.34	9.29	9.30	11.8	2.1		01	9.37	9.24	9.13	9.25	20.8	2.0
	02	9.15	9.14	9.19	9.16	11.8	2.1		02	9.13	9.13	9.10	9.12	21.1	2.3
	03	9.12	9.13	9.24	9.16	11.9	2.2		03	9.28	9.34	9.32	9.28	21.0	2.2
	04	9.15	9.18	9.21	9.18	11.7	2.0		04	9.38	9.26	9.13	9.25	21.0	2.2
	05	9.24	9.29	9.31	9.28	11.9	2.2		05	9. 30	9.54	9.25	9.36	21.3	2.5
	06	9.35	9.43	9.25	9.34	11.9	2.2		06	9.21	9.15	9.26	9.21	21.1	2.3
20-12	07	9.22	9.07	9.16	9.15	11.9	2.2	**20-21**	07	9.28	9.54	9.23	9.35	21.9	3.1
	08	9.32	9.34	9.20	9.29	11.9	2.2		08	9.18	9.15	9.17	9.17	21.0	2.2
	09	9.30	9.23	9.23	9.25	11.9	2.2		09	9.15	9.18	9.17	9.17	21.1	2.3
	10	9.21	9.31	9.22	9.25	11.9	2.2		10	9.28	9.27	9.24	9.26	21.0	2.2
	11	9.19	9.21	9.27	9.22	11.9	2.2		11	9.26	9.48	9.22	9.32	21.2	2.4
	12	9.14	9.09	9.16	9.13	11.9	2.2		12	9.22	9.17	9.21	9.20	21.1	2.3
	13	9.20	9.23	9.19	9.21	11.9	2.2		13						
				Mean	**9.23**	**11.9**	**2.2**					**Mean**	**9.24**	**21.1**	**2.3**
	01	9.17	9.18	9.17	9.17	14.6	2.4		01	9.17	9.17	9.20	9.18	27.8	2.4
	02	9.27	9.19	9.21	9.22	14.8	2.6		02	9.18	9.14	9.13	9.15	27.8	2.4
	03	9.17	9.15	9.08	9.13	14.8	2.6		03	9.26	9.12	9.20	9.19	27.9	2.5
	04	9.18	9.23	9.23	9.21	14.9	2.7		04	9.22	9.17	9.21	9.20	27.9	2.5
	05	9.23	9.12	9.17	9.17	14.9	2.7		05	9. 20	9.38	9.18	9.25	27.9	2.5
	06	9.15	9.22	9.16	9.18	14.9	2.7		06	9.14	9.17	9.07	9.13	27.9	2.5
20-15	07	9.20	9.16	9.16	9.17	14.8	2.6	**20-28**	07	9.32	9.55	9.33	9.40	27.9	2.5
	08	9.14	9.19	9.18	9.17	14.8	2.6		08	9.18	9.18	9.16	9.17	27.9	2.5
	09	9.13	9.19	9.14	9.15	14.8	2.6		09	9.24	9.50	9.21	9.32	27.9	2.5
	10	9.15	9.12	9.17	9.15	14.9	2.7		10	9.21	9.29	9.20	9.23	27.9	2.5
	11	9.26	9.22	9.18	9.22	14.9	2.7		11	9.16	9.10	9.16	9.14	27.9	2.5
	12	9.14	9.16	9.15	9.15	14.9	2.7		12	9.16	9.17	9.19	9.17	27.8	2.4
	13	9.16	9.19	9.29	9.21	14.9	2.7		13						
				Mean	**9.18**	**14.8**	**2.6**					**Mean**	**9.21**	**27.9**	**2.5**

Table 3.5. Measured thickness, notch diameter and hole clearance for specimens with 45º and transverse (90º) material orientation.

Specimen		Measured thicknesses (t,mm)			Average (t,mm)	Notch (d_n,mm)	Clearance hole (mm)	Specimen		Measured thicknesses (t,mm)			Average (t,mm)	Notch (d_n,mm)	Clearance hole (mm)
(1)	(2)	(3)			(4)	(5)	(6)	(1)	(2)	(3)			(4)	(5)	(6)
45-12	01	9.23	9.16	9.19	9.19	11.8	2.1	**90-12**	01	9.20	9.16	9.20	9.19	11.8	2.1
	02	9.02	9.12	9.10	9.08	11.8	2.1		02	9.05	9.05	9.05	9.05	11.8	2.1
	03	9.20	9.20	9.18	9.19	11.8	2.1		03	9.03	9.02	9.03	9.03	11.8	2.1
	04	9.09	9.10	9.03	9.07	11.7	2.0		04	9.05	9.05	9.05	9.05	11.8	2.1
	05	9.25	9.24	9.25	9.24	11.9	2.2		05	9.05	9.10	9.05	9.07	11.8	2.1
	06	8.97	8.95	8.95	8.96	11.8	2.1		06	9.15	9.15	9.12	9.14	11.8	2.1
				Mean	**9.12**	**11.8**	**2.1**					**Mean**	**9.09**	**11.8**	**2.1**
45-15	01	9.18	9.18	9.18	9.18	14.8	2.6	**90-15**	01	9.05	9.12	9.07	9.08	14.8	2.6
	02	9.09	9.10	9.14	9.11	14.8	2.6		02	9.07	9.09	9.09	9.08	15.0	2.8
	03	8.88	8.90	8.90	8.90	14.8	2.6		03	9.22	9.15	9.21	9.19	14.8	2.6
	04	9.20	9.23	9.23	9.22	14.8	2.6		04	9.10	9.13	9.10	9.11	14.9	2.7
	05	8.93	8.93	8.95	8.94	14.8	2.6		05	9.05	9.12	9.07	9.08	14.8	2.6
	06	9.27	9.24	9.17	9.23	14.7	2.5		06	9.08	9.07	9.08	9.07	14.8	2.6
				Mean	**9.10**	**14.8**	**2.6**					**Mean**	**9.10**	**14.8**	**2.6**
45-21	01	9.07	9.04	9.09	9.07	20.9	2.1	**90-21**	01	9.22	9.22	9.19	9.21	20.9	2.1
	02	9.23	9.24	9.24	9.24	20.8	2.0		02	9.16	9.16	9.19	9.17	20.9	2.1
	03	9.21	9.23	9.24	9.23	20.9	2.1		03	9.13	9.13	9.12	9.13	20.9	2.1
	04	8.90	8.90	8.90	8.90	20.9	2.1		04	9.20	9.16	9.17	9.17	20.9	2.1
	05	8.98	8.95	8.97	8.96	20.9	2.1		05	9.16	9.16	9.19	9.17	20.9	2.1
	06	9.27	9.28	9.18	9.24	20.9	2.1		06	9.16	9.16	9.20	9.18	20.9	2.1
				Mean	**9.11**	**20.9**	**2.1**					**Mean**	**9.17**	**20.9**	**2.1**
45-28	01	8.87	8.88	8.88	8.88	27.8	2.4	**90-28**	01	9.14	9.17	9.20	9.17	27.9	2.5
	02	9.00	8.97	8.98	9.11	27.8	2.4		02	9.08	9.04	9.05	9.06	27.8	2.4
	03	9.06	9.05	9.06	9.06	27.8	2.4		03	9.18	9.20	9.18	9.19	27.8	2.5
	04	9.22	9.25	9.20	9.22	27.8	2.4		04	9.24	9.30	9.25	9.26	279	2.5
	05	9.23	9.23	9.16	9.21	27.8	2.4		05	9.20	9.19	9.18	9.19	27.9	2.5
	06	9.09	9.09	9.10	9.09	27.8	2.4		06	9.21	9.25	9.25	9.23	27.8	2.4
				Mean	**9.10**	**27.8**	**2.4**					**Mean**	**9.18**	**27.9**	**2.5**

In section 2.3.2 on the historical review of test methods for pin-bearing strength it is recognised that to calculate a safe nominal (design) strength by using Equation (2.1), it is essential that F_{θ}^{br} account for the strength reduction due to hole clearance, and for much larger material thicknesses and bigger bolt sizes found in practice. In what follows the author provides the test methodology used to calculate a safe nominal (design) strength, test rig and test procedure.

3.3 Warwick University Test Method for Pin-bearing Strength

On reviewing the scope and limitations of the existing standard test methods (e.g., ASTM D953-02, ASTM D 5961-05, BS EN 13706-2:2002) Mottram (2009b) found that none can satisfy the requirements needed to establish a characteristic pin-bearing strength for Equation (2.1). Reasons for this finding are that current standards do not require bearing strength to be determined when there is a clearance hole and the much larger material thicknesses and bigger bolt sizes permitted in practice. A fourth reason that was identified is that the size of the largest tension loaded coupon is too big to be cut from pultruded structural shapes, such as those tabulated in Anonymous (2012a,b) and shown in Figure 3.3. An alternative arrangement for applying the bearing load is sought that can accommodate a smaller coupon size that can be cut from structural shapes.

Using 6.35 mm (1/4 in.) thick flat sheet material the preliminary study by Mottram (2009b), presents a useful comparison of pin-bearing strengths determined by using two different test methods. A key finding is that the two test methods do not give significantly different pin-bearing strength measurements. One method is in the spirit of Annex E to BS EN 13706-2 that has the tensile loaded specimen shown in Figure

2.6, while the second method, requiring a much smaller compression specimen, is in the spirit of the test method ASTM D5764-97a (reapproved 2007). This approach for 'timber' materials removes the tensile specimen size problem and has previously been used to characterise bearing strengths of laminated FRPs (Wang *et al*., 1996). A compression loading rig and specimen holder used at University of Warwick (UoW) for the latter test method is shown in Figures 3.7. This arrangement is based on compressing a plain shank pin (for no bolt thread) into small rectangular specimens with a semi-circular notch positioned at the centre of specimen. The specimen is held vertically in a steel holder having uniform grooves in the side walls to accommodate the material thickness. With the required specimen blank size of 125 mm by 100 mm, for the biggest bolt diameter of 25.4 mm (see Figures 3.4 and 3.5), these plan dimensions remove the tensile specimen size problem of requiring (BS EN 13706-2) a blank 300 by 150 (6*d*) mm. It is possible only to cut the much bigger BS EN 13706-2 blank from flat sheet, and pultruders are not known to produce sheeting with the fiber architecture of their standard structural shapes.

Figures 3.7(a) and 3.7(b) show the UoW in-house compression die set with fixtures to apply compressive loading via steel pin. In Figure 3.7(a) the pin, cut from the smooth shank of a black steel bolt (Grade 8.8), has diameter of 25.4 mm (1 in.) and in Figure 3.7(b) it has the smallest of the four diameters at 9.7 mm (3/8 in.). The specimen holder accommodates the nominal specimen thickness (see Tables 3.1 to 3.6) of 9.2 mm. The purpose of the holder is to keep the specimen vertical and to provide it with a degree of lateral restraint against out-of-plane flexural deformation. Load is applied under a constant stroke rate of -0.01 mm/s using a DARTEC 9500 hydraulic testing machine with a ±250 kN load cell.

To establish the maximum compressive force at bearing failure, 0.338 kN is added to the maximum machine reading to allow for the dead weight of the top plate and rocker transfer fixture (as seen in Figures 3.7(a) and 3.7(b)). A Solartron SI 3531 data acquisition system is used to monitor the load and stroke in real time, at the rate of one pair of readings every two seconds. To reach the maximum load the duration of testing can be over 120 seconds.

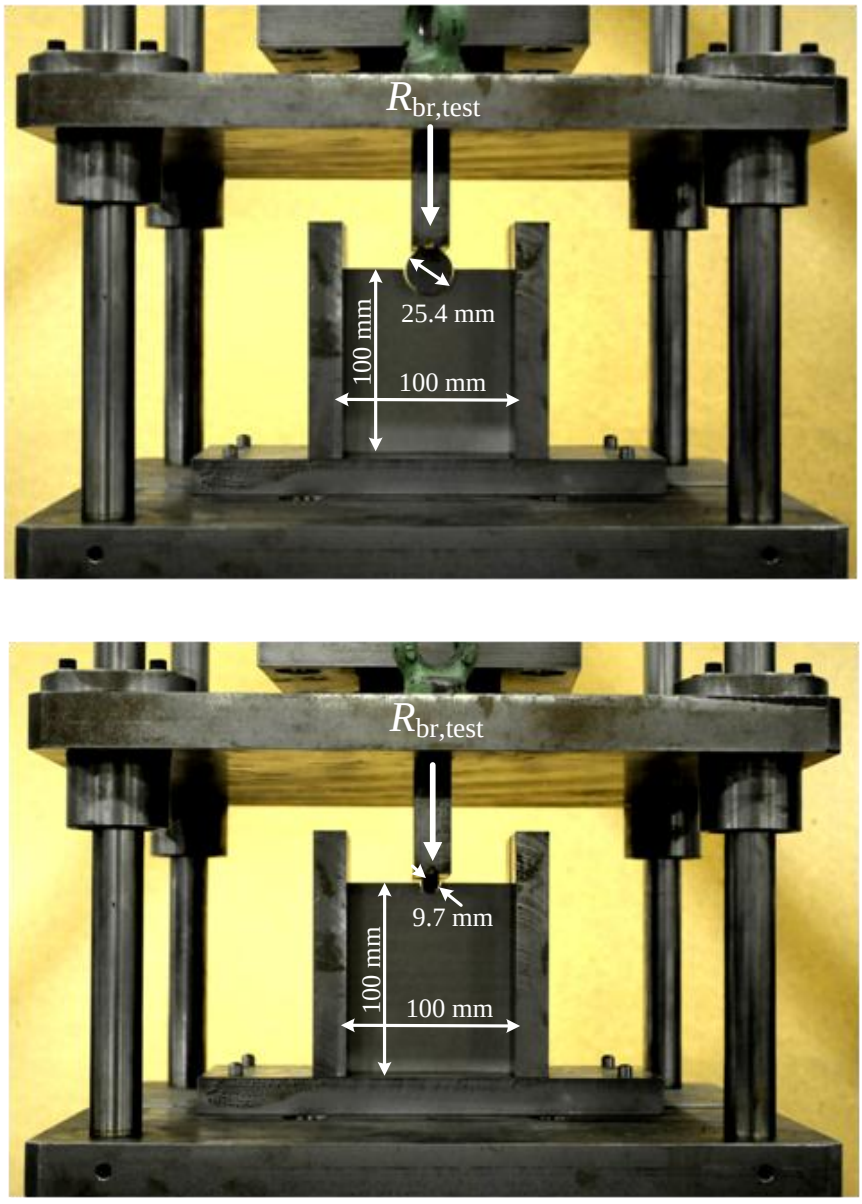

Figure 3.7. UoW pin-bearing strength test rig with a specimen ((a) nominal d = 25.4 mm, (b) nominal d = 9.7 mm).

To determine the pin-bearing strength compressive force ($R_{br,test}$) is the maximum attained (case (a) in Figure 2.5). This is because the author believes that the definition (c) (Johnson and Matthews, 1979) is not suitable as 4% elongation of connection hole can be too high for PFRP. Moreover, Mottram (2009b) identified that failure definitions (d) to (g) had not been observed in pultruded materials for pin-bearing tests and (b) did not occur for the longitudinal direction. Therefore, the bearing strengths should be determined using failure load (a), the maximum load. Figure 3.8 shows load-stroke plots from pin-bearing tests using the UoW loading arrangement introduced in Mottram (2009b).

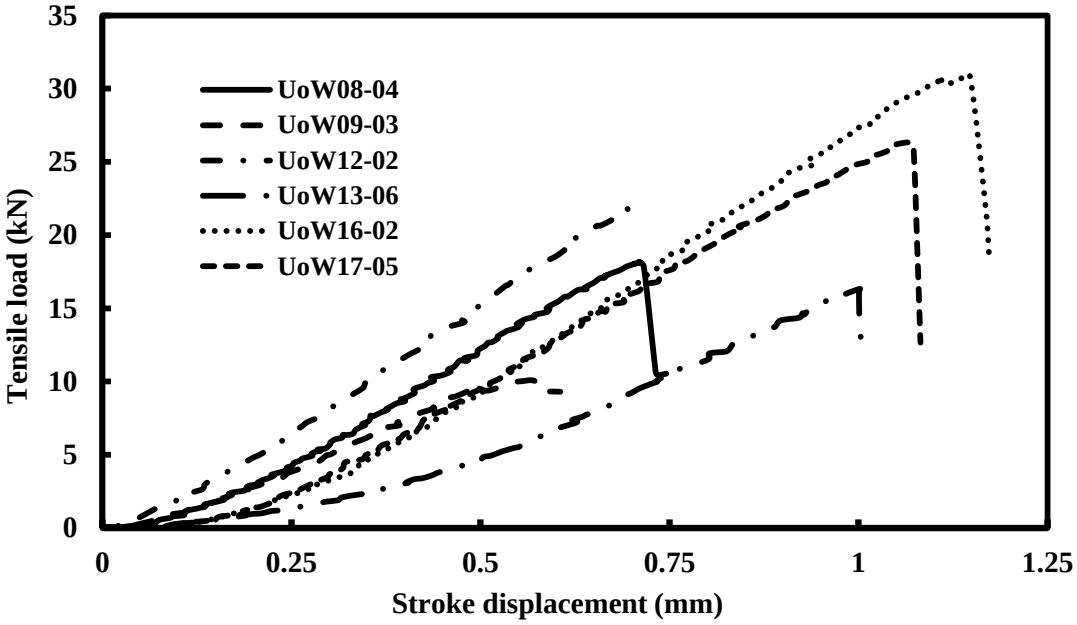

Figure 3.8 Load-stroke plots from pin-bearing tests using the UoW test method (reproduced from Figure 7 in Mottram (2009b)).

3.4 Test Results and Discussion

Test results for 0, 5, 10, 20, 45 and 90° material orientations are obtained from a series of pin-bearing strength tests using the UoW test method at room temperature.

Tables 3.6 and 3.11 present a summary of the test results, with the ordering for orientations of 0° to 90°. The tables have the following content. Entries in the row of columns to the right of it have the name of the property. The rest of the columns, in order from left to right, are for the four different pin diameters (d) of 9.7 mm, 12.2 mm, 18.8 mm and 25.4 mm (see the entries of row three) with their batch for the labelling given in row two. Directly beneath the row of title of table with the content of orientation of web material the first and second rows list, for the batch of specimens, the mean thickness (t) and the mean notch diameter (d_n). The mean measured of thicknesses (t), diameters (d and d_n) and hole clearance (d_n - d) per batch, taken from Tables 3.1 to 3.5 (nominal pin diameters are not included), are given in rows one to four. It is to be noted that the minimum clearance of 2.1 mm (from row four of Tables 3.1 to 3.5) is above the 1.6 mm ($1/16^{th}$ in. recommended in pultruders' design manuals (Anonymous,2012a,b)) and the clearance size was dictated by the available drill bit diameters. It can therefore be expected that strength measurements are on the low (safe) side since bearing strength reduces with clearance hole size. For each batch the mean, Standard Deviation (SD) and Coefficient of Variation (CV) are given in rows six to eight on the assumption that the strength population fits the Gaussian distribution. Strengths are given in units of N/mm^2 (MPa) and specimen results were determined by Equation (2.1) with maximum test load $R_{br,test}$ and measured d and t. Characteristic values in row nine are determined using the guidance in Annex D7 (General principles for statistical evaluation) of Eurocode 0 (BS EN 1990:2002), and they may be associated with a pin-bearing strength when using Equation (2.1) to design a bolted connection. The CV is typically between 5 and 10% which implies it is known. Based on Eurocode 0 for CV known and for the batch size of six the characteristic value (in unites N/mm^2)

is equal mean (N/mm^2) – 1.77 SD. For the batch sizes of ten to thirteen the characteristic values is obtained from mean (N/mm^2) – 1.72 SD. The tenth and final row entries in the tables give the mean pin diameter-to-material thickness ratios (d/t).

Table 3.6. Statistical test results for longitudinal pin-bearing strengths using the UoW test method with web material from a 203×203×9.53 mm wide flange shape.

Longitudinal web material				
Name of property	0-12	0-15	0-21	0-28
Mean web thickness, t (mm)	9.16	9.14	9.12	9.14
Mean notch diameter, d_n (mm)	11.8	14.8	20.9	27.9
Mean pin diameter, d (mm)	9.7	12.2	18.8	25.4
Mean clearance, d_n - d (mm)	2.1	2.6	2.1	2.5
Number of nominally identical specimens	11	11	11	11
Mean pin-bearing strength, F_0^{br} (N/mm^2)	188	170	154	136
SD (N/mm^2)	6.2	9.1	12.7	14.8
CV (%)	3.3	5.3	8.4	10.9
Characteristic value* (N/mm^2)	177	155	133	120
Mean d/t ratio	1.06	1.34	2.05	2.78

* Mean – 1.72SD

Table 3.7. Statistical test results for 5^o pin-bearing strengths using the UoW test method with web material from a 203×203×9.53 mm wide flange shape.

5^o web material				
Name of property	5-12	5-15	5-21	5-28
Mean web thickness, t (mm)	9.18	9.18	9.21	9.22
Mean notch diameter, d_n (mm)	12.0	14.8	21.1	27.8
Mean pin diameter, d (mm)	9.7	12.2	18.8	25.4
Mean clearance, d_n - d (mm)	2.3	2.6	2.3	2.4
Number of nominally identical specimens	10	12	11	11
Mean pin-bearing strength, F_5^{br} (N/mm^2)	179	172	147	129
SD (N/mm^2)	7.4	11.7	7.3	7.2
CV (%)	4.1	6.8	5.0	5.6
Characteristic value* (N/mm^2)	166	152	135	117
Mean d/t ratio	1.06	1.33	2.04	2.76

* Mean – 1.72SD

Table 3.8. Statistical test results for 10^o pin-bearing strengths using the UoW test method with web material from a 203 × 203 × 9.53 mm wide flange shape.

10^o web material				
Name of property	10-12	10-15	10-21	10-28
Mean web thickness, t (mm)	9.18	9.20	9.20	9.24
Mean notch diameter, d_n (mm)	11.9	14.9	21.1	27.8
Mean pin diameter, d (mm)	9.7	12.2	18.8	25.4
Mean clearance, d_n - d (mm)	2.2	2.7	2.3	2.4
Number of nominally identical specimens	11	11	11	11
Mean pin-bearing strength, F_{10}^{br} (N/mm^2)	178	165	144	128
SD (N/mm^2)	11.6	8.6	12.3	5.1
CV (%)	6.5	5.2	8.5	4.0
Characteristic value* (N/mm^2)	158	150	123	119
Mean d/t ratio	1.06	1.33	2.04	2.75

* Mean – 1.72SD

Table 3.9. Statistical test results 20^o pin-bearing strengths using the UoW test method with web material from a 203×203×9.53 mm wide flange shape.

20^o web material				
Name of property	20-12	20-15	20-21	20-28
Mean web thickness, t (mm)	9.23	9.18	9.24	9.21
Mean notch diameter, d_n (mm)	11.9	14.8	21.1	27.9
Mean pin diameter, d (mm)	9.7	12.2	18.8	25.4
Mean clearance, d_n - d (mm)	2.2	2.6	2.3	2.5
Number of nominally identical specimens	13	13	12	12
Mean pin-bearing strength, F_{20}^{br} (N/mm^2)	175	161	139	134
SD (N/mm^2)	12.4	11.1	10.7	11.6
CV (%)	7.1	6.9	7.7	8.7
Characteristic value* (N/mm^2)	154	142	120	114
Mean d/t ratio	1.05	1.33	2.03	2.76

* Mean – 1.72SD

Table 3.10. Statistical test results for 45º pin-bearing strengths using the UoW test method with web material from a 203×203×9.53 mm wide flange shape.

45º web material				
Name of property	45-12	45-15	45-21	45-28
Mean web thickness, t (mm)	9.12	9.10	9.11	9.10
Mean notch diameter, d_n (mm)	11.8	14.8	20.9	27.8
Mean pin diameter, d (mm)	9.7	12.2	18.8	25.4
Mean clearance, d_n - d (mm)	2.1	2.6	2.1	2.4
Number of nominally identical specimens	6	6	6	6
Mean pin-bearing strength, F_{45}^{br} (N/mm^2)	174	158	134	118
SD (N/mm^2)	10.3	8.4	7.5	4.4
CV (%)	5.9	5.3	5.6	3.7
Characteristic value* (N/mm^2)	156	143	121	111
Mean d/t ratio	1.06	1.34	2.06	2.79

* Mean – 1.77SD

Table 3.11. Statistical test results for transverse pin-bearing strengths using the UoW test method with web material from a 203×203×9.53 mm wide flange shape.

Transverse web material				
Name of property	90-12	90-15	90-21	90-28
Mean web thickness, t (mm)	9.09	9.10	9.17	9.18
Mean notch diameter, d_n (mm)	11.8	14.8	20.9	27.9
Mean pin diameter, d (mm)	9.7	12.2	18.8	25.4
Mean clearance, d_n - d (mm)	2.1	2.6	2.1	2.5
Number of nominally identical specimens	6	6	6	6
Mean pin-bearing strength, F_{90}^{br} (N/mm^2)	168	146	120	110
SD (N/mm^2)	10.5	13.7	10.1	7.2
CV (%)	6.2	9.3	8.5	6.6
Characteristic value* (N/mm^2)	149	122	102	97
Mean d/t ratio	1.07	1.34	2.05	2.77

* Mean – 1.77SD

It is observed that the minimum mean value for F_0^{br} of 136 N/mm^2 is below the BS EN 13706-3:2002 minimum required pin-bearing strength of 150 N/mm^2 for grade 23 material. An even less favourable finding is that the minimum characteristic value of 111 N/mm^2 is 26% below this EN minimum. For F_{90}^{br} the minimum mean and characteristic values of 110 N/mm^2 and 97 N/mm^2, respectively, are found to be well in excess of the EN 13706-3 minimum of 70 N/mm^2.

Figures 3.9 to 3.13 present pin-bearing stress against stroke plots. The stroke is that measured by the DARTEC 9500 testing machine and because of the much higher axial stiffness of test fixtures, steel pin, and testing machine this stroke is dominated by the compressive deformation of the (100 – d_n/2) mm high FRP specimen. Load-stroke plots in Figure 3.8 (Mottram, 2009b) shows when the compressive load is aligned with the pultrusion direction (0º) it has been found that the load-stroke curves are virtually linear until the maximum load is attained and that there is a sudden load reduction as significant bearing failure occurs. Because of knowing the plot shape from previous study the author did not provide the plot for 0º here. The typical plots for stress against stroke in Figures 3.9 to 3.13, in order, are for the test conditions when load is in 5, 10, 20, 45 and 90^o orientation. As expected the sudden reduction in load at onset of bearing failure is less than when loading is in the 0^o direction (Mottram, 2009b). The curves in these five figures show that when the hole diameter is 28 mm the curves are also fairly linear to the maximum load (also see Figure 3.14). The same linearity can be seen when the hole diameter is 21 mm and web material orientation is of 45 and 90^o. For the smaller hole diameter of 15 mm this is also true for the 45^o loading case. For the hole size of 21 mm and at 10 and 20^o loading, and also for smaller hole size of 15 mm at 90^o orientation the four

curves show a form of 'ductility' with the maximum load higher than at first peak. The same form of ductility from progressive failure development can be seen for the smallest hole diameter of 12 mm, with 10, 20, 45 and 90^o loadings. For the case of the smallest pin diameter (9.7 mm) the stress-stoke plot in Figure 3.13 show that the maximum load is, actually, significantly higher and this might have an influence on the statistical strengths reported in the tables. It can also be seen that the sudden reduction in load, at onset of bearing failure, is found to be less at 20^o than for the specimens with orientations of 0, 5 and 10°; this is an expected finding.

Figure 3.13 shows that the maximum load is more than just slightly higher for the single case of 90^o orientation having the 12 mm hole diameter. This is the only example of a pin-bearing test where the failure load could be defined by (b) in Figure 2.5.

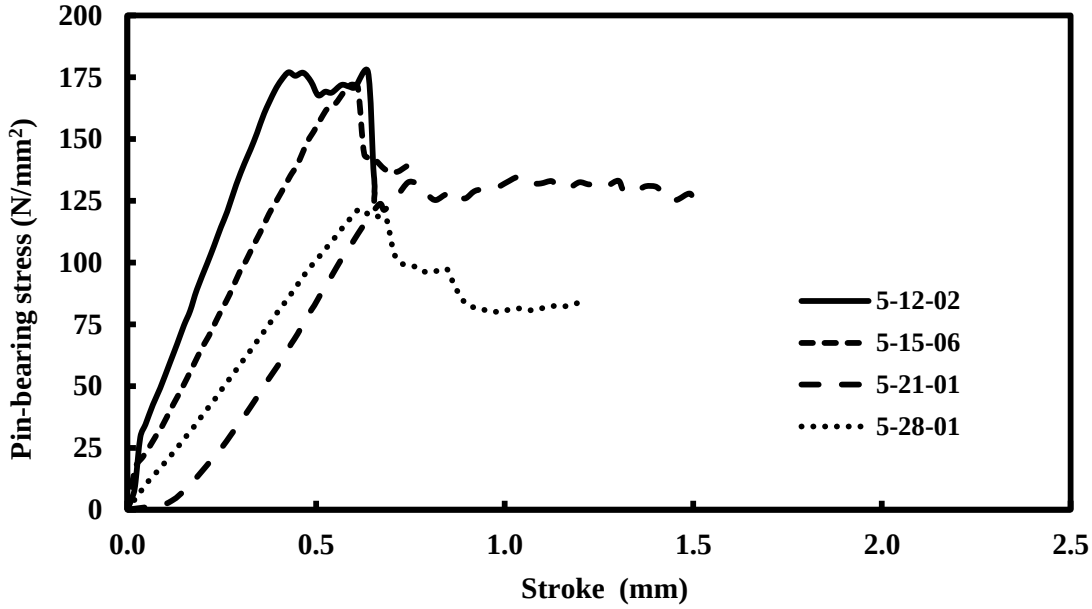

Figure 3.9. Pin-bearing stress (in N/mm^2) with stroke (in mm) curves for 5º of the web material with four pin diameters from 9.7 to 25.4 mm.

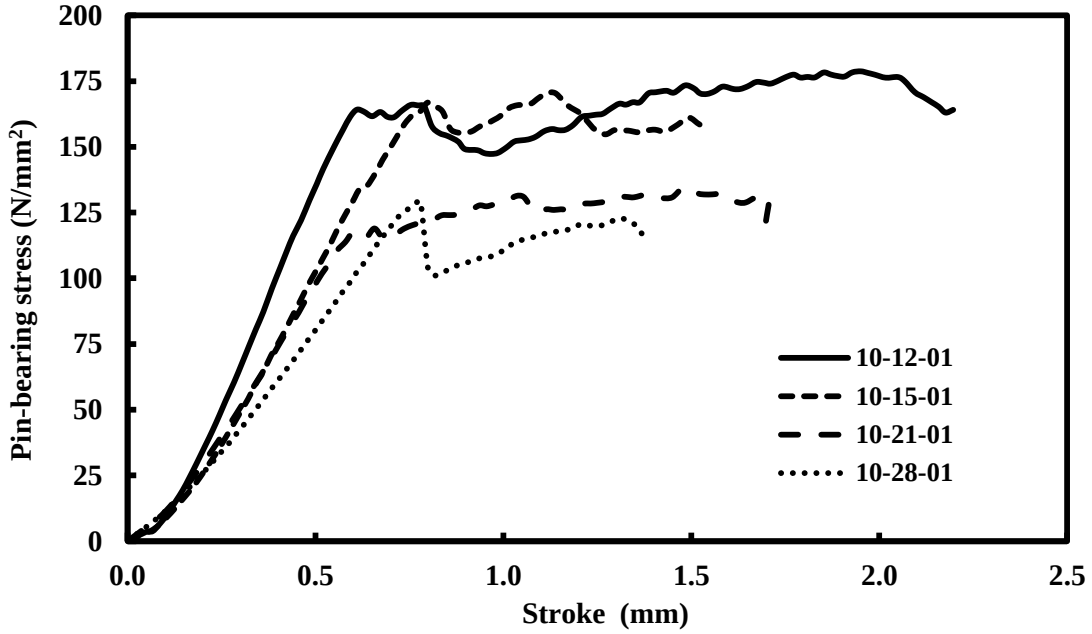

3.10. Pin-bearing stress (in N/mm^2) with stroke (in mm) curves for 10º of the web material with four pin diameters from 9.7 to 25.4 mm.

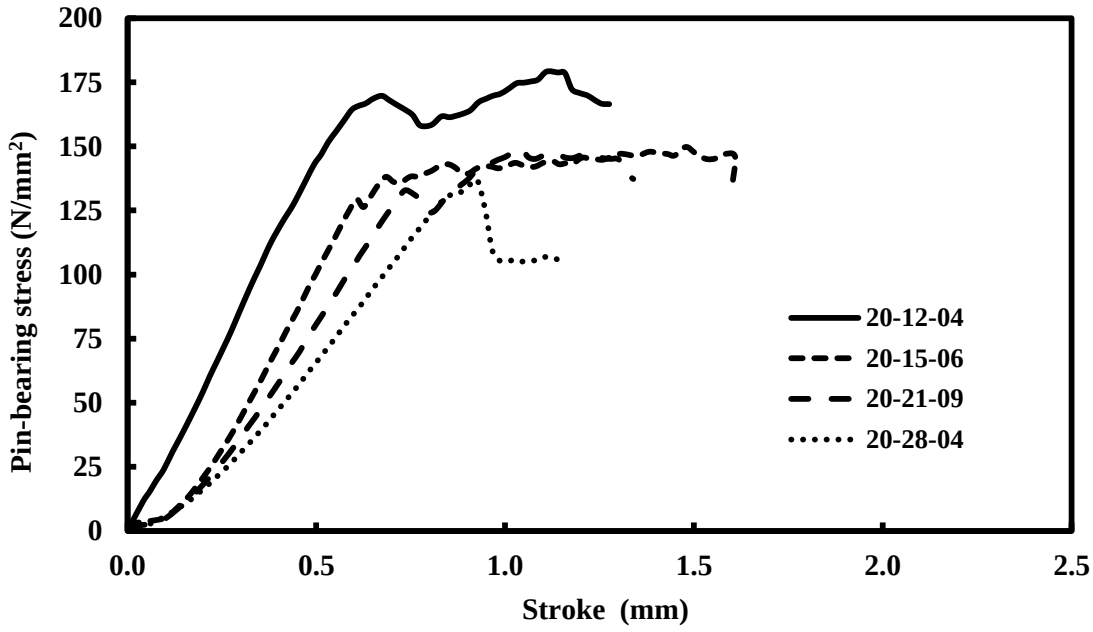

3.11. Pin-bearing stress (in N/mm^2) with stroke (in mm) curves for 20º of the web material with four pin diameters from 9.7 to 25.4 mm.

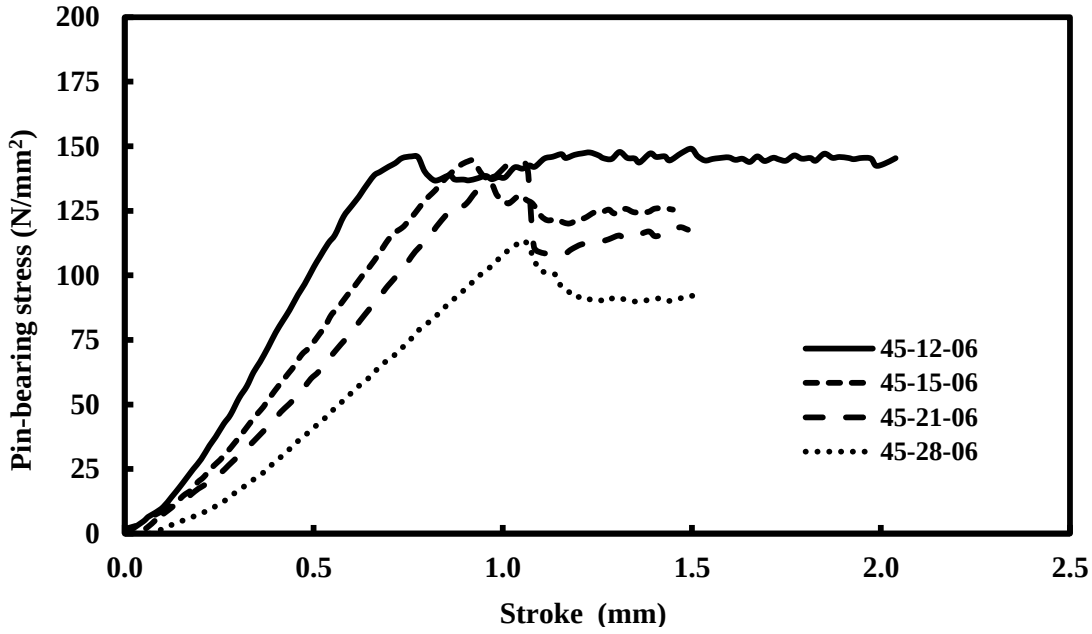

Figure 3.12. Pin-bearing stress (in N/mm^2) with stroke (in mm) curves for 45^o of the web material with four pin diameters from 9.7 to 25.4 mm.

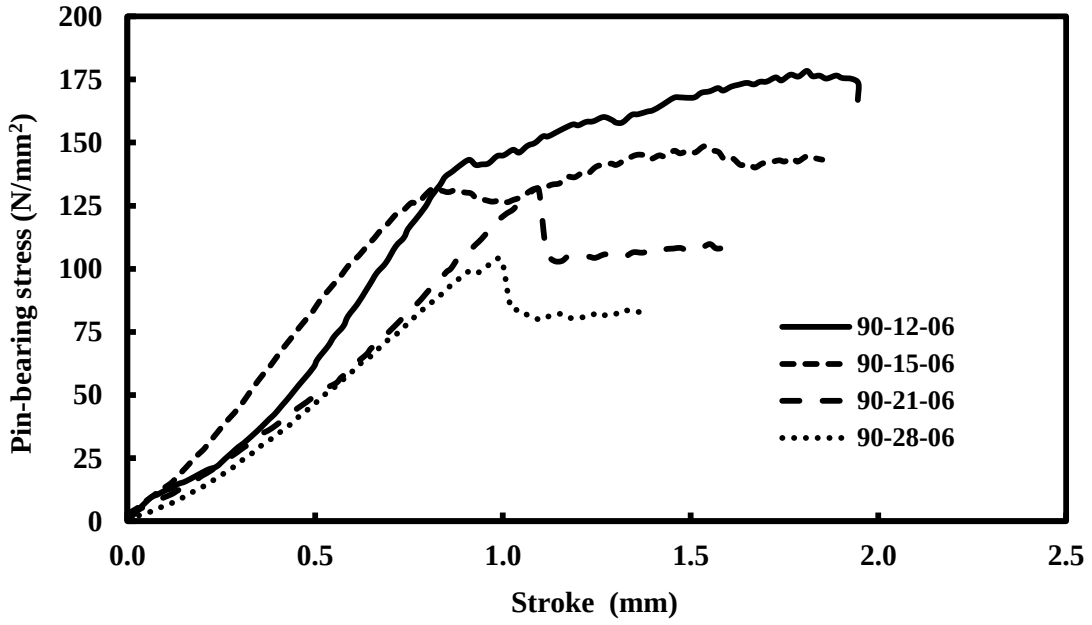

Figure 3.13. Pin-bearing stress (in N/mm^2) with stroke (in mm) curves for 90^o of the web material with four pin diameters from 9.7 to 25.4 mm.

Plotted in Figure 3.14 are typical stress-stroke curves at the six material orientations for tests with the 28 mm hole and 25.4 mm pin diameter. Their characteristics are similar with the maximum load occurring at a stroke of about 0.6 mm to 1.0 mm and in descending magnitude with increase of material orientation. After the initial embedding stage the slope of the linear part of stress-stroke curve should be proportional to the modulus of elasticity. The ratio of gradients (for stroke between 0.4 and 0.8 mm) for the 0 and 90^o tests is 1.72; very close to 1.7 given by the 'resin burn-off' moduli reported in the PhD thesis by Lane (2002). Using the gradient for the 45^o test in Figure 3.14 we find that the 45^o modulus of elasticity is 11.2 kN/mm^2, which is 12% higher than in the transverse direction. For the pin-bearing strengths not governed by UD roving reinforcement we find the ratio $F_{45}^{\mathrm{br}}/F_{90}^{\mathrm{br}}$ is 1.13 using the mean of the four characteristic strengths in Tables 3.10 and 3.11 This suggests that for orientations away from 0^o there may be a correlation between the modulus of elasticity and the pin-bearing strength.

From the characteristic values in Tables 3.6 and 3.11 the lowest value to the ratio $F_0^{\mathrm{br}}/F_{90}^{\mathrm{br}}$ is 1.19 (mean of the four values is 1.23) and this confirms the previously understood lower bound ratio of 1.2 (Mottram, 2009b). Given that the ratio of the directional modulus of elasticity is 1.7 it is observed that this pin-bearing strength ratio is not proportional to the modulus ratio. An explanation for this finding could be that the mechanism for the bearing mode of failure has changed with orientation, and this is the subject of research.

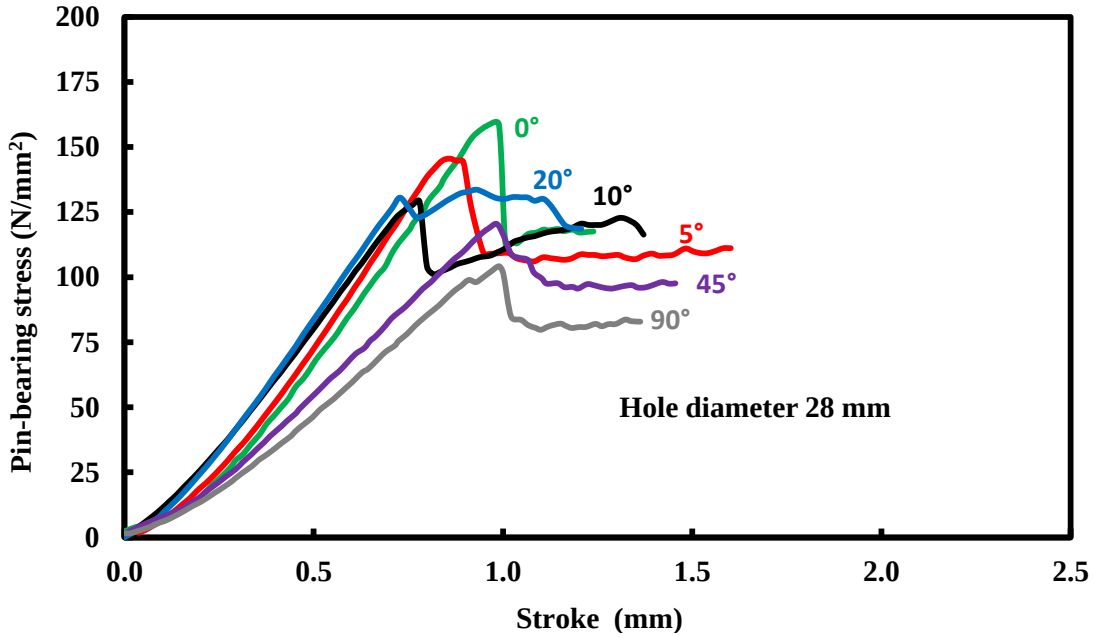

Figure 3.14. Pin-bearing stress (in N/mm^2) with stroke (in mm) curves for the web material at the six orientation of 0, 5, 10, 20, 45 and 90º and pin diameter of 25.4 mm.

In Figure 3.15 the characteristic strengths from Tables 3.6 to 3.11 are plotted against the mean bolt diameter-to-material thickness ratio (d/t). It is assumed that there is a linear variation between the data points. The legend defines the plots that are for 0, 5, 10, 20, 45 and 90° orientations with green, red, black, blue, purple and gray coloured, respectively. As the d/t ratio increases from 1.05 to 2.79 (the minimum and maximum value in Tables 3.6 to 3.11) the pin-bearing strength is seen to reduce, thereby adding evidence to our need to insist that the characteristic strength to be used with Equation (2.1) has to be determined using the most severe design parameters found in practice. The trend of the strength reduction, for all six orientations, might be modelled linearly, but confirmation does require more test results. The trends also highlight that there is a relatively small change in F_θ^{br} between 5 and 0° and that their curves have a tendency to coincide for the

highest *d*/*t* ratios. It is seen that the curves for characteristic strength at the two orientation of 20 and 45° are crossed each other.

As expected the highest strength is in the 0º direction and the decrease of F_0^{br} with *d*/*t* is the most dramatic. Whereas Creative Pultrusion Inc. state that the maximum longitudinal bearing strength, F_0^{br}, using ASTM D 953-02 is 207 N/mm^2 the characteristic results in Table 3.11 show it can be much lower and this has to be accounted for should bolt bearing failure govern the typing force requirement.

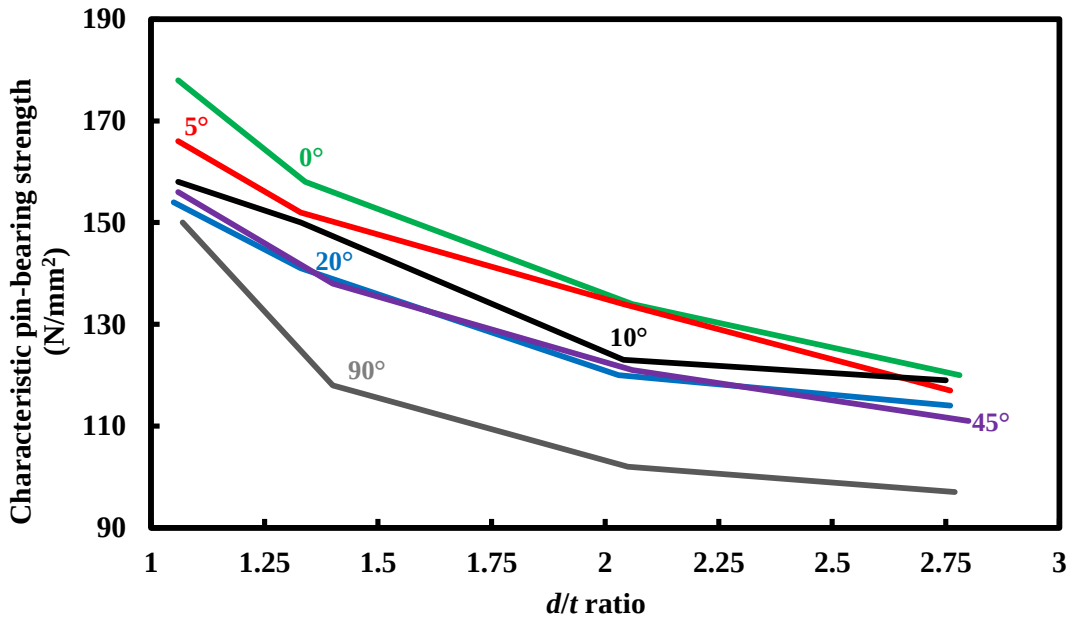

Figure 3.15. Characteristic pin-bearing strengths (in N/mm^2) of 9.2 mm thick web material with *d*/*t* ratio and hole clearance of 2.1 mm or larger.

Presented in Table 3.12 and 3.13 are normalized mean and characteristic strengths, at six orientations, based on 0^o material test results. Nominal four pin diameters are given in first row of the tables and in the second row the average value of mean pin diameter-to-material thickness ratios (*d*/*t*) for six orientation, obtained from row

tenth of Tables 3.6 to 3.11, are presented. Entries in third row of Table 3.12 and 3.13, in order, are mean and characteristic strengths for 0^o used as the base line values to normalize the other orientation values from rows five to ten.

Comparing the pin-bearing strength for 0^o material with test results of 5, 10, 20, 45 and 90° it is found that the strength has reduced by about 3.3%, 6%, 10%, 7.2 % and 18.2 %, respectively, if we take the average of the mean strengths for the four different pin diameters given in Table 3.12. The equivalent reduction when the concern is the average of characteristic strength, reported in Table 3.13, are 2.5%, 5.2%, 6%, 10 % and 16.7 %. The small reduction of strength value at 5° gives evidence to confirm what is currently proposed in the LRFD pre-standard (Anonymous, 2012d) of taking pin-bearing strength as the 0^o value when $0^o < \theta < 5^o$. These results also show that for orientations of 20° and 45^o the percent of strength reduction is still ≤ 10%.

Table 3.12. Normalised mean batch strengths at 0^o, 5^o, 10^o, 20^o, 45^o and 90° and for four different pin (bolt) diameters.

Pin diameter *d* (mm)	9.7	12.2	18.8	25.4	
Mean *d/t* ratio	1.06	1.34	2.05	2.77	Average
Mean strength F_0^{br} (N/mm^2)	188	170	154	136	
Material orientation	Normalised strength				
0^o	1.000	1.000	1.000	1.000	1.000
5^o	0.952	1.012	0.955	0.949	0.967
10^o	0.947	0.970	0.935	0.941	0.948
20^o	0.931	0.947	0.896	0.985	0.940
45^o	0.926	0.929	0.877	0.868	0.900
90^o	0.883	0.859	0.779	0.809	0.833

Table 3.13. Normalised characteristic batch strengths at 0^o, 5^o, 10^o, 20^o, 45^o and 90° and for four different pin (bolt) diameters.

Pin diameter *d* (mm)	9.7	12.2	18.8	25.4	
Mean *d/t* ratio	1.06	1.34	2.05	2.77	Average
Characteristic strength F_0^{br} (N/mm^2)	177	155	133	120	
Material orientation	Normalised strength				
0^o	1.000	1.000	1.000	1.000	1.000
5^o	0.938	0.981	1.015	0.975	0.977
10^o	0.893	0.967	0.925	0.992	0.940
20^o	0.871	0.916	0.903	0.950	0.900
45^o	0.881	0.923	0.910	0.925	0.928
90^o	0.842	0.787	0.768	0.808	0.818

Figures 3.16 to 3.19 show a normalised pin-bearing strength, now based on the 0^o mean value, against material orientation. In each figure there are a solid curve using the UoW test results for four pin sizes of 9.7 mm to 25.4 mm given in Table 3.12 for the strength values at the six orientations are given by diamond, square, triangle and circle markers. Error bars to the data points in the figures present the range of test results from a batch of nominally identical specimens. The variation in stress range is seen to be independent of hole diameter, and, except for the 20^o orientation, the range per batch might only be influenced by the sample size; it is 10 to 13 for 0, 5, 10 and 20^o and 6 for 45 and 90^o. The four dashed curves, given in Figure 3.16 to 3.19, with the same 0 and 90^o values are plotted for pin diameters of 9.7, 12.2, 18.8 and 25.4 mm using the Hankinson's Equation (3.1). It can be seen that whereas Equation (3.1) predicts a very gradual fall off in strength with orientation, the four test solid curves, shown in Figures 3.16 to 3.19, show that it falls away much more rapidly with θ from 0^o, before levelling off at higher orientations (> 45^o). Perhaps because of too few data points the UoW generated curves show a 'wavy' profile on curve fitting. Figure 3.20 shows nine plots for a normalised pin-bearing strength, eight of them are replotted from the curves in Figures 3.16 to 3.19 and the curve with

the lowest normalized strength, at all orientations, has been replotted using the test data generated by Ascione, Feo and Maceri (2009) and shown in Figure 2.7.

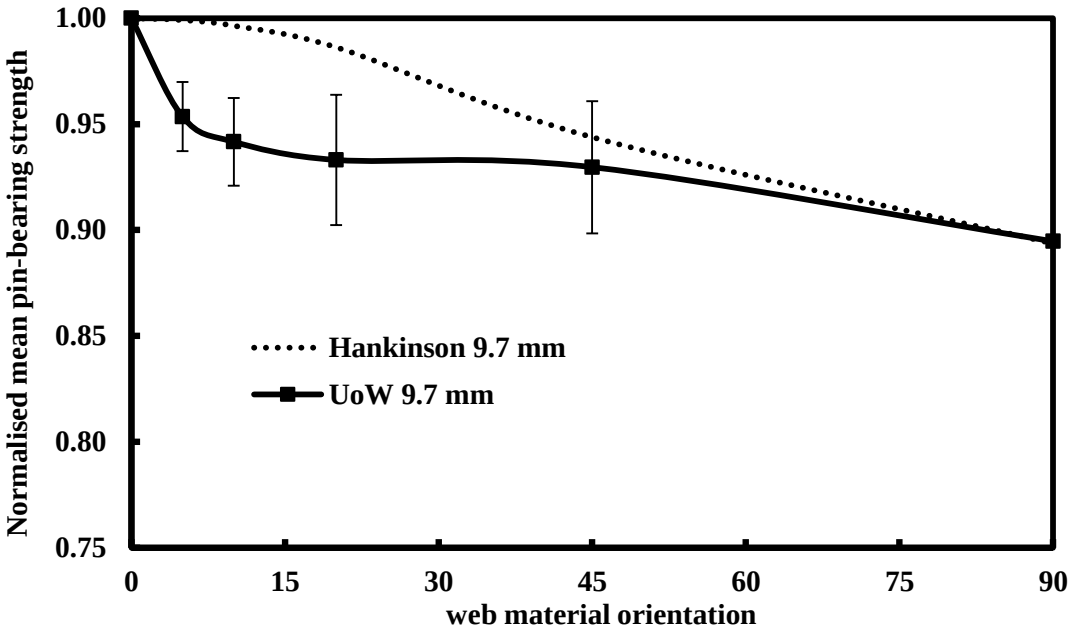

Figure 3.16. A comparison for Hankinson Equation with UoW normalised mean pin-bearing strength of diameter 9.7 mm.

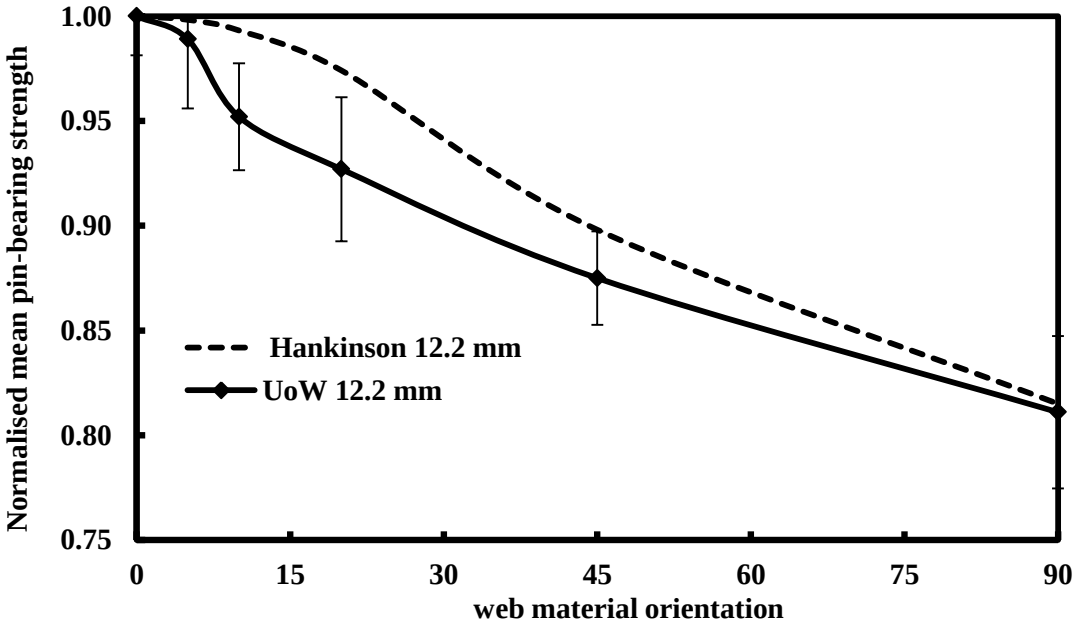

Figure 3.17. A comparison for Hankinson Equation with UoW normalised mean pin-bearing strength of diameter 12.2 mm.

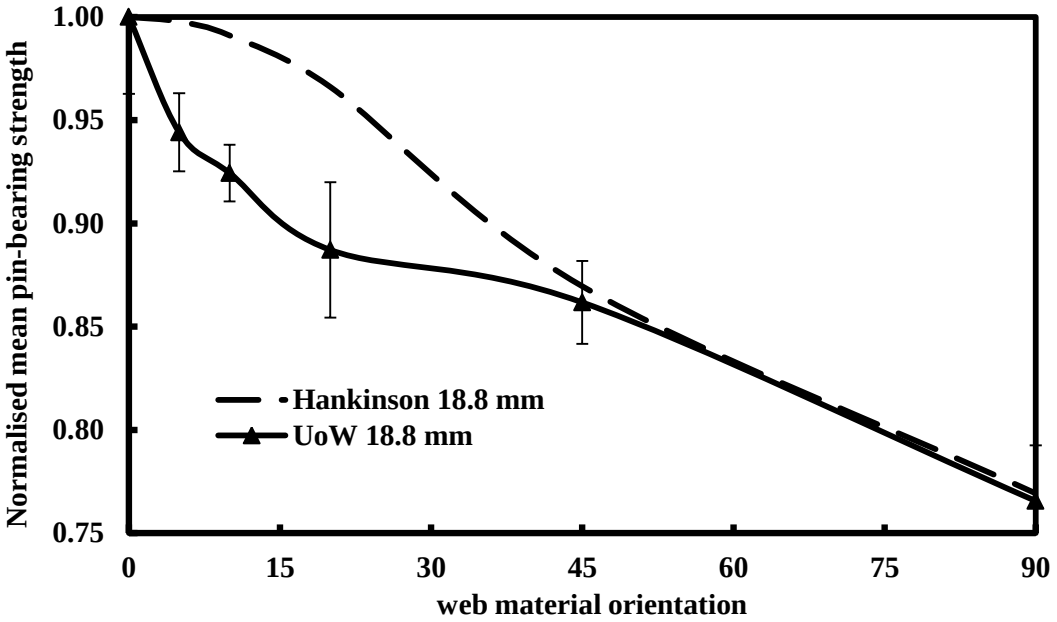

Figure 3.18. A comparison for Hankinson Equation with UoW normalised mean pin-bearing strength of diameter 18.8 mm.

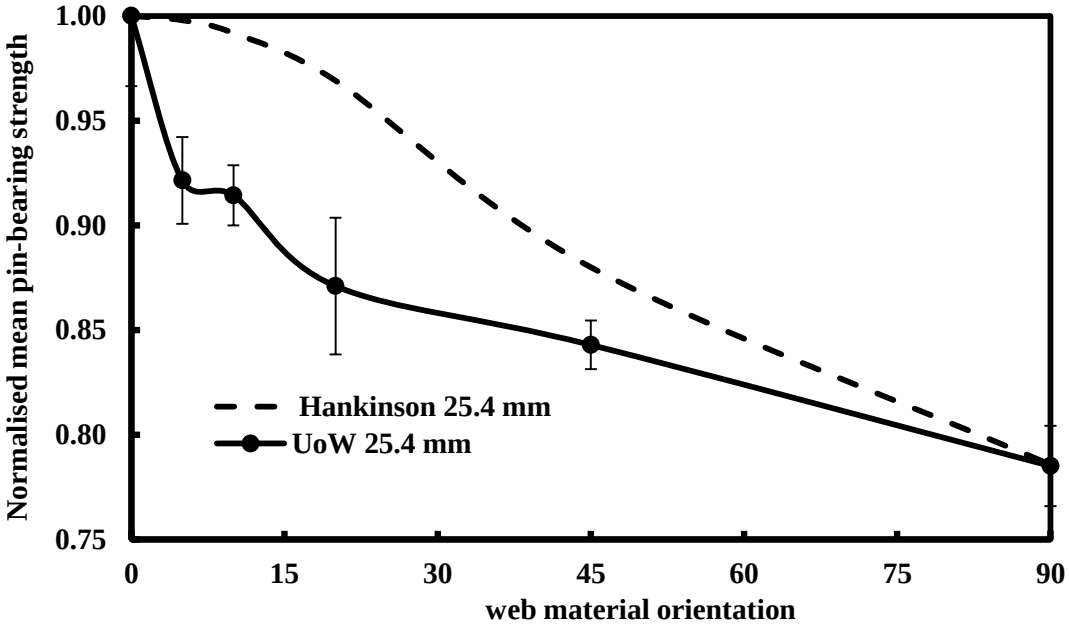

Figure 3.19. A comparison for Hankinson Equation with UoW normalised mean pin-bearing strength of diameter 25.4 mm.

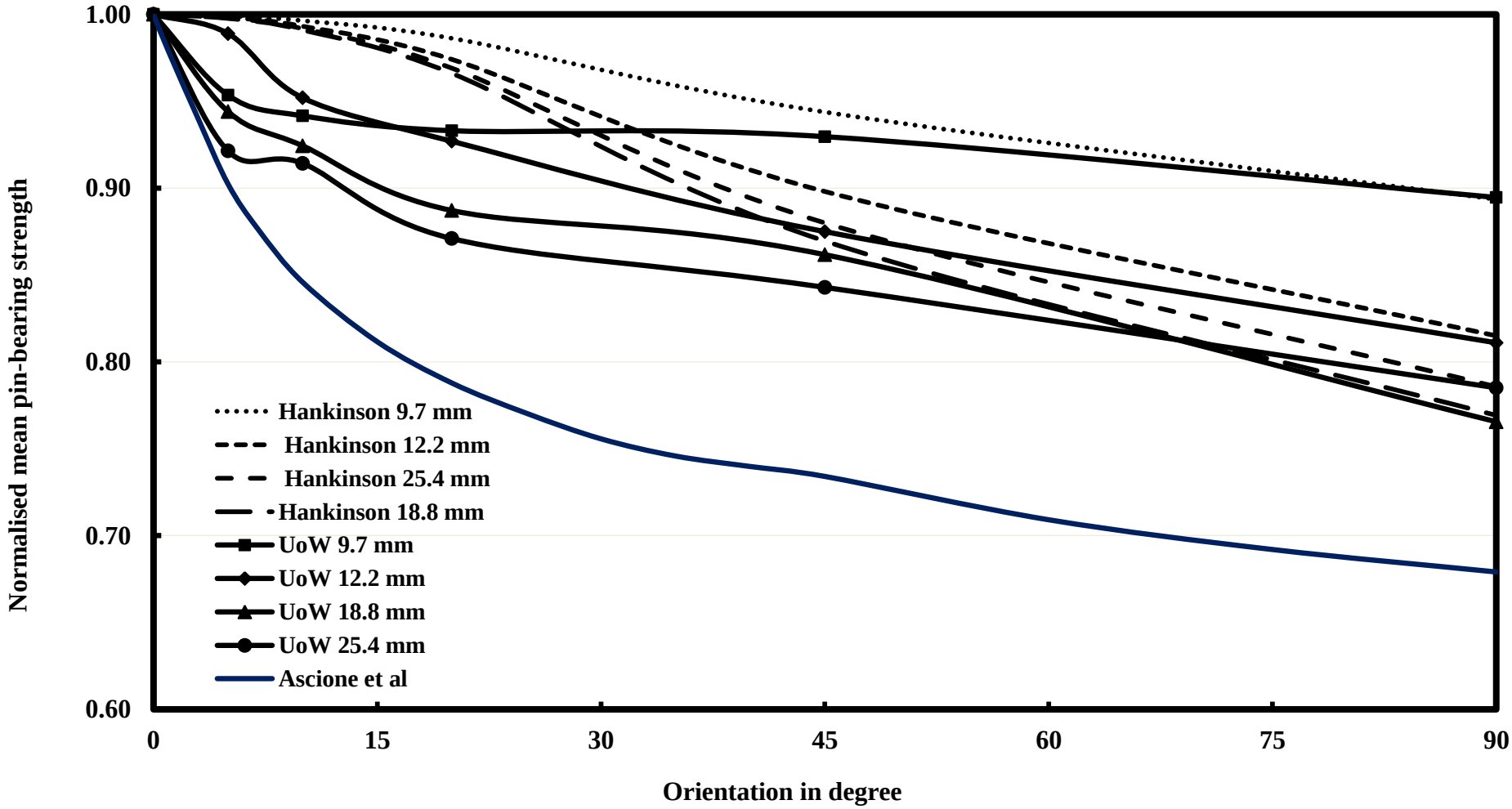

Figure 3.20. A comparison for Hankinson Equation with UoW and Ascione *et al.* (2009) normalised mean pin-bearing strength.

The shape of the curves generated from the Ascione *et al*. and UoW test results in Figure 3.20 show a similarity that cannot be determined using the Hankinson equation. It can be seen that the Ascione *et al*. data, given by curve fitting to 16 points, gives a smooth and continuous profile from F_0^{br} to F_{90}^{br}. It can be shown that to establish a curve fit, having an acceptable correlation coefficient, requires a polynomial of order six. This order would not be suitable as a formula in a standard for routine design.

3.5 Concluding Remarks

Salient test results for pin-bearing strengths of a pultruded material at the six orientations of 0, 5, 10, 20, 45, 90^{o} for four pin diameters of 9.7 mm, 12.2 mm, 18.8 mm and 25.4 mm are reported. Characteristic values are calculated in accordance with Eurocode 0. The bolt diameter-to-material thickness ratio was varied from 1.05 to 2.79, and to represent site application a minimum clearance hole of 2.1 mm (> 1.6 mm) was present. By plotting characteristic values it is found that strength decreases with increase of *d*/*t* ratio. The trend might be linear, but confirmation requires more test results. It is found that the minimum characteristics values are obtained with the biggest steel bolt diameter (at 25.4 mm). The results indicated that based on the minimum characteristic strengths a decrease of 40-50% can be found on increasing bolt diameter from 9.7mm to the 25.4mm. It is observed that the longitudinal and transverse strengths at 120 and 97 N/mm^2, respectively, cannot be associated with the maximum (pin) bearing strengths of 207 and 126 N/mm^2, respectively, given in the Creative Pultrusion Inc. design manual (Anonymous, 2012a).

The mean test results show a trivial reduction in strength in going from 0 and 5^o and that, at the highest *d*/*t* ratios, there is a tendency for their means to coincide. This finding does not contradict the proposed design guidance in an American pre-standard (Anonymous, 2012d) to use the 0^o characteristic value for orientations between 0 and 5^o and the 90^o strength for all other orientations. In America, the wood standard (ASCE, 1995) offers the Hankinson strength equation to calculate dowel strength with orientation of the connection force to the grain of the timber. By using normalized plots it is shown that the variation of pin-bearing strength of the pultruded material cannot be predicted by the Hankinson equation, which requires only the 0 and 90^o values to be determined. Moreover, the same poor correlation is found on comparing the Hankinson curve with independent test results for a different FRP material that had pin-bearing strength measured by a different test method. To establish a curve fit to the variation with orientation can require a polynomial of order six. This order would not be suitable as a formula, to replace Equation (2.1) in a standard for routine design.

Concerning the characterisation of pin-bearing strength one of the the main conclusion from the study reported in this chapter is that it will be necessary to relax the requirements given in the standard test methods (e.g., ASTM D953-02, ASTM D 5961-05, BS EN 13706-2:2002) currently used by pultruders and researchers. To be able to determine all the required characteristic strengths it will be necessary to use a test methodology similar to that developed by the University of Warwick (Mottram, 2009b), and to ensure that the test matrix involves material orientations and thicknesses, and pin and hole diameters found in practice. This test matrix recommendation can be established by way of the scope permitted in the bolted

connection chapter to the future LRFD standard (Anonymous, 2007). It is further recommended that the minimum batch size be set at 10 and that characterisation must involve environmental conditioning (refer to Chapter 4) that will cover the likely forms of material degradation around bolt holes over the intended service lives of pultruded FRP structures.

Chapter 4

Effect of hot-wet aging on the pin-bearing strength

4.1 Introduction

FRP materials are believed to possess potentially high overall durability. The lack of reliable data to assess the characteristics of naturally environmentally aged structures is a crucially barrier that heightens a concern on our ability to determine the long-term durability structures having FRP component.

This chapter presents test results to illustrate the effect of hot-wet conditioning on the pin-bearing strength of a PFRP material. Knowledge of this strength property, taking account of any reduction over the service lives of structures, is required to use Equation (2.1) to calculate strength for the bearing failure mode when designing bolted connections.

In Chapter 3 the characteristic pin-bearing strengths of the same web material, without aging, taken from the 203×203×9.53 mm Wide Flange shape (see Figure 3.3) from the 1525 series produced by the Creative Pultrusions Inc. (Anonymous, 2012a) were reported. Specimens from this series of tests were prepared using lengths of the shape that had been stored outside and exposed to natural weathering conditions for up to 15 years. During the external storage period the only loading would have been that of dead weight in the pile of shapes. All pin-bearing strength testing was carried out under ambient laboratory conditions (20^{o}C).

In this chapter new test results will be presented using the web material, same test method and same test matrix after specimens had been subjected to a known environmental conditioning in the form of hot-wet aging (3000 hours under water at 40^{o}C). To compare with Chapter 3 the reported strengths in this chapter are for the three material orientations of 0, 45 and 90^{o}.

The aim of environmental hot-wet conditioning was to accelerate material aging to simulate what could occur when bolted connections are exposed to weather over the service life of pultruded structures (see Section 2.5). One objective of the study is to find out if the 12 characteristic strengths from the text matrix are similarly lowered after the bearing surface has been subjected to the hot-wet aging. For this study to show that the strength reduction might be dependent on either material orientation or bolt size would add another consideration towards the development (and verification) of a standard test method that will overcome the known limitations, as discussed in Chapter 3, of the current test methods ASTM D953-02, ASTM D5961-05 and BS EN 13706-2:2002.

In accordance with Section 2.4.4(a) of the American LRFD pre-standard (Anonymous, 2012d), PFRP material immersed in distilled water for 1000 hours at a temperature of 38 ± 2º that cannot retain at least 15% of their characteristic values is not permitted. The clause states that for sustained end-use condition that differ from the reference condition (including short-term loading, ambient temperature, not protective coating structural products, new structural products and single members or connection without load sharing or composite action) the knock down (adjustment) factors shall be determined by tests stipulated by the Engineer of Record. In the

absence of such tests, it is permitted to use adjustment factors given in the Table 2.4-1 in Section 2.4.4. In this table the reduction factor for polyester material in moisture condition (C_M) is 0.80. There is also a reduction factor for temperature (C_T) that is given by $C_T = 1.9 - 0.01T$, when temperature is in the range of $90F^o < T \leq 140F^o$. This reduction factor should be used for a sustained in-service temperature higher than 90º F (32ºC), but for less than $T_g - 40$ Fº.

It is noteworthy that should shapes of 1525 series material be constantly exposed at the moderated elevated temperature of 38°C (100°F) Creative Pultrusions Inc. recommend that the ultimate stress be taken as 85% of the tabulated value (refer to Table 6.1 in Anonymous (2012a)).

4.2 Material and Hot-Wet Conditioning for Aged Specimens

After preparation the specimens using the same procedure as given in Section 3.2, the test samples were immersed under tap water in a Grant SUB36 water tank and aged for 3000 hours at a constant temperature of 40°C. The full surface of the semi-circular notch was in contact with the warm water for the duration of the aging process. From a private communication with the resin manufacturer the glass transition temperature of the Series 1525 polyester resin is 100°C; well above the 40°C in the hot-wet aging. The moderately elevated temperature of 40°C was selected because, at higher temperatures, another material degradation mechanism might exist and this would unwittingly amplify the property loss leading to a likely incorrect conservative determination of the actual long-term strength reduction (Nishizaki and Meiarashi 2002).

Because the lengths of the WF shape had been stored outside, for over 15 years at the mean UK temperature of 10.4°C (Beddows *et al*. 2002), it would be economical with the truth to state that the material had not already experienced a level of aging. The extent of material degradation has to remain unknown because properties of the 'virgin state' material were not determined when the shapes arrived at the university. This fact does not detract from the added value of the study reported in this thesis since the comparison of aged material is made with test results, given in Chapter 3, using non-aged material from the same (15 year old) stock. In other words the starting state of material for the specimens in the two series of tests is going to be very similar, if not the same.

After 3000 hours of soaking in the warm water the specimens were tested for their pin-bearing strength at room temperature (see Figure 3.7), following a wipe down with a paper towel to remove surface moisture. It was observed that a number of the specimens had surface spots of a slightly dark brownish color. Figure 4.1 shows an aged specimen with some these brownish spots. These spots were predominately on the cut edges of the specimens where the matrix and fibers are exposed. This localized color change maybe due to a possible chemical reaction that had occurred in the matrix. Nishizaki and Meirarashi (2002) reported seeing a similar color change after hot-wet aging of their vinylester pultruded material. They did not provide us with an explanation to the color change.

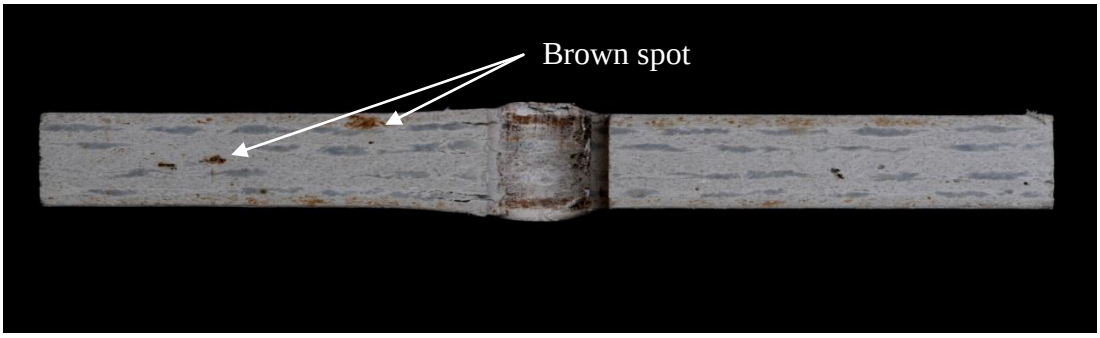

Figure 4.1. Spots of dark brownish color on the surface of the cut edge of a specimen after immersing for 3000 hours in water with constant temperature of 40º C.

The 12 batches of aged specimens (three orientation × four pin sizes) were labelled with the same scheme for specimens given in Chapter 3 with additional prefix of a small letter of **a** to distinguish them from non-aged specimens.

Presented in the Tables 4.1 and 4.2 are measured thickness, semi-notch diameter and clearance hole per specimen in millimeter for all 12 batches of nominally identical aged specimens. The column numbering has the same arrangement as columns in Tables 3.1 to 3.6. The average measured thickness (t) at three points of *A*, *B* and *C*, shown in Figure 3.6, to the nearest 0.05 mm, is found in the range of 8.83 to 9.38 mm. The minimum measured clearance hole ($d_n - d$) is 2.2 mm. Number of nominally identical specimens per batch for the orientations of 0, 45 and 90^o, in order, is 10, 5 and 6. This batch property is reported in column (2) of Tables 4.1 and 4.2. In total there are 84 coupon specimens for conducting aged pin-bearing strength tests.

Table 4.1. Measured thickness, notch diameter and hole clearance for aged specimens for longitudinal (0º) material orientation.

Specimen		Measured thicknesses (t,mm)			Average (t,mm)	Notch (d_n,mm)	Clearance hole (mm)	Specimen		Measured thicknesses (t,mm)			Average (t,mm)	Notch (d_n,mm)	Clearance hole (mm)
(1)	(2)	(3)			(4)	(5)	(6)	(1)	(2)	(3)			(4)	(5)	(6)
a-0-12	01	9.22	9.26	9.25	9.24	12.0	2.3	**a-0-21**	01	8.89	8.91	8.90	8.90	21.0	2.2
	02	9.26	9.25	9.20	9.24	12.0	2.3		02	9.12	9.21	9.15	9.16	21.0	2.2
	03	8.88	8.87	8.92	8.89	12.0	2.3		03	9.16	9.23	9.24	9.21	21.0	2.2
	04	8.91	8.95	8.92	8.93	12.0	2.3		04	9.19	9.10	9.12	9.17	21.0	2.2
	05	9.24	9.25	9.21	9.23	11.9	2.2		05	9.25	9.31	9.22	9.26	21.0	2.2
	06	8.90	8.90	8.94	8.91	12.0	2.3		06	8.91	8.92	8.86	8.90	21.0	2.2
	07	9.22	9.21	9.11	9.18	12.0	2.3		07	9.19	9.25	9.19	9.21	21.0	2.1
	08	9.11	9.26	9.25	9.23	12.0	2.3		08	9.40	9.38	9.35	9.38	21.1	2.3
	09	9.19	9.24	9.17	9.20	12.0	2.3		09	9.24	9.16	9.19	9.20	21.0	2.2
	10	9.29	9.28	9.34	9.30	12.1	2.4		10	9.28	9.21	9.24	9.24	21.0	2.2
				Mean	**9.16**	**12.0**	**2.3**					**Mean**	**9.16**	**21.0**	**2.2**
a-0-15	01	9.22	9.27	9.25	9.25	14.9	2.7	**a-0-28**	01	8.91	8.96	8.94	8.94	27.8	2.4
	02	9.31	9.26	9.26	9.28	14.9	2.7		02	9.13	9.36	9.17	9.22	27.9	2.5
	03	8.90	8.94	8.91	8.92	15.0	2.8		03	8.85	8.86	8.94	8.88	27.8	2.4
	04	9.24	9.28	9.30	9.27	15.0	2.8		04	9.21	9.27	9.29	9.26	27.8	2.4
	05	9.16	9.24	9.13	9.18	15.0	2.8		05	9.18	9.16	9.11	9.15	27.8	2.4
	06	9.22	9.19	9.15	9.19	15.0	2.8		06	9.24	9.51	9.10	9.28	27.8	2.4
	07	9.20	9.25	9.28	9.24	14.9	2.7		07	9.20	9.48	9.35	9.34	27.8	2.4
	08	9.22	9.22	9.26	9.23	15.0	2.8		08	9.18	9.41	9.26	9.28	27.8	2.4
	09	9.21	9.20	9.34	9.25	14.9	2.8		09	9.24	9.26	9.25	9.25	27.9	2.5
	10	9.16	9.19	9.21	9.19	15.0	2.7		10	9.24	9.30	9.16	9.23	27.9	2.5
				Mean	**9.20**	**15.0**	**2.8**					**Mean**	**9.18**	**27.8**	**2.4**

Table 4.2. Measured thickness, notch diameter and hole clearance for aged specimens for 45º and transverse (90º) material orientation.

Specimen		Measured thicknesses (t,mm)			Average (t,mm)	Notch (d_n,mm)	Clearance hole (mm)	Specimen		Measured thicknesses (t,mm)			Average (t,mm)	Notch (d_n,mm)	Clearance hole (mm)
(1)	(2)	(3)			(4)	(5)	(6)	(1)	(2)	(3)			(4)	(5)	(6)
a-45-12	01	9.20	9.23	9.24	9.22	12.0	2.3	**a-90-12**	01	9.13	9.10	9.11	9.21	12.0	2.3
	02	9.32	9.34	9.34	9.33	12.0	2.3		02	9.09	9.11	9.09	9.10	12.0	2.3
	03	9.36	9.35	9.32	9.34	11.8	2.1		03	9.18	9.18	9.16	9.17	12.0	2.3
	04	9.20	9.21	9.21	9.21	12.0	2.3		04	9.16	9.16	9.17	9.16	12.0	2.3
	05	9.32	9.40	9.49	9.37	12.0	2.3		05	9.19	9.22	9.21	9.21	12.0	2.3
									06	9.20	9.18	9.17	9.18	12.0	2.3
				Mean	**9.12**	**12.0**	**2.3**					**Mean**	**9.16**	**12.0**	**2.3**
a-45-15	01	9.28	9.41	9.36	9.35	15.0	2.8	**a-90-15**	01	9.18	9.18	9.19	9.18	15.0	2.8
	02	9.27	9.30	9.33	9.30	14.9	2.7		02	9.16	9.13	9.17	9.15	14.9	2.7
	03	9.31	9.36	9.24	9.30	15.0	2.8		03	9.17	9.16	9.19	9.17	15.0	2.8
	04	9.26	9.26	9.20	9.24	15.0	2.8		04	9.09	9.25	9.19	9.18	14.9	2.7
	05	9.28	9.24	9.18	9.23	15.0	2.8		05	9.16	9.16	9.17	9.16	15.0	2.8
									06	9.16	9.16	9.17	9.16	15.0	2.8
				Mean	**9.29**	**15.0**	**2.8**					**Mean**	**9.17**	**15.0**	**2.8**
a-45-21	01	9.17	9.21	9.19	9.19	21.0	2.2	**a-90-21**	01	8.82	8.81	8.86	8.83	20.9	2.1
	02	9.26	9.30	9.30	9.29	21.0	2.2		02	9.13	9.14	9.15	9.14	21.0	2.2
	03	9.35	9.35	9.28	9.33	21.0	2.2		03	9.07	9.09	9.10	9.09	20.9	2.1
	04	9.29	9.38	9.33	9.33	21.1	2.3		04	9.09	9.09	9.06	9.08	20.9	2.1
	05	9.29	9.29	9.31	9.30	21.0	2.2		05	9.14	9.20	9.12	9.15	21.0	2.2
									06	9.13	9.17	9.14	9.15	21.1	2.3
				Mean	**9.29**	**21.0**	**2.2**					**Mean**	**9.07**	**21.0**	**2.2**
a-45-28	01	8.81	8.82	8.86	8.83	27.9	2.5	**a-90-28**	01	9.09	9.17	9.14	9.13	27.8	2.4
	02	8.91	9.10	8.90	8.97	27.9	2.5		02	8.85	8.83	8.81	8.83	27.8	2.4
	03	9.24	9.26	9.28	9.26	27.8	2.4		03	8.85	8.84	8.82	8.84	27.7	2.3
	04	9.29	9.36	9.24	9.30	27.9	2.5		04	9.11	9.24	9.13	9.16	27.9	2.5
	05	9.30	9.42	9.27	9.33	27.8	2.4		05	8.84	8.86	8.85	8.85	27.9	2.5
									06	8.84	8.91	8.84	8.86	27.8	2.4
				Mean	**9.10**	**27.9**	**2.5**					**Mean**	**8.95**	**27.8**	**2.4**

Following the literature review information the author now presents the equivalent service life, with the full bearing surface in contact with 'tap' water. If the function, for Equation (2.2), in Figure 2.8 from Robert *et al*. (2010) is assumed to be valid for 1525 series material it can be estimated that aging for 3000 hours at 40^{o}C is equivalent to 3.5 service years in Canada, where the mean annual (service) temperature is 6^{o}C.

Inputting into the boxes on the web-page (www.saecanet.com/calculation_page/000376_000505_accelerating_factor.php) for *Calculation of Acceleration factor by Arrhenius equation* the 'accelerated temperature' at 40^{o}C (313.2 K), the 'practical use temperature' to 10.4^{o}C (283.6 K), and the other parameters of 'activation energy', 'Boltzmann constant' and 'aging Term' (time in number of hours), the SaECaNEt calculator gives the 'Acceleration factor' to be 4.8. With the 'aging Term' equal to 3000 hours the aging corresponds to 1.6 years of immersion in water at the constant annual mean UK (service) temperature of 10.4^{o}C. Note that for the 'practical use temperature' set to the Canadian mean annual temperature of 6^{o}C the calculator gives an 'Acceleration factor' of 6.2 and a corresponding service time of 2.1 years. This is less than 3.5 years using the curve in Figure 2.8 of the paper by Robert *et al*. (2010); one reason for the difference will be the change of polymer resin from vinylester to polyester.

Having estimated the aged time in the UK as 1.6 years (which is not long for service lives of tens of years) there are further issues to consider if we are to reliably know what the actual aged time is for bolted connection design. To elaborate on this challenge, it should be acceptable that, as long as: the bolting remains tightened;

there are washers with the bolt head and nut; the surfaces in the bolt connection are flat and parallel, it will take a long time, if at all, before the 'clearance hole' void fills up with water. This issue alone suggests that the calculated 1.6 years is for a much longer service time. Other physical issues that will exist in field applications, such as the influence of stress and or other environmental factors (e.g. exposure to chemicals, UV radiation) could, however, be counter influences to speed up the rate (acceleration factor) of material degradation to bearing failure.

Using $C_T = 1.9 - 0.01T$, given in the American pre-standard (Anonymous, 2012d) to obtain temperature reduction (adjustment) factor for the Series 1525 polyester material, C_T is found to be 0.86. Having moisture reduction factor (C_M) of 0.8 for our material, it can be estimated for the purpose of structural design that the total reduction factor for the strength properties of the WF shape, based on American pre-standard, will be 0.7. It is important to mention that the reduction factors which can be obtained by using the American pre-standard are for sustained end-used condition of structural products after being used in moisture and temperature condition in their service lives whereas, in the author's test programme the moisture and temperature are used to accelerate aging of the material to simulate what could occur when PFRP structures are exposed to the out door's environment over the service life. Another important concern about using the reduction factors from the American pre-standard is that the reference strength and stiffness should be determined in accordance with ASTM D7290. To be able to apply ASTM D7290 to determine a characteristic value the minimum batch size is 10.

As a consequence of the review in Section 2.5 of previous research on accelerated aging of PFRP materials the author recognizes that the test results in this chapter can only be applied to give an insight into how pin-bearing strength might reduce over service lives in the tens of years. This weakness in the work is acceptable because the series of tests were carried out with the aim of finding out whether or not the level of reduction in the pin-bearing strength is found to be dependent on the bolt diameter to material thickness ratio.

4.3 Test Results and Discussion

Presented in Tables 4.3 to 4.5 are pin-bearing strength results and their statistical analysis for characteristic values. These characteristic values are determined using Annex D7 in Eurocode 0 (BS EN 1990:2002). The Coefficient of Variation (CV) is typically between 3 and 10%, with a highest value for this normalized measure of dispersion of the probability distribution occurring with the largest pin diameter of 25.4 mm. It was therefore acceptable to calculate the characteristic strengths on the assumption that CV is known *a priori*. Tables 3.6, 3.10 and 3.11 in Chapter 3 are for the equivalent strengths for non-aged PFRP and the material orientations of 0^o, 45^o and 90^o. To allow a direct comparison Tables 4.3 to 4.5 have the same content for these three material orientations.

Table 4.3. Statistical test results for aged longitudinal pin-bearing strengths using the Warwick University test method with 9.2 mm web material from a 203×203×9.53 mm Wide Flange shape.

Longitudinal web material				
Name of property	a-0-12	a-0-15	a-0-21	a-0-28
Mean web thickness, t (mm)	9.16	9.20	9.16	9.18
Mean notch diameter, d_n (mm)	12.0	15.0	21.0	27.8
Mean pin diameter, d (mm)	9.7	12.2	18.8	25.4
Mean clearance, d_n - d (mm)	2.3	2.8	2.2	2.4
Number of nominally identical specimens	10	10	10	10
Mean pin-bearing strength, F_0^{br} (N/mm^2)	147	128	115	107
SD (N/mm^2)	11.1	8.0	20.6	9.2
CV (%)	7.6	7.0	9.2	10.1
Characteristic value* (N/mm^2)	128	114	96	91
Mean d/t ratio	1.06	1.33	2.05	2.77

Note: 1. Mean – 1.72SD

Table 4.4. Statistical test results for aged 45^o pin-bearing strengths using the Warwick University test approach with 9.2 mm web material from a 203 × 203 × 9.53 mm Wide Flange shape.

45^o orientation of web material				
Name of property	a-45-12	a-45-15	a-45-21	a-45-28
Mean web thickness, t (mm)	9.12	9.29	9.29	9.10
Mean notch diameter, d_n (mm)	12.0	15.0	21.0	27.9
Mean pin diameter, d (mm)	9.7	12.2	18.8	25.4
Mean clearance, d_n - d (mm)	2.3	2.8	2.2	2.5
Number of nominally identical specimens	5	5	5	5
Mean pin-bearing strength, F_0^{br} (N/mm^2)	142	123	105	92
SD (N/mm^2)	7.4	4.2	5.2	6.9
CV (%)	5.4	3.4	4.9	8.5
Characteristic value* (N/mm^2)	125	116	96	80
Mean d/t ratio	1.04	1.31	2.02	2.78

Note: 1. Mean – 1.80SD

Table 4.5. Statistical test results for aged transverse pin-bearing strengths using the Warwick University test method with 9.1 mm web material from a 203 × 203 × 9.53 mm Wide Flange shape.

90^o orientation of web material				
Name of property	a-90-12	a-90-15	a-90-21	a-90-28
Mean web thickness, t (mm)	9.16	9.17	9.07	8.95
Mean notch diameter, d_n (mm)	12.0	15.0	21.0	27.8
Mean pin diameter, d (mm)	9.7	12.2	18.8	25.4
Mean clearance, d_n - d (mm)	2.3	2.8	2.2	2.4
Number of nominally identical specimens	6	6	6	6
Mean pin-bearing strength, F_0^{br} (N/mm^2)	126	110	94	86
SD (N/mm^2)	5.5	7.0	8.2	10.9
CV (%)	4.7	7.2	10.3	16.2
Characteristic value* (N/mm^2)	116	97	80	67
Mean d/t ratio	1.06	1.33	2.07	2.84

Note: 1. Mean – 1.77SD

Measured mean thickness (t), for the aged batches of specimens, shows a small difference of up to ±1% from those for the non-aged batches, refer to Table 3.6, 3.10 and 3.11. The minimum hole clearance is 2.2 mm (see Tables 4.1 and 4.2) and this size is higher than the minimum 1.6 mm (1/16 in.) specified in practice (Anonymous, 2012a,b). Clearance hole size was dictated by the available drill bit diameters. As would be expected, owing to natural variability in the pultrusion process, there are small differences in the geometries of the 92 (Chapter 3) and 84 specimens for non-aged and aged material. Characteristic values in row 9 of Tables 4.3 to 4.5 were obtained on the assumption that the strength population fits the Normal (Gaussian) distribution.

Prior to discussing and evaluating the strengths reported in Tables 3.6, 3.10, 3.11 and 4.3 to 4.5, the forms of the stress-stroke curves for the aged specimens will be presented. For non-aged specimens similar plots are given in Figures 3.12 to 3.14. Figures 4.2 to 4.4 present plots of pin-bearing stress against stroke. In the three

figures, for the 0, 45 and 90^{o} material orientations, there is a curve for a single aged specimen with each of the four pin diameters (*d*). Due to a loss of data when testing material at orientation of 90^{o} no stress-stroke curve is plotted for a specimen with the notch diameter of 12.0 mm. When the compressive load ($R_{br,test}$) is aligned with 0^{o} the plots in Figure 4.2 show the curves to be virtually linear until bearing failure, when there is sudden loss in the load. As might have been expected, from the material's composition, the sudden load reduction at bearing failure is less noticeable in Figure 4.3 when the orientation is 45^{o}; the same can be seen in Figure 4.4 for the 90^{o} material orientation. Figure 4.3 shows that, for a 'matrix' dominated deformation, the stress-stroke curve shows the presence of pseudo-ductility. It further identifies that, with pin diameters of 9.7 and 12.2 mm, the maximum load can be a little higher than attained at the end of the elastic response. The curve for the specimen with the 18.8 mm pin diameter indicates that it gave a sudden loss in load. Plotted curves for the martial orientation of 90º in Figure 4.4 shows that this sudden loss has happened for specimen with the 25.4 mm pin diameter.

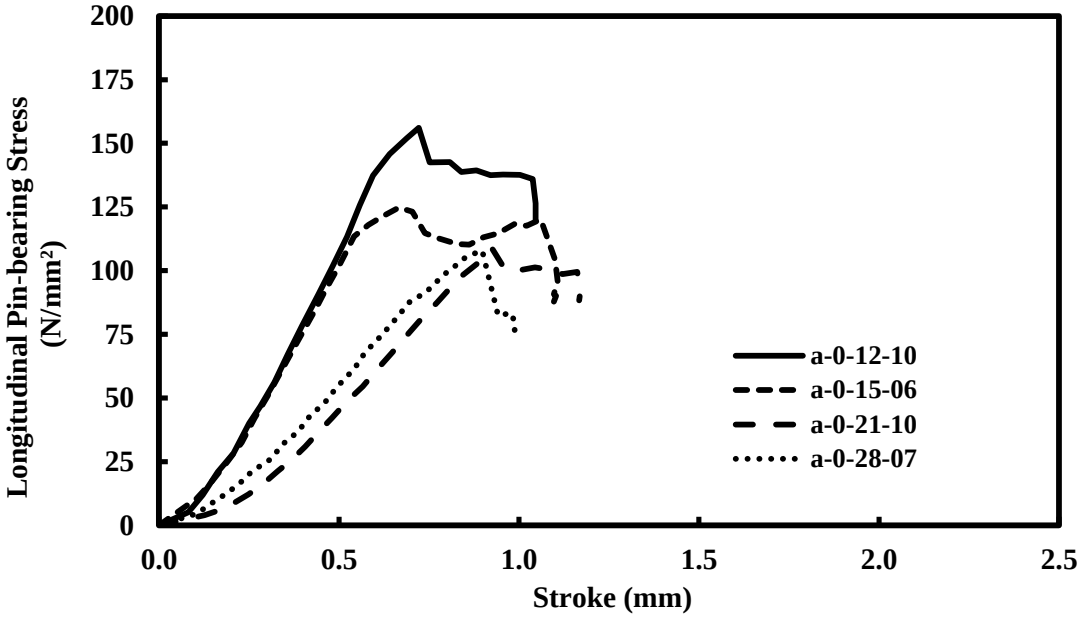

Figure 4.2. Pin-bearing stress against stroke curves with pin diameters from 9.7 to 25.4 mm for longitudinal (0^{o}) web material after hot-wet aging.

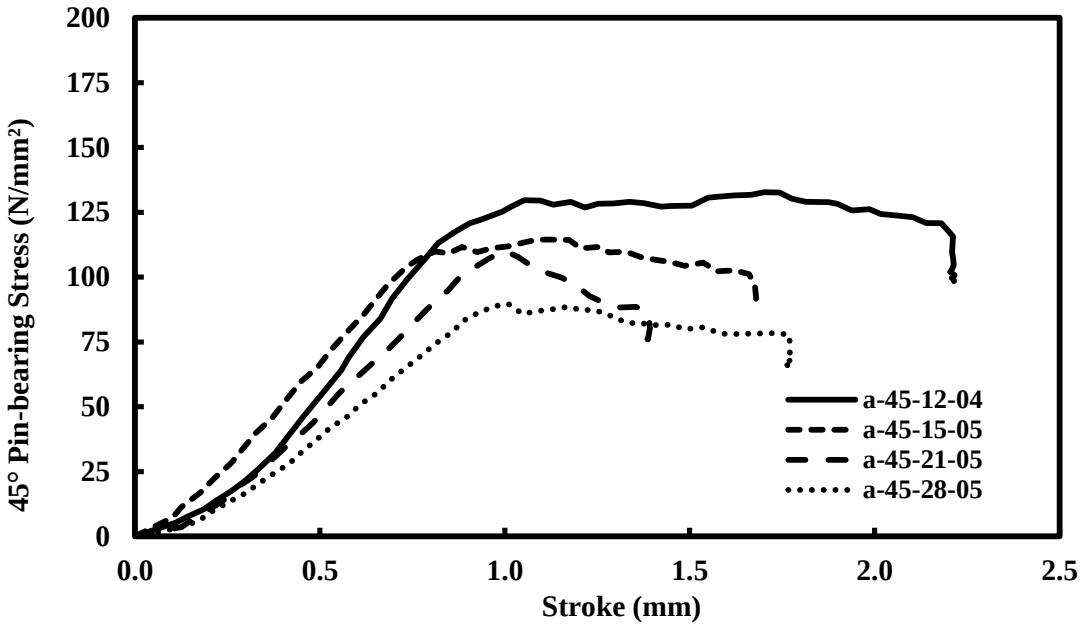

Figure 4.3. Pin-bearing stress against stroke curves with pin diameters from 9.7 to 25.4 mm for 45^{o} web material after hot-wet aging.

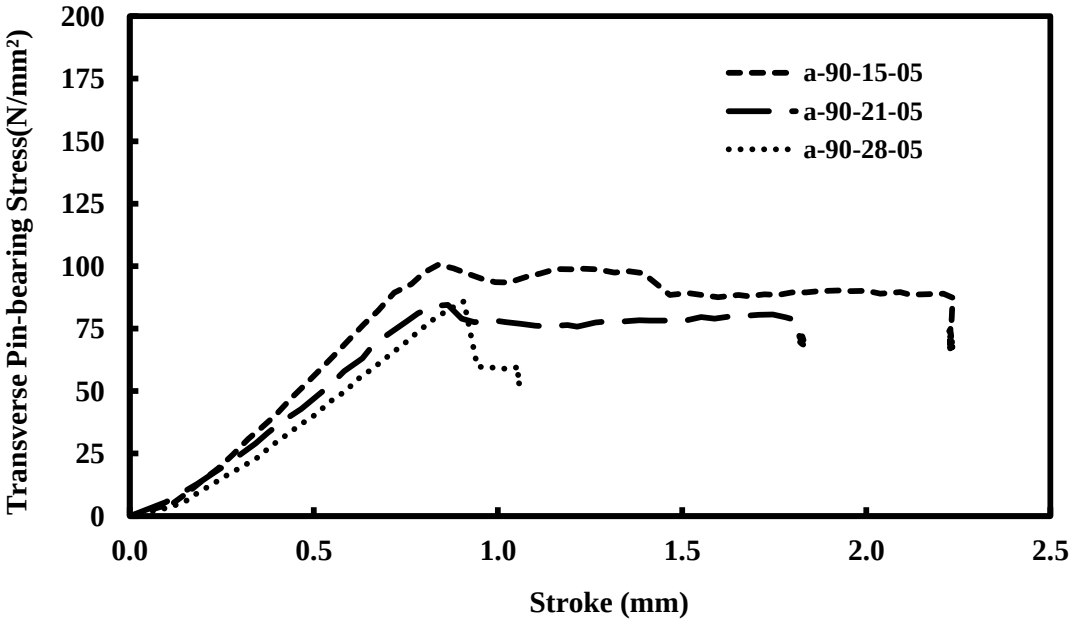

Figure 4.4. Pin-bearing stress against stroke curves with pin diameters from 9.7 to 25.4 mm for transverse (90^{o}) web material after hot-wet aging.

Plotted in Figures 4.5 to 4.7 are three pair of non-aged and aged curves at 0, 45 and 90^{o} material orientations for pin diameter of 25.4 mm, 9.7 mm and 18.8 mm. Each

solid black curve is obtained from a single non-aged specimen, whereas the gray coloured curve is for a specimen after aging. The plots in Figures 4.5 and 4.6 show that the response of aged material is similar to non-aged, whereas, for the Figure 4.7 the curves suggest there is material softening (degradation) following the environmental conditioning. The results in all three figures show that, independent of material orientation, the load-stroke curves are often virtually linear to maximum load attainment. Thereby, the load-stroke plots support the author's recommendation in Chapter 3 that pin-bearing strength is to be determined from the maximum failure load, and not by one of the other six choices for the failure load, which are defined in Johnson and Matthews (1979). It is the maximum load from testing that is required when establishing F_{θ}^{br} for Equation (2.1).

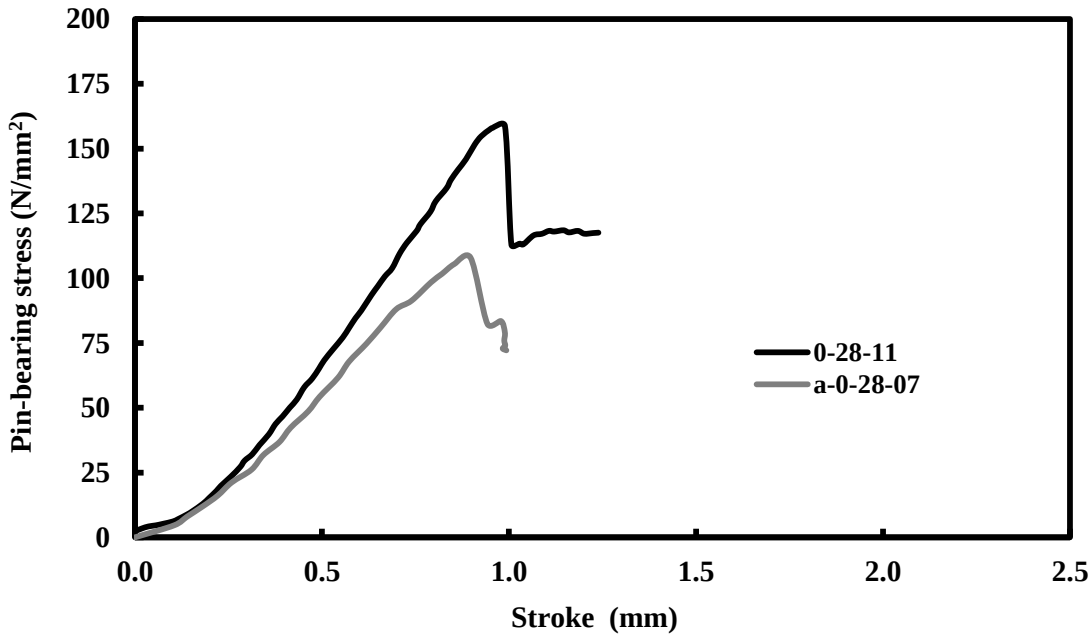

Figure 4.5. A pair of pin-bearing stress against stroke curves for non-aged and aged specimen with pin diameters of 25.4 mm for 0^{o} web material.

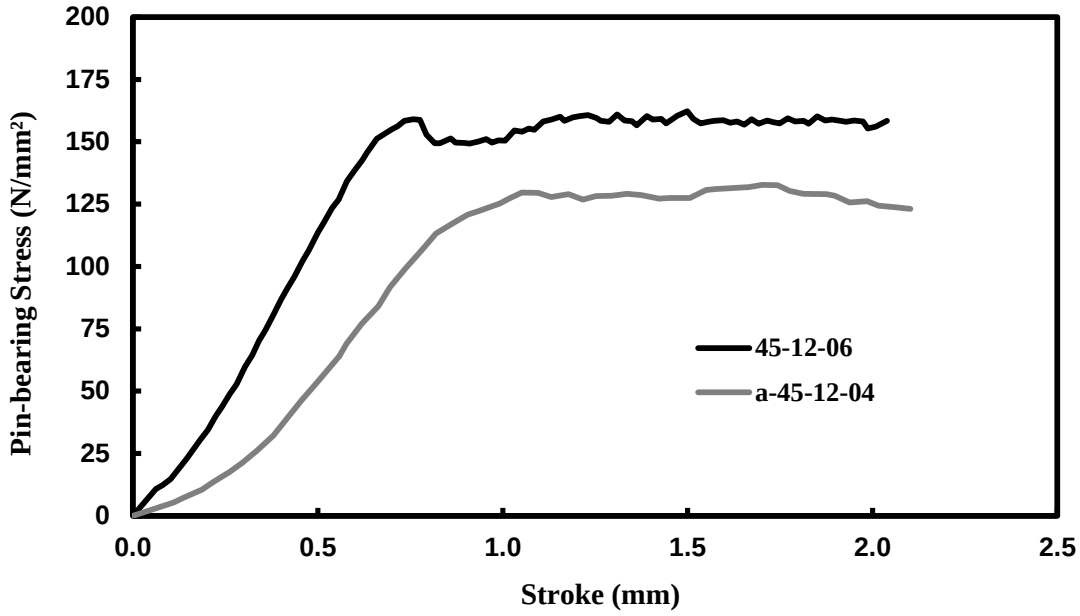

Figure 4.6. A pair of pin-bearing stress against stroke curves for non-aged and aged specimen with pin diameters of 9.7 mm for 45^{o} web material.

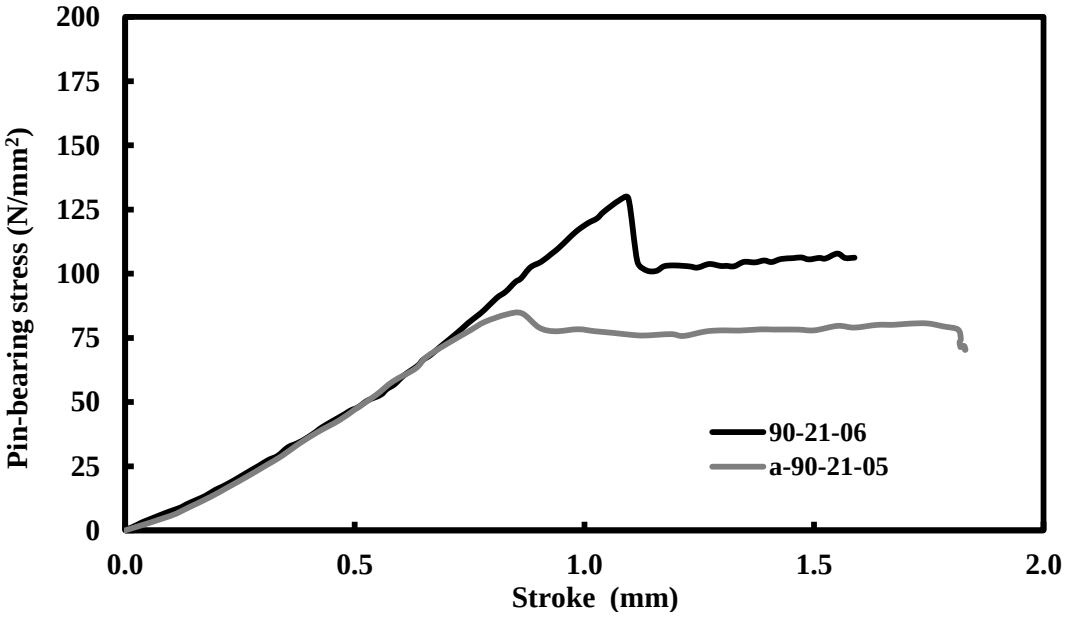

Figure 4.7. A pair of pin-bearing stress against stroke curves for non-aged and aged specimen with pin diameters of 18.8 mm for 90^{o} web material.

Plotted in Figure 4.8 are typical stress-stroke curves using a single aged specimen for each of the three material orientations of 0^{o}, 45^{o} and 90^{o} and the pin diameter of 25.4

mm. Their characteristic shapes are similar to those for non-aged material (for the same orientation given in Figure 3.14), with the maximum load occurring at a stroke of about 1.0 mm and in descending magnitude with increase of orientation. After the initial embedding stage, the slope of the linear part of load-stroke curve can be assumed to be proportional to the directional modulus of elasticity. The ratio of gradients (for stroke between 0.4 and 0.8 mm) from the 0^o and 90^o tests is 1.3. It is found that the 0^o and 45° measurements also give the same stiffness ratio. For the non-aged material the F_0^{br}/F_{90}^{br} ratio was higher at 1.7 (see Section 3.4). Using the 0^o load-stroke gradient in Figure 4.8 the longitudinal modulus of elasticity is estimated to be 15 kN/mm^2. This is a 12% reduction from 17 kN/mm^2 for the non-aged material (see Section 3.4), and is 30% higher than the modulus in the 45° and 90^o directions. This finding indicates that the web material has been degraded by the hot-wet aging conditioning.

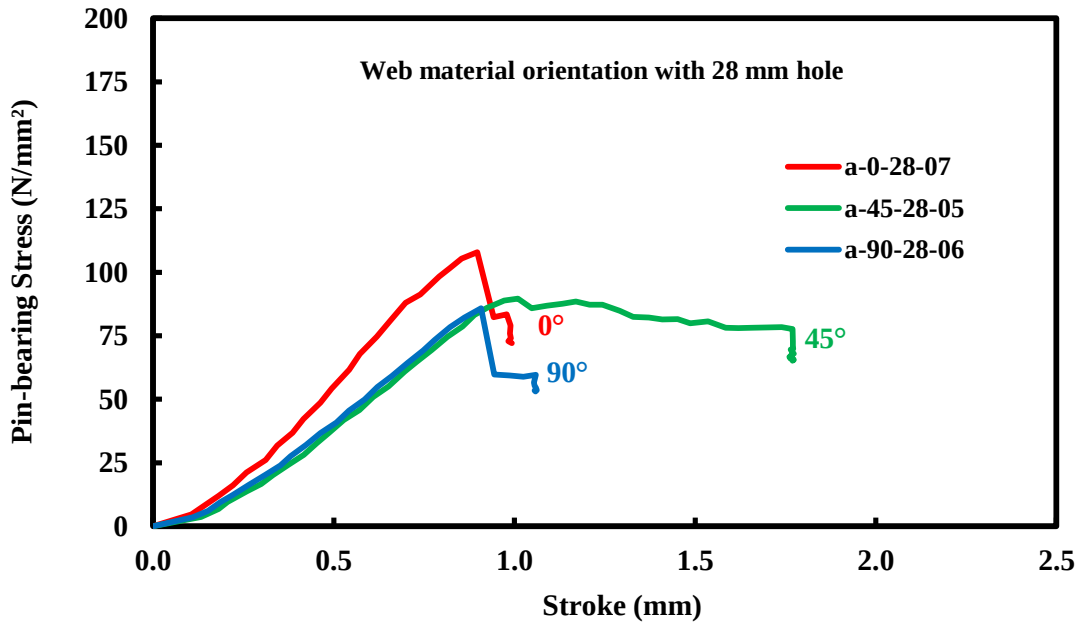

Figure 4.8. Pin-bearing stress with stroke curves for web material after hot-wet aging at the three orientations of 0^o, 45^o and 90^o with pin diameter of 25.4 mm.

It will be instructive to compare the minimum values of the 0^o and 90^o characteristic strengths in Tables 4.3 and 4.5, respectively, after aging with bearing strengths reported by the pultruder (Anonymous, 2012a) and in BS EN 13706-3:2002. Minimums were determined with the largest pin diameter of 25.4 mm, and, from Table 4.3, F_0^{br} is 91 N/mm^2 (CV is 10.1%) and, from Table 4.5, F_{90}^{br} is 67 N/mm^2 (CV 16.2%). Based on the 'maximum bearing strength' of F_0^{br} = 206 N/mm^2 and F_{90}^{br} = 124 N/mm^2 reported by Creative Pultrusions Inc. for non-aged material it is found that the characteristic strength for the longitudinal (LW) and transverse (CW) orientations, given in Table 4.3 and 4.5, have a reduction values of 56% and 46%, respectively. These reductions are about four and three times higher than the 15% reduction that is recommended by Creative Pultrusions Inc. (refer to Table 6.1 in Anonymous (2012a)). The 15% reduction to be used for ULS design for shapes of 1525 series material when they are to be constantly exposed to the moderated elevated temperature of 38^oC (100^oF).

Comparing the reduction (adjustment) factor of 0.7 obtained from Table 2.4-1 in Section 2.4.4 of the LRFD pre-standard (Anonymous, 2012d) for the purpose of structural design when using the Series 1525 polyester material (see Section 4.2 of the chapter), it can be seen that the reduction values of 56% and 46% are about 14% and 24% higher than that permitted by the American pre-standard. It is important to mention that the reduction factor obtained from Table 2.4-1 of the LRFD pre-standard should be used for a sustained in-service temperature higher than 90º F (32ºC), and for less than T_g – 40 Fº.

The EN 13706 standard is for non-aged material and the minimum pin-bearing strengths that are required for Grade 23 can be read from Table 1 of Part 3. From the results in Tables 4.3 and 4.5 the minimum EN 13706 values of F_0^{br} = 150 N/mm^2 and F_{90}^{br} = 70 N/mm^2 cannot be met after the additional environmental conditioning. Had the strength testing itself been carried out at the evaluated temperature of 40^{o}C the strength loss is likely to be higher still.

For the two pin-bearing strengths that are not expected to be governed by the stiffer UD roving reinforcement the ratio F_{45}^{br}/F_{90}^{br} = 1.16, using the mean of the four characteristic strengths in Tables 4.4 and 4.5. The importance of this finding, which is similar to the non-aged ratio of 1.13 (see Section 3.4), is that knowing F_{90}^{br} effectively gives us the strength F_θ^{br} for θ from 45 to 90. Testing with material orientations between 15^o and 45^o will identify the limit on θ when it will no longer be acceptable for F_{90}^{br} to be taken, in Equation (2.1), as the pin-bearing strength.

Table 4.6 has been constructed to report the percentage reductions in characteristic strength following the aging process using the results in Tables 3.6, 3.10, 3.11 and 4.3 to 4.5. Column (1) gives the name of the information entered in columns (2) to (5), which are for the four pin diameters of 9.7 mm, 12.2 mm, 18.8 mm and 25.4 mm. For each of the three material orientations the non-aged and aged characteristic strengths from their table are given and, directly below their row entries, the percentage difference is given using the expression (non-aged – aged)×100/(non-aged).

Table 4.6. Percentage reduction in characteristic pin-bearing strength as a result of aging.

(1)	(2)	(3)	(4)	(5)
Pin diameter (mm)	9.7	12.2	18.8	25.4
Characteristic strength F_0^{br} (N/mm^2)		0^o material orientation		
Non-aged	177	155	133	120
Aged	128	114	96	91
% reduction based on non-aged	27.7	26.5	27.8	24.2
Characteristic strength F_{45}^{br} (N/mm^2)		45^o material orientation		
non-aged	156	143	121	111
Aged	125	116	96	80
% reduction based on non-aged	19.9	18.9	20.7	27.9
Characteristic strength F_{90}^{br} (N/mm^2)		90^o material orientation		
Non-aged	149	122	102	97
Aged	116	97	80	67
% reduction based on non-aged	22.2	20.5	21.6	30.9

To show the characteristic strengths they are plotted in Figures 4.9 to 4.11 against the pin diameter-to-material thickness (*d*/*t*) ratio. The Eurocode 0 strengths are taken from the ninth row in Tables 3.6, 3.10, 3.11, 4.3, 4.4 and 4.5 and the four values for *d*/*t* from the last row entries. The different pin diameters can be identified as *d/t* increases from 1.04 to 2.84 by the solid symbols for the batch test results. The non-aged batch results are given by the diamond symbols and the aged batch results by the square symbols. To construct the non-aged and aged strength curves in the three figures it is assumed that there is a piecewise linear relationship between the four (pin diameter) data points.

With non-aged material, presented in Chapter 3, it was found that the characteristic strength decreases with increasing *d*/*t* ratio. This trend is seen in Figures 4.9 to 4.11 to be followed when the material has been subjected to hot-wet aging. This finding adds to the growing evidence that the pin-bearing strengths for Equation (2.1) must

be determined using a standard test method that accounts for the most severe *d*/*t* ratio and clearance hole size found in practice.

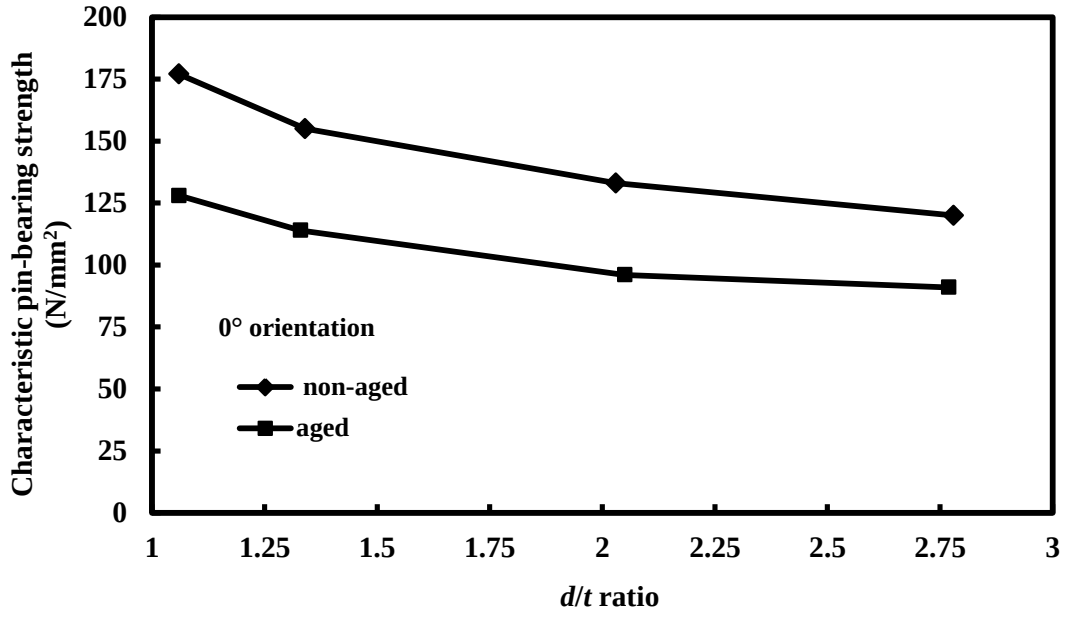

Figure 4.9. Characteristic pin-bearing strengths (N/mm^2) of 0° material with *d*/*t* ratio.

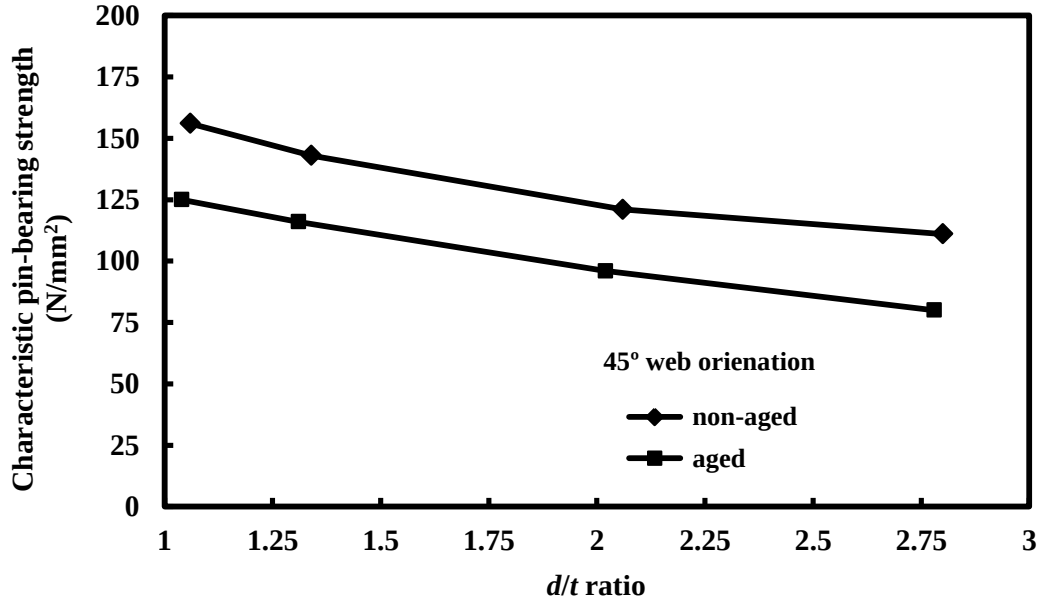

Figure 4.10. Characteristic pin-bearing strengths (N/mm^2) of 45° material with *d*/*t* ratio.

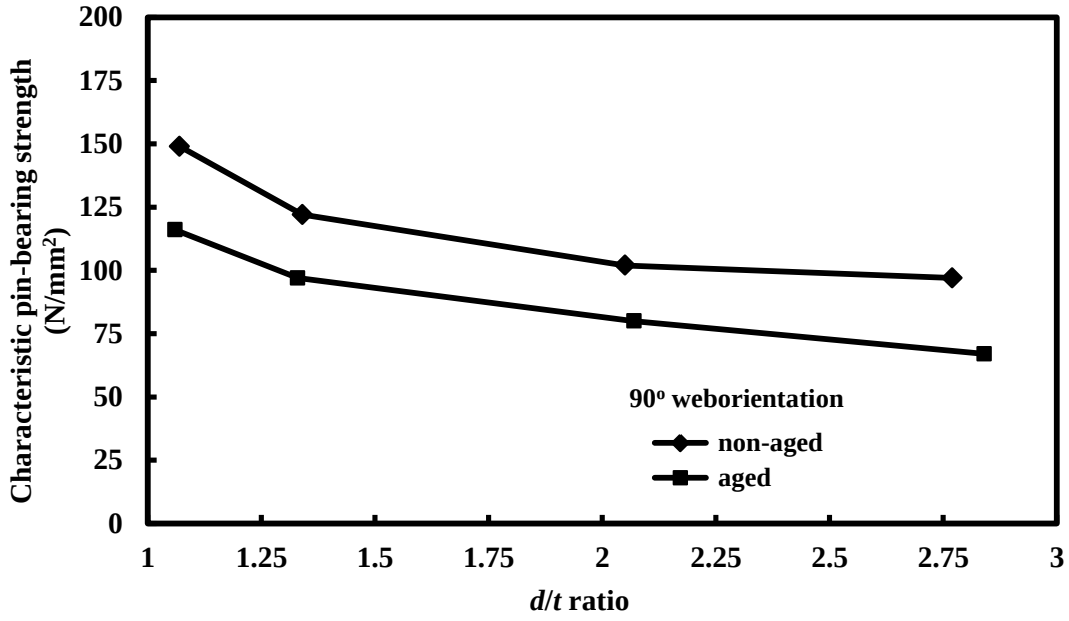

Figure 4.11. Characteristic pin-bearing strengths (N/mm^2) of 90° material with *d*/*t* ratio.

When using the statistical derived characteristic values to evaluate whether the strength loss trend has changed due to the aging it has to be recognized that the Coefficient of Variation (CV) is not constant. Inspection of the row eight entries in Tables 3.6, 3.10, 3.11 and 4.3 to 4.5 show that the CVs are not too dissimilar for the three pin diameters of 9.7 mm, 12.2 mm and 18.8 mm. This inspection of the tables further identifies that the CV can be very different when the pin has its largest diameter of 25.4 mm. To further emphasize an important finding it can be seen from the information in Table 4.6 that reductions (to nearest percentage), ignoring the 25.4 mm pin, are 27 to 28% for 0^o orientation, and 19 to 21% and 21 to 22% for the 45^o and 90^o orientations. Taking the mean percentage reductions for pins of diameter 18.8 mm and lower, it is observed that the loss is highest, and over 25%, for the longitudinal (0^o) material when the UD roving reinforcement influence the resistance and is lower, at about 20%, when strength is less influenced by these fiber layers. It is further observed from the Table 4.6 analysis (for pin diameters from 9.7 mm to

18.8 mm) that the loss in characteristic strength is nearly a constant percentage of the non-aged strength. This finding is very important because it indicates that the number of batches can be reduced to a manageable number when characteristic strengths for Equation (2.1) are to be determined.

With the 25.4 mm pin size the percentage reductions from Table 4.6 are 24%, 28% and 31% for 0^o, 45^o and 90^o, respectively. Further research is required to explain why these characteristic strengths do not follow the orientation reductions (27 to 28% (0^o), 19 to 21% (45^o) and 21 to 22% (90^o)), obtained with the three smaller pin diameters. It is essential that we gain a physical understanding to explain this finding, since the test results presented in Tables 3.6, 3.10, 3.11, 4.3, 4.4 and 4.5 confirm the need to determine pin-bearing strength with the largest bolt diameter found in practice, and bolts up to 1 in (25.4 mm) in diameter may be used.

Characteristic values for both Chapter 3 and 4 (in Tables 3.6, 3.10, 3.11, 4.3, 4.4 and 4.5) have been determined in accordance with Annex D7 in Eurocode 0 (BS EN 1990:2002) based on the Normal (Gaussian) probability distribution function. For LRFD design the statistically-based properties of FRPs are to be determined in accordance with ASTM D7290 (2006). Now the probability distribution function is assumed to follow the two-parameter Weibull distribution. The characteristic value calculated represents the 80% lower confidence bound on the 5^{th}-percentile value of a specified population and D7290 accounts for statistical uncertainty due to a finite sample (batch) size. This is achieved by specifying the value of the data confidence factor, Ω, which is used to adjust the sample's nominal value for uncertainty. To use

D7290 a minimum of 10 samples must be tested for a characteristic value to be calculated (D'Alessendro 2010).

Because of the lower limit on batch size of 10, only the test results for the 0^o material (Tables 3.6 and 4.3) can be analyzed following the procedure given in D7290. This was done using the benchmarked spreadsheet written by D'Alessendro (2010). Figure 4.12 reproduces the characteristic strength plots of Figure 4.9 with the addition of characteristic values in accordance with D7290. The 'Weibull distribution' strengths (in N/mm^2) are given in the figure next to their solid symbol (diamond for non-aged and square for aged), and dashed lines are used to indicate the piecewise curves that D7290 give. It is seen from the plotting that D7290 strengths are lower and that the level of difference is batch dependent. The Eurocode 0 values, from row nine of Tables 3.6 and 4.3, can be used to show that the differences on using the two statistical analyses lie in the range 4 to 18% for the test matrix and batch (sample) sizes covered.

It is instructive, in finishing the discussion on the aged test results, to know that the material properties quoted earlier from the Creative Pultrusion Design Manual (Anonymous, 2012a) are those for standard structural shapes produced years ago. Because the 203×203×9.53 mm sections arrived at the University of Warwick in the mid 1990s these properties are associated to the material characterized in Chapter 3 and 4. Current pultruded sections, such as the Pultex® Fiber Reinforced Polymer SuperStructurals from Creative Pultrusion Inc. (2012a), are likely to have a different construction and/or constituent material composition. As a result of advances in constituent materials and the manufacturing processes the detrimental effect of

environmental conditioning on today's pultruded materials could be different to that reported in Chapter 3 and 4.

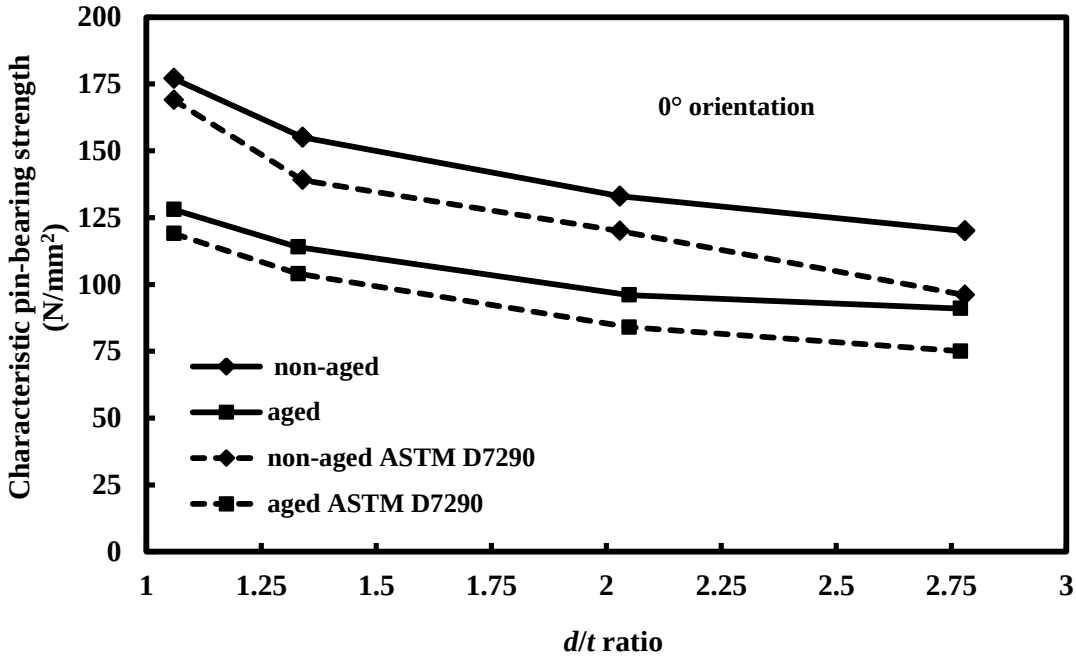

Figure 4.12. Characteristic pin-bearing strengths (in N/mm^2) of 0° material in accordance with BS EN 1990:2002 and ASTM D7290.

4.4 Concluding Remarks

Aged pin-bearing strengths have been determined for a material, after the specimens had received hot-wet conditioning to simulate aging for an unknown number of service years. To represent how bolted connections are found in practice the hole diameter is bigger than the pin diameter by a minimum of 2.2 mm. Test results for twelve batches are presented and the characteristic strengths are determined in accordance with Eurocode 0, allowing for the acceptable assumption that the coefficient of variations are not greater than 10%. The test matrix of three material orientations (0^o, 45^o and 90^o) and four pin diameter-to-thickness ratios (1.1, 1.3, 2.0 and 2.8 (to nearest 0.1)) is identical to that for the results presented in Chapter 3,

when the material had not received additional aging. By aging the specimens in water at a constant temperature of 40^{o}C for 3000 hours a pin-bearing strength is found to have reduced by 20 to 30% of its non-aged characteristic value. It is found that characteristic strengths determined with the biggest pin diameter of 25.4 mm do not fit in statistically with those obtained using the three smaller pin sizes. By ignoring results for this pin size, the mean reduction is highest, at nearly 30%, for the longitudinal (0^{o}) material (when the unidirectional roving reinforcement layers govern), and lower, at about 20% for the 45^{o} and 90^{o} material orientations.

It is further observed from inspecting plots and tabulation of the Eurocode 0 characteristic strengths that the loss in strength, for pin diameters between 9.7 and 18.8 mm, is a constant percentage of the non-aged strength. The strength reduction for these pin sizes are about 30% for 0^{o} orientation and 20% for 45^{o} and 90^{o} directions.This finding is important as it indicates that costly testing could be limited to a relative low number of batches with the outcome that we can more readily establish the characteristic pin-bearing strengths required for the design of bolted connections, when the mode of failure is bearing.

The lowest characteristic strengths are obtained with the largest pin of 25.4 mm diameter. For the 0^{o} orientation this strength is found to be 91 N/mm^{2}. It is 67 N/mm^{2} when the web material is oriented at 90^{o}. With Creative Pultrusions Inc. giving, for non-aged material, these two orthogonal strengths as 206 N/mm^{2} and 124 N/mm^{2}, respectively, it is essential that designers recognize the appropriateness of the tabulated (maximum) bearing strengths in a pultruder's design manual. Comparing these values reported by Creative Pultrusions Inc. for non-aged material with the

lowest characteristic strengths, it is found that the strengths for the longitudinal (LW) and transverse (CW) orientations have a reduction values of 56% and 46%, respectively. These reductions are about four and three times higher than the 15% reduction that is recommended by Creative Pultrusions Inc. (refer to Table 6.1 in Anonymous (2012a)).

Having moisture reduction factor (C_M) of 0.8 and 0.86 for temperature reduction factor (C_T), the American pre-standard allows the total reduction factor of 0.7 to adjust the strength loss for the purpose of structural design when using polyester material. Based on this reduction (adjustment) factor, it can be seen that the reduction values of 56% and 46% are about 14% and 24% higher than reduction factor permitted by the American pre-standard. It is important to mention that the reduction factors which can be obtained by using the American LRFD pre-standard are for sustained end-used condition of structural products after being used in moisture and temperature condition in their service lives.

In Part 3 to the European standard EN 13706 Table 1 reports, again, for non-aged material, the required minimum pin-bearing strengths. It is observed from the aged strengths reported herein that the 0^o and 90^o minimums of 150 and 70 N/mm^2 are not met after the web material had been subjected to the hot-wet aging. The strength loss is likely to have been higher still, had strength testing itself been carried out at the evaluated temperature of 40^oC. It is therefore imperative that the determination of pin-bearing strength is carried out with test conditions that allow for the worse probable reduction that could be realized at the end of the service life of a pultruded structure with bolted connections.

Because the number of specimens per batch for the 0^{o} material was above the minimum of 10 it was feasible to compare the characteristic values determined using the Eurocode 0 statistical procedure (BS EN1990:2002), based on the Normal (Gaussian) distribution, with those calculated using a different scheme in ASTM D7290 (2006), based on the two-parameter Weibull distribution. It is this latter standard that is to be used with a LRFD design standard (Anonymous, 2012d) to establish characteristic strength and stiffness values for the strength formulae. By making this comparison it is found that a characteristic strength calculated using D7290 is lower and that the difference between the two statistical analyses can be significant and batch size dependent.

Chapter 5

Startlink Dowel Connections

5.1 Introduction

To construct a lightweight building system the engineering solution to the design of the Startlink house (see section 2.6.2) was developed based on a family of bespoke pultruded shapes, which have the closed geometries shown in Figure 2.15. It was, therefore, for the Startlink consortium to select the method of connection to be suitable for joining and assembling these thin-walled shapes. Moreover, to meet Code level 6 criteria (DCLG, 2006) for overall house thermal resistance, it made engineering sense to reduce the risk of thermal bridging, to almost zero, by having no metal fasteners.

Because there was a risk that the initial concept of using 'snap-fit' connections would not satisfy the design requirements for the SLBS (see Section 2.6.2) the structural system was developed to have portal frames shown in Figure 2.17 for the primary load bearing structure. Connections and joints were formed using FRP solid dowel (rod) and adhesive bonding for primary framing connections and by employing PFRP closed shapes as dowelling (see Figure 2.18) for secondary member connections.

Figures 5.1(a) to 5.1(c) schematically show a stage in the SLBS assembly with internal walls and secondary dowels of tube and square box shapes. From Figure

5.1(a) it can be seen how these two shapes are employed to make dowel connections within the stud columns and floor beams.

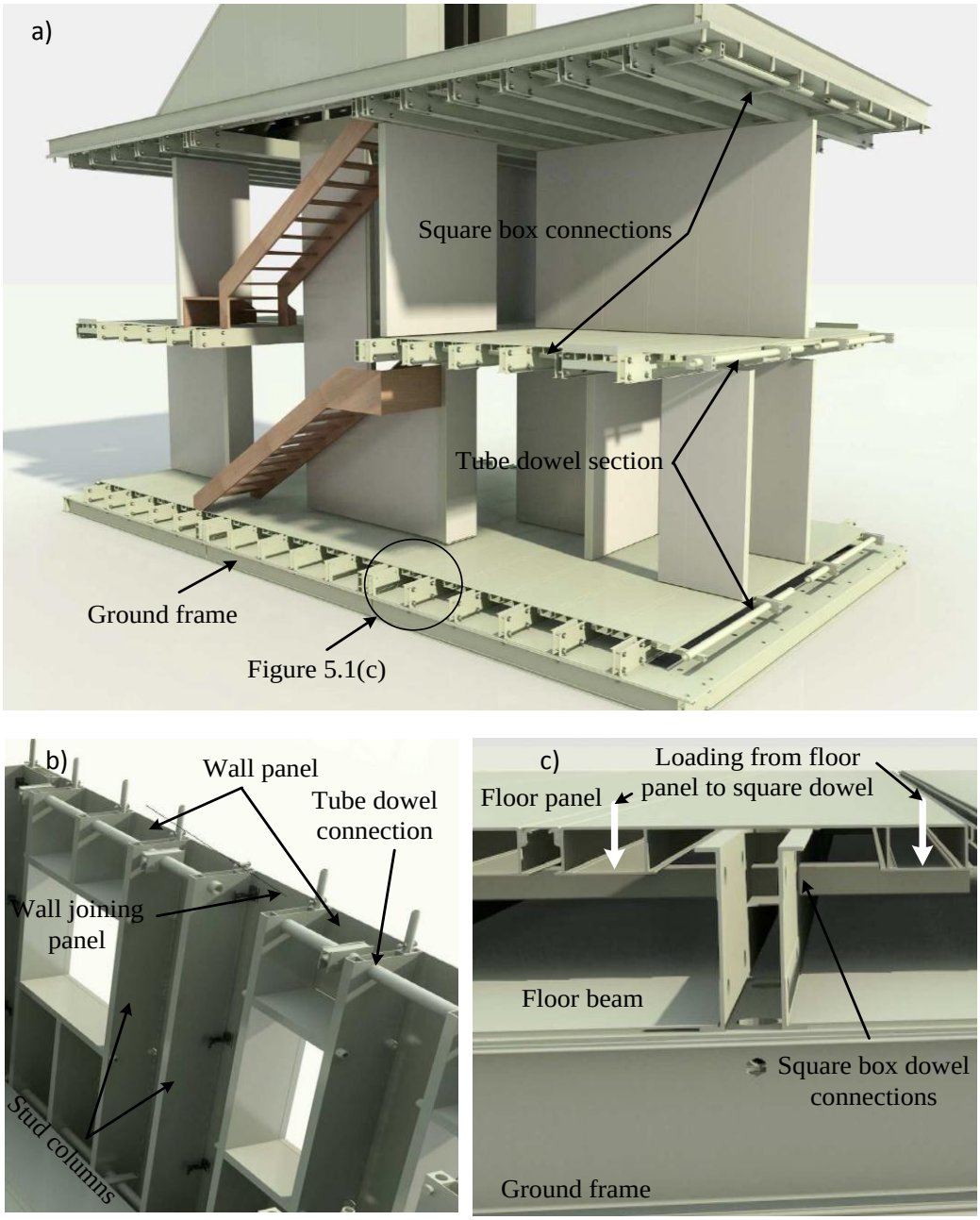

Figure 5.1. Startlink house assemblies; a) A stage of house with internal walls and hollow dowel shapes of square box and tube sections; b) Wall panel showing tube dowel connections; c) Floor panel showing square box dowel connections.

Figure 5.1(b) shows a section of wall panelling a ‘continues’ horizontal tube on the inner side that makes dowel connections with the vertical stud columns at 600 mm spacing.

By way of further dowel connections the secondary tube member passes through box-sections to join the stud columns to either a floor or roof assembly. Figure 5.1(c) shows a close view of a dowel connection between a square box shape and floor beam. The figure also shows how vertical load is transferred from the bottom surfaces of the down stands in the floor panel to the floor beam through the square box shape. This secondary member is required to provide transverse stiffening to the floor panel.

The purpose of this chapter is to report the results from a fact finding series of static coupon- sized tests to determine the strength of the tube and square shapes for their dowel connections. Testing was carried out using five load arrangements. The four load arrangements shown in Figures 5.2 to 5.5 are for: pin-bearing; ‘pure’ shear; shear-moment and plane compression. The fifth arrangement is shown in Figure 5.6 and it is for the ‘pure’ shear load arrangement after modification following evaluation of two results from the other four arrangements. The reason for conducting tests for the ‘pure’ shear case with two distinct configurations was the adverse influence from applying load by way of the stiff 30 mm diameter steel pins seen in the Figure 5.3. It was observed that the stress field for the tube dowel is very localised, complex and involving high stress concentrations. It was believed that the initial load configuration of the ‘pure’ shear case in the Figure 5.3 cannot actually represent how the tube is used (see Figure 5.1(b)) in the Startlink house. To

overcome the loading problem the steel pins were replaced by two notched rectangular box sections as seen in Figure 5.6. Further information about the five loading arrangements will be given in Section 5.3.

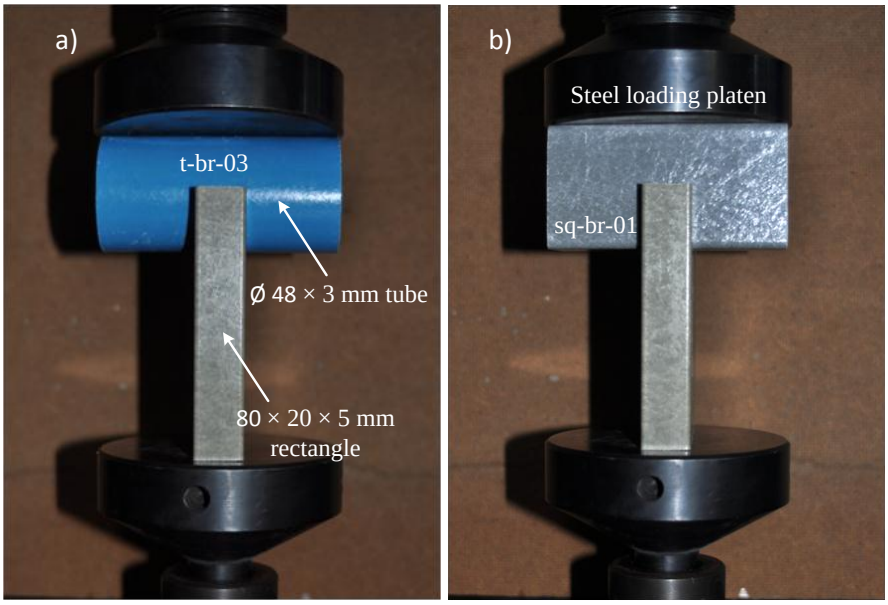

Figure 5.2. Pin-bearing strength test arrangement for determination of strength of: (a) tube shape; (b) square shape.

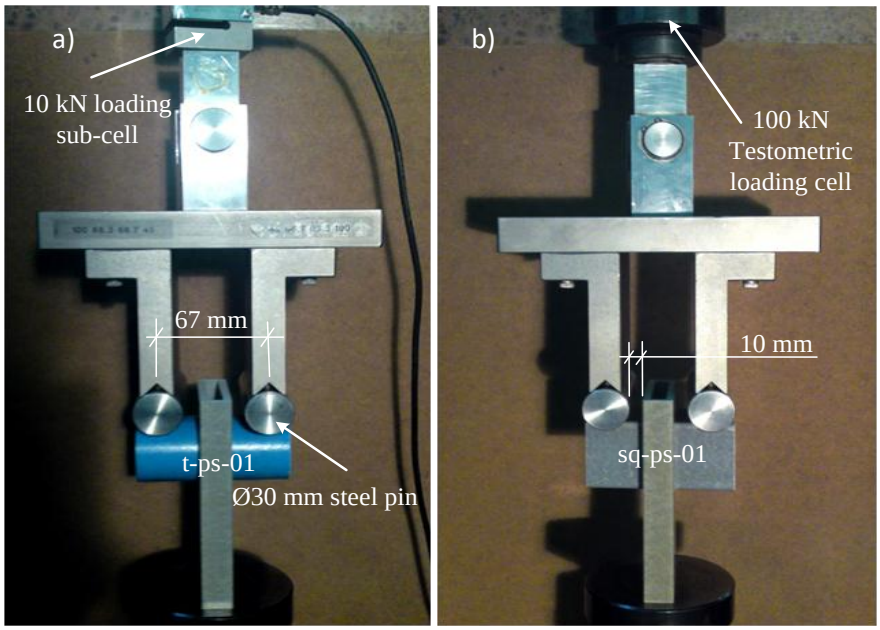

Figure 5.3. Pure shear strength test arrangement for determination of strength of: (a) tube shape; (b) square shape.

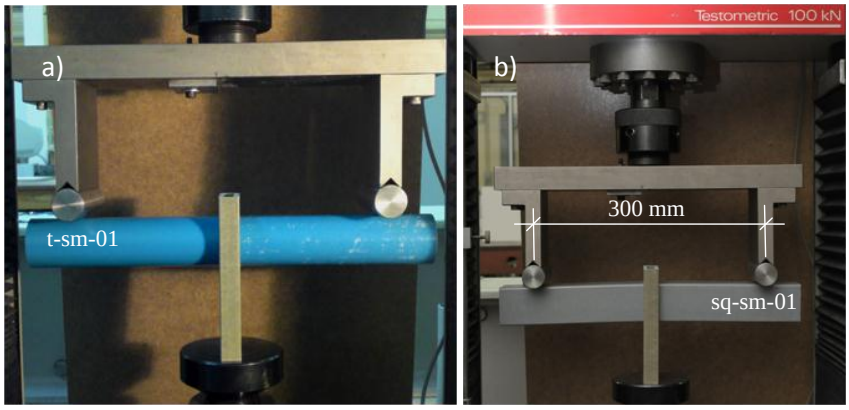

Figure 5.4. Shear moment strength test arrangement for determination of strength of: (a) tube shape; (b) square shape.

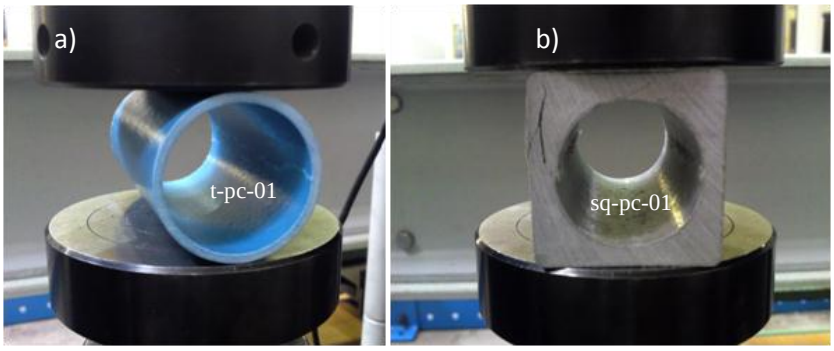

Figure 5.5. Plane compression strength testing of dowel sections without rectangular shape: (a) tube shape; (b) square shape.

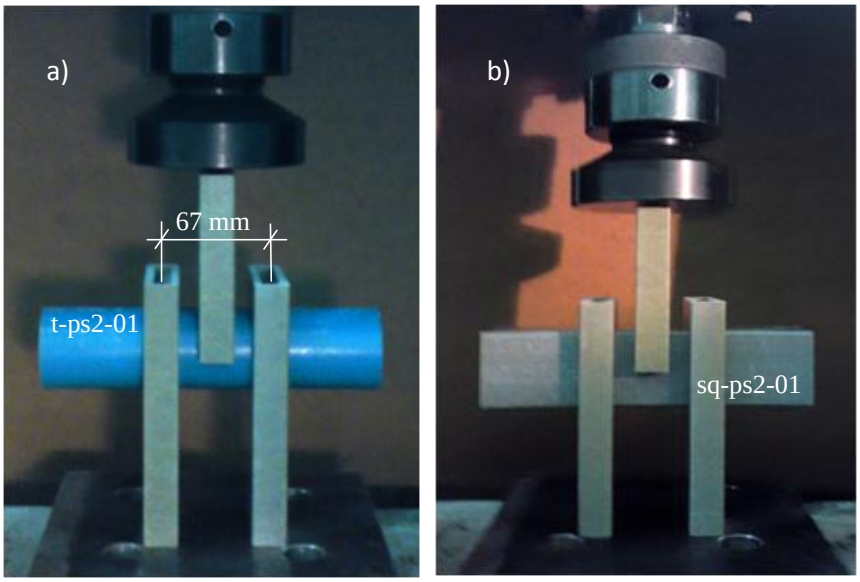

Figure 5.6. Modified fifth load arrangement for pure shear (ps) loading where the steel pins of 30 mm diameter have been replaced by two lengths of the 80 × 20 × 5 mm rectangular shape: (a) with tube specimen; (b) with square specimen.

In what follows the author reports the material specification for the dowel shapes, their geometries and details of the specimens for each load arrangement. The test procedure and results are reported and a discussion given on what had been achieved. The main objective was to determine what can be a damage load for dowel connection design.

5.2 Materials and Specimens

Figure 5.7(a) and 5.7(b) show the cross-section of two off-the-shelf shapes chosen as dowels for the transverse secondary members and assemblies. The (blue) tube shape (PD1570) has a nominal diameter of 48.2 mm and 3 mm wall thickness and a (grey) square shape (PD0821) has nominal side lengths of 51 mm and a hollow circular centre of nominal diameter 38 mm. The both shapes are pultruded by EXEL Composites UK and have different E-glass reinforcement architecture and matrix material. Their fibre architectures are given in Tables 5.1 and 5.2. Throughout the rest of the chapter these tube and square sections will be referred to as dowels.

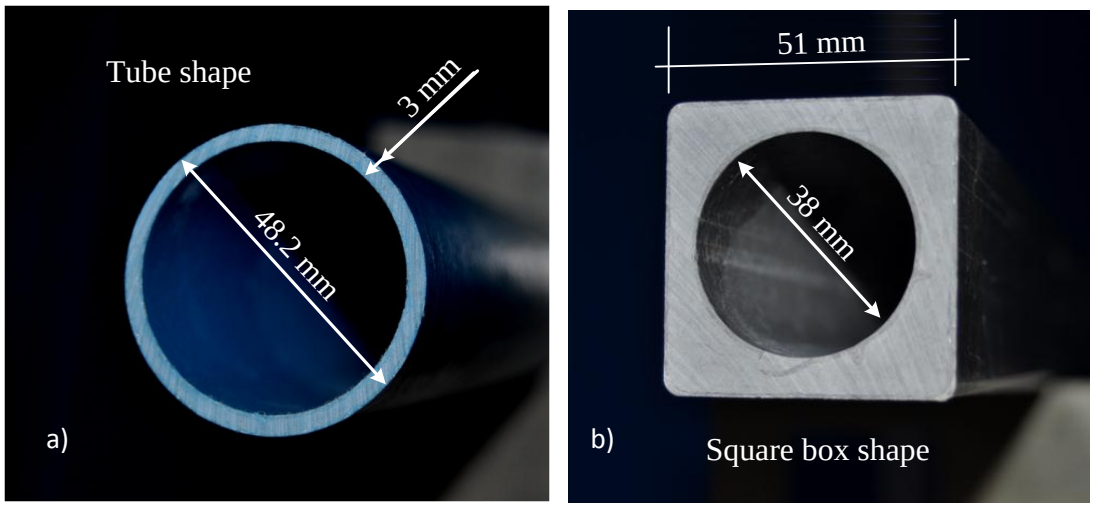

Figure 5.7. Two shapes used to make dowel connection: a) Tube shape; b) Square box shape.

Table 5.1. Fibre architecture for EXEL Composites tube section ϕ48.2×3 mm (PD1570), which is coloured blue.

layer	Material reinforcement	Density (g/m^3)	Weight (g/m^2)	Fibre mass (g/m)	Fibre width (mm)	No. Plies
(1)	(2)	(3)	(4)	(5)	(6)	(7)
A	Polester Veil NLC 10/350N-15-1500 35gsm	1.38	35	5.6	160	1
B	CFM M8643 450 GSM	2.43	450	72.0	160	1
C	Advantex 111A x27 4800tex	2.55	-	316.8	-	-
D	CFM M8643 450 GSM	2.43	450	67.5	150	1
E	Mock Spun ECR 698 2400 Tex E Glass	2.55	-	4.8	-	-
F	Polester Veil NLC 10/350N-15-1500 35gsm	1.38	35	1.4	40	1

Table 5.2. Fibre architecture for EXEL Composites square section 51×ϕ38 mm (PD0821), which is coloured grey.

layer	Material reinforcement	Density (g/m^3)	Weight (g/m^2)	Fibre Mass (g/m)	Fibre width (mm)	No. Plies
(1)	(2)	(3)	(4)	(5)	(6)	(7)
A	Polester Veil N27 20 GSM	1.38	20	4.2	210	1
B	CFM M8643 450 GSM	2.43	450	85.5	190	1
C	CFM M8643 450 GSM	2.43	450	60.8	135	1
D	Advantex 111A x27 4800tex	2.55	-	1536.0	-	-
E	CFM M8643 450 GSM	2.43	450	20.3	45	1
F	Mock Spun ECR 698 2400 Tex E Glass	2.55	-	9.6	-	-
G	Polester Veil N27 20 GSM	1.38	20	1.0	50	1

In column (1) the reinforcement layers are given in order from the surface veil to the inner layer that forms the pultruded laminate. In column (2) the reinforcement types are introduced. Given in columns (3), (4) and (5) are the physical properties for density (g/m^3), weight (g/m^2) and fibre mass (g/m) for each layer and in column (6) the width of the fibre reinforcements is given. Column (7) refers to the number of reinforcements per laminate layer.

During 2010, when this fact finding investigation was conducted, there were no Startlink pultrusions. It was decided that the dowel connections to be tested should be made with an off-the-shelf rectangular shape, which is seen in Figure 5.1(b). The nearest in size and in stock, was the rectangular shape (PD1515) of size 80×20×5 mm. Figure 5.8 shows the cross-section of the off-the-shelf rectangular box shape (PD1515) that is used herein to represent SLBS structural shapes (refer to Figures 5.2 to 5.4 and 5.6). The influence that dissimilarity in dimensions between the rectangular shape and the actual Startlink floor beam and stud column shapes might have on the test results has not been considered. The rectangular shape can also be seen in Figures 5.2 to 5.4 and 5.6, and is oriented such that the dowel's bearing force is aligned with the direction of pultrusion.

EXEL Composites UK prepared a total of ten batches specimens for the five load arrangements (five load arrangements × two dowel shapes). For the four load arrangements shown in Figures 5.2 to 5.5 there were eight batches of three nominally identical specimens. To establish the damage load it was judged by the author's supervisor that batches of three specimens should be appropriate for this fact finding

characterisation work. Greater certainty towards reliable strength determination does, however, require a batch size with, say, a minimum of 10 (Mottram, 2009a).

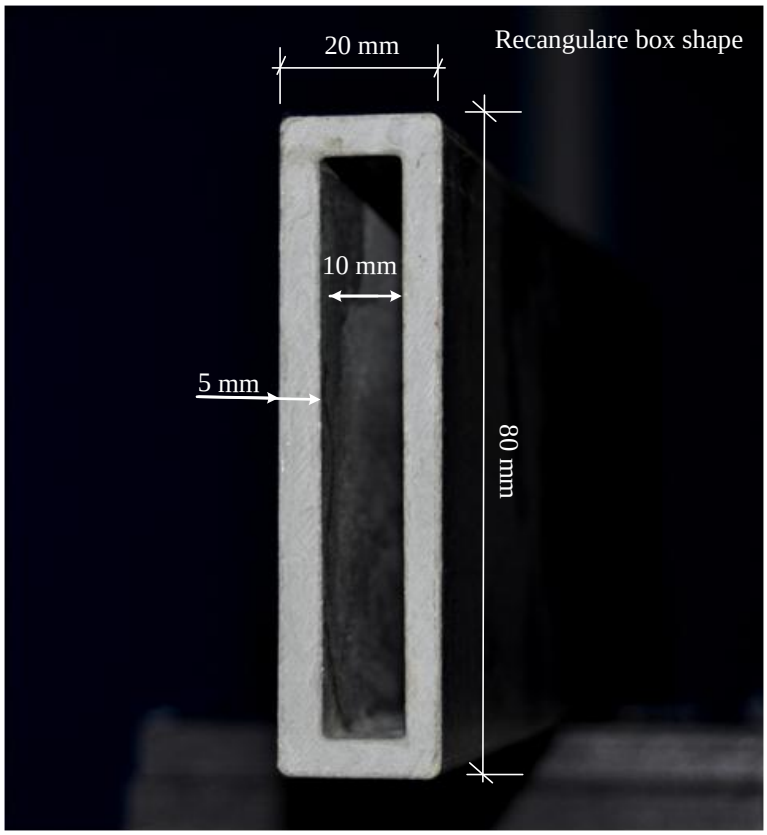

Figure 5.8. Cross-section of the rectangular box shape.

Figures 5.9(a) to 5.9(c) show the pin-bearing, 'pure' shear and shear-moment specimens, respectively. As it can be seen from Figure 5.5 that the specimens for plane compression loading case were simply a plane length of two dowels without rectangular shape.

The eight batches were given specimen labels. The first character in the scheme is **t** or **sq** for **t**ube or **sq**uare specimen followed by the loading arrangement of **br** for pin-**b**ea**r**ing, **ps** for '**p**ure' **s**hear and **sm** for **s**hear **m**oment and, lastly, with the number of

specimen. As examples, t-br-03 is for the specimen with a **t**ube dowel, loaded in pin **b**ea**r**ing and number **3** in the batch and sq-sm-01 is for the specimen with a **sq**uare dowel, loaded in **s**hear **m**oment and number **1.**

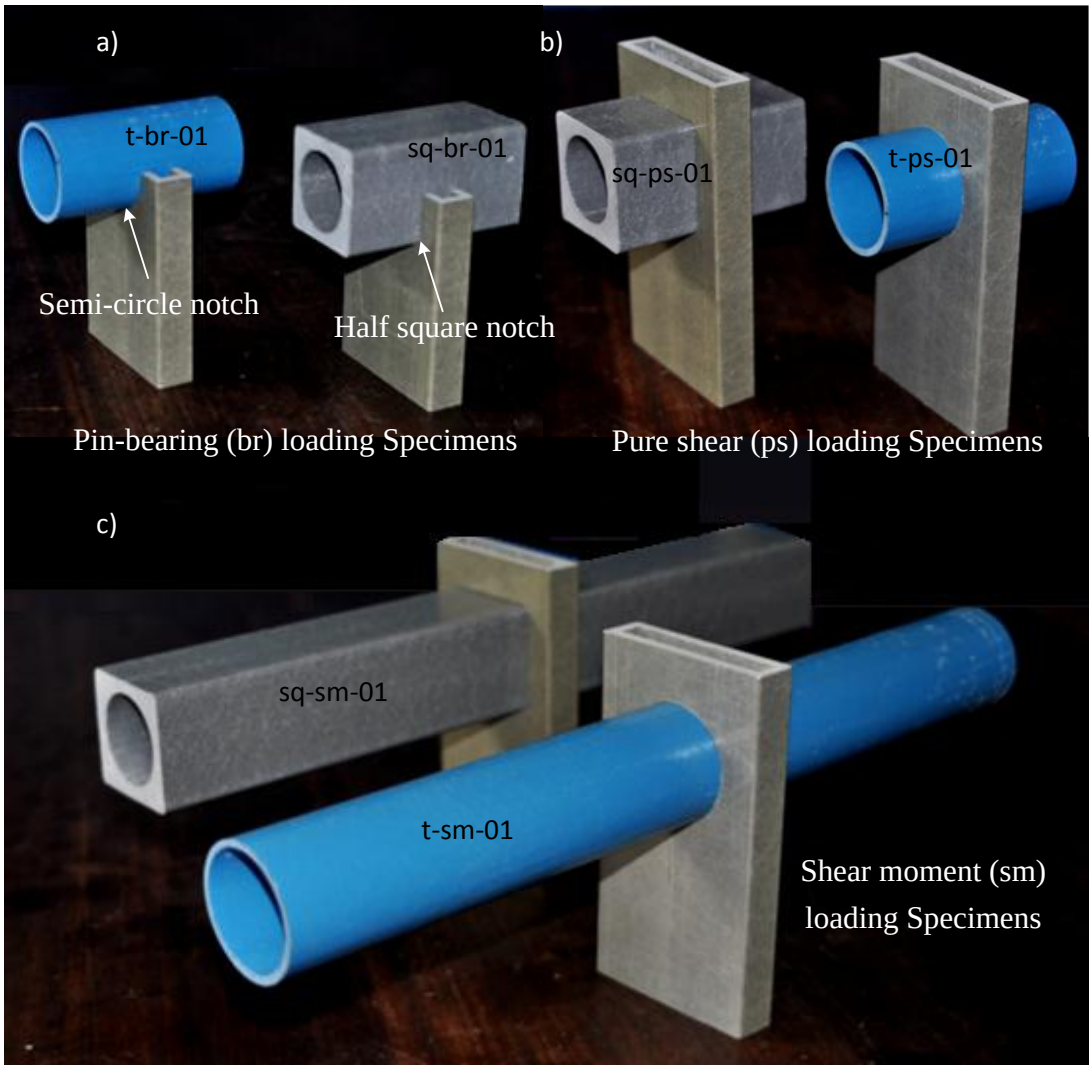

Figure 5.9. Specimens for the three loading arrangements with the rectangular shape: (a) pin-bearing; t-br-01 and sq-br-01; (b) 'pure' shear; t-ps-01 and sq-ps-01; (c) moment-shear; t-sm-48-01 and sq-sm-01.

Figure 5.10 shows the modified test specimens for the second load configuration of 'pure' shear (fifth arrangement) with a tube (t-ps2-01) and square (sq-sp2-01) specimens. As stated in Section 5.1 the 30 mm diameter steel pins were replaced by

lengths of the 80×20×5 mm rectangular shape with appropriately shaped notches to eliminate the ‘too harsh’ loading from the pins and also to represent how the dowels are loaded in the Startlink house (refer to Figures 5.1(b) and 5.1(c)). In the rest of this chapter the term of second load configuration for ‘pure’ shear or ‘modified ps load configuration’ is used for the fifth load arrangement.

To improve the reliability of the results the second change in the series of tests with the modified loading was to increase the specimen batch size from three to 10. For this load configuration (see Figure 5.6) the geometry is the same as for the ps load arrangement in Figures 5.3. Since the modified test configuration has similar dimensions to that called ‘ps’ in the ‘first pure shear configuration’ tests, the author suffix the ‘ps’ identifier with a ‘2’ to indicate a specimen from the second test series.

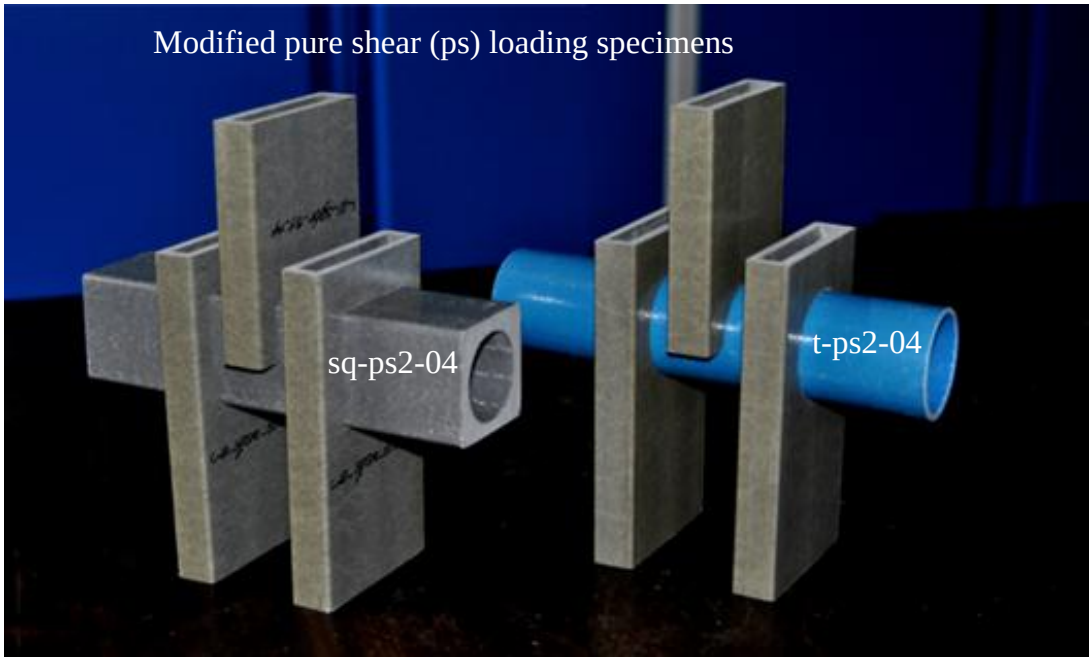

Figure 5.10. Pure shear (ps) specimens for modified fifth load arrangement when the steel pins of 30 mm diameter have been replaced by two lengths of the 80×20×5 mm rectangular shape.

For the tube shape (PD1570) measured diameters and wall thicknesses are reported in Tables 5.3 and 5.4, respectively. The mean diameter is 48.1 mm and the mean wall thickness is 3 mm. Its nominal cross-sectional area is 425 mm^2. The mean, standard deviation (SD) and coefficient of variation (CV) for the diameter of the semi-circle notch in the pin-bearing specimens (br) is 48.27 mm, 0.06 and 0.1(%) respectively. The difference in diameters shows that the hole clearance is 0.3 mm or less; this size of clearance gives a tight fit, which is desirable in a dowel connection. The same tight fit was experienced when inserting a length of the tube shape through a circular hole in the rectangular 80 × 20 × 5 mm shape (PD1515).

Table 5.3. Mean, standard deviation (SD) and coefficient of variation (CV) for the outer diameter of the ϕ48×3 mm tube shape.

Specimen			Measured diameters (mm)			Average (mm)	SD (mm)	CV %
Blue tube shape ϕ48.2×3- wall thickness								
t	br	01	48.05	48.15	48.20	48.13	0.08	0.2
		02	48.40	48.15	47.95	48.17	0.23	0.5
		03	48.40	48.15	47.70	48.08	0.35	0.5
	ps	01	48.25	48.20	47.95	48.13	0.16	0.3
		02	48.20	48.30	47.95	48.15	0.18	0.4
		03	48.10	48.20	48.20	48.17	0.06	0.1
	sm	01	48.20	48.30	47.85	48.12	0.24	0.5
		02	48.10	48.10	48.20	48.13	0.06	0.1
		03	48.15	48.30	47.95	48.13	0.18	0.4
	pc	01	48.05	48.30	47.75	48.03	0.28	0.4
		02	48.05	48.20	47.95	48.07	0.13	0.3
		03	48.20	48.30	47.80	48.10	0.26	0.6
t-ps2		01	48.00	47.93	47.90	47.94	0.05	0.1
		02	48.22	48.15	48.10	48.16	0.06	0.2
		03	48.12	48.15	47.90	48.06	0.14	0.3
		04	48.15	48.00	48.00	48.05	0.09	0.2
		05	48.07	48.00	48.00	48.02	0.04	0.1
		06	48.15	48.07	47.90	48.04	0.13	0.3
		07	48.10	48.05	47.95	48.03	0.08	0.2
		08	48.18	48.06	48.05	48.10	0.07	0.2
		09	48.20	48.10	48.06	48.12	0.07	0.2
		10	48.10	48.05	48.05	48.07	0.03	0.1
					Mean	**48.09**	**0.13**	

The mean width of the sides of the square shape (PD0821) and its lowest wall thickness are reported in Table 5.5 and 5.6. The mean width is 50.7 mm and the mean minimum wall thickness is 6.41 mm; twice the thickness in the tube section (see Table 5.4). This shape has a nominal cross-sectional area of 1410 mm^2; 3.3 times that of the tube. It was noted that the square section is not exactly symmetrical and that it side length (width) is in the range 50.55 to 51.5 mm; on occasions it was necessary to rotate a square section through 90 degrees to be able to insert it through a tight fitting square shaped hole. Another geometric feature of the square shape is that the side walls are slightly concave, and this means that when compression load is applied the corner regions transfer all of the force.

Table 5.4. Mean, standard deviation (SD) and coefficient of variation (CV) for the wall thickness of the ϕ48×3 m tube section (PD1570).

Specimen			Measured thicknesses (mm)			Average (mm)	SD (mm)	CV %
Blue tube shape ϕ48.2×3- wall thickness								
t	br	01	3.21	3.09	2.89	3.06	0.22	7
		02	3.31	2.93	2.77	3.00	0.25	8
		03	3.29	3.09	2.75	3.04	0.25	8
	ps	01	2.73	3.11	3.30	3.05	0.25	8
		02	3.29	3.01	3.22	3.17	0.12	4
		03	2.81	3.28	3.04	3.04	0.21	7
	sm	01	3.19	3.31	2.85	3.12	0.22	7
		02	2.93	3.38	2.74	3.01	0.29	10
		03	2.73	3.31	3.18	3.07	0.24	8
	pc	01	3.17	3.11	2.83	3.03	0.17	6
		02	3.36	3.01	2.76	3.04	0.25	8
		03	3.27	2.97	2.73	2.99	0.24	8
t-ps2		01	3.10	2.93	2.97	3.00	0.09	3
		02	3. 30	2.90	2.73	2.82	0.12	4
		03	3.21	3.02	2.79	3.01	0.21	7
		04	3.30	3.10	2.80	3.07	0.25	8
		05	3.33	2.90	2.73	2.99	0.31	10
		06	3.32	3.12	2.73	3.06	0.30	10
		07	3.38	2.95	2.70	3.01	0.34	11
		08	3.29	3.05	2.75	3.30	0.27	9
		09	3.32	3.00	2.70	3.01	0.31	10
		10	3.30	2.95	2.73	2.99	0.29	10
					Mean	**3.0**	**0.24**	

Table 5.5. Mean, standard deviation (SD) and coefficient of variation (CV) for width of the square section 51×ϕ38 mm (PD0821).

Specimen			Measured diameters (mm)		Average (mm)	SD (mm)	CV %
Grey square shape 51 × ϕ38 mm - width							
sq	br	01	51.20	50.55	50.88	0.46	0.9
		02	51.50	50.55	51.03	0.67	1.3
		03	50.80	50.55	50.68	0.18	0.4
	ps	01	50.80	50.70	50.75	0.07	0.1
		02	50.85	50.65	50.75	0.14	0.3
		03	50.90	50.65	50.78	0.18	0.3
	sm	01	50.80	50.70	50.75	0.07	0.1
		02	50.70	50.75	50.73	0.04	0.1
		03	50.70	50.75	50.73	0.04	0.1
	pc	01	51.00	50.55	50.78	0.32	0.6
		02	50.60	50.70	50.65	0.07	0.1
		03	50.65	50.75	50.70	0.07	0.1
Sq-ps2		01	50.70	50.69	50.70	0.01	0
		02	50.67	50.70	51.69	0.02	0
		03	50.76	50.57	50.67	0.13	0.3
		04	50.65	50.66	50.66	0.01	0
		05	50.70	50.69	50.70	0.01	0
		06	50.67	50.69	50.68	0.01	0
		07	50.73	50.57	50.65	0.11	0.2
		08	50.75	50.63	50.69	0.08	0.2
		09	50.69	50.64	50.67	0.04	0.1
		10	50.76	50.64	50.70	0.08	0.2
				Mean	**50. 72**	**0.12**	

Table 5.6. Mean, standard deviation (SD) and coefficient of variation (CV) for minimum wall thickness of the square section 51×ϕ38 mm (PD0821).

Specimen			Measured diameters (mm)				Average (mm)	SD (mm)	CV %
Grey square shape 51 × ϕ38 mm - wall thickness									
sq	br	01	5.55	6.90	7.10	5.80	6.34	0.78	12
		02	5.90	6.80	6.90	5.75	6.34	0.60	9
		03	6.65	6.85	7.10	6.35	6.74	0.32	5
	ps	01	6.70	6.90	7.05	6.80	6.86	0.15	2
		02	5.85	6.90	7.00	5.70	6.36	0.68	11
		03	7.25	5.95	7.00	5.60	6.45	0.80	12
	sm	01	6.85	5.70	7.20	5.85	6.40	0.74	12
		02	6.00	7.00	7.10	5.90	6.50	0.64	10
		03	5.90	7.05	7.10	6.10	6.54	0.63	10
	pc	01	6.00	7.00	7.10	5.80	6.48	0.67	10
		02	5.85	6.90	7.00	5.60	6.34	0.72	11
		03	5.95	6.80	7.00	5.70	6.36	0.63	10

Sq-ps2	01	6.95	7.06	5.48	5.92	6.35	0.67	11
	02	7.01	7.10	5.62	5.72	6.36	0.69	11
	03	6.75	6.87	5.76	5.61	6.25	0.57	9
	04	7.10	6.82	5.45	5.70	6.27	0.71	11
	05	6.92	6.85	5.80	5.70	6.32	0.57	9
	06	6.86	7.20	5.70	5.60	6.34	0.70	11
	07	7.00	6.94	5.95	5.76	6.41	0.56	9
	08	6.84	6.97	5.65	5.55	6.25	0.66	10
	09	6.92	6.94	5.62	5.64	6.28	0.65	10
	10	7.03	7.00	5.70	5.95	6.42	0.60	9
					Mean	**6.41**	**0.63**	

For rectangular shape (PD1515) itself, it is relevant to observe that it is not symmetrical about its principal minor axis. The measured mean thicknesses of the two side walls at 5.32 and 4.60 mm are, from 38 individual measurements per side, reported in Tables 5.7 and 5.8. It should be mentioned that the reported thicknesses for 20 modified test specimens have been measured from the top rectangular shape of modified test specimens.

Table 5.7. Mean, standard deviation (SD) and coefficient of variation (CV) for the wall thickness of the thicker side of the rectangular shape 80×20×5 mm (PD1515).

Specimen			Measured thicknesses (mm)			Average (mm)	SD (mm)	CV %
Grey rectangular shape 80 × 20 × 5 mm – thicker wall thickness								
t	br	01	5.55	5.35	5.10	5.33	0.18	3
		02	5.55	5.20	5.00	5.25	0.23	4
		03	5.50	5.30	5.00	5.27	0.21	4
	ps	01	5.55	5.30	5.00	5.28	0.22	4
		02	5.55	5.30	5.00	5.28	0.22	4
		03	5.50	5.35	5.10	5.32	0.16	3
	sm	01	5.50	5.40	5.10	5.33	0.17	3
		02	5.55	5.35	4.95	5.28	0.25	5
		03	5.60	5.35	5.05	5.33	0.22	4
sq	br	01	5.50	5.30	5.00	5.27	0.21	4
		02	5.50	5.35	5.10	5.32	0.16	3
		03	5.55	5.40	5.10	5.35	0.19	4
	ps	01	5.60	5.30	5.05	5.32	0.22	4
		02	5.55	5.40	5.10	5.35	0.19	4
		03	5.60	5.40	5.10	5.37	0.21	4
	sm	01	5.55	5.35	5.05	5.32	0.21	4
		02	5.60	5.35	5.05	5.33	0.22	4
		03	5.55	5.40	5.10	5.35	0.19	4

t-ps2	01	5.55	5.20	5.00	5.33	0.23	4
	02	5.50	5.30	5.00	5.25	0.28	5
	03	5.50	5.40	5.00	5.27	0.25	5
	04	5.60	5.45	5.10	5.30	0.26	5
	05	5.50	5.35	5.10	5.38	0.26	5
	06	5.60	5.35	5.05	5.27	0.20	4
	07	5.65	5.35	5.10	5.32	0.28	5
	08	5.60	5.45	5.10	5.35	0.28	5
	09	5.50	5.30	5.00	5.27	0.26	5
	10	5.50	5.35	5.10	5.35	0.25	5
Sq-ps2	01	5.55	5.40	5.10	5.37	0.20	4
	02	5.50	5.30	5.00	5.28	0.23	4
	03	5.60	5.35	5.10	5.25	0.25	5
	04	5.60	5.40	5.10	5.42	0.25	5
	05	5.55	5.25	5.00	5.37	0.25	5
	06	5.55	5.20	5.00	5.28	0.25	5
	07	5.70	5.45	5.10	5.25	0.28	5
	08	5.70	5.40	5.10	5.42	0.30	6
	09	5.55	5.35	5.10	5.40	0.30	6
	10	5.55	5.20	5.00	5.33	0.23	4
Mean					**5.32**	**0.23**	

Table 5.8. Mean, standard deviation (SD) and coefficient of variation (CV) for the wall thickness of the thinner side of the rectangular shape 80×20×5 mm (PD1515).

Specimen			Measured thicknesses (mm)			Average (mm)	SD (mm)	CV %
Grey rectangular shape 80 × 20 × 5 mm – thinner wall thickness								
t	br	01	4.35	4.65	4.90	4.63	0.22	5
		02	4.30	4.60	4.90	4.60	0.24	5
		03	4.35	4.60	4.80	4.58	0.18	4
	ps	01	4.35	4.60	4.80	4.58	0.18	4
		02	4.30	4.70	4.90	4.63	0.25	5
		03	4.30	4.60	4.85	4.58	0.22	5
	sm	01	4.35	4.60	4.80	4.58	0.18	4
		02	4.30	4.70	4.90	4.63	0.25	5
		03	4.30	4.60	4.85	4.58	0.22	5
sq	br	01	4.40	4.60	4.85	4.62	0.18	4
		02	4.35	4.60	4.85	4.60	0.20	4
		03	4.30	4.60	4.80	4.57	0.21	5
	ps	01	4.30	4.60	4.90	4.60	0.24	5
		02	4.35	4.60	4.90	4.62	0.22	5
		03	4.30	4.60	4.85	4.58	0.22	5
	sm	01	4.35	4.60	4.90	4.62	0.22	5
		02	4.30	4.60	4.85	4.58	0.22	5
		03	4.30	4.55	4.80	4.55	0.20	4

t-ps2	01	4.40	4.50	4.80	4.57	0.21	5
	02	4.60	4.65	4.90	4.72	0.16	3
	03	4.40	4.65	5.00	4.68	0.30	6
	04	4.40	4.55	4.80	4.58	0.20	4
	05	4.35	4.50	4.85	4.57	0.26	6
	06	4.40	4.65	4.85	4.63	0.23	5
	07	4.35	4.55	4.95	4.62	0.31	7
	08	4.35	4.55	4.80	4.57	0.23	5
	09	4.25	4.60	4.85	4.57	0.30	7
	10	4.40	4.65	4.90	4.65	0.25	5
Sq-ps2	01	4.40	4.60	4.85	4.62	0.23	5
	02	4.35	4.60	4.85	4.60	0.25	5
	03	4.30	4.60	4.80	4.57	0.25	6
	04	4.30	4.50	4.70	4.50	0.20	4
	05	4.35	4.65	4.90	4.63	0.28	6
	06	4.35	4.60	4.90	4.62	0.28	6
	07	4.45	4.70	5.00	4.72	0.28	6
	08	4.30	4.55	4.80	4.55	0.25	5
	09	4.30	4.55	4.80	4.55	0.25	5
	10	4.40	4.55	4.75	4.57	0.27	4
Mean					**4.60**	**0.23**	

The effect, a 10% difference in side wall thickness has on the strength results has not been established by this series of tests. It is important that the distance of only 10 mm between the inner two wall faces is much less than the 54 mm distance in stud column or 64 mm in the floor beam (refer to Figures 2.15 and 5.8), and this constraint on the test dimensions has to be taken into account when the damage and/or design loads (in kN) are used to check structural design calculations for the secondary member dowel connections in the Startlink house.

To be able to cut-out the square notch and square hole from the rectangular section it was necessary for EXEL Composites to drill pilot holes at the corners. Their presence meant that the bearing length was reduced to an average of 40.3 mm; it would be 50.7 mm if the notch and hole were precisely to the shape of the square section.

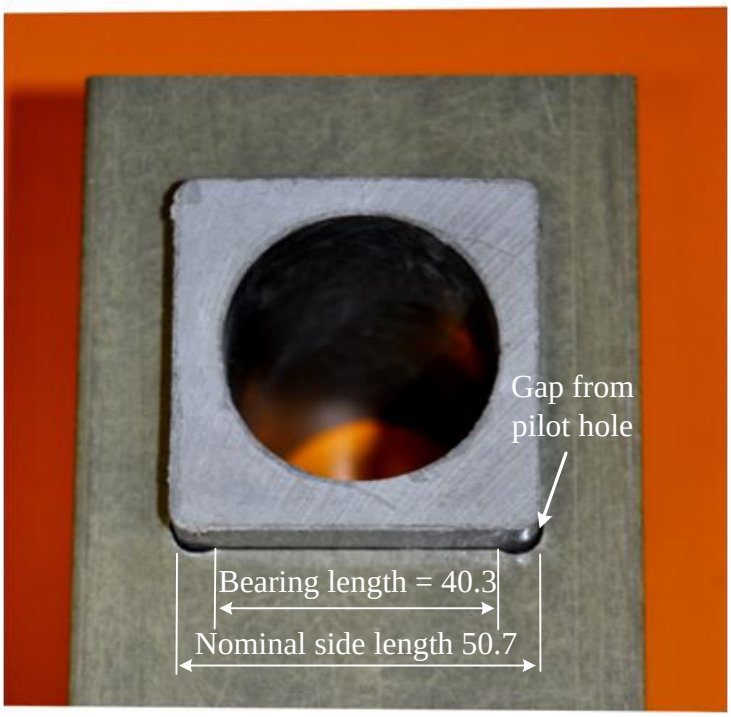

Figure 5.11. Bearing length in millimetre in square notch with presence of drill pilot holes at the corners of the rectangular shape.

5.3 Test procedure

Figure 5.12 to 5.16 present engineering drawings for the five load arrangements of br, ps, sm, pc and modified ps. Testing was conducted using a 100 kN Testometric testing machine and a 10 kN sub-cell for the tube specimens and the 100 kN main load cell for the square specimens (refer to Figures 5.3(a) and 5.3(b)).

Figures 5.12 and 5.2 show the loading arrangement referred to as pin-bearing. Compression force is applied directly onto the top of the shape, which is bearing directly against the rectangular shape in a semi-circular (for t-br) or half square notch (for sq-br). The height of the 80×20×5 mm rectangular shape is 106 mm. It can be

seen how the ‘compression’ displacement was made to be constant over the majority of the 98 mm length of the tube and square shapes.

For the other two load arrangements (ps and sm) using the rectangular shape, a short length of the tube or square is inserted into a close fitting hole through the 80 mm wide sides. Figure 5.13 show the load arrangement for the load case call pure shear (ps), where the distance between the two (symmetrical) loading pins is 67 mm. The dowel connection does experience a flexural deformation, which has been minimised in terms of the test set-up constraints. The load pins are of steel and diameter of 30 mm, and their separation is specified by what a four-point bending test rig allows. The separation distance of 67 mm also satisfies the walls distance of stud column, which has a centre-to-centre distance of 57 mm. As can be seen in Figure 5.3 the air gap between the circumference of pins and the walls of the rectangular shape is only 10 mm.

The shear-moment (sm) loading arrangement is shown in Figure 5.14. The dowel section is now 398 mm long and the separation between the two steel loading pins is 300 mm. This arrangement can be seen to represent the situation where there is loading onto a dowel member from the down stands of the Startlink floor panel, which have a centre-to-centre spacing of 150 mm(see Figure 5.1(c)). The bending moment from a lever arm of 150 mm is about five times higher than for the pure shear situation. To accommodate the dowel passing through a hole the height of the rectangular shape has been increased to 150 mm.

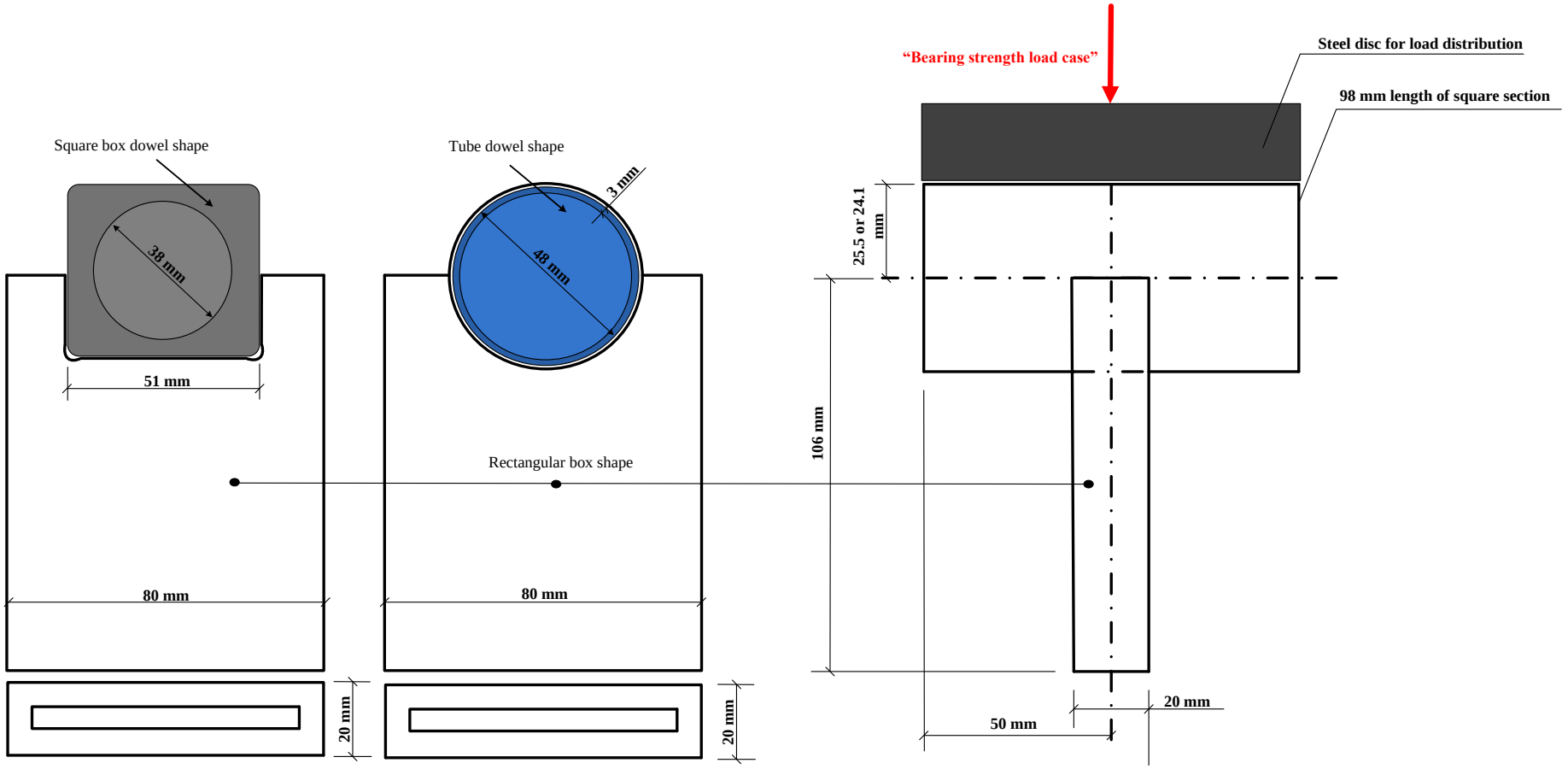

Figure 5.12. Test arrangement for load case of pin-bearing with tube and square box shapes.

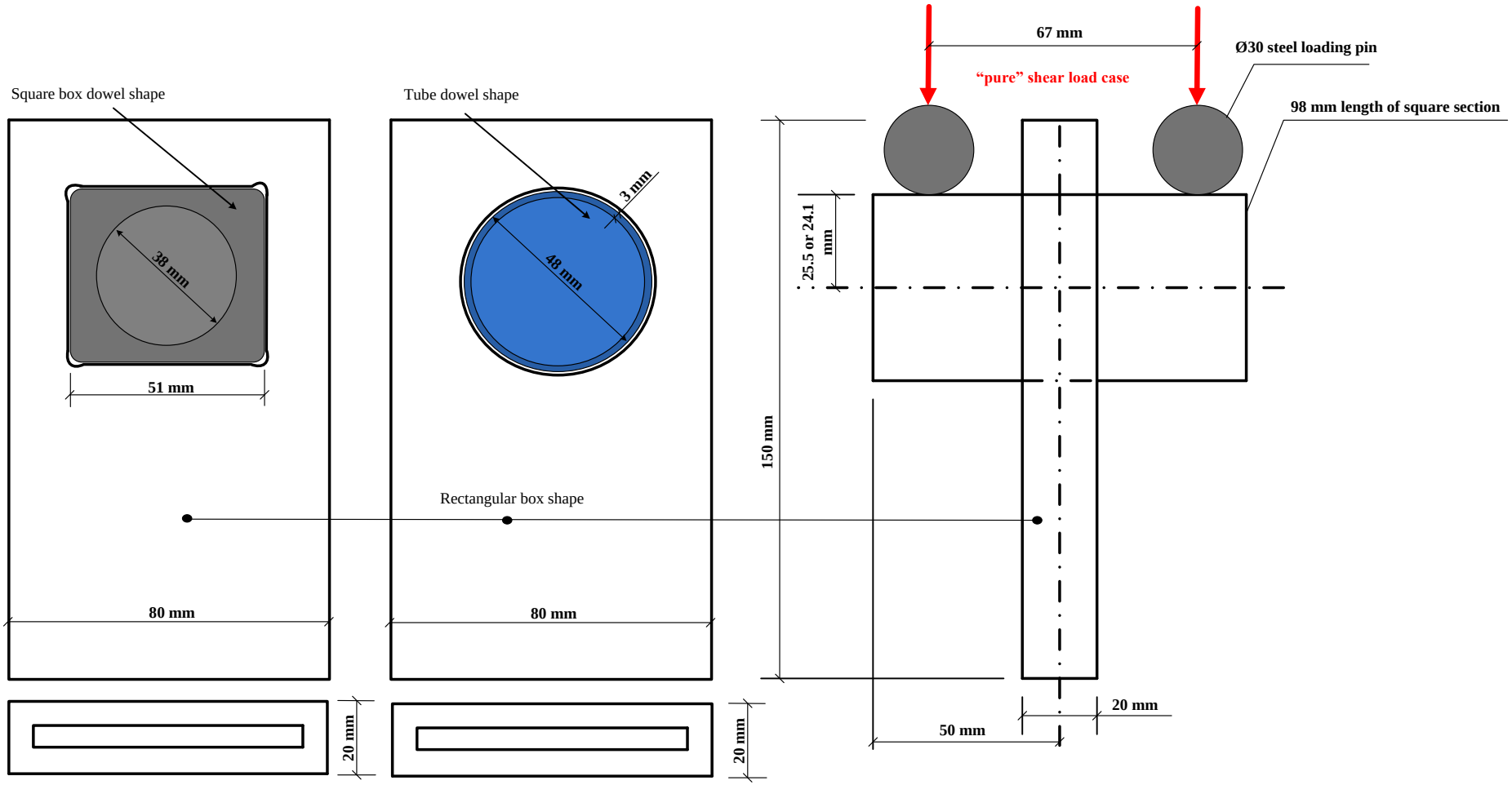

Figure 5.13. Test arrangement for load case of 'pure' shear with tube and square box shapes.

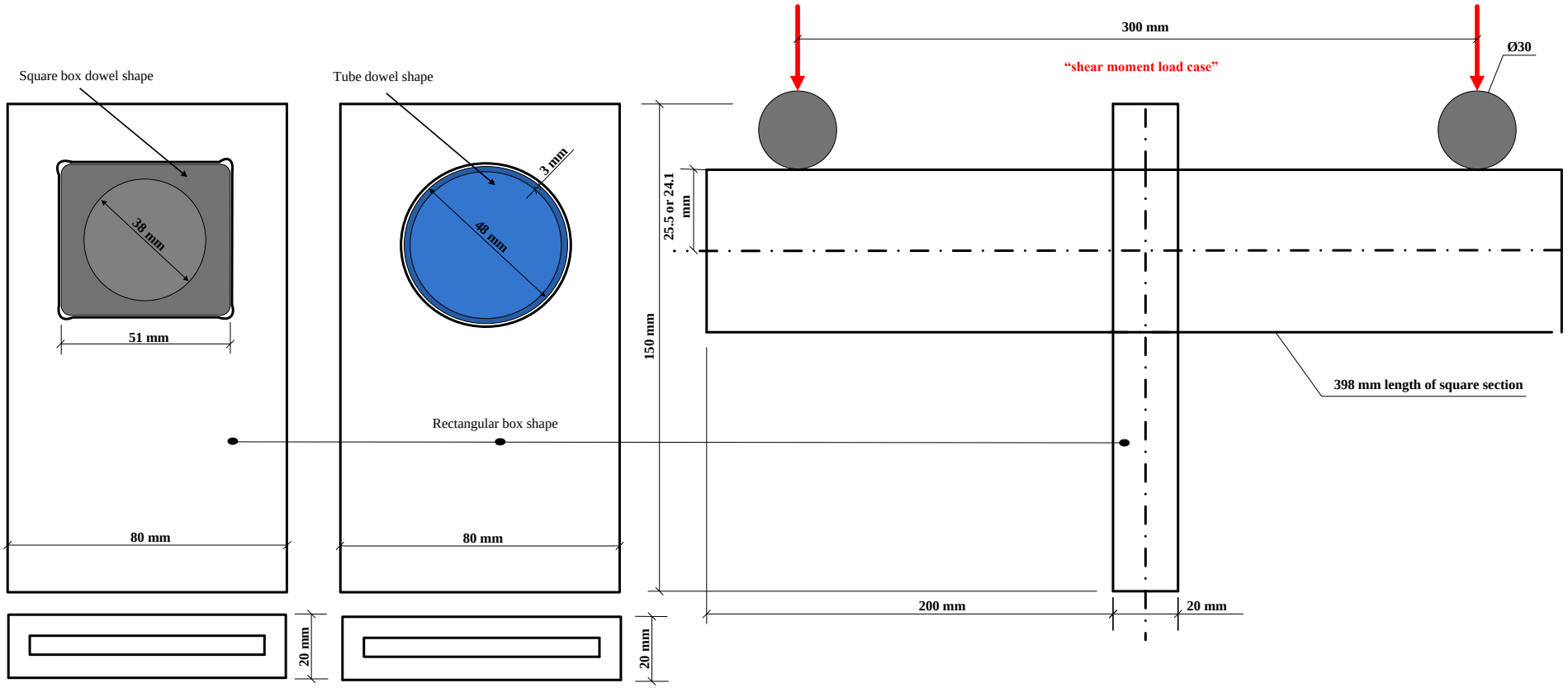

Figure 5.14. Test arrangement for load case of 'shear-moment' with tube and square box shapes.

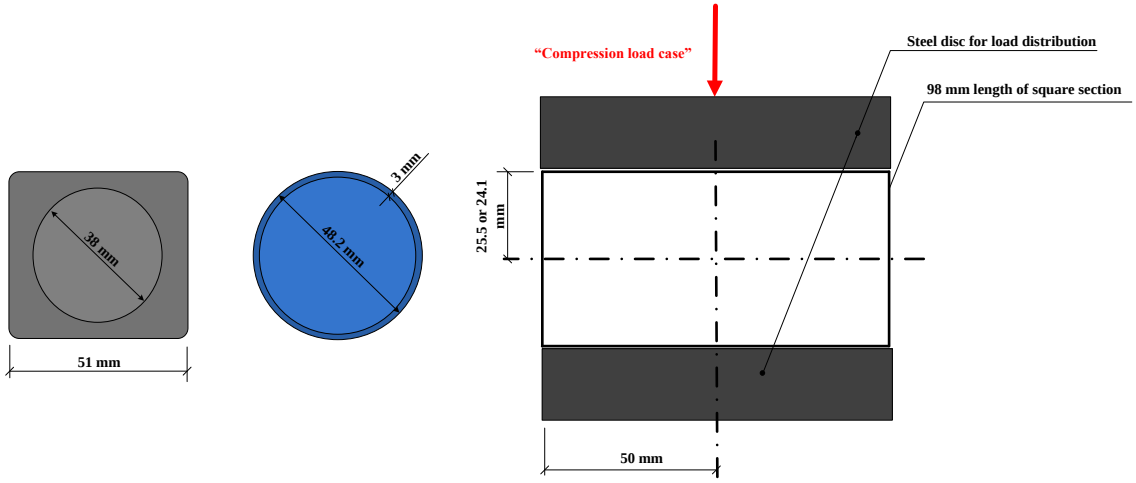

Figure 5.15. Test arrangement for load case of 'compression' with tube and square box shapes.

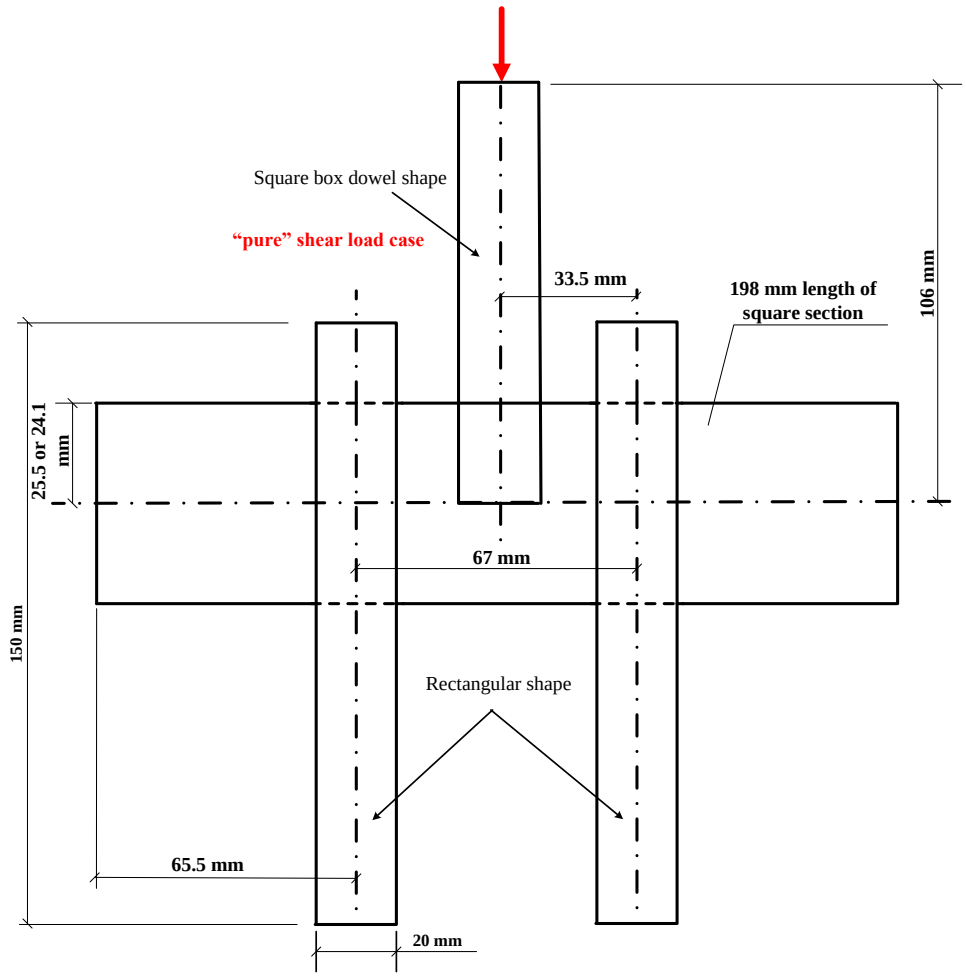

Figure 5.16. Modified test arrangement for load case of 'pure' shear whereby loading by the steel pins were replaced by two notched PD1515 rectangular shapes.

Because initial testing with these three loading arrangements showed that failure was always within the dowel, it was decided to involve the fourth load arrangement call plane compression shown in Figure 5.15. Now a short length of tube or square was tested, in isolation, by compression loading to both the upper and lower surfaces, applied directly from steel platen fixtures connected to the Testometric testing machine.

To overcome a major limitation from loading through steel pins another series of tests were performed, whereby the steel pins were replaced by two notched PD1515 rectangular shapes. The side view drawing in Figure 5.16 shows this modified test configuration. Note that to gain stability in testing it was convenient to position the two supports below the specimen; the steel pins were positioned above, because they are part of a steel test fixture that goes above the specimen (Figure 5.13). The height of the top semi-notch rectangular shape (applying the compressive load), for tube and square dowel shapes is 106 mm; the height and distance of two side supports of the rectangular section are 150 and 67 mm, respectively. The length of both dowel shapes is set at 198 mm. Although not identical to how the transverse members are used with the SBLS the loading arrangement in Figure 5.16 is believed to be more representative of practice.

To apply compressive load the stroke rate was set to 1 mm/min. The short-term static tests were conducted at room temperature ($21 \pm 2^{\circ}C$). The test procedure used was to load the specimen in load increments. When the load indicator on the Testometric testing machine showed that an increment in load had been reached, the increasing stroke was stopped, while the relative displacement (from zero load) and

compression force readings were recorded. Load was read to the nearest 0.1 kN. Before readings were taken, it was necessary to allow for the specimen to reach its equilibrium state (the stroke was kept constant for a least 60 seconds). This also allowed the specimen to be visually inspected and for all observations to be recorded. Attention was paid to audible noise coming from the specimen, as 'sudden cracking sounds' are an indication that there is material failure. A test was stopped when there was evidence that the specimen had experienced material failure (i.e. the damage load had been reached). The 'maximum' load in the test procedure is called the 'damage load'. Note that although this bearing stress is taken to be the bearing strength for the dowel it is in fact the average stress acting over the bearing area between the dowel and the rectangular section or, for the specific case of pc, one of the two steel loading plates (see Figure 5.15) for the plane compression load arrangement.

It is important to emphasise that the obtained strengths are a measure of the average compression stress over the bearing area from a dowel shape pressing into a notched rectangular shape. In other words the strengths from four load arrangements need to be called the: pin-bearing bearing strength, pure share bearing strength, shear moment bearing strength and compression bearing strength.

5.4 Results and Discussion

Presented in Table 5.14 are measured damage loads (maximum compressive force in kN) for the 44 test specimens to characterise the two dowel shapes by way of the five different load arrangements shown in Figures 5.2 to 5.6 and 5.12 to 5.16, using eight batches of three nominally identical specimens for br, ps, sm and pc and two batches

of ten nominally identical specimens for modified ps (or ps2). In columns (1) and (3) of Table 5.14 are the specimen labels (e.g. t-br-01 and sq-ps2-01) using the scheme explained in Section 5.2. Columns (2) and (4) give the damage laods for the tube and square dowelling, respectively.

Table 5.14. Damage loads for the two dowels from the 44 test specimens with the five load arrangements of Figures 5.12 to 5.16.

Specimen			Damage load (kN)	Specimen			Damage load (kN)
(1)			(2)	(3)			(4)
t-	br-	01	3.4	sq-	br-	01	33.0
		02	3.8			02	22.5
		03	3.4			03	44.2
	ps-	01	2.8		ps-	01	27.6
		02	1.7			02	27.9
		03	1.7			03	26.1
	sm-	01	2.8		sm-	01	45.5
		02	2.3			02	41.1
		03	2.6			03	41.6
	pc-	01	2.0		pc-	01	69.0
		02	1.7			02	68.0
		03	1.6			03	69.4
t-ps2-		01	17.1	sq-ps2-		01	25.3
		02	15.7			02	27.2
		03	15.2			03	27.8
		04	18.2			04	25.7
		05	17.7			05	32.1
		06	22.5			06	40.2
		07	16.3			07	22.5
		08	20.2			08	26.1
		09	16.4			09	27.4
		10	20.1			10	22.2

In terms of a bearing strength the damage loads for the load arrangements, excluding plane compression (pc), are given in Table 5.15. In the first column is the specimen labels (i.e. t-br-01) for each batch of the tube dowel and below every batch of specimens are the headers for the statistical results. Columns (2) gives the ‘pin-bearing’ bearing strength, the ‘pure shear’ bearing strength (ps), the ‘shear-moment’ bearing strength (sm) and the modified ‘pure shear’ bearing strength (ps2),

respectively. Columns (3) and (4) present the same content of column (1) and (4) for the square dowel shape.

Table 5.15. Damage load test results for four loading cases of tube (PD1570) and square (PD0821) sections using test configuration shown in Figures 5.12 to 5.16.

Specimen label (blue tube)		Bearing strength (MPa)	Specimen label (grey square)		Bearing strength (MPa)
(1)		(2)	(3)		(4)
t-br-	01	7.1	sq-br-	01	83.5
	02	7.8		02	56.4
	03	7.0		03	110
Mean		7.3	Mean		83.4
SD		0.5	SD		26.9
CV %		6.3	CV %		32.3
Characteristic value		6.4	Characteristic value		33
t-ps-	01	5.8	sq-ps-	01	68.2
	02	3.5		02	69.4
	03	3.5		03	64.9
Mean		4.3	Mean		67.4
SD		1.4	SD		2.3
CV %		31.6	CV %		3.4
Characteristic value		1.7	Characteristic value		63
t-sm-	01	5.9	sq-sm-	01	114
	02	6.6		02	103
	03	5.3		03	105
Mean		6	Mean		107
SD		0.6	SD		6.3
CV %		10.6	CV %		5.8
Characteristic value		4.8	Characteristic value		96
t-ps2-	01	36.6	sq-ps2-	01	64
	02	32.6		02	68.2
	03	31.7		03	69.4
	04	38		04	64.6
	05	36.8		05	67.6
	06	47.1		06	100
	07	33.9		07	55.6
	08	42.1		08	64.8
	09	34.2		09	68.1
	10	42		10	55.5
Mean		33.6	Mean		65.5
SD		2.6	SD		7.31
CV %		7.8	CV %		11.2
Characteristic value		29.2	Characteristic value		53

Notes: 1. Specimen sq-ps2-06 has been rejected from belonging to the population base on the Chauvenet's criterion ($|x_m - x|/s = 2.4 > 1.96$) for rejection of outlier in test results (Kennedy and Neville, 1986).

In Figure 5.17 plotted are characteristic bearing strength from the damage loads for the load arrangements that are given in Table 5.15 for the tube dowel and square dowel. The garphaical test results for 'pin-bearing' (br), the 'pure shear' (ps), the 'shear-moment' (sm) and the modified 'pure shear' (ps2) bearing strengths are provided as this makes it much easier to compare the results for the resistance shear force of the blue tube dowel and gray square dowel.

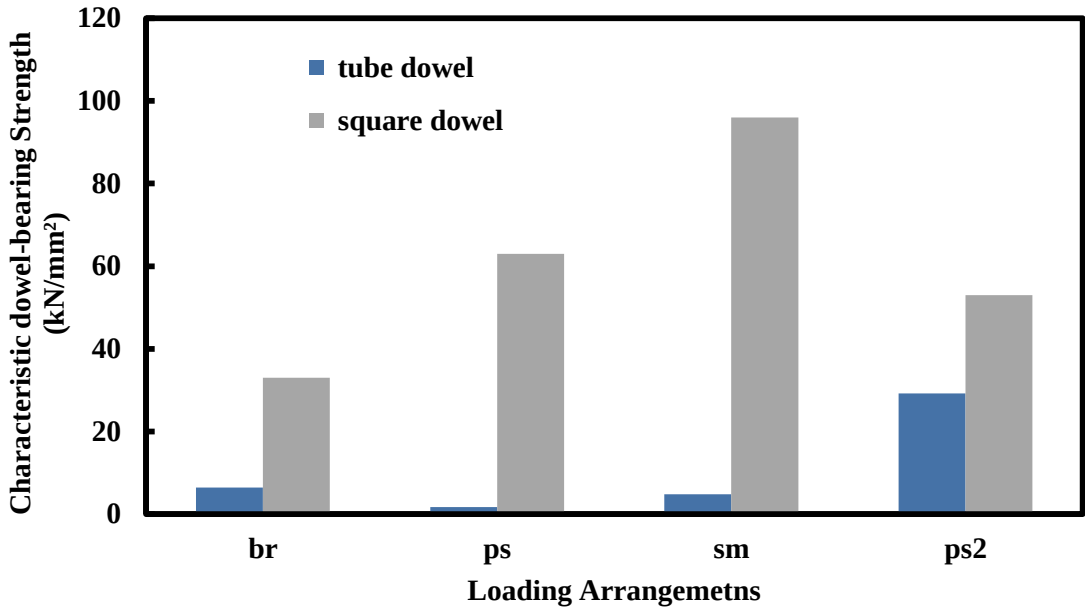

Figure 5.17. Damage load test results for 'pin-bearing' (br), the 'pure shear' (ps), the 'shear-moment' (sm) and the modified 'pure shear' (ps2) loading of tube (PD1570) and square (PD0821) shapes using test configuration shown in Figures 5.12 to 5.16.

A bearing strength is calculated by dividing the damage load (from Table 5.14) by the shape's bearing area. For the tube dowel this area is 480 mm^2, and is given by the nominal tube diameter (48.2 mm) times the sum of the two mean wall thicknesses of the 80×20×5 mm rectanguar shape (i.e. 9.9 mm). The same mean total wall thickness for the rectangular shape is used to calculate the bearing area (400 mm^2) for the square dowel. The other dimension is the section's nominal width of 50.7 mm minus

the distance for the small holes used to cut out the square notch or hole (refer to Figure 5.11). This gives a bearing length of 40.3 mm; in reality the initial bearing length is lower because of the concave shape to the side walls.

Assuming a lognormal distribution the mean, standard deviation (SD) and Coefficient of Variation (CV) is calculated for each batch of specimens. Using Annnex D to BS EN1990:2002 and assuming the CV is known (it should be close to, or < 10%) the characteristic value is determined. Note that because the number of specimens for br, ps and sm is three the characterisitc strength is Mean – 1.89SD. For modified ps which the batch size is ten the characterisitc strength is Mean – 1.72SD. The number of SDs taken from the mean has reduced by 0.17 with the batch size increased from three to10. Moreover, it is known that characteristic values using the Eurocode approach are on the safe side. Because of the uncertainty in the determination of charactersitic values, on two occasions the batch CV is >> 10%, these two strengths in Table 5.14 have only been given to two significant figures.

Comparing the bearing strengths presented in Tables 5.15 or the damage loads reported in Table 5.14 for the br, ps and sm load arrangements, it is obvious that the square shape gives a dowel connection with a resistance many times higher (> 10) than that of the tube shape; yet the cross-section area is only 3.3 times larger. From an evaluation of the test results presented in Tables 5.15 it is observed that the pure shear load case is the most severe, and that this situation is the one most likely to correspond to how the tube dowel is used the Startlink house (see Figure 5.1(b)). The lowest measured strength with the tube (both specimens t-ps-02 and t-ps-03) failed at 1.7 kN, and because of the very high CV, at 32%, the characteristic bearing strength

is very low, at 1.7 MPa (or 0.81 kN). Taking the lowest measured ps strength (sq-ps-01) the square dowel is found to possess a damage load of 27.6 kN. The CV for this load arrangement is only 3.4% and so the characterisitc bearing strength is 63 MPa (or 25 kN). Based on this evaluation the square shape has a characteristic resistance over 30 times higher than the tube (or 10 times per unit cross-sectional area). Contributions to this finding are shape, dimensions, E-glass reinforcement architecture, loading fixtures, and the too small batch size. The lowest measured strength for the square shape (PD0821) is 22.5 kN and is from pin-bearing loaded specimen sq-br-02.

From a batch size of three specimens (t-pt-01 to -03 for tube and sq-pt-01 to 03 for square), the test results from the plane compression (pc) load arrangement, shown in Figures 5.15, are as follows. The mean, SD, characteristic value and CV for the tube shape (PD1570) is 6.1 (MPa), 0.69 (MPa), 4.7 (MPa) and 11.4%. For this pc loading the bearing area is taken as the dowel length (98 mm) times an assumed bearing width (at damage failure load) of 3 mm. The equivalent test results for the square shape (PD0821) are 13.8 (MPa), 0.14 (MPa), 13.5 (MPa) and 1.0%. Bearing area is now 98 mm times the 51 mm full width of the square section. Note that the bearing stresses (strengths) from the plane compression load arrangement cannot be readily compared with the bearing strengths in Tables 5.15.

Comparing the ps characteristic value for the tube (from Figure 5.13 loading) in Table 5.15 with its equivalent modified ps value (from Figure 5.16 loading) shows a significant increased from 1.7 to 29.2 MPa. This increase is about 17 times and is accompanied by the CV decreasing from 32 to 8%. It is impoatant to mention that

with respect to the cross-sectional area of dowels the tube shape gives now about two times higher resistance than the square shape. This finding clearly demonstrates that the bearing resistance of a tube section is going to be highly dependent on how the shear force is applied to the curved surface of the thin-walled section.

The same comparision can be made for the square section using the results in Table 5.15. It is found that the charactersitic strength using the test configuration in Figure 5.16 is 53 MPa. This strength is 16% lower than when the loading (Figure 5.13) is applied through the 30 mm diameter steel pins. The CV has also increased from 3 to 11%. This finding indicates again that the bearing strength resistance of the square shape is a function of the load arrangement too.

For the all five load arrangements it is believed that material failure always occurred first within the dowel. It was found that further loading, in the post damage failure region, would cause the rectangular shape to fail when the dowel is the square. The mode of failure is transverse tensile rupture at the lower corners of the notch and it can be seen in Figure 5.18(c). When the load arrangement is that of pin-bearing (br) the dowels fail as seen in the images of Figures 5.18(a) to 5.18(c). From Figure 5.18(a) it can be seen that, when the rectangular shape is present, to fully restrain the deformation of the lower half of the tube (t-br-03), the tube cracks longitudinally, directly below the steel loading pad. Figures 5.18(b) and 5.18(c) are for two photographs showing a failed sqaure shape (sq-br-01). The two images show the specimen immediately there is damage (Figure 5.18(b)) and post-failure (Figure 5.18(c)), after further stroke had been applied to develop the failure pattern. On removing the dowel, to inspect its bottom surface, it was found that the square

section had indents, due to very localised material crushing, near to the lower two corners. When further stroke displacment was applied, to progress material failure, there appeared a longitudinal crack located at the wall's lowest thickness in the top face. On one side of the square dowel, and in its lower flange there is a longitudinal crack due to a shear mode of failure. This is the result of the higher bearing force concentration in this region. Also seen in Figure 5.18(c) is longitudinal cracking in the rectangular section at the corners of the square notch; these cracks are caused by bulging of the side walls pushing against the upstands of the notched rectangular shape, to create a splitting action where tensile cracks are seen to initiate from.

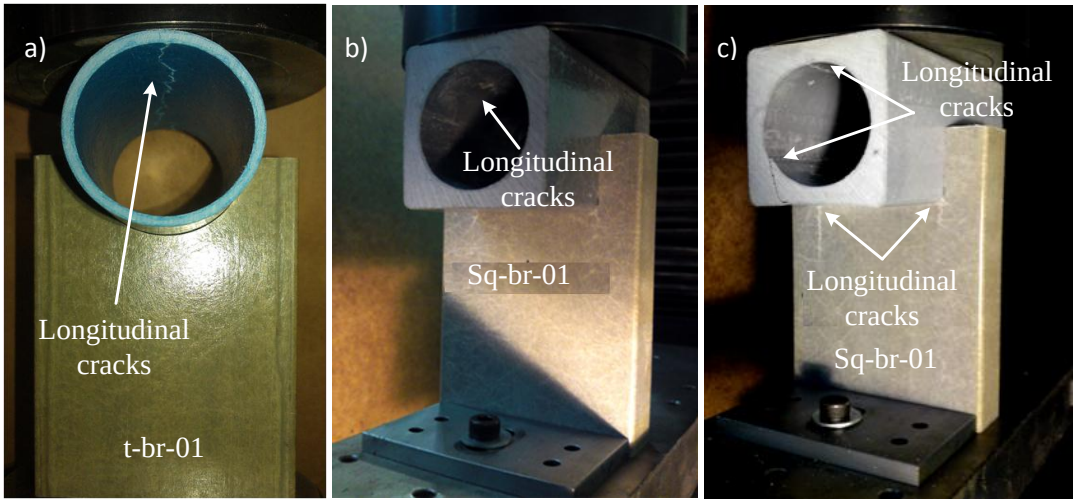

Figure 5.18. Failures with pin-bearing loading arrangement: (a) failure mode for tube shape; (b) failure mode for square shape at failure and; (c) at post-failure.

Figures 5.13 shows the test configuration for 'pure' shear and loading is via 30 mm steel pins. Figures 5.19(a) and 5.19(b) show the resulting failure modes. It can be seen that the 'rigid' pins has caused the stress field in the curved tube (Figure 5.19(a)) and square (Figure 5.19(b)) dowels to be very localised, complex and involving high stress concentrations.

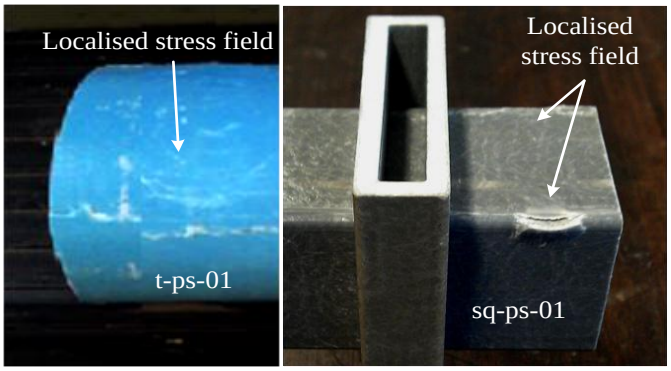

Figure 5.19. Failures with pure shear loading arrangement: (a) failure mode for tube shape; (b) failure mode for square shape.

When the load arrangement is that for shear-moment shown in Figures 5.14 it was observed that failure of the dowels is, again, linked to the very localised stress field from loading through steel pins. Figures 5.20 and 5.21 show the progressive failure in the tube and square dowels. Initial material failure for the damage load observed as cracking through the wall thickness at the top of dowel. Further deformation in the post-failure region with this sm load case will produce longitudinal cracks at mid-depth of the shape, as seen in the four images in Figures 5.20(d), 5.21(c) and 5.21(d). The photographs for a pc tube specimen in Figure 5.5(a) and for a pc square specimen in Figure 5.5(b) show that both dowels failed at mid-depth, on the tension face of the walls, as a result of the compression forcing the walls to displace outwards; this deformation is restrained in a dowel connection.

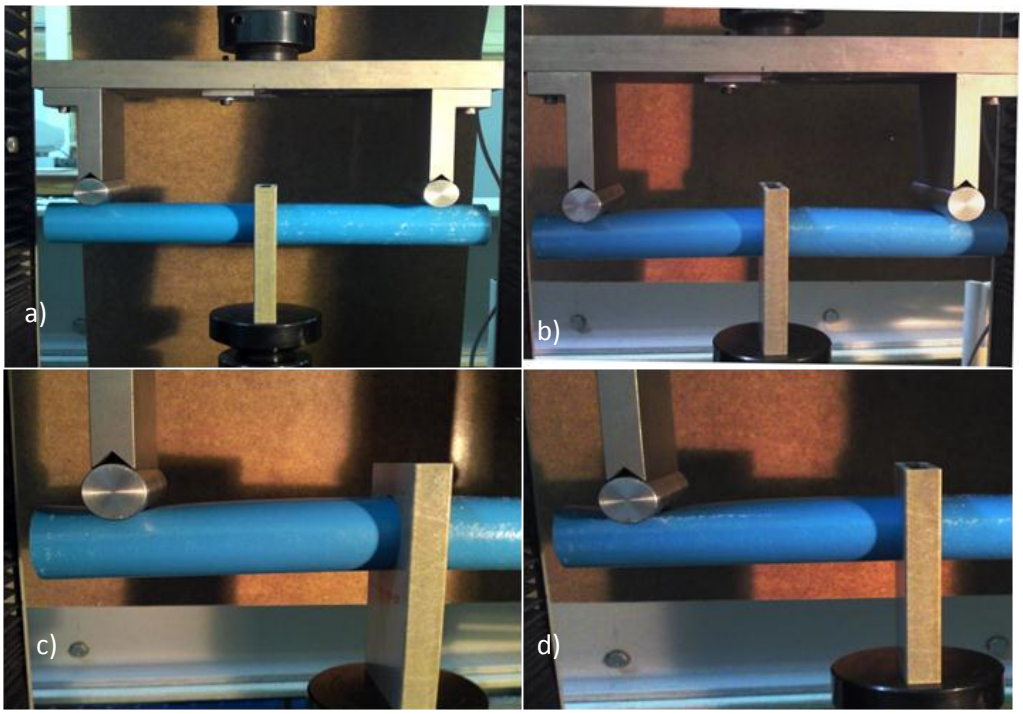

Figure 5.20. Progressive failure of tube dowel for the shear-moment load arrangement: (a) at first stage of loading (b) failure mode for tube shape; (c) close up for tube at failure and; (d) at post-failure with longitudinal cracks at mid-depth.

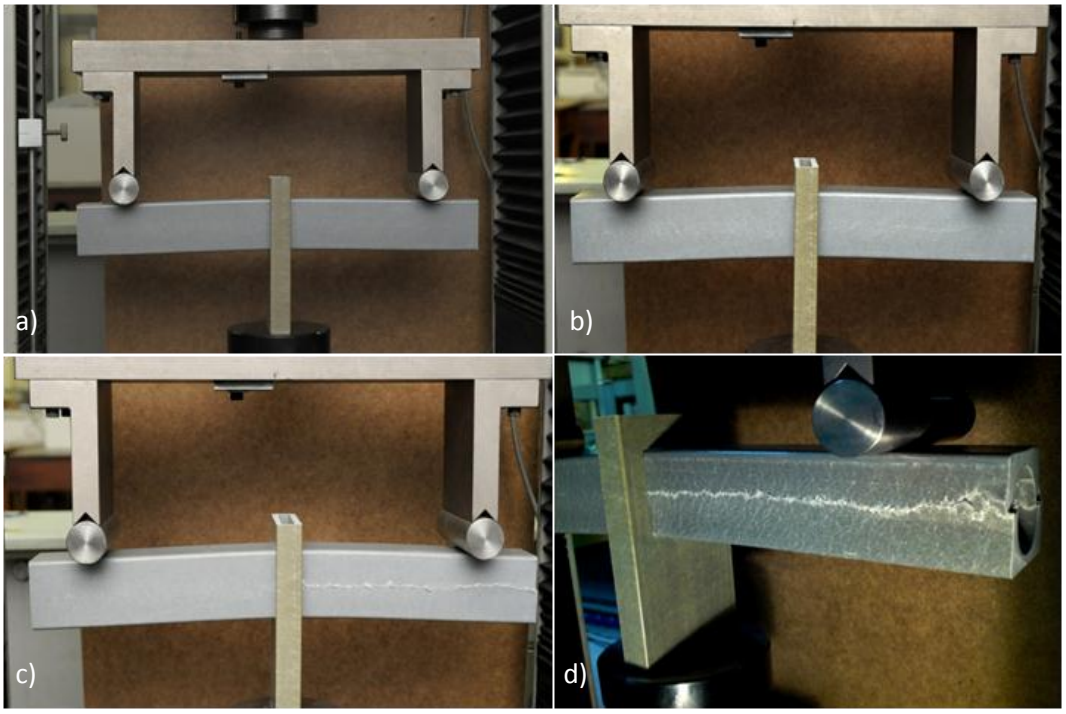

Figure 5.21. Progressive failure of square dowel for the shear-moment load arrangement : (a) at loading stage (b) failure mode for square shape; (c) at post failure and; (d) close up view at post-failure with longitudinal cracks at mid-depth.

To illustrate how the two dowels failed in the fifth laoding arrangemen of Figures 5.6 and 5.16 Figures 5.22 and 5.23 comprise of three parts. For the tube the modes of failure are shown in Figures 5.21(a) and 5.22(b), and similarly for the square there are shown in Figures 5.23(a) and 5.23(b). By overcoming the weakness of having too high localised stresses when loading through the steel pins, dowel failure is now by localised compression deformation over a much higher bearing area. Further deformation in the post-damage region allows the rectangular section to fail by the tensile splitting mode seen in Figure 5.22(c) and 5.23(c). Figures 5.22(a) to 5.22(c) show how the tube section fails when load is more uniformly distributed using the two loading components with a semi-circular notch. Figure 5.22(a) shows specimen t-ps2-01, with the two side supports still in position, and the indentation marks clearly visible from the impression of the top rectangular section (see Figure 5.6(a)). In Figure 5.22(b) there is a close-up of the top surface of the two tubes t-ps2-01 and t-ps2-02. The extent of the indentations from the two walls (4.6 and 5.3 mm thick) of the rectangular section show that the material fracture could be due to a combination of punching shear and material crushing.

The same set of three photographs for the square section are given in Figure 5.23. In Figure 5.23(a) and 5.23(b) it can be seen that the square dowel is crushed at the top corners where the compressive loading is transferred into it from the centrally located semi-notch rectangular section. After additional post-failure deformation the two images in Figure 5.23(c) show that there are now longitudinal tension cracks in the central and support rectangular sections (see Figure 5.6(a)). This failure mode was previously observed for the br load arrangement tests (see Figure 5.19(c)).

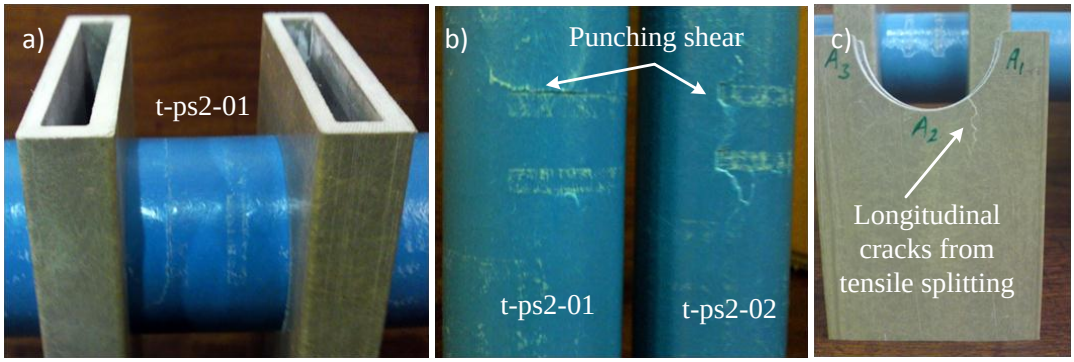

Figure 5.22. Observed failures with tube dowel: (a) indentations in tube from central rectangular shape; (b) punching shear failure of tube; (c) tensile splitting of central rectangular shape.

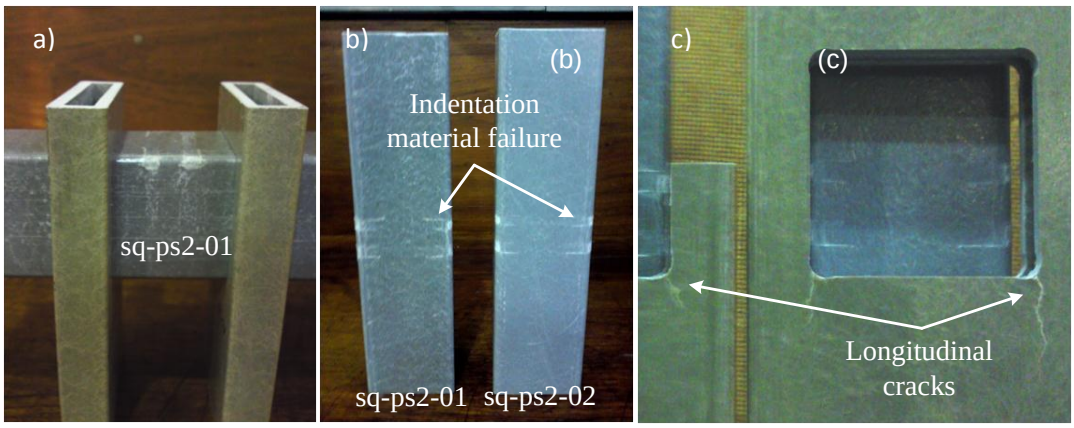

Figure 5.23. Observed failures in square dowel: (a) indentations in square from central rectangular shape; (b) indentation material failure of square shape; (c) tensile splitting of central rectangular shape at corners of square hole.

To determine a design value from either the lowest batch damage load or a characteristic ‘bearing’ strength a pragmatic knock-down approach is required. Assuming an allowable load of one-half of a characterictic value the maximum shear force which can be allowed to transmited by the tube shape in dowel connections (PD1570) using ps laod configuration is 0.4 kN. Applying the same pragmatic approach using the modified ps load configuration the allowable shear force can be increased from 0.4 kN to 6.9 kN. To find out the allowable design shear force for the square shape (PD0821) as it can be seen in Figure 5.1(c) the sm load arrangement is

the most likely case found in the the Startlink house. The characteristic from this load arrangement is 38 kN and this gives a design value of 19 kN. It is importation to mention that the lowest measured strength is 22.2 kN and is from the modified ps test with specimen sq-ps2-10. The characterisitc bearing strength now for this batch of tests is 53 MPa (or 19 kN). This suggest that a safe maximum working shear force of 9.5 kN will be accaptable when using the square section to transfer shear force in the Startlink house.

5.5 Concluding Remarks

A series of fact finding tests have been carried out with the aim of obtaining strength data when using two closed pultruded shapes dowel connections. One section was of tube shape and the other of square cross-section. A total of five different loading arrangements were used, with two distinct configurations for the most severe load case (that caused failure at the lowest compressive load) that is referred to as pure shear. The justification for having a second loading configuration, that more closely represents what might be found in practice, is because the strength measurements from the first pure shear configuration were found to be adversely affected by using stiff steel pins for load application.

The characteristic bearing strength of 29.2 MPa obtained for ‘pure’ shear from the second load arrangement, having the compression (shear force) load distributed (uniformly) over sufficient bearing area, was a considerable increase for the 1.7 MPa determined using the first load arrangement. This increase is about 17 times and is

accompanied by the CV decreasing from 32 to 8%. The increase in resistance in terms of mean strength was found to be lower, at about eight times.

If the same comparision is made for the square shape using the equivalent results it is found that the charactersitis strength, from the second load configuration, at 53 MPa is 16% lower than given from the first load configuration, when the loading is applied through the 30 mm diameter steel pins. The CV has also increased from 3 to 11%. The reason for this finding of a lower strength with the more favarable loading condition is unknown.

The test results presented in this chapter clearly demonstrate that the shear resistance of PFRP dowelling is going to be highly dependent on how the shear force is applied to the surface of the dowel shape. In other words the shear resistance will be a function of the load case and this fact needs to be account for when the strength data is being used to verify structural engineering designs for dowel connection with the SLBS.

Chapter 6

Startlink Frame Joints

6.1 Introduction

The Startlink Lightweight Building System (SLBS) is an engineered solution from the work of a consortium with the partnership of six companies, led by EXEL Composites UK, together with the University of Warwick (UoW). The goal of the SLBS project is to produce a family of pultruded shapes that can be assembled off-site to construct the superstructure for housing which, with integrated energy management, meets the UK Government's requirements for Code Level 6 (2007).

To be able to engineer the superstructure of the Startlink house unit and its tailored shapes, knowledge of the mechanical properties of the pultruded shapes, the way that its structural members connect together and the stiffness (vertical, lateral and torsional) of the whole system is needed. To support a number of structural engineering features, the author has been conducting, and evaluating, several series of physical tests, from coupon to sub-assembly size on materials and joint components. The objective of this chapter is to report results from experimental tests on four full-sized Sub-Assembly Joints (SAJs) having beam-to-column dowel connections. In Figure 6.1 the Startlink portal frame (members not to scale) and the SAJ specimen for external frame joint at a typical first floor level are shown schematically. Four individual specimens were either with or without hole clearance

and one specimen with hole clearance had adhesive bonding (bond connection) between common surfaces of the members. Using the test results an evaluation is made on the performance of joints in the SLBS portal frames.

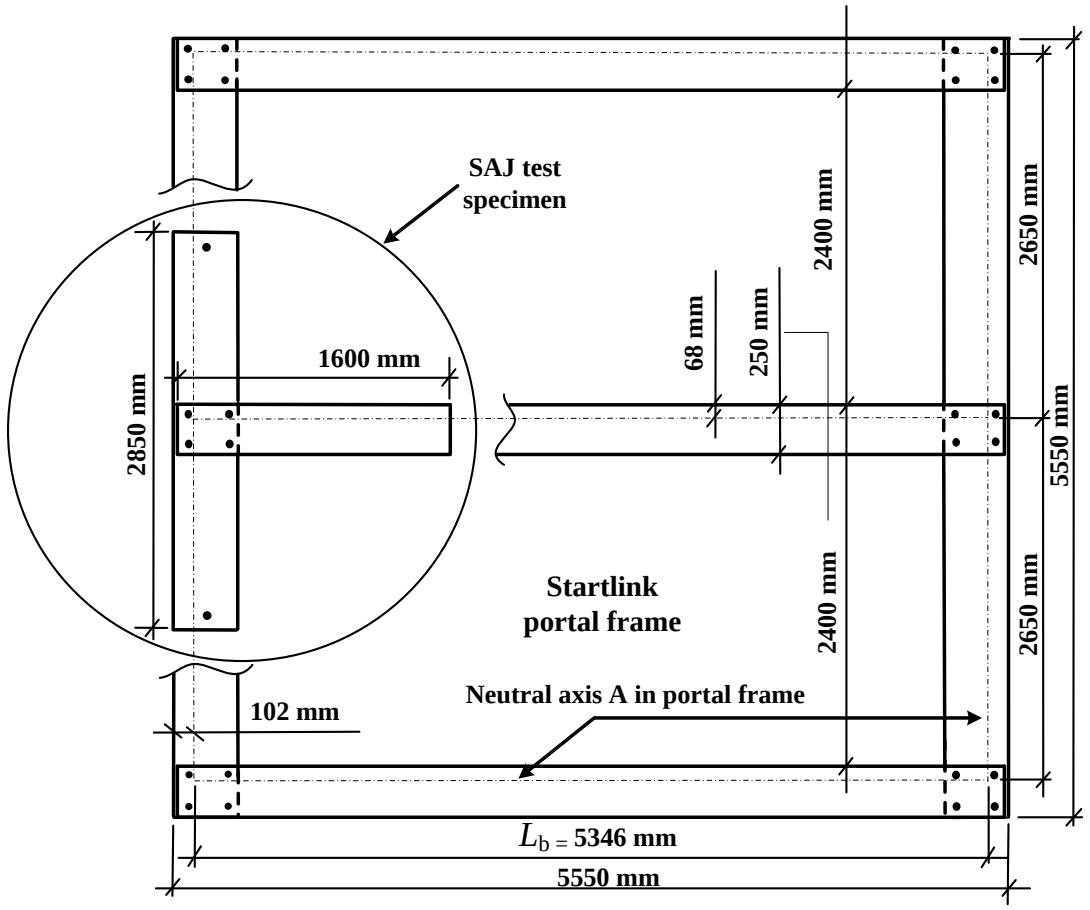

Figure 6.1. Startlink portal frame with specimen of external frame joint (SAJ) at the first floor level.

Figure 6.2 shows details of SAJ specimen components with dimension. It can be seen that SAJ takes the form of a stud column and a ‘cantilever’ floor beam. All members are of PFRP.

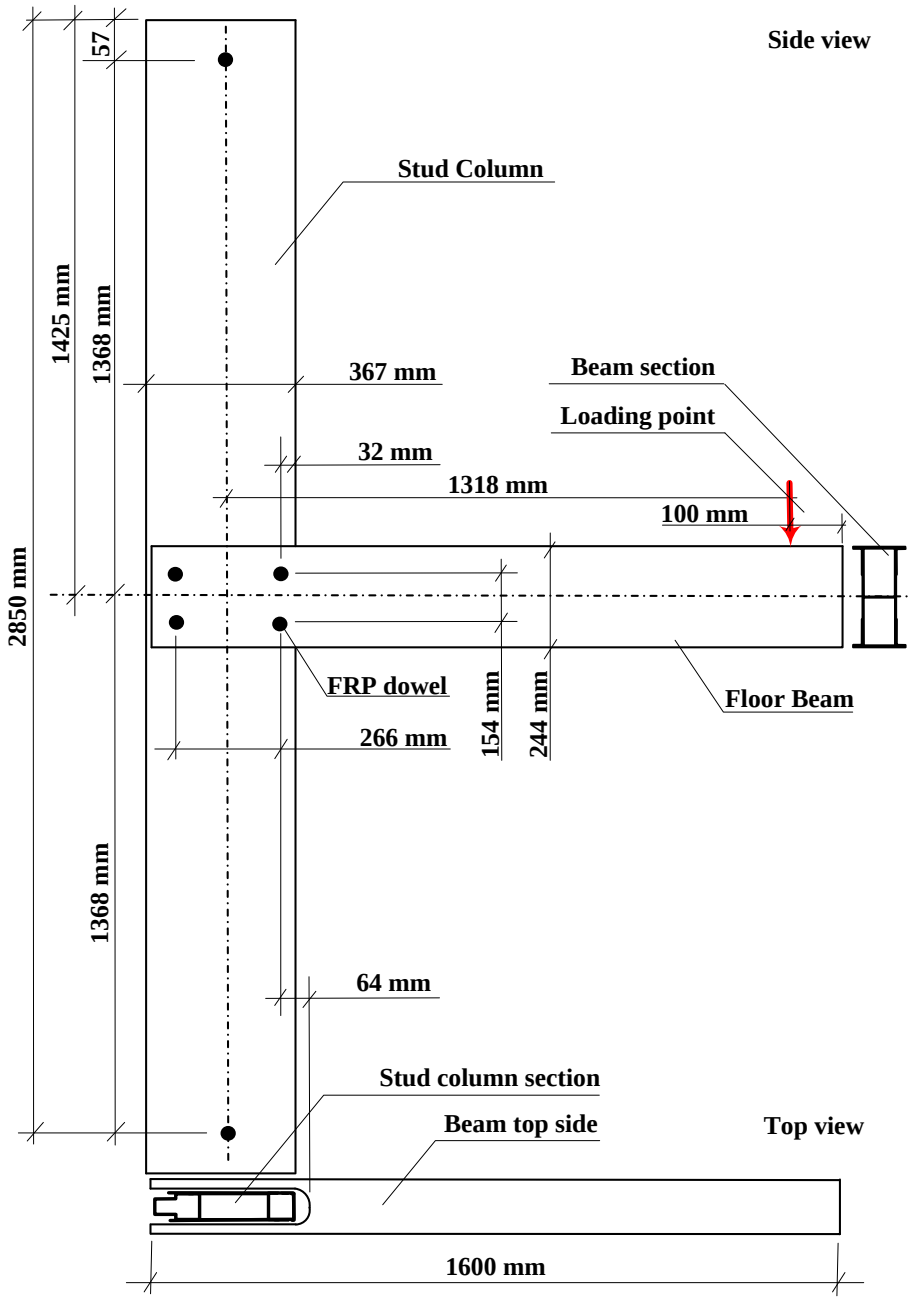

Figure 6.2. SAJ specimen with dimensions of components.

It is recognised that the safe and reliable design of connections and joints is one of the most critical aspects for a primary load bearing structure. The initial concept design for the structural load bearing members of the SLBS was based around FRP pultrusions with joints that click together, known as ‘snap-fit’ connections (Singleton, 2004). However, due to the reasons which were discussed in Section

2.6.2 the consortium concluded that the Startlink needed connections and joints that would impart greater resistance and stiffness against several different load cases, particularly for the cases with lateral loading. The structural system of Startlink house was progressed by having portal frames for the primary load bearing structure using dowel and adhesive bonding connections. Figure 6.3 shows how the portal frame has been employed together with wall and floor panels, at every 0.6 m, with the aim of having adequate vertical and lateral stiffness. Based on the design analysis of the Startlink house (Kendall, 2010), portal frames are used to provide the lateral resistance against wind load in the transverse direction. The building's system has been designed to factory assemble wall panel and floor panel sub-assemblies. This would need the wall and floor panels to act as stiff shear panels, with sufficient shear connection between them, to provide lateral and twisting resistance along the length of the SLBS house.

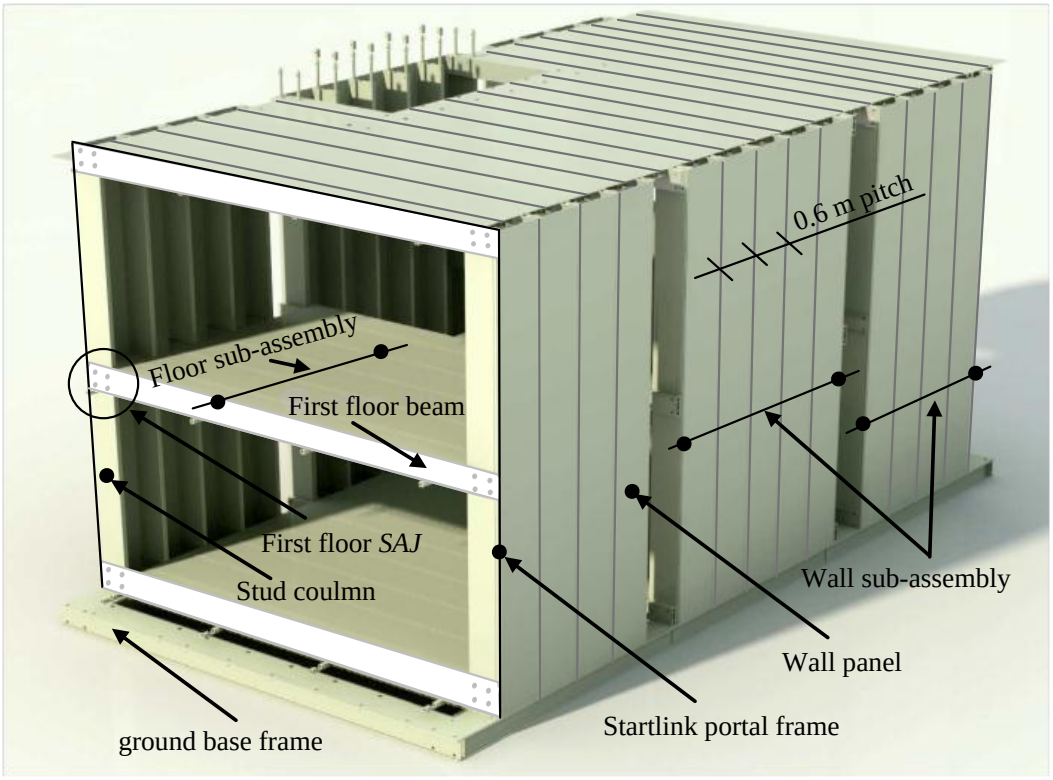

Figure 6.3. Startlink superstructure with members and subassemblies.

The moments, shear forces and axial forces in portal frame have been determined under the characteristic design load combination due to variable (live) loads, permanent (dead), and with wind load. Live load values which have been used during construction for concentrated (applied over 50×50 mm area) and distributed are 1400 N and 1500 N/m^2, respectively. The equivalent values under service load are 2000 N and 1500 N/m^2. Concentrated live load on walls is 500 N SLS. Dead loads in order of ground, first and roof floor are 830 N/m^2, 890 N/m^2 and 1000 N/m^2. Dead loads for each beam (at 0.6 m pitch) are 500 N/m, 530 N/m and 600 N/m. The wind loading on the structure has been assessed in accordance with BS6399-2:1997. This has been based on a dynamic pressure of 1000 N/m^2, which is expected to cover the majority of UK house building sites. For the Startlink building system the load factors (γ_f) and material factors (γ_m) are in accordance with Eurocomp (1996). The load factor 1.5 is to be applied to the SLS for the ULS and material factor for short and long term loads are 1.5 and 3.2, respectively. The deflection limits under SLS loading for floor span of 5.35 m (vertical) and floor height (horizontal) are assumed to be *L*/460 and *H*/300. These values are from design with timber construction.

The portal frame has been analysed using the Engissol software (two-dimensional), with frame elements modelled along the members' neutral axes as shown in Figure 6.4. The neutral axes can be seen in Figure 6.1. In the figure, represented loads are for a single portal frame (0.6 m pitch) under SLS loading.

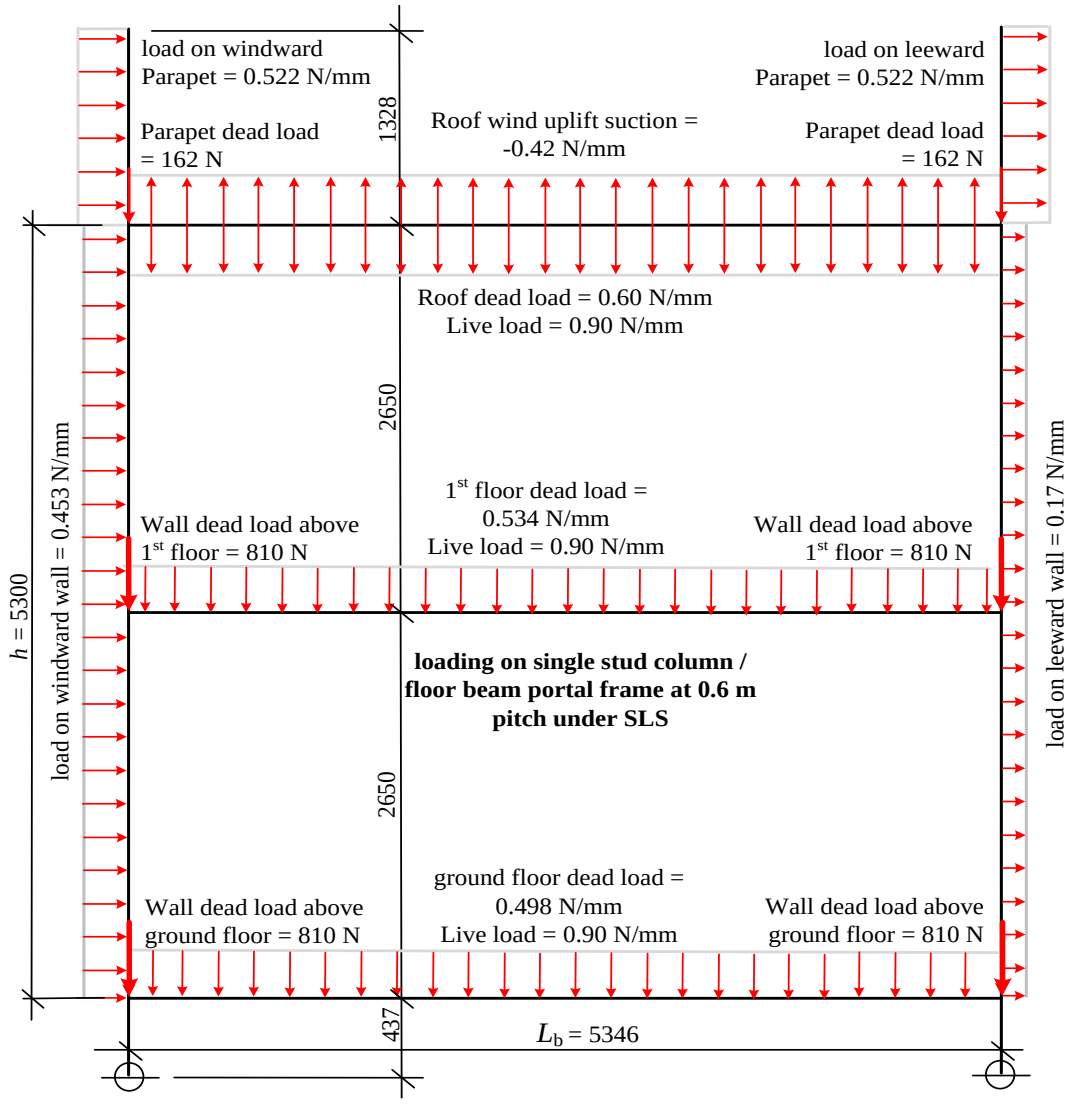

Figure 6.4. SLBS portal frame under SLS loading cases.

The frame has been analysed for the design loads mentioned and four combinations. The base of the portal frame has been modelled with either pinned or fully fixed restraints to show the possible range of deformations and reaction loads. Tabulated in Table 6.1 are the deflection results obtained from four SLS load cases with pinned and fixed based restraint. Column (1) gives the case numbering with a number followed by an additional letter (a or b) for pinned and fixed supports. Column (2) defines the loading cases. Vertical and horizontal deflections at ground, first and roof

floor levels are given in columns (3) to (8). Based on the design of the Startlink portal frame by Kendall (2010), the critical loading case for the ground and first floors joints has been identified as case 4a. This case is for dead, wind and live loads with pinned base supports. From Table 6.1 it can also be seen that the maximum deflections all belong to load case 4a.

Table 6.1. Deflection results for four SLS load combination cases and two support displacements conditions.

Deflection under SLS loading							
(1)	**(2)**	**(3)**	**(4)**	**(5)**	**(6)**	**(7)**	**(8)**
	Loading cases	Ground floor		1st floor		Roof floor	
		V*	H*	V	H	V	H
1a	Dead Loads, pinned	0.9	0.0	1.0	0.0	1.4	0.0
1b	Dead Loads, fixed	0.9	0.0	1.0	0.0	1.4	0.0
2a	Dead + Live Loads, pinned	2.4	0.0	2.6	0.0	3.5	0.0
2b	Dead + Live Loads, fixed	2.4	0.0	2.6	0.0	3.5	0.0
3a	Dead + Wind Loads, pinned	0.9	1.0	8.2	0.0	1.4	0.0
3b	Dead + Wind Loads, fixed	0.9	0.1	1.0	4.2	0.4	8.7
4a	Dead + Wind + Live Loads, pinned	2.4	1.0	2.6	8.2	2.4	13.8
4b	Dead + Wind + Live Loads, fixed	2.4	0.1	2.6	4.2	8.7	15.8

V* is the vertical deflection for mid-span in mm
H* is the horizontal deflection for mid-span in mm

Figure 6.5 shows the graphical bending moment profiles for case 4a. It can be seen that the maximum joint moment at the ground and first floor levels are nearly the same. As seen in Figure 6.5 the measurement joint moments in order are of 6.9 kNm and 6.8 kNm. Due to the ground base frame being below the ground floor joint (shown in Figure 6.3), the first floor joint is the most critical joint and hence it has been subjected to the experimental investigation. The design of the Startlink portal joint of the floor beam to stud column (Kendall, 2010) has been driven by the bending moment (6.8 kNm) to be transferred from the floor beam into the stud

column and vertical shear force (5.1 kN) from roof and first floor level into stud column. To conduct the SAJs tests the author had to apply a joint moment of 6.8 kNm, for SLS loading. The load factor 1.5 is applied to obtain the ULS loading of 10.1 kNm (from 6.8 × 1.5).

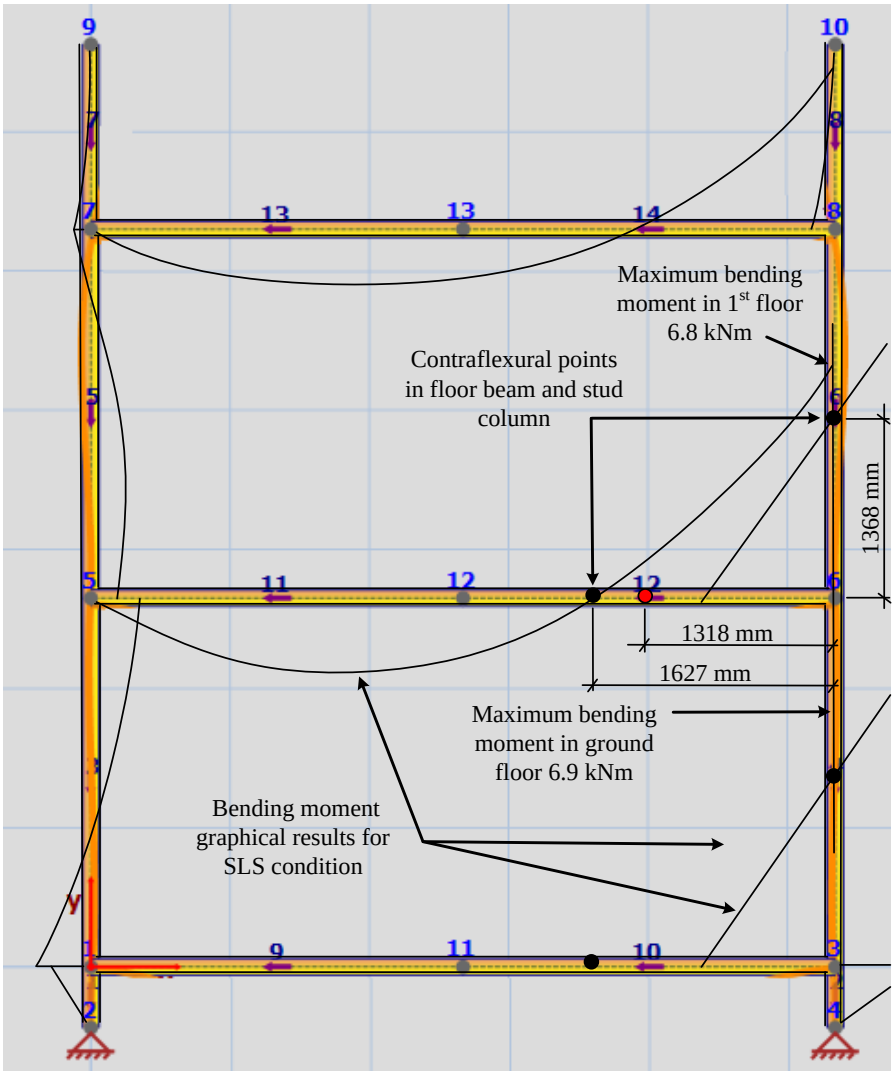

Figure 6.5. Bending moment distribution for load case 4a.

It is well known that structural portal frame systems have to have semi-rigid or rigid joints to develop overall frame stiffness. To make use of a semi-rigid joint there could be no need for a vertical structural bracing system. Based on the design of the Startlink house (Kendall, 2010), the structural system does not possess vertical

bracing and, therefore, overall frame stiffness relies on the joint. In frame analysis it is assumed that the frame seen in Figures 6.1 and 6.3 has beam-to-column joints that are fully rigid. Clearly this not achievable in practice and deflections of the frame's members, under SLS loading, will be higher than reported in Table 6.1. The aim of the research is to determine the moment-rotation (*M*-Ø) response of practical joint details to establish what should be executed when the demonstrator house at Bourne, Lincolnshire, was constructed in June to August 2012.

Startlink portal frame joints are assembled by inserting four FRP dowels into holes through the members. Figure 6.6 shows the situation for holes and dowels, at ground floor level, which has the same holes geometry as SAJ (see Figure 6.2) at first floor level. The photo shows the situation before members are positioned so that the dowels are inserted. Holes perimeters of connections and dowels are coated with a structural adhesive before engaging the members to provide moment resistance in the presence of any clearance hole.

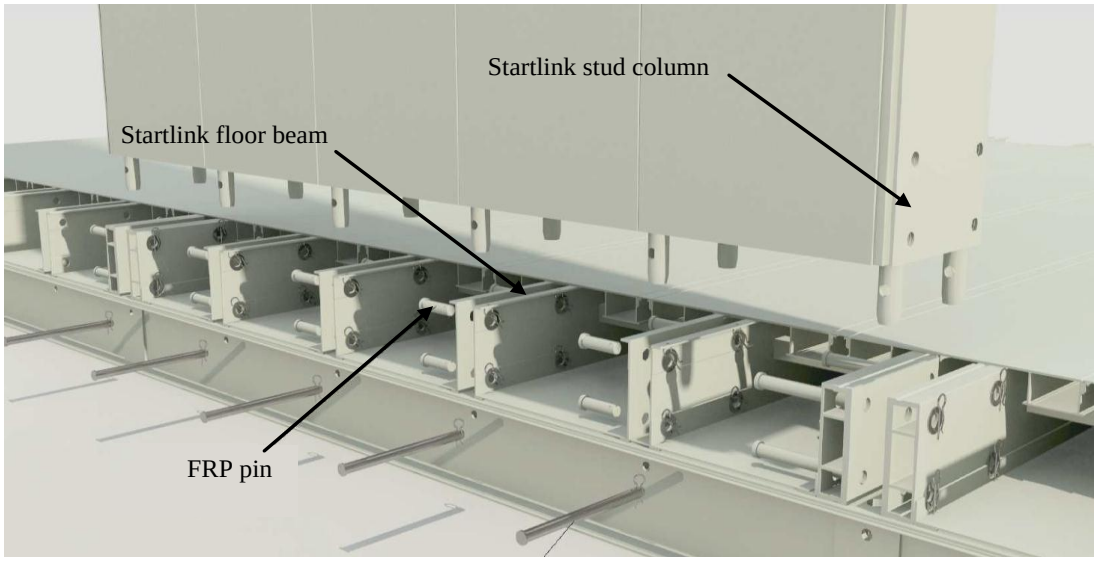

Figure 6.6. Joint holes and FRP dowels at ground floor level.

Because semi-rigid to rigid joints transmit moment, their presence in a frame reduces the deflections due to variable and permanent design loads. In pultruded structures the increased frame stiffness from relatively stiff joints is especially important since beam design is often controlled by serviceability (i.e. deflections). In other words, if rotational restraint can be provided by the beam-to-column joint the design of pultruded frame structures will be more efficient (Bank, 2006).

Although, structural frames are usually designed on the basis that beam-to-column connections are either pinned or fully rigid, the actual stiffness (even when assumed to be pinned) is between these two extremes, resulting in ‘‘semi-rigid’’ behaviour (Mottram and Zheng, 1996). This behaviour of joints can be characterised through the moment-rotation (M-$\emptyset$) curves having properties of rotational stiffness, M and $\emptyset$ values at SLS loading, at the onset of damage, and for ultimate moment and rotation capacity.

According to BS EN 1993-1-8:2005 for the classification of joints of steel structures, the joints details should fulfil the assumptions made in the relevant design method (i.e. pinned or rigid), without adversely affecting any other part of the structure. It is assumed that classification of joints for steel structures can be used to classify joints in equivalent frame structures of PFRP members as the construction material should not make a difference in the classification process. Later the rotational stiffness of SAJs will be classified by the clauses in BS EN 1993-1-8:2005. Eurocode 3 permits joint classification by stiffness and by strength. For the design of beam-to-column joints in pultruded structures the dominant criterion is stiffness and, therefore, the four SAJs are classified by their stiffness. Classification of stiffness for unbraced

frames uses the initial rotational stiffness $S_{j,int}$ and the classification boundaries for the three zones shown in Figure 6.7. The boundaries are given by:

- if $S_{j,int} \geq K_b EI_b / L_b$ the joint is rigid for an unbraced frame if the value of $K_b \geq 25$ (zone 1), provided that in every storey $K_b / K_c \geq 0.1$.
- for $S_{j,int} \leq 0.5\ EI_b / L_b$ the joint is classified as nominally pinned (zone 3) and,
- all joints with $S_{j,int}$ between the former and the latter are classified as semi-rigid (zone 2).

Here E is E_L, the longitudinal flexural modulus of elasticity of the PFRP shape and I_b is the second moment of area of the beam member. L_b is the span of the portal frame shown in Figure 6.1 (from neutral axis to neutral axis of columns). K_b is the mean value of I_b / L_b for all the beams at the top of that storey and K_c is the equivalent value for the columns in that storey. Based on the design of the Startlink frame (Kendall, 2010), the values of I_b and E_L are 58.3×10^6 mm^4 and 24 kN/mm^2, respectively.

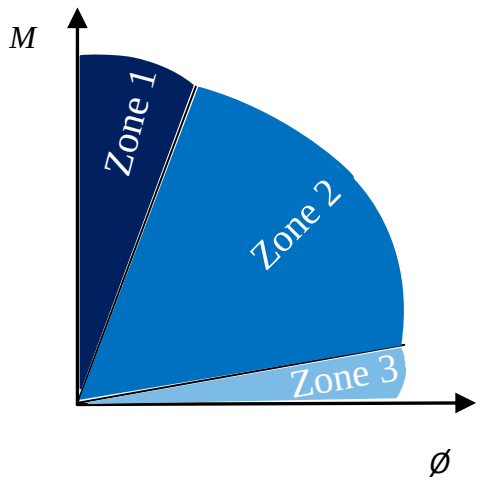

Figure 6.7. Classification of the joint stiffness by *M*-Ø zones.

In what follows the author provides information on materials and details of the joints, the methodology used to assemble the SAJs, the main issues related to their practical fabrication, test rig and test procedure. Moment-rotation (M-$\emptyset$) curves for the SAJs under static load at SLS loading, ULS loading and for the onset of damage are obtained. The values of ultimate moment and rotational stiffness are evaluated and modes of failure are discussed. Creative ideas for assembling the Startlink portal frame on site with achievable tight fit connections for the stiffest joints possible are given at the end of the chapter.

Prominent results presented in this chapter can be used to develop an overall understanding of the unbraced Startlink frame in Figure 6.1 with regard to its stiffness and structural performance of the unique joints with dowelling as the method of connection.

6.2 Materials and Specimens

The floor beam and stud-column consist of two pultruded multi-cell box section shapes. Figures 6.8(a) and 6.8(b) show the cross-sections of the floor beam and the stud column with nominal dimensions (in mm), respectively. The two members have been specifically designed to be structural elements in the Startlink light weight building system. Both members were pultruded by EXEL Composites UK in 2011 and have E-glass reinforcement with a polyester matrix. Material specifications for beam and stud column are given in Tables 6.2 and 6.3, respectively. In column (1) the composite layers of E-glass reinforcing material are given in order from the surface veil to the inner layer that constructed multi-layered shape. In column (2) the reinforcement types are presented. Given in columns (3) and (4) are the weight and

the effective width of the fibre reinforcements. Column (5) refers to the number of the reinforcements per layer.

Table 6.2. Material specification for the Startlink beam (244mm × 120mm).

layer	Material reinforcement	Weight (g/km)	Effective width (mm)	Number
(1)	(2)	(3)	(4)	(5)
A	NLC10/350 Veil	37	275	2
B	CFM	600	275	2
C	CFM	600	90	4
D	CFM	600	110	2
E	CFM	600	85	4
F	CFM	600	120	2
G	CFM	600	130	2
H	Rovings	4800	-	24
I	Rovings	9600	-	266
J	Peelply (938/120)	-	120	1
K	NLC10/350 Veil	37	120	1

Table 6.3. Material specification for the Startlink stud column (367 mm × 60mm).

layer	Material reinforcement	Weight (g/km)	Effective width (mm)	Number
(1)	(2)	(3)	(4)	(5)
A	NLC10/350	37	375	2
B	CFM	450	375	2
C	CFM	600	115	4
D	CFM	600	95	1
E	CFM	600	140	1
F	CFM	450	190	2
G	CFM	450	100	2
H	Rovings	4800	-	636
I	Mock Spun	2400	-	4
J	NLC10/350	37	80	1

Figure 6.2 shows the SAJ specimen with dimension of components. The beam has a length of 1600 mm to satisfy the lever arm 1318 mm from joint centre to where the vertical load is applied. This distance corresponds to the point of contraflexure taken from graphical plot of moment for the worse SLS load case, shown in Figure 6.5.

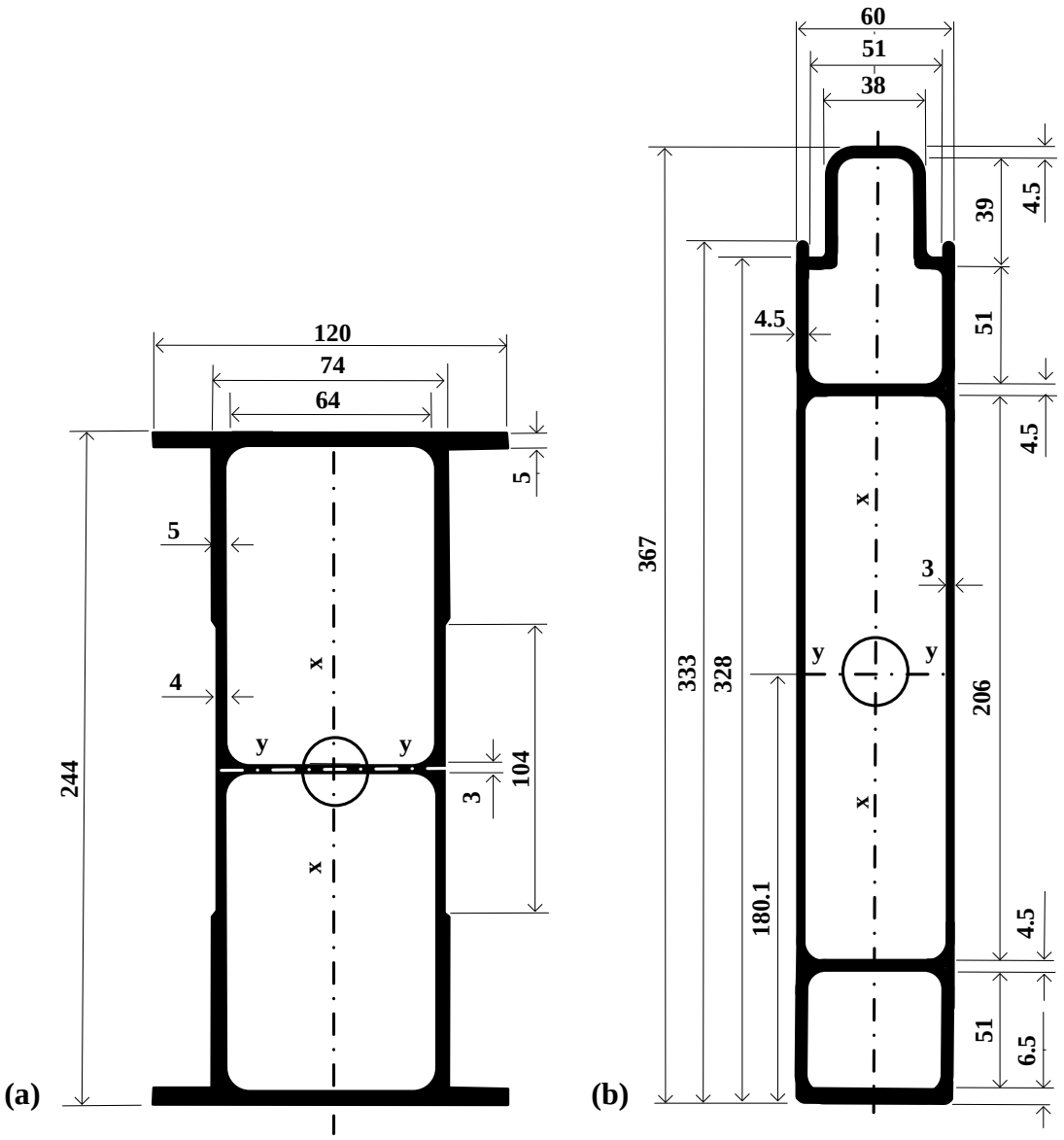

Figure 6.8. a) Startlink floor beam shape; b) Startlink stud-column shape

It is noteworthy to mention that to determine the lever arm in the SAJ specimen the original distance from the contraflexure point to centre of joint has been specified to match the SLS shear force and joint moment. This required a reduction in the distance to include the effect of shear force. As a result the distance from joint centre to point load has been changed from 1627 mm to 1318 mm. These two points are shown in Figure 6.5. For testing, the beam is 100 mm longer so that there is sufficient section length to place the steel loading plate on the top flange. This test

fixture is needed to distribute the point load in to the FRP member. As seen in Figure 6.2 the height of the stud-column is set at 2850 mm. The centre of the joint divides the column into two equal lengths of 1425 mm. Each length of stud column represents the distance from the joint centre to the point to contraflexure as calculation the rigid joint frame analysis. There is a small difference between the exact contraflexural points and the pinned ends in the test. This is because the locations end points were dictated by the 4 inch centre-to-centre for the holes in the meccano sections. Distances from centre of joint to pinned ends are therefore 1368 mm. The stud column extends a further 57 mm at both ends.

The eight sections for the four SAJ specimens were labelled with a scheme for hole dimension measurements. The scheme is illustrated in Figures 6.9(a) and 6.9(b). Figure 6.9(a) shows the South side of the beam member, from the top, with the positioning scheme of the connection holes. At the bottom of the figure, the top side of the beam can be seen to introduce of North wall and South wall. Figure 6.9(b), similarly, shows the same scheme for the stud column member. For example, **B1-TLS** is for the **B**eam member of specimen SAJ-**1** and the hole at the **T**op **L**eft position in **S**outh wall. **SC3-BRN** is for the **S**tud **C**olumn member in SAJ-**3** and the hole at the **B**ottom **R**ight in **N**orth wall. Each joint specimen has been assembled using a beam and a column with the same number. For example, member B2 and SC2 form the SAJ-2 specimen. The nominal distances between pairs of holes shown in Figures 6.9(a) and 6.9(b) are the mean values taken from the eight measurements given in Tables 6.4 and 6.5.

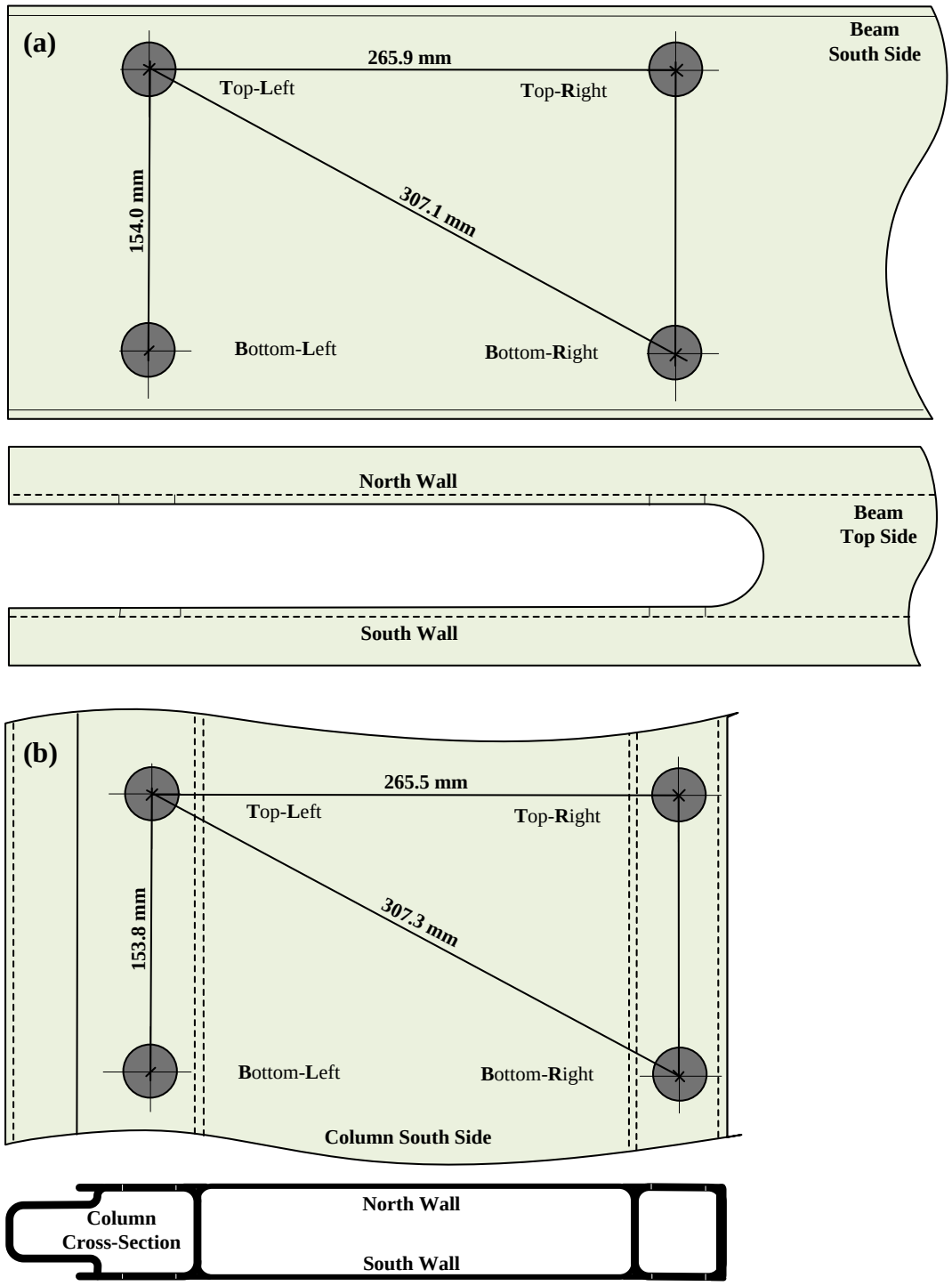

Figure 6.9. Engineering drawing of Startlink members: (a) beam section with holes positions and the nominal distances between pairs of holes; (b) column section with holes positions and the nominal distances between pairs of holes.

Presented in Tables 6.4 and 6.5 are the measured hole distances for the four beams of B1 to B4 and the stud-columns of SC1 to SC4. In both tables column (1) gives the

beam and stud members for the SAJs specimens. Columns (2) and (3) report the horizontal centre-to-centre hole distances. The equivalent measurements for vertical and diagonal distances are given in columns (4) to (7). In all columns from (2) to (7) the holes distance in the South side is given first, followed by the same distance on the North side. Every pair of distances is separated from others by bold vertical lines. Holes centre to centre distances were determined by adding measured distance of holes perimeters to the holes' radiuses obtained from the holes diameters given in Table 6.8.

Table 6.4. Horizontal, vertical and diagonal hole distances in beam member.

Member	Horizontal distance		Vertical distance		Diagonal distance	
	(2)	(3)	(4)	(5)	(6)	(7)
	TLS-TRS	BLS-BRS	TLS-BLS	TRS-BRS	TLS-BRS	TRS-BLS
(1)	TLN-TRN	BLN-BRN	TLN-BLN	TRN-BRN	TLN-BRN	TRN-BLN
B1	265.2	265.2	153.1	154.2	307.2	306.2
	265.3	265.2	154.4	154.2	307.2	307.2
B2	266.1	265.2	153.2	153.3	307.2	307.1
	266.2	265.3	154.1	154.2	306.3	307.2
B3	266.2	265.2	154.2	154.2	307.2	307.2
	266.2	265.1	155.2	154.2	307.2	307.2
B4	266.0	266.0	154.0	154.0	307.4	307.4
	266.0	266.0	154.0	154.0	307.4	307.4
Mean	265.9	265.4	154.0	154.0	307.1	307.1

Table 6.5. Horizontal, vertical and diagonal hole distances in stud-column member.

Member	Horizontal distance		Vertical distance		Diagonal distance	
	(2)	(3)	(4)	(5)	(6)	(7)
	TLS-TRS	BLS-BRS	TLS-BLS	TRS-BRS	TLS-BRS	TRS-BLS
(1)	TLN-TRN	BLN-BRN	TLN-BLN	TRN-BRN	TLN-BRN	TRN-BLN
SC1	264.2	266.3	154.3	154.2	307.2	307.3
	265.5	266.8	153.9	154.4	307.9	308.5
SC2	264.8	266.3	153.8	152.9	307.1	306.6
	266.5	265.1	153.1	154.5	306.6	308.4
SC3	266.4	265.3	153.6	154.2	307.4	307.3
	264.9	265.6	152.5	155.0	307.2	308.3
SC4	266.0	266.0	154.0	154.0	307.4	307.4
	266.0	266.0	154.0	154.0	307.4	307.4
Mean	265.5	265.9	153.7	154.2	307.3	307.7

Measured wall thicknesses for the beams B1 to B4 and the stud columns SC1 to SC4 are reported in Tables 6.6 and 6.7, respectively. Column (1) in the tables is for the members' for the SAJs. Column (2) has the label for the connections. The three thicknesses, in column (3), are for measurements at 60º spacing around the hole perimeter. Mean thickness per hole location is given in column (4). In bold text the overall mean wall thickness for each member is listed.

Table 6.6. Mean thickness of walls in Startlink floor beam shape.

Specimen		Measured thicknesses (mm)			Mean (mm)
(1)	(2)	(3)			(4)
B1	TLS	4.52	4.21	4.39	4.37
	TLN	5.55	5.53	5.61	5.56
	TRS	4.46	4.65	4.61	4.57
	TRN	5.75	5.44	5.56	5.58
	BLS	4.55	4.07	4.36	4.33
	BLN	5.74	5.44	5.36	5.51
	BRS	4.55	4.75	4.62	4.63
	BRN	5.30	5.44	5.42	5.39
Mean for B1					**4.99**
B2	TLS	4.90	4.67	4.84	4.80
	TLN	5.21	5.08	5.72	5.34
	TRS	4.27	4.68	4.52	4.49
	TRN	5.44	5.67	5.55	5.55
	BLS	4.64	4.41	4.77	4.61
	BLN	5.27	5.05	5.16	5.16
	BRS	4.27	4.67	4.46	4.47
	BRN	5.44	5.39	5.66	5.50
Mean for B2					**4.99**
B3	TLS	4.32	4.57	4.48	4.46
	TLN	5.47	5.66	5.62	5.58
	TRS	4.77	4.60	4.68	4.68
	TRN	5.33	5.23	5.22	5.26
	BLS	4.38	4.67	4.49	4.51
	BLN	5.49	5.77	5.59	5.62
	BRS	4.78	4.61	4.70	4.70
	BRN	5.19	5.05	5.25	5.16
Mean for B3					**5.00**
B4	TLS	4.67	4.87	4.88	4.81
	TLN	5.16	5.28	5.31	5.25
	TRS	4.69	4.88	4.92	4.83
	TRN	5.23	5.23	5.11	5.19
	BLS	4.75	4.70	4.42	4.62
	BLN	5.31	5.22	5.05	5.19
	BRS	4.49	4.61	4.75	4.62
	BRN	5.56	5.31	5.52	5.46
Mean for B4					**5.00**

Table 6.7. Mean thickness of walls in Startlink stud column shape.

Specimen		Measured thicknesses (mm)			Mean (mm)
(1)	(2)	(3)			(4)
SC1	TLS	4.25	4.51	4.33	4.36
	TLN	4.74	4.88	4.91	4.84
	TRS	4.25	4.32	4.27	4.28
	TRN	4.72	4.95	4.84	4.84
	BLS	4.01	3.94	3.98	3.98
	BLN	5.23	5.13	5.11	5.16
	BRS	4.09	3.93	4.03	4.02
	BRN	5.20	5.06	5.08	5.11
Mean for SC1					**4.53**
SC2	TLS	4.16	4.23	4.21	4.20
	TLN	4.97	4.88	4.90	4.92
	TRS	4.10	4.16	4.20	4.15
	TRN	5.04	4.88	4.96	4.96
	BLS	3.95	4.07	3.94	3.99
	BLN	5.12	5.24	5.17	5.18
	BRS	3.92	4.06	3.85	3.94
	BRN	5.16	5.21	5.24	5.20
Mean for SC2					**4.56**
SC3	TLS	4.21	4.36	4.25	4.27
	TLN	4.95	5.06	4.90	4.97
	TRS	4.22	4.20	4.26	4.23
	TRN	5.01	4.71	4.91	4.88
	BLS	3.90	3.97	3.93	3.93
	BLN	5.15	5.09	5.13	5.12
	BRS	3.93	3.93	3.98	3.95
	BRN	5.07	5.14	5.09	5.10
Mean for SC3					**4.55**
SC4	TLS	4.12	4.23	4.31	4.22
	TLN	5.29	5.03	4.99	5.10
	TRS	3.98	3.94	4.09	3.97
	TRN	5.17	5.28	5.18	5.21
	BLS	4.28	4.40	4.36	4.35
	BLN	4.89	4.96	4.68	4.84
	BRS	3.92	4.07	4.16	4.05
	BRN	5.14	5.22	5.03	5.13
Mean for SC4					**4.61**

It is seen from Tables 6.6 and 6.7 that the shapes have a different web thickness on the South and North sides. The mean values for the South and North are 4.56 mm and 5.39 mm. The equivalent thicknesses from Table 6.7 for stud columns are 4.12 mm and 5.04 mm. Results in the tables also indicate that the beam has a mean web thickness of about 5 mm whereas the stud column mean wall thickness is lower at

about 4.6 mm. These values show that the overall mean of the wall thickness for all beams and columns have a good match to the nominal design dimensions given in Figures 6.8(a) and 6.8(b).

To assemble a SAJ specimen the top and bottom flange of beam is cut off so that the two webs can go around the stud-column. This design feature in the Startlink building system is shown in Figure 6.10. Because the opening in the beam is 64 mm wide there a gap of +2 mm on both sides of the 60 mm wide column.

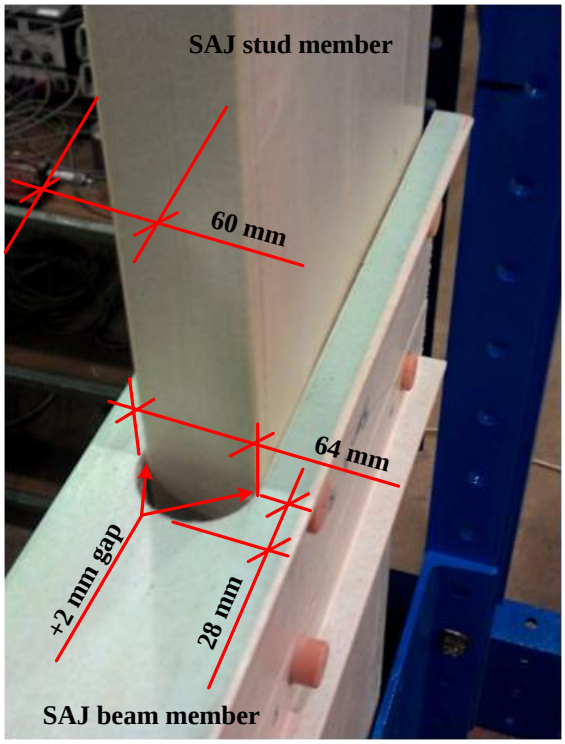

Figure 6.10. Startlink frame joint viewed from top flange of floor beam.

A SAJ is assembled using four FRP dowels, which are bonded into the holes having a nominal diameter of 31 mm. Nominal geometry for the joint is illustrated in Figure 6.11. The horizontal, vertical and diagonal distances between holes are based on the

design geometry of the first floor level joint in Startlink frame by Kendall (2010). The bending moment of 6.8 kNm and vertical shear force of 5.1 kN are from design calculation obtained from loading case 4a shown in Figures 6.4 and 6.5.

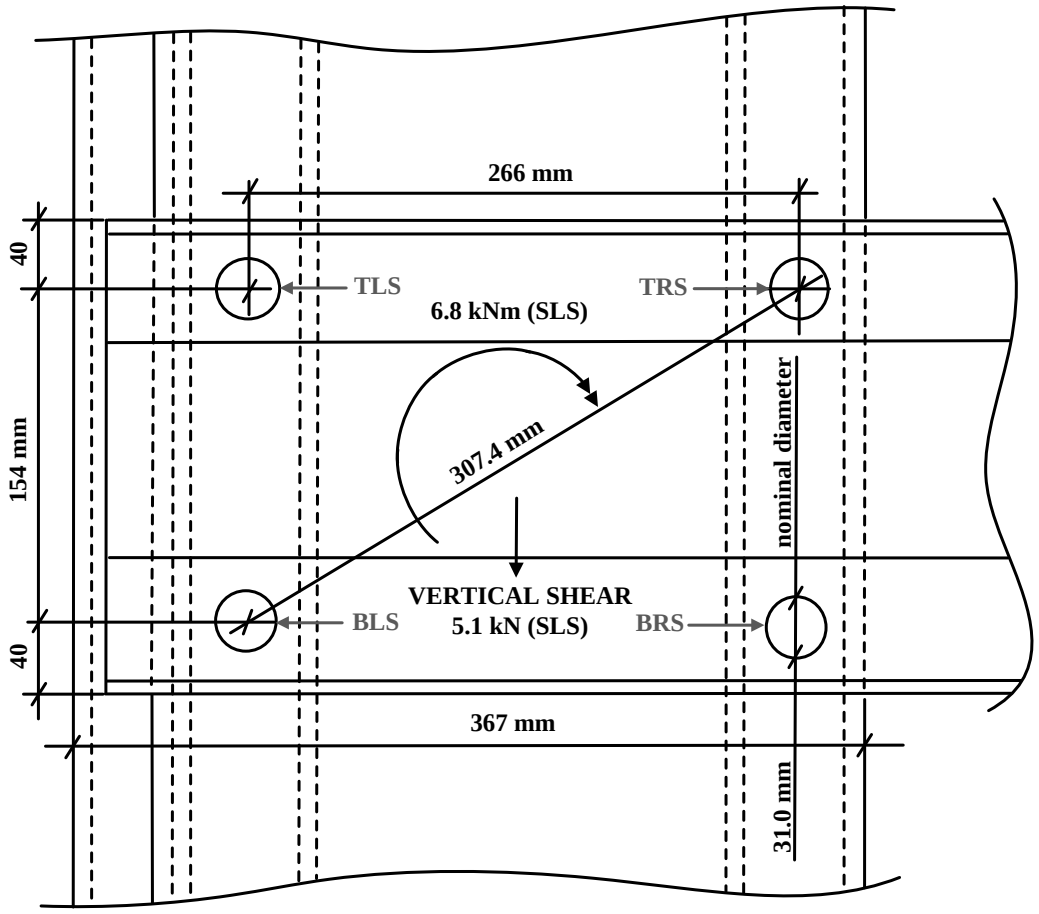

Figure 6.11. Details of SAJ connections.

To assemble SAJ-1 to SAJ-3 specimens, the members were delivered to the structures laboratory of Warwick University by EXEL Composites UK in one batch. The connection holes for these specimens were already drilled by hand drill by Odour Control Systems Ltd (OCS). The members for the SAJ-4 were delivered later after being requested by author for more material and the connection holes were drilled and reamed by CNC machine (Butler Hydrabore Horizontal Borer) in the

Engineering Workshop at Warwick University. The hole diameters for SAJs' members were measured with a three point internal micrometer to the nearest ±0.01 mm. Presented in Table 6.8 are the measured hole diameters for the four beams of B1 to B4 and their associated stud-columns of SC1 to SC4 in specimens SAJ-1 to SAJ-4. In column (1) the hole positions on the South wall are given on the left side (of each row), and those, followed by a comma, are for the associated hole positions on the North wall. Beam and column member labels are given in columns (2) and (4). Given in columns (3) and (5) are the measured hole diameters for beams and columns, respectively. 31.31 mm is the mean value of hole diameters taken from B1 to B3 and SC1 to SC3 for the SAJ-1 to SAJ-3 members given in Tables 6.8.

Table 6.8. Diameter of holes in Startlink floor beams and stud-columns.

Position	Specimen	Measured diameters (mm)	Specimen	Measured diameters (mm)
(1)	(2)	(3)	(4)	(5)
TLS, TLN	**B1**	31.14 , **31.37**	**SC1**	31.20 , 31.93
TRS, TRN		31.14 , 31.33		31.42 , 31.86
BLS, BLN		31.15 , 31.16		31.14 , **31.06**
BRS, BRN		31.12 , 31.23		31.16 , 31.77
TLS, TLN	**B2**	31.17 , 31.22	**SC2**	**32.02** , 31.13
TRS, TRN		31.21 , 31.27		31.57 , 31.09
BLS, BLN		**31.07** , 31.18		31.67 , 31.77
BRS, BRN		31.17 , 31.30		31.12 , 31.18
TLS, TLN	**B3**	31.20 , 31.24	**SC3**	31.68 , 31.11
TRS, TRN		31.14 , 31.17		31.46 , 31.86
BLS, BLN		31.16 , 31.17		31.13 , 31.66
BRS, BRN		31.15 , 31.13		31.17 , 31.35
TLS, TLN	**B4**	29.99 , 30.04	**SC4**	29.99 , 30.03
TRS, TRN		29.99 , 30.05		29.98 , 30.04
BLS, BLN		29.98 , 30.06		30.03 , 30.07
BRS, BRN		29.99 , 30.04		29.99 , 30.03

Minimum and maximum diameters of 31.07 mm and 31.37 mm for B1 to B3 are highlighted in bold in column (3). In column (5), the minimum and maximum diameters for holes in SC1 to SC3 are 31.06 mm and 32.02 mm, respectively. For

members B4 and SC4 it can be seen that their four holes have the smallest variation, with the diameters in the range of 29.98 mm to 30.07 mm.

Figures 6.12(a) to 6.12(c) show three sets of FRP dowels with nominal diameters of 28.9 mm to 31.0 mm and with a constant length of 100 mm. The length of dowels has been specified by the 74 mm width of the beam's webs and an additional 12.5 mm on both each sides. The dowels have been machined from a pultruded fibre glass solid rod having pure UD roving. It can be seen in the photographs (in Figures 6.12(b) and 6.12(c)) that the two sets of dowels of 31 mm and 30 mm diameter have a head cap at one end. SAJ-1 and SAJ-2 have been assembled using sets of dowels with the nominal diameter of 28.9 mm shown in Figure 6.12(a), whereas SAJ-3 and SAJ-4 used sets of dowels with the nominal diameters of 31.0 mm and 30.0 mm, respectively.

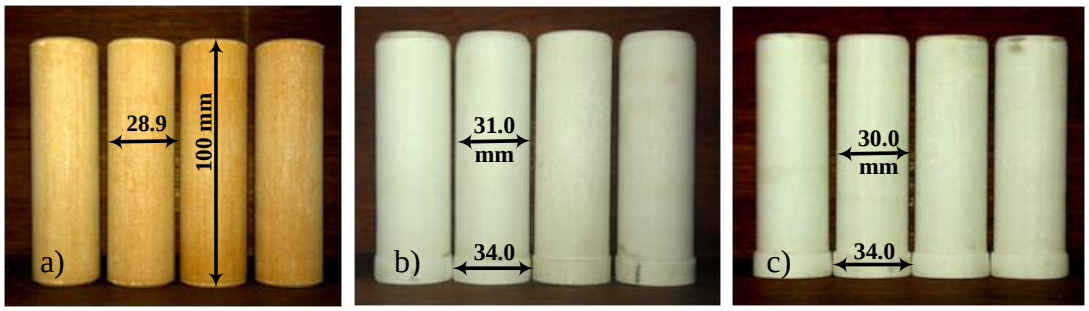

Figures 6.12. Three sets of dowels used to form four SAJs: (a) SAJ-1 and 2; (b) SAJ-3 and (c) SAJ-4.

For the dowels, the design shear and flexural strengths are 60 N/mm^2 and 350 N/mm^2, respectively. The group of four dowels have been designed (Kendall, 2010) to resist shear force and the moment that will be transferred from the floor beam to stud-column.

6.3 Details of Joints

Details of specimens SAJ-1 to SAJ-4 are presented in the photographs of Figures 6.13 to 6.16.

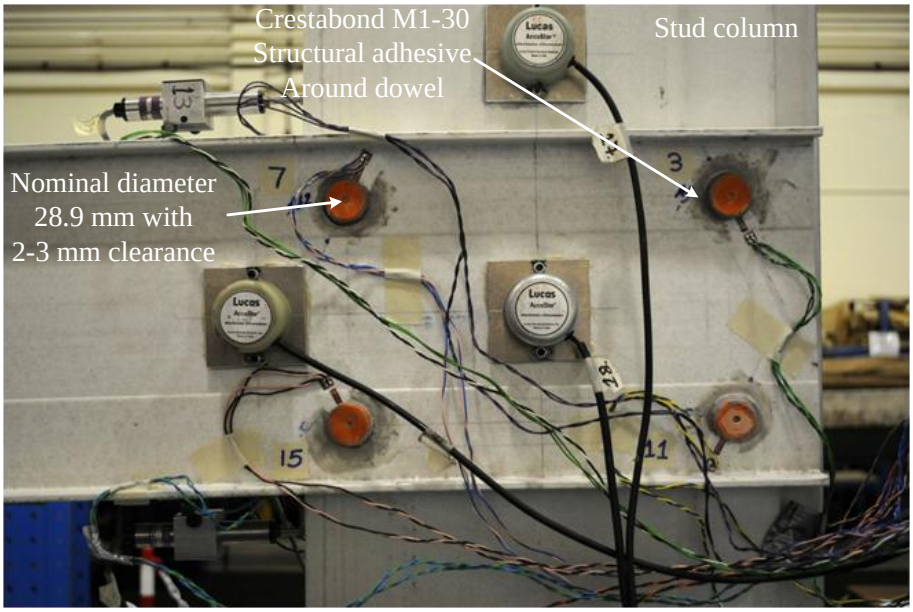

Figures 6.13. SAJ-1 viewed from the North side.

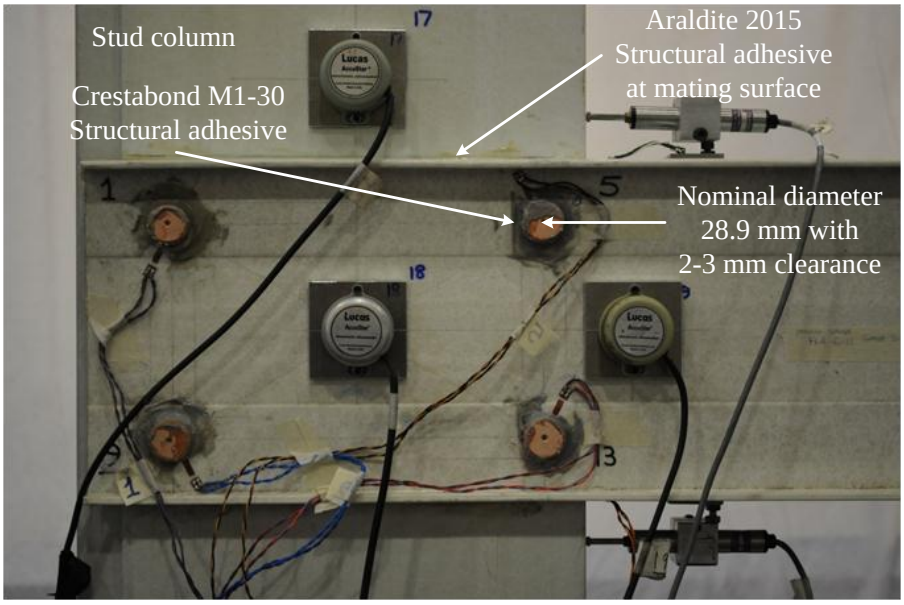

Figures 6.14. SAJ-2 viewed from the South side.

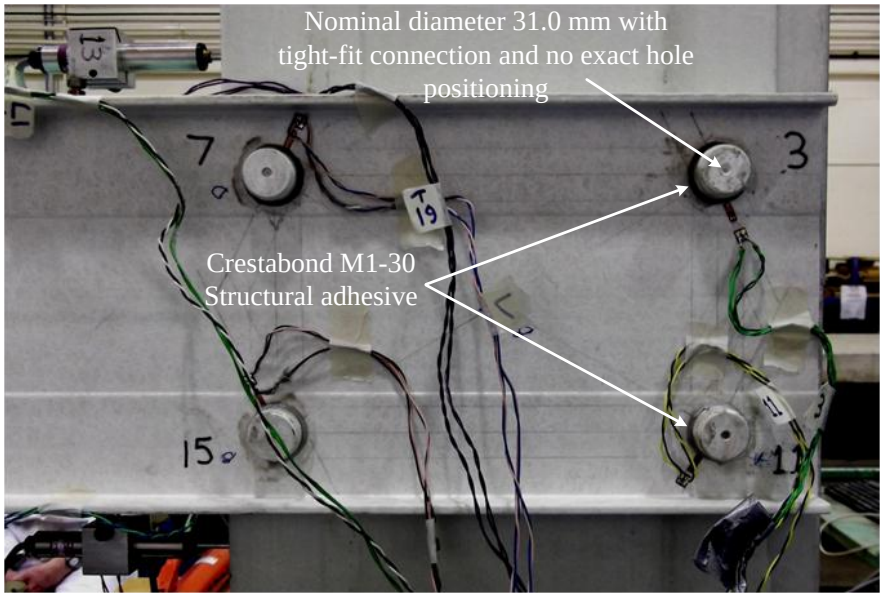

Figures 6.15. SAJ-3 viewed from the North side.

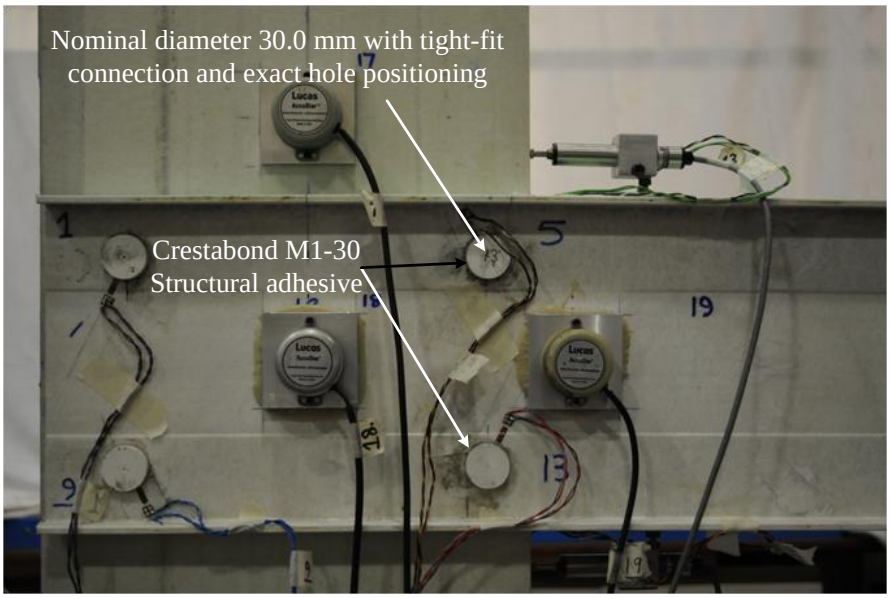

Figures 6.16. SAJ-4 viewed from the South side.

Figure 6.13 shows SAJ-1 specimen after assembling the joint using the set of dowel with nominal diameter of 28.9 mm. Subtracting this dowel diameter from the minimum and the maximum hole diameters for beam B1 in Table 6.8 it is found that the clearance hole was in the range of 2.2 mm to 2.5 mm. This range is found to be higher from 2.2 mm to 3.0 mm, for stud column SC1 measurements in Table 6.8. It

is important to mention that the total relative values for hole clearance between B1 and SC1, with the with 28.9 mm nominal diameter dowel, is 4.4 to 5.5 mm. This magnitude of clearance will ensure that the joint will be classified as nominally pinned. In Figure 6.17 the photograph shows the size of the clearance hole at the TLS connection in SAJ-1 prior to adhesive bonding.

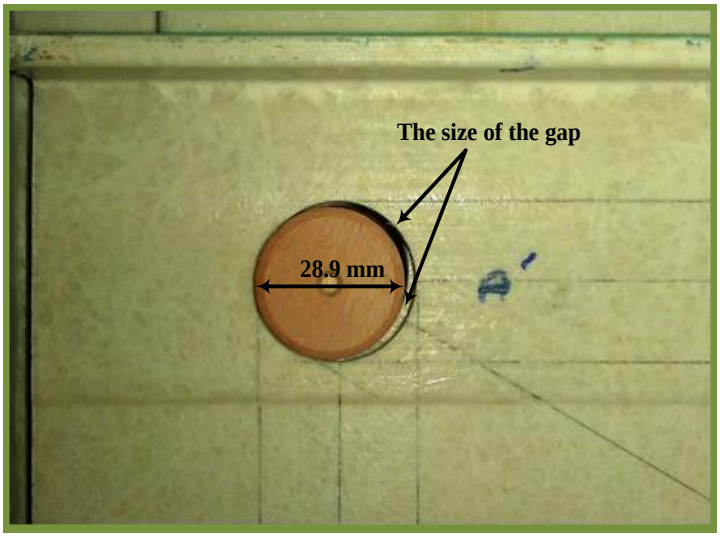

Figure 6.17. Millimetre clearance after B1 and SC1 members and dowel were fully engaged.

In his structural design for the Startlink portal frame, Kendall (2010) states that, the maximum clearance hole per member should not exceed 0.5 mm. It must be recognised that with the same hole clearance in both beam and column members this total clearance is still 1.0 mm (before allowing for tolerance on hole preparation). This gap between dowel and members would give the joint a non-restricted rotation before there would be resistance upon the contacting of the dowels with the joint's members. Figure 6.18 shows schematically the rotation of the joint having a clearance hole of 0.5 mm. The solid line shows the diagonal between centres of pins where placed at the centre of the TLS and BRS holes. By rotation of the beam

around the centre of joint the pins will contact the member after 0.5 mm displacement in perpendicular direction to the diagonal. The new position of the diagonal is shown by dashed line. Having the same rotation with the stud column gives another 0.5 mm displacement. Using basic mathematical formula to obtain rotation when one of the pins relatively displaced 1 mm gives rotation of about 6 mrad ((1/153.7) × 10^3 = 6.4).

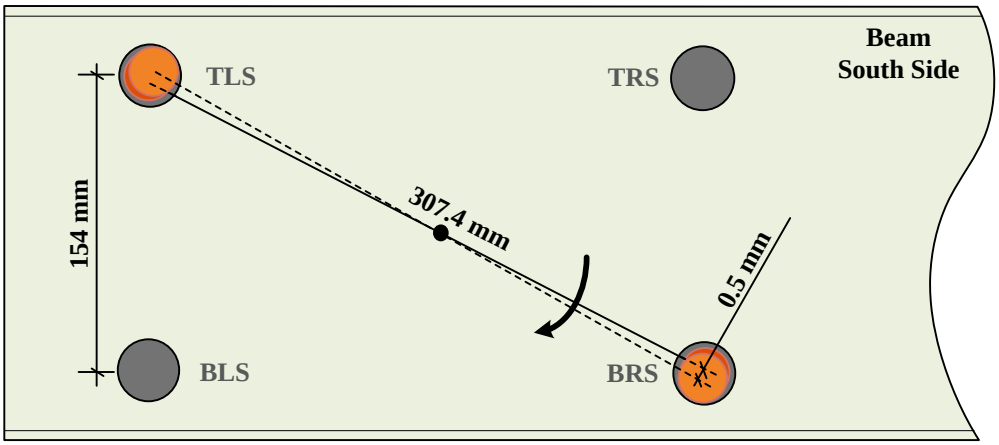

Figure 6.18. Rotation of the joint with a 0.5 mm clearance hole.

Having a connection in SAJ-1 with a minimum of 4.4 mm (2.2 mm for each member) clearance indicates that SAJ-1 joint have a maximum 'clearance hole' rotation (Ø) of about 20 mrad. It is noteworthy to mention that for the beam member in the Startlink portal frame with SLS vertical deflection limit of *L*/460 under uniformly distributed load the end rotation is 4.5 mrad. In other words the presence of a 'free' rotation of 20 mrad ensures that, without additional methods of connection, the Startlink joint would be classified as nominally pinned. It must be recognised that with the presence of this oversized holes (or undersized pins) in joints the Startlink portal frame will not possess the required rotational stiffness for the frame not to deform more than the SLS limit. In other words, the oversized holes

will deliver a ‘pin’ connection in portal frame joints, the exact opposite, in terms of the required joint rotational stiffness, assumed in the design process.

To provide moment resistance in the presence of the oversized holes, SAJ-1 was assembled with a structural adhesive to bond the ‘undersized’ dowels into the holes. This specimen is shown in Figure 6.13. As a result the unrestrained joint rotation was first opposed by the stiffness and strength of the adhesive bonding. It should be considered that in this situation the Startlink frame joint no longer has dowel connections. To form the bonded connection a liberal amount of M1-30 Crestabond (Scottbader, 2012) was applied around the holes before inserting the adhesively coated dowels to assemble the joint. M1-30 Crestabond has tensile strength of 17 to 20 N/mm^2 (MPa) and tensile modulus of 750 to 1000 N/mm^2 (Scottbader, 2012). Prior to testing the SAJ-1 had been kept at room temperature for, at least, 48-hour to make sure that the adhesive bonding had achieved full cure. Full cure time for Crestabond M-30 structural adhesives is 24 hours at room temperature.

The issue with this method of assembly is that there is no way of knowing if the adhesive bonding will overcome the looseness of a potential ‘pinned’ connection. In other words, can adhesive bonding provide the necessary level of continuity (void filling) for reliable transfer of the connection forces? Moreover, it is a major practical challenge to work out how to get the adhesive to fill the voiding between the dowel pin and stud column walls, before either the adhesive sets or some volume is lost, into the voiding beyond the inner surfaces of the stud column.

The reason for testing SAJ-1, with clearance hole of 2-3 mm, was to preoperatively assess a practical approach for the construction of the Startlink superstructure with large floor and wall subassemblies. Figure 6.3 shows the floor and wall subassemblies. As can be seen, each wall subassembly panel has five stud columns and four wall panels. At every floor level the floor panel comprises five floor beams and four floor panels. Based on the execution of the Startlink house the 2.4 m wide panels are fabricated off-site to minimise site assembly. Each joint between a stud and beam requires alignment of eight holes in the stud (TLS, TRS, BLS, BRS, TLN, TRN, BLN and NRS) with eight holes in the floor beam. To connect a floor panel this has to happen in five positions area a panel's width, and on two sides too. To make this arrangement practicable on site an appropriate clearance hole is required. It is the consortium's belief that, because of manufacturing tolerances, a tight fit connection with 0.2 to 0.3 mm clearance is unachievable. The author recommends that when Startlink house go into production that the application of CNC machines for hole drilling and member length cutting be explored for the possibility of having holes that have centres aligned with a maximum hole clearance of 0.3 mm.

It is recognised by the author that tolerances mean that the dowel connection design geometry is not going to be realised. But there are some options to make the right decisions to minimise (or eliminate) any 'looseness' and stress concentration from having hole clearance. One suggestion is to fabricate one pilot hole per joint at each level of stud column and each corner of floor subassembly and connect the existing holes/pins in the site and then afterwards, go back around and put the rest of dowel pins connections at each position, by drilling on site with a hole cutter the size of a pin. This means that when the beam and column sections are jointed together we can

have a tight fitting dowel connection with 0.2 to 0.3 mm clearance hole. Ideally, it is a goal that the connection forces in the four dowel connections are to be fairly uniform (this assumes there is a fairly constant localised stiffness opposing the four bearing forces per member).

Although the measurements in Table 6.8 for 48 hole diameters in B1 to B3 and SC1 to SC3 show a relatively big clearance with a 28.9 mm dowel, the author observed that the distances in Tables 6.4 and 6.5 between pairs of holes from TL to TR; and from BR and BL in Figures 6.9(a) and 6.9(b), are relatively constant.

The similarity of the positions of the hole centres on the beam and stud column for SAJ-1, SAJ-2 and SAJ-3 show that there is scope to assemble the joint, with a minimum clearance, if the dowel pins have a nominal diameter of 31.0 mm (this being two millimetre bigger than the 28.9 mm diameter of the original dowels for the Startlink house).

To allow the frame joints to possess a relatively ‘high’ rotational stiffness, the author offers two options to reduce the influence of having oversized hole in the next two SAJs specimens. These options are:

1. Along with bonding-in the dowels, there could be liberal adhesive bonding over the surfaces common to the beam and column sections.
2. To have set of four dowels with a nominal diameter of 31 mm and holes of the same diameter with a hole clearance of about 0.2 to 0.3 mm. Note that with a clearance of 0.3 mm the unrestrained joint rotation will be about 3 mrad.

Following option 1 specimen SAJ-2 was assembled using the same set of 28.9 mm diameter dowels that has been employed for assembling SAJ-1. Specimen SAJ-2 is shown in Figure 6.14. Structural adhesive Araldite 2015 was liberally applied over the North and South side surfaces between the beam and column section (78200 mm^2 for each side) to make the joint have a combination of dowel and bonded connections. As noted earlier there is a gap of 2 mm on both sides that had to be filled with the adhesive to make the bonded connections. There were two reasons for using Araldite 2015 instead of the M1-30 Crestabond. Firstly, SAJ-1 which was assembled before SAJ-2, had relatively a very low level of stifness in the joint as the result of using the M1-30 Crestabond. Secondly, the author had confidence that Araldite 2015 would provide the required rotational stiffness (Mottram and Zhang, 1999). Prior to testing the specimen had been kept at room temperature for, at least, 48-hour to make sure that the adhesive bonding had achieved full cure. Full cure time for Araldite 2015 structural adhesives is 4 hours at room temperature.

To satisfy the option 2, specimen SAJ-3 was assembled using a set of dowels with the larger nominal diameter of 31 mm. This joint is shown in Figure 6.15. Although this new set of dowels could provide the required tight-fit connection the inherent tolerance of 1.1 to 2.5 mm (calculated from results in tables 6.4 and 6.5) for distances between the holes means that when the drilled beam and column members are in position the four sets of four holes do not exactly have all their centres aligned. A light mallet was used to tap the dowels into the connection hole to fabricate the connections for joint SAJ-3. It is recognised that non-coincident holes will lead to a different bearing force at the four holes. This could lead to premature material failure since design assumes a uniform constant bearing force per dowel connection.

From Tables 6.4 and 6.5 the hole diameters for SAJ-4 show an exact match for members B4 and SC4. In the SAJ-4 members the hole diameters are in the, close, range of 30.0 mm to 30.1 mm. This excellent tolerance on hole diameters will aid assembly providing the centre of the holes also match up. The latter was achieved by having B4 and SC4 drilled and reamed in the Engineering Workshop after members have been clamped together in their final positions for specimen SAJ-4.

For assembling the SAJ-4 joint the dowel of 30.0 mm nominal diameter used. SAJ-4 was therefore assembled with tight-fit dowel connections. It was aimed at assembling the SAJ-4 specimen with the dowel of 31.0 mm nominal diameter which the same dowel size was using for assembling the SAJ-3. But, because of the availability of the 30 mm drill bit size in the Engineering Workshop at Warwick University this diameter has been chosen for fabricating holes in the SAJ-4 joint. It is noteworthy to mention that reducing the diameter of dowel for the SAJ-4 specimen from 31 mm to 30 mm has no significant influence on the joint properties. To complete the fabrication M1-30 Crestabond structural adhesive (Scottbader, 2012) is placed around the hole circumference before driving adhesively coated dowels through the holes. Application of adhesive bonding in preparation SAJ-4 is the same as for SAJ-3. Because of the tight fit it was necessary to use a light mallet to apply impact force to overcome the inherent resistance to insertion.

Table 6.9 shows the geometric configuration of the four different beam-to-column joints with dowel connections, and with and without adhesively bonded connections, were assembled so that their rotational stiffnesses and modes of failure could be determined.

Table 6.9. Geometric configuration of the four different beam-to-column Sub-Assembly Joints (SAJs) with dowel connections.

Specimens	Hole clearance (mm)	Bonded connection
SAJ-1	2-3	-
SAJ-2	2-3	between overlapping surfaces of the members
SAJ-3	tight fit	-
SAJ-4	'pseudo' tight fit	-

6.4 Test Configuration and Test Procedure

Figure 6.19 illustrates the loading configuration used. For SAJ testing the bending moment and vertical shear force at the joint, due to a UDL loading is converted to a single vertical force applied at a distance of 1318 mm from the centre of joint. The lever arm distance of 1318 mm is convenient the contraflexural point determined from the frame analysis as explained in section 6.1.

The top and bottom end of the column is pinned, using M20 steel bolts with nominal Ø20 mm, to the test supports fixture, which allows 'free' in-plane rotation (in the plane of portal frame in Figure 1). The reason for using pinned supports is to satisfy the fact that the only actions transferred at the contraflexural points are shear and axial forces. To ensure there is not bearing failure where the 20 mm steel pin passes through the two 3 mm thick walls of the stud column, two aluminium plates of 333×114×3 mm, with a central 21 mm hole, are bonded to the side walls of stud-column.

Figure 6.19 schematically shows the dimensions of the specimen and the locations of the instrumentation, consisting of three inclinometers, three displacement transducers, twelve strain gauges and load cell. Rotations and axial displacements

are measured using the three Accustar® electronic inclinometers shown in Figure 6.20 and three strain gauge based displacement transducers labelled DTB, DBB and DPL seen in Figure 6.21.

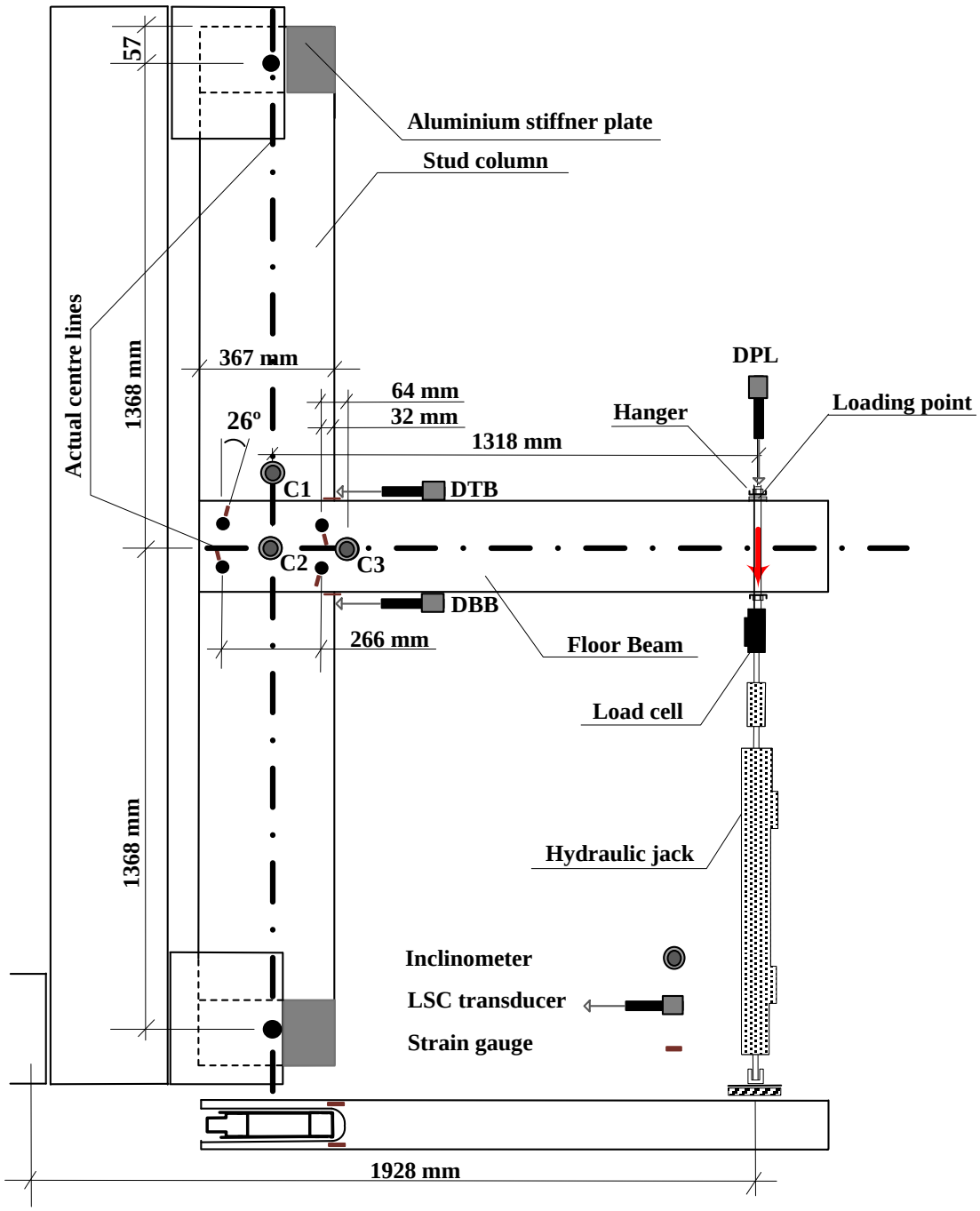

Figure 6.19. Test rig with instruments locations and loading configuration.

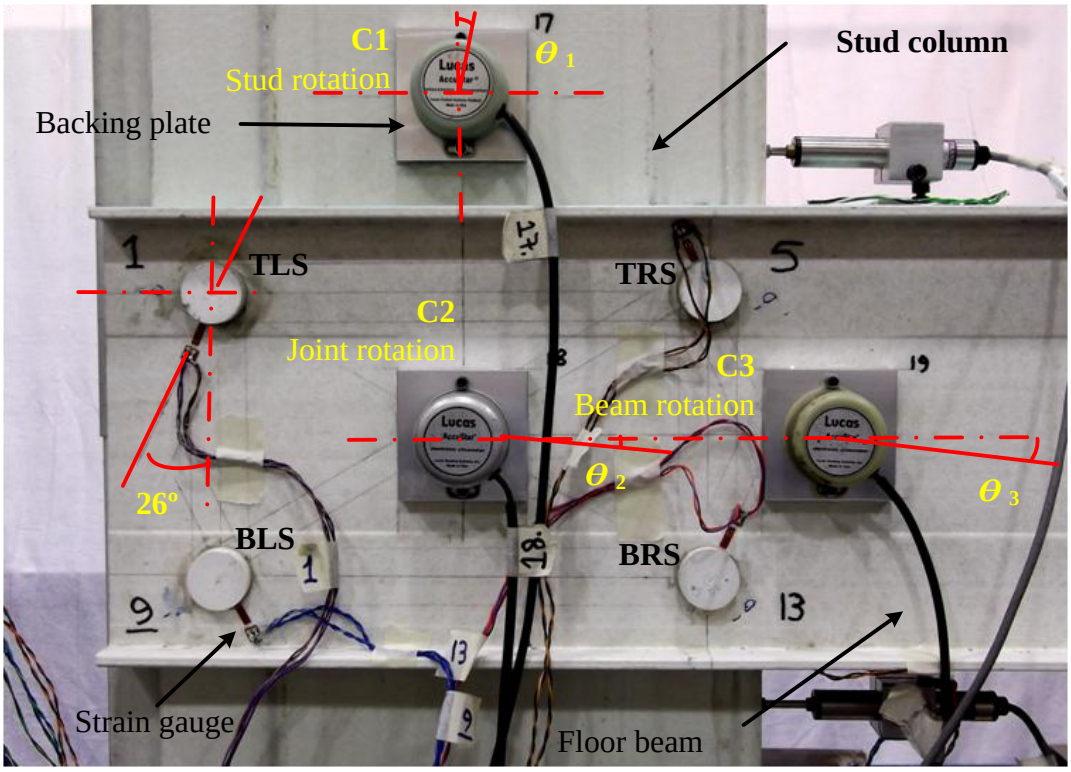

Figure 6.20. Inclinometers and their rotations.

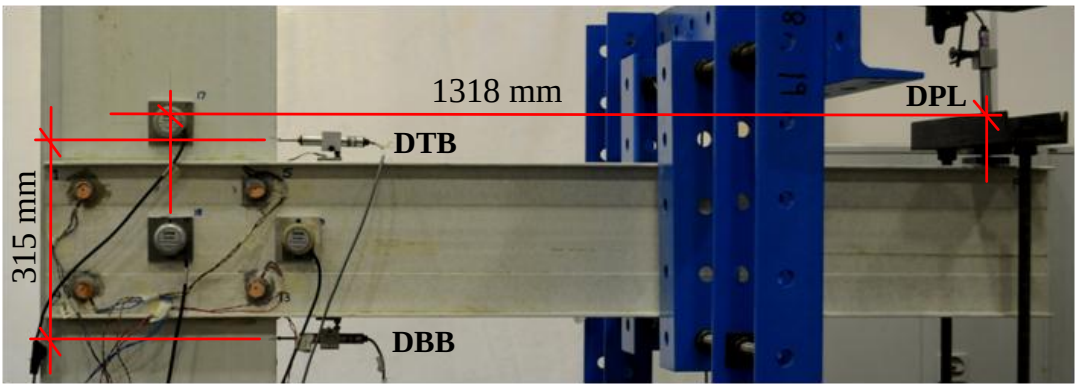

Figure 6.21. SAJ with the position of displacement transducers.

In Figure 6.20 can be seen the rotations (amplified for visualisation) of the stud column just above the top flange of the beam (θ_1), the joint (θ_2) and the beam (θ_3) are measured by inclinometers C1, C2 and C3. C1 is placed on the actual centre line of

the stud-column that is passed from the top and bottom supports bolts and also joint centre (see Figure 6.19). It is located at a vertical distance of 60 mm from top flange of beam. This distance allows beam to rotate without any interaction with the backing plate supporting C1. This square metal plate is bonded to the wall of the stud-column. Inclinometer C2 is positioned of the centre of the dowel connections, which coincides with the intersection at the centre lines of the column and the beam member. The difference between the joint and the column rotations (i.e., $\theta_2 - \theta_1$) gives the measured joint rotation $\emptyset_j$. It is assumed that θ_1 is the same column rotation as does exist at the centre of the joint, this rotation cannot be determined. C3 is sited on the actual centre line of the beam and just beyond the end of the column. It is worth mentioning that at this section of the beam, where the flanges have been cut away, has the minimum value of the second moment of area ($I_{b,min} = 1.97 \times 10^6$ mm^4). As a consequence this section is the most flexible in the length of the beam. C3 placed on this section as close as practical to the joint's end to measure the beam's rotation and, subsequently, the difference between this and the column rotation (i.e., $\theta_3 - \theta_1$) gives the measured beam rotation $\emptyset_b$.

Relative horizontal movement to the column at the top and the bottom of the beam's flanges are measured by a pair of displacement transducers, designated as DTB and DBB in Figure 6.21. The first letter, D denotes Displacement, and second and third letters are for show Top of the Beam and Bottom of the Beam, respectively. As seen in Figure 6.21 the vertical separation between the DTB and DBB transducers is set at 315 mm. The vertical deflection of the beam at the load point is measured by displacement transducer DPL. These three transducer readings are used to determine

the rotational response of the beam. To calculate the beam rotation using DTB and DBB the following geometric relationship is used:

$$\emptyset_{\mathrm{L\,T,B}} = \arctan\left(\frac{lt+lb}{l}\right) \times 1000 \qquad \text{mrad} \qquad (6.1)$$

where *lt* and *lb* are the horizontal displacement measured by transducers DTB and DBB and *l* is their vertical separation (315 mm). It is noteworthy, that there is no significant difference in the moment-rotation curves using Equ. 6.1, or inclinometer C3. No test results are therefore presented using DTB and DBB.

Figure 6.22 schematically shows three sides of a SAJ's beam member with the positions and orientations of the direct strain gauges. 12 conventional 3 mm (can add make and product identifier) gauges give representative measurements of 'bearing' strain, around the dowel holes and tensile and compressive strains at the top and bottom of beam flanges, respectively. Eight strain gauges are placed around the four joint holes at 1 mm distance away from the perimeter. Four are on the North side and four on the South side. As seen in Figure 6.22 there have an orientation of 26º which is the theoretical direction for the resultant bearing force. The directions for the resultant forces are obtained from the vector of forces using conventional engineering analysis that combines the joint moment and shear force components. The remaining four strain gauges are used to determine tensile strains in the top flange on the South and North Sides and compressive strains in the bottom flange. Bearing strain given by eight gauges around the connections enables author to analyse the condition of the load distribution at each dowel/member contact.

Furthermore, recorded bearing, tensile and compressive strain capacity can be used to identify and check failure processes.

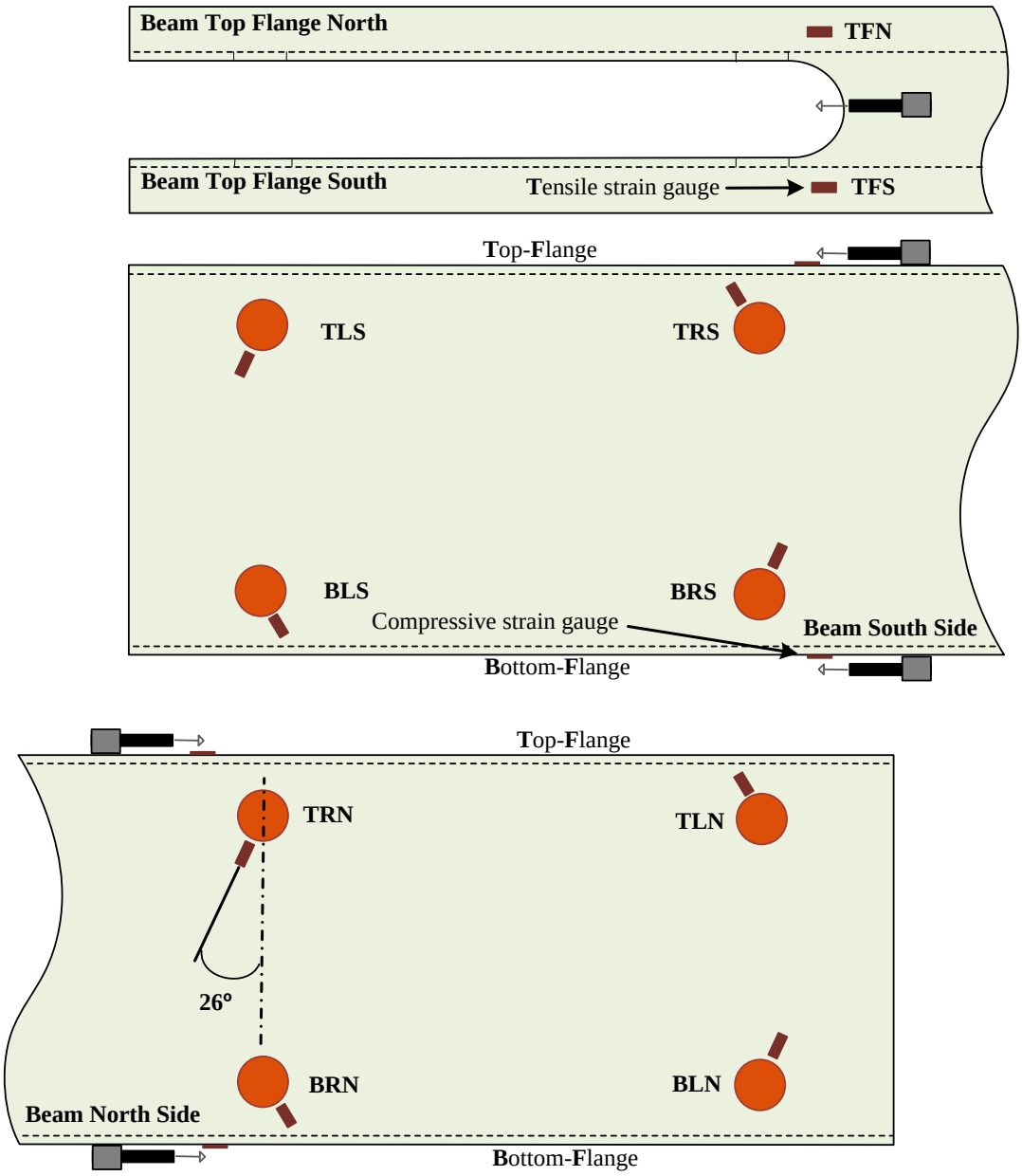

Figure 6.22. Position of strain gauges and displacement transducers.

In real time transducers reading are stored to an ORION 3531D Schlumberger data logger, which automatically records the specified values at each load/rotation

increment, and after 5 minutes form application of a load or rotation increment. Rotations were recorded to a resolution of 0.02 mrad (linear to ±1% over a 10^{o} range) and axial displacements to ±0.01 mm. Sensors were calibrated for linearity, before and after the series of tests. Measurements are displayed and stored on a computer, connected to the data logger, for the primary aim of monitoring the current state of the specimen while the test is being performed. Figure 6.23 shows the test rig with attached ORION 3531D Schlumberger data logger and computer in the structures laboratory at the University of Warwick.

Figures 6.23 and 6.24 show that the load is applied into the beam by means of a hanger assembly and a ball bearing placed in a semicircular socket at the centre of a steel loading plate. This plate of thickness 12 mm is attached, using screw clamp on both ends, to the top flange area which the load is distributed by the clamping system seen in Figure 6.21. The use of a 12.7 mm ball bearing ensures vertical alignment of the load during all load/rotation increments, even when the test specimen undergoes large rotations ($\emptyset > 30$ mrad), with minimal axial and lateral force components. To design the load capacity of the testing the maximum vertical deflection was specified to be 40 mm. The limit on applied end load was set to be three times that required to generate the ULS design moment of 10.1 kNm. The applied force is measured through a tension load cell, having capacity of 9 tonnes (i.e. 90 kN), and as seen in Figures 6.23 it is connected, in series, with manually operated (independent) hydraulic tension jacks.

Figure 6.23. Test rig with attached ORION 3531D data logger, the computer, hanger assembly, load cell and instrumented specimen.

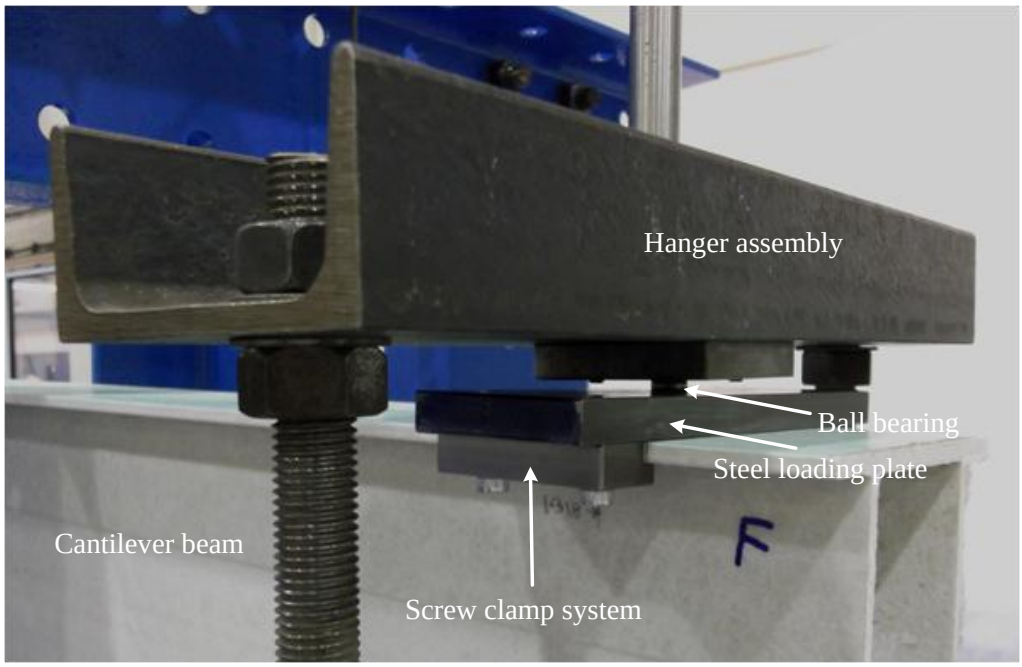

Figure 6.24. Local fixture to ensure point load is applied through the shear centre of the beam section.

Each SAJ specimen was deformed, under static load control, in increments of 0.5 kN (0.66 kNm), until joint experienced SLS loading of 5.1 kN (Kendall, 2010) or 6.8 kNm. When SLS loading reached the specimen was unloaded. After three times reloading-unloading to the SLS load the joint was left under constant deformation for a period of 24-hour to find out if there was a significant change in stiffness with time. The specimen was then loaded, in increments of 0.66 kNm to its predicted ULS load which corresponds to a moment of 10.1 kNm. The factor of safety from SLS to ULS was specified by Kendall (2010) to be 1.5. Prior to continuing loading in the post-ULS region, a specimen was subjected to three unloading-reloading cycles up to the ULS moment. A test was terminated when either the joint could no longer take an increased moment or when the deformation was considered to be excessive and there was a likelihood that specimen would lose stability.

Joint moment, *M*, is recorded at each increment during the entire loading procedure. A time interval of 5 minutes between two increments is chosen to make visual observations for any material damage (deterioration) and to record manually, sensor measurements.

Individually relative rotation of the joint ($\emptyset_j = \theta_2 - \theta_1$) and of the beam ($\emptyset_b = \theta_3 - \theta 1$) to the stud-column rotation are obtained and their corresponding rotational stiffness ($S = M / \emptyset$) was determined throughout the test. The *M*-$\emptyset$ curves are obtained and values for *M*, $\emptyset$ and relative *S*, at the initial, SLS loading and ULS loading are determined. This has allowed the author to evaluate the rotational stiffness of the joint and of the beam separately. For stiffness classification, K_b

values determined in accordance with the BS EN 1993-1-8; 2005, using the classification boundaries given in section 6.1.

6.5 Results and Discussion

Presented in Figure 6.25 to 6.28 are both the measured 'joint' and 'beam' *M-Ø* curves for specimens SAJ-1 to SAJ-4. To compare the relative performances of the four SAJs the curves in the figures have the same scale. To establish the *M-Ø* characteristic two measured rotations are considered. The joint rotation $Ø_j$ is given by $\theta_2 - \theta_1$ and the beam rotation $Ø_b$ is given by $\theta_3 - \theta_1$. As shown in Figure 6.20 the two rotation measurements were obtained by subtracting the stud column rotation (C1) from the joint rotation (C2), and from the beam rotation (C3), respectively. The former rotation is for on the response of the joint relative to column member, whereas, the latter is a measure for the joint rotational stiffness that accounts for the flexibility of the floor beam, to where inclinometer C3 is positioned. In Figures 6.25 to 6.28 $Ø_j$ curves SAJ-1′ to SAJ-4′ are given by the solid curves and $Ø_b$ curves SAJ-1″ to SAJ-4″ are given by the dashed curves. The *M-Ø* curves are crossed by two horizontal lines for the SLS and ULS moments of 6.8 kNm (M_s) and 10.1 kNm (M_u), which had been established from the design calculation by Kendall (2010). Each *M-Ø* curve is constructed by joining, with straight lines, the data points recorded at each load increment during the entire test procedure. At each increment there is a pair of *M-Ø* points, one taken immediately, after applying 'load' increment and the second after another 5 minutes had elapsed.

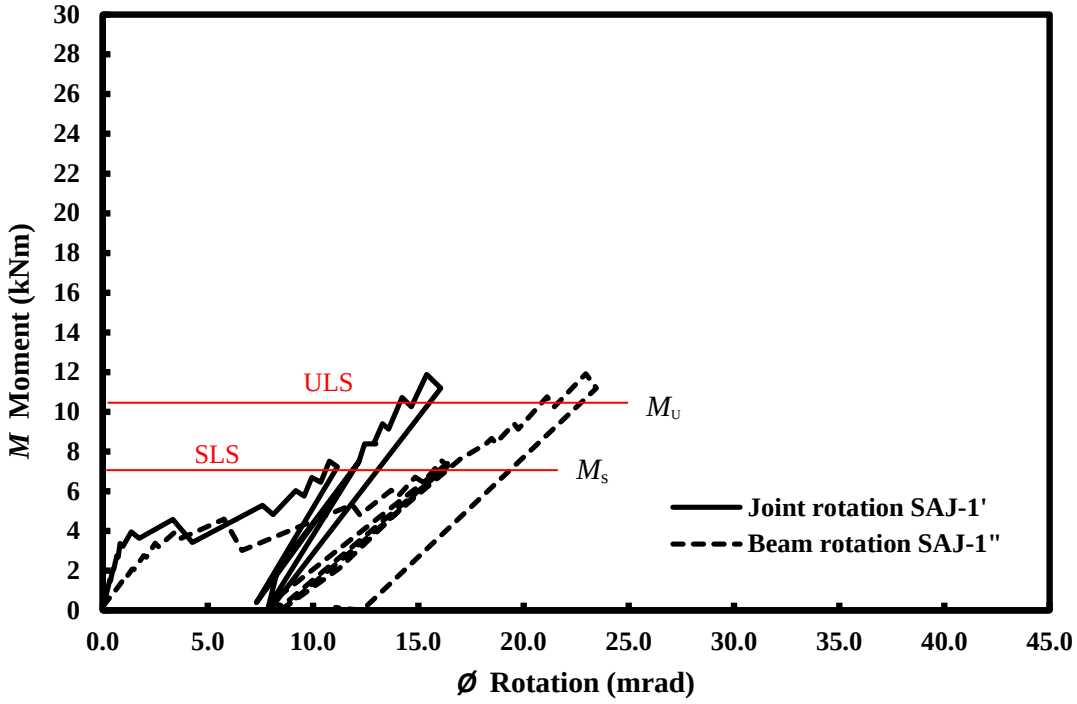

Figure 6.25. *M-Ø* curves for SAJ-1.

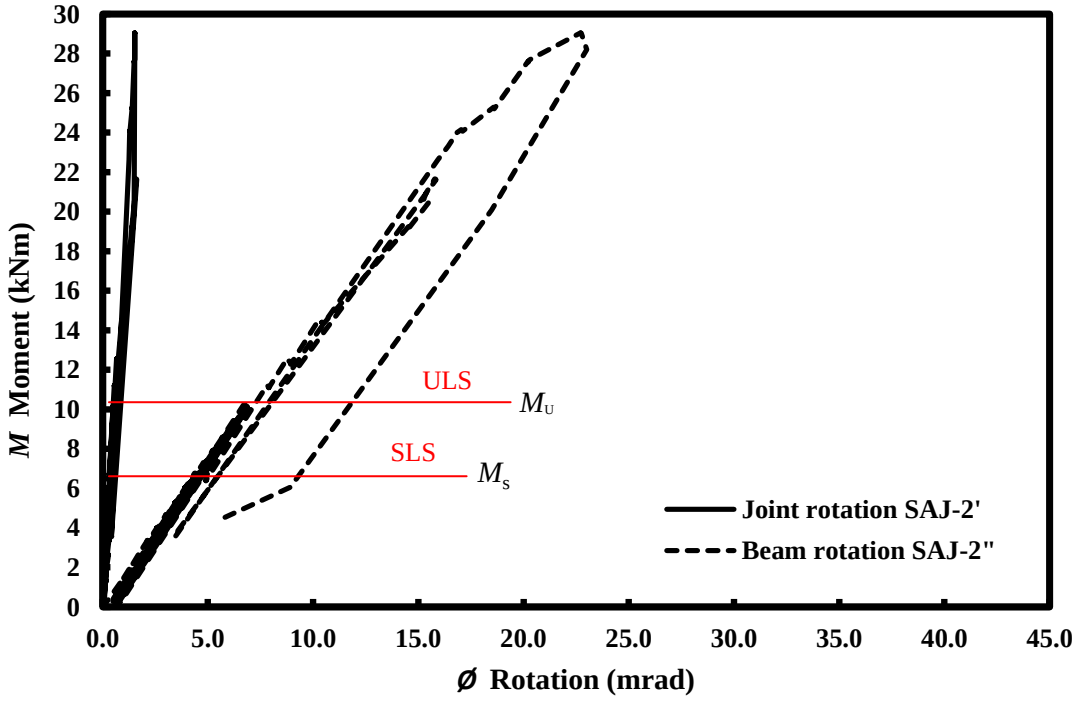

Figure 6.26. *M-Ø* curves for SAJ-2.

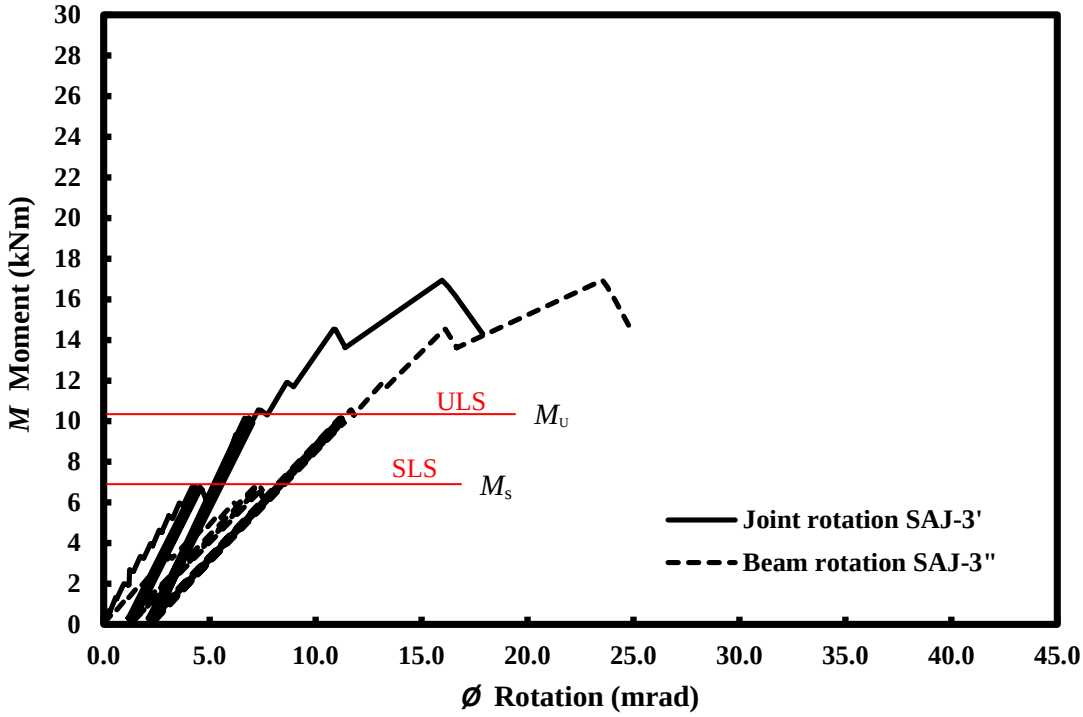

Figure 6.27. *M*-Ø curves for SAJ-3.

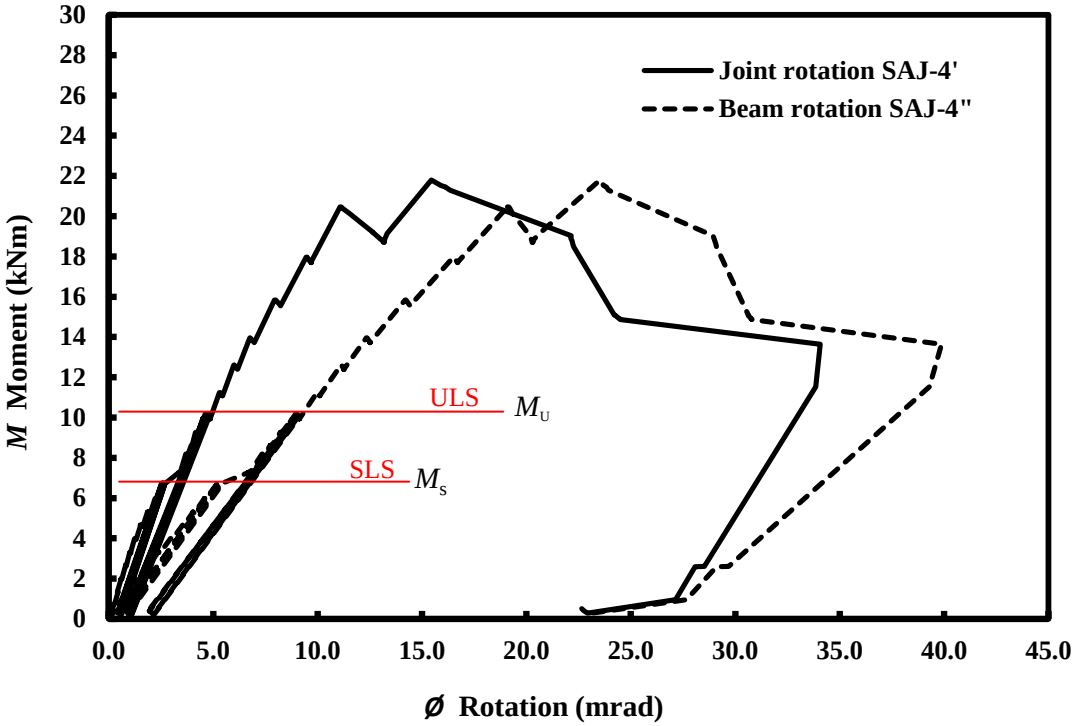

Figure 6.28. *M*-Ø curves for SAJ-4.

Figures 6.25 to 6.28 show that the *M*-Ø curves for the SAJs′ (solid line) give stiffer responses than the SAJs" (dashed line), from the beginning of the load test. It can also be seen that the curves are discontinuous, with a saw-tooth pattern, because, at each load increment, there is a reduction in moment over the five minutes at the constant deformation. The lowering in *M*, with time, shows that the joint's response is experiencing FRP viscoelastic relaxation and/or damage growth. As would be expected, the reduction in *M* becomes more prominent as ultimate failure, at M_{fail}, is approached.

In Figure 6.25, the *M*-Ø curves SAJ-1' and SAJ-1" show that non-linear behaviour in SAJ-1 started at an early load stage and the joint rotational stiffness, to compare with a desired level of practical rotational stiffness, is too low when *M* reached M_s. Figure 6.26 gives the same *M*-Ø curves for SAJ-2. It can be seen that the SAJ-2' and SAJ-2" responses stay linear up to, about, three times M_u Both SAJ-2' and SAJ-2" show a relatively high rotational stiffness for the joint. Characteristics of *M*-Ø curves for joints SAJ-3 and SAJ-4 up to M_{max} are similar, but the former joint has the lower rotational stiffness.

It can be seen from the shape at the curves in Figures 6.25 to 6.28 that nonlinear behaviour of the SAJ' and SAJ" appeared at the same *M*, or in the former started at higher value of *M*. Only for the SAJ-3' the *M*-Ø curve deviates from linearity earlier than the SAJ-3". The author cannot find a physical explanation that justifies why the SAJ-3' linearity (due to $Ø_j$) starts to go the nonlinear at a lower *M* than the SAJ-3" (due to $Ø_b$).

In the discussion to follow on the characteristics of the test results for SAJ-1 to SAJ-4, the joints are presented in the order matching the Startlink design requirements, with regards to design/required joint resistance and 'rigid' rotational stiffness. The order of presentation is therefore SAJ-2, SAJ-4, SAJ-3 and SAJ-1.

Figure 6.26 presents the *M*-Ø curves for SAJ-2, which has dowel connections with oversized clearance hole of 2-3 mm (in both members) and adhesive applied to the beam and column 'mating' surfaces. It is seen that the response remains linear until *M* is at about 24.1 kNm for both joint (SAJ-2') and beam (SAJ-2") rotations.

First audible acoustic emissions were heard when *M* was 16.5 kNm, but with no visible sign of material failure. Curve SAJ-2" starts to go non-linear for $M > 24.1$ kNm, and it is observed that failure had initiated in the bottom flange of beam, in the form of a local buckle. The flange deformation for this failure mode can (just about) be seen in the photographs of Figure 6.29(a) and 6.29(b). By increasing *M* in the post-failure region to 29.1 kNm the response of SAJ-2' remains linear and this results provide no evidence for there being joint failure on the column member. It is noteworthy to mention that 29.1 kNm is about three times higher than the design ULS moment of 10.1 kNm. No further joint rotation was applied to SAJ-2 because there was a danger of specimen instability. $\emptyset_j$ was measured to be 1.5 mrad at 29.1 kNm, and this joint rotation is about $1/15^{th}$ of $\emptyset_b$.

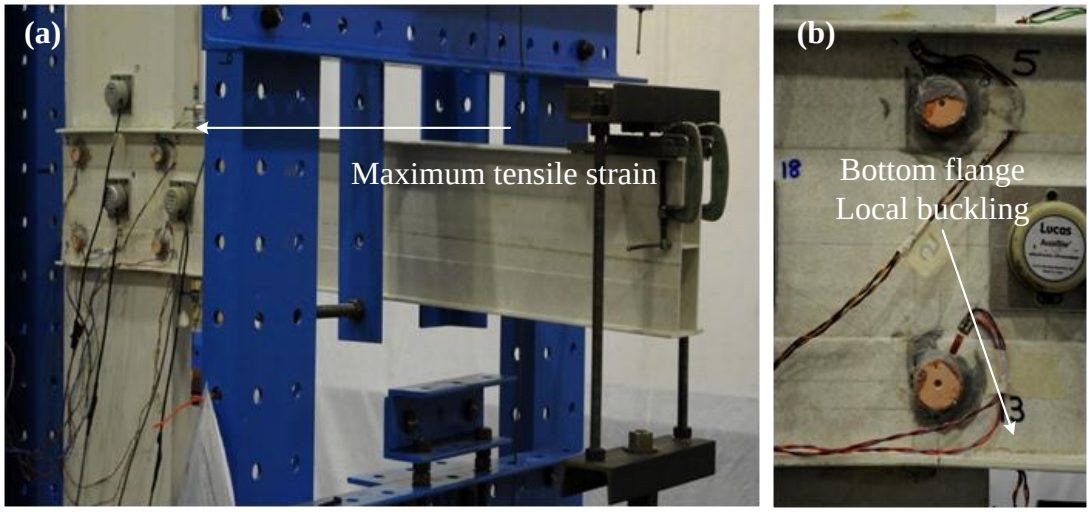

Figures 6.29. SAJ-2 failure mode; (a) whole specimen, (b) local to compression flange adjacent to the dowelling and adhesive bonding.

Figure 6.30 shows the unloading-reloading *M-Ø* curve for SAJ-2 up M_s (6.8 kNm) for joint rotation ($Ø_{j,s}$) and beam rotation ($Ø_{b,s}$), respectively. Figure 6.31 is for the same results up to the ULS moment (M_u). These curves have been extracted from the SAJ-2' and SAJ-2" curves in Figure 6.26. To highlight the results for the two designs load cases the scales on the axes in 6.30 and 6.31 are different. Cyclic loading was in the test procedure, because the 'joint' and 'beam' stiffnesses on reloading might be more representative of what will exist in the Startlink house. For both curves, the linear trend line's equation, and R^2 (or linear regression) are reported in the figure. Values of $R^2 > 0.91$ show there to be a good linear relationship. From the SLS curves in Figure 6.30 the rotational stiffnesses for the joint is 15700 kNm/rad ($S_{j,s}$) and for the beam is 1590 kNm/rad ($S_{b,s}$). These values were determined from the gradients of the linear trends of SAJ-2' and SAJ-2" up to M_s. It is found that the rotational stiffness of the joint is about ten times higher than the beam rotational stiffness. Figure 6.31, similarly, shows the *M-Ø* curves up M_u for joint rotation ($Ø_{j,u}$) and beam rotation ($Ø_{b,u}$). At the design ULS loading the rotational stiffnesses of $S_{j,u}$ and beam

$S_{b,u}$ are 18700 kNm/rad and 1560 kNm/rad, respectively. Values of rotations (($\emptyset_j$ and $\emptyset_b$) and rotational stiffness (S_j and S_b) under the SLS and ULS loading will be collated in Section 6.6 (in Tables 6.9 and 6.10), when the Startlink joints have their stiffness classified in accordance with the clauses of section 5.2.2 in Eurocode 3 (BS EN 1993-1-8:2005).

It was found that there is a negligible increase (change) in $\emptyset_j$ and $\emptyset_b$ when SAJ-2 was unloaded and reloaded and, therefore, the response can be presumed to remain linear and elastic to M_u.

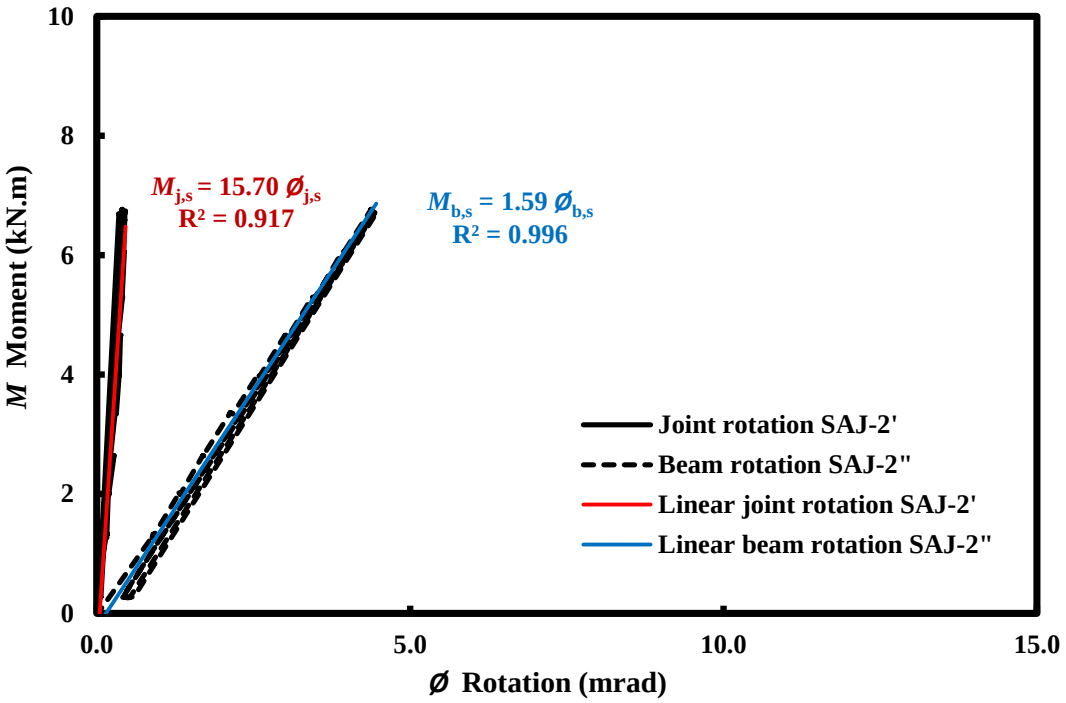

Figure 6.30. Cyclic *M*-Ø curves up to the design SLS moment for SAJ-2.

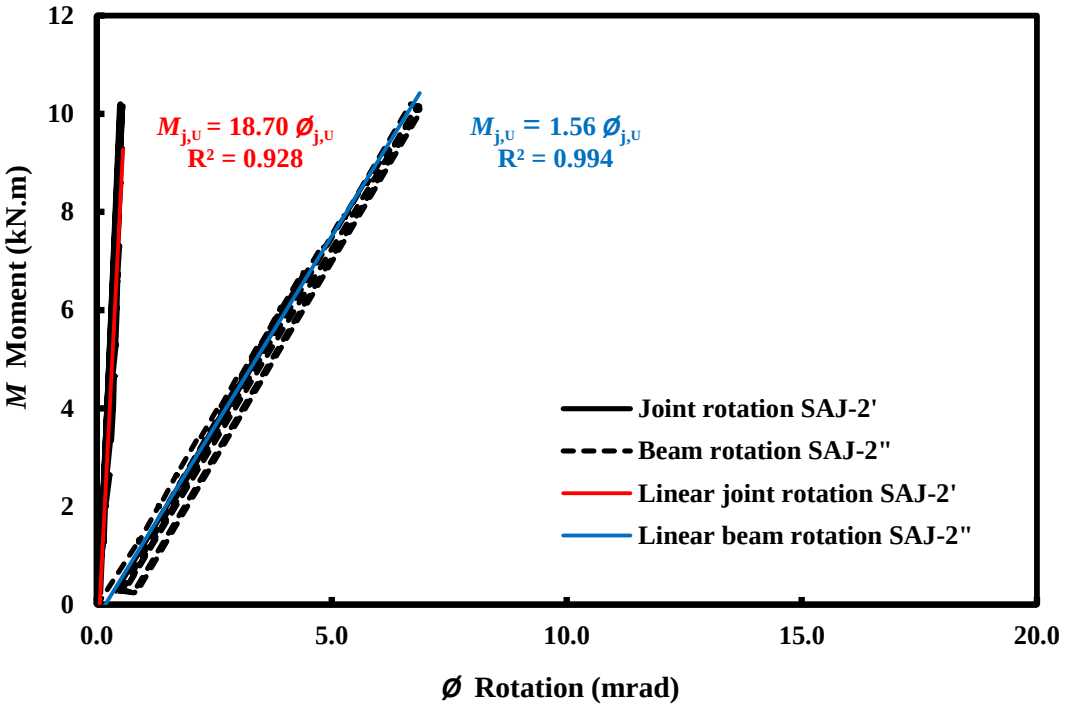

Figure 6.31. Cyclic *M*-Ø curves up to the design ULS moment for SAJ-2.

It is believed that *M* is locally transferred from the beam into stud column through the bonded connection. The dowels remain relatively unloaded until adhesive fails, which it did not. Let us assume the bonded connection has completely failed at *M* equals 29.1 kNm and the four dowels are resisting this failure joint moment. The shear force taken by each dowel is 47.3 kN (= 29100 / (4×153.7)). The first number in brackets is $M_{j,fail}$ in kNmm, the second is the number of dowels and the third is the distance from joint centre to each dowel centre. As a result the average shear stress will be 36 N/mm^2 (= (47.3×1000) / 656×2). The denominator is a 28.9 mm diameter dowel's cross-section area in mm^2 times two for double shear. Based on the design of the Stratlink frame joint the design shear strength of the FRP dowelling is 60

N/mm^2. It is important to mention that the failure joint moment of 29.1 kNm (testing ultimate failure) is about three times higher than the ULS design moment.

Figure 6.32 shows the moment-strain (M-ε) curves determined from the strain gauges (TLS, TRS, BLS and BRS) the four connection holes. The positions of gauges are seen in Figure 6.22. The axial strain recorded by these gauges was compression. It can be seen from the plots that the maximum bearing strain, when M is 29.1 kNm, is about 4000 με (or 0.4 %) and that it occurs at hole position TRS. Equivalent recorded compressive strains at TLS, BLS, and BRS are 1250 με, 800 με, and 1900 με, respectively.

Because there is a complex stress field in the region where the connection (bearing) force is transferred between the FRP dowel and the wall of beam the compressive strain for bearing failure is an unknown and unquantifiable value. It may be assumed that, at the distance of 1 mm from the hole perimeter to the centre of a strain gauge, the compressive strain will exceed 1 % before there is bearing failure. This assumption presumes that the resultant connection force is aligned with the direction of the strain gauge.

The values of bearing strain for all the dowel connections of the SAJ-2 joint indicate that the loading has effectively been transferred through the bond connection.

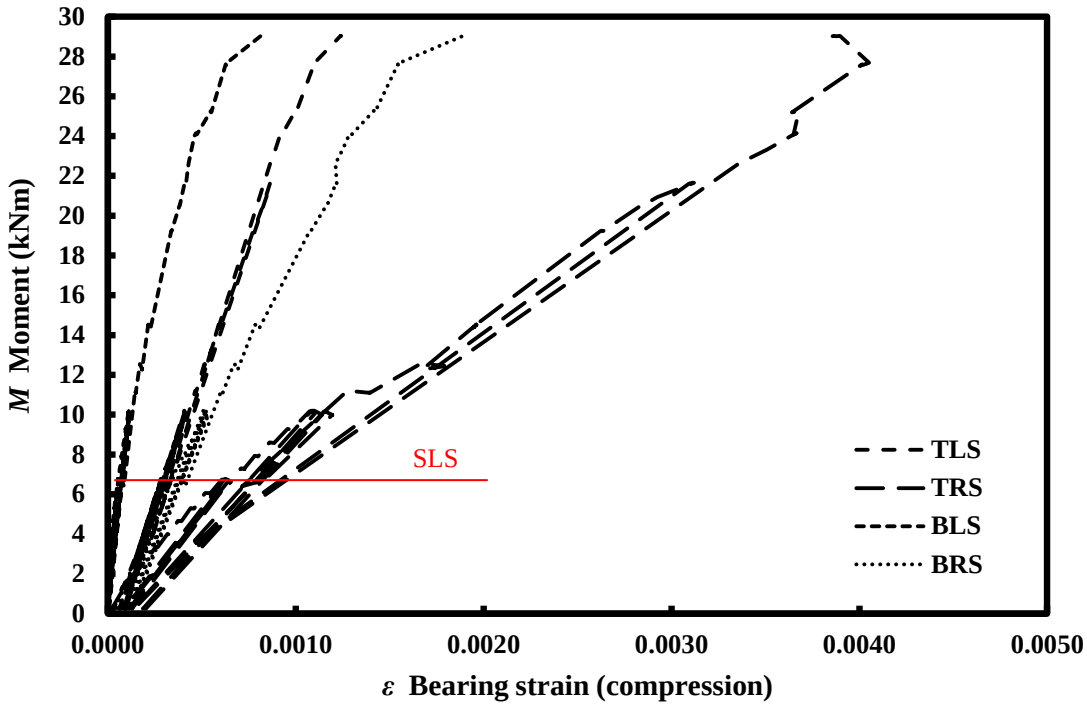

Figure 6.32. *M-ε* curves for SAJ-2.

It is acceptable to state that failure of specimen SAJ-2 is related to geometry and methods of connection, and not because of a PFRP material strength. Another piece of evidence to confirm this finding is that the joint's stiffness ($M/\emptyset_j$), remains linear to 29.1 kNm, with no discernible form of material failure.

Let's now consider the test results with specimen SAJ-4. Plotted in Figure 6.28 are the *M-Ø* curves, for the joint having geometric configuration of the tight-fit connections following drilling of holes in the Engineering Workshops at Warwick University. SAJ-4 had been fabricated to imitate the situation that the frame joint would experience with ideal tight fitting connections. This joint detailing therefore represents the stiffness and strongest that can be assembled without the addition of adhesive bonding over the area where the beam member overlaps the stud column member.

It is seen that the *M*-Ø response for both SAJ-4' and SAJ-4" remains, perfectly, linear until *M* is about 16.5 kNm. Audible acoustic emissions were then heard, without there being any visible sign of material failure. Behaviour stays, approximately, linear until *M* is 20.4 kNm, when there is adhesive bond fracture at TRN and BRN connections. It was observed that immediately after this bond failure then was, bearing failure too. As the joint lost its structural integrity and the moment transferred continually reduced progressive material failure led to excessive web deformation and curl. Bearing failure at connection TRN and the large beam deformation on the North side are shown in Figures 6.33(a) and 6.33(b), respectively. It is worth mentioning that the South wall of the beam did not experience the same amount of web deformation because the dowels, on this side, portending heads to provide high restraint against web displacement in the lateral direction.

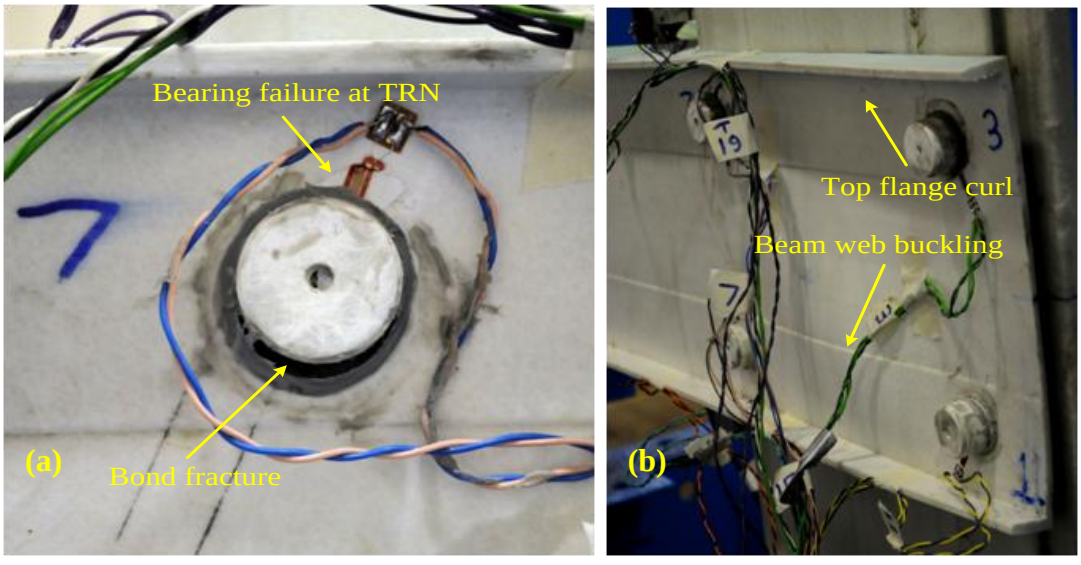

Figure 6.33. SAJ-4 failure mode: (a) bearing failure; (b) beam web local buckling.

Figures 6.34 shows the unloading-reloading *M*-Ø curves for SAJ-4 to M_s for joint rotation ($Ø_{j,s}$) and beam rotation ($Ø_{b,s}$), respectively. Figure 6.35 gives the same *M*-Ø results to M_U. These curves for three cyclic loadings have been extracted from the SAJ-4' and SAJ-4" curves in Figure 6.28. It was found that there is a negligible increase in $Ø_j$ and $Ø_b$ when SAJ-4 was unloaded and reloaded and, therefore, the response is found to have remained elastic. The R^2 values are 0.94 or higher to the linear trend lines. This shows that the rotational stiffness is fairly constant to M_U (10.1 kNm). From the curve fits in Figure 6.34 the SLS rotational stiffnesses for the joint is 2650 kNm/rad ($S_{j,s}$) and for the beam it is 1300 kNm/rad ($S_{b,s}$). Using the test results in Figure 6.35, the ULS rotational stiffnesses for $S_{j,U}$ and $S_{b,U}$ are 2190 kNm/rad and 1150 kNm/rad, respectively. Values for $Ø_{j,U}$, $Ø_{b,U}$, $S_{j,U}$ and $S_{b,U}$ will be collated in Section 6.6 and Tables 6.9 and 6.10 when joint SAJ-4 stiffness is classified for joint.

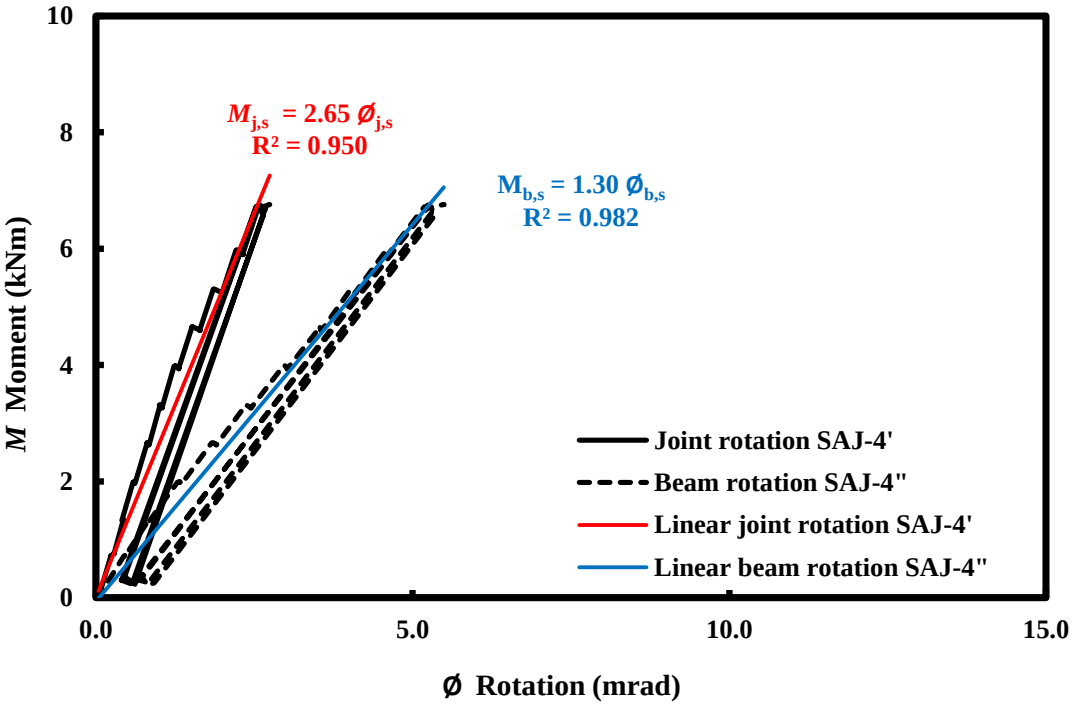

Figure 6.34. Cyclic *M*-Ø curves up to the design SLS moment for SAJ-4.

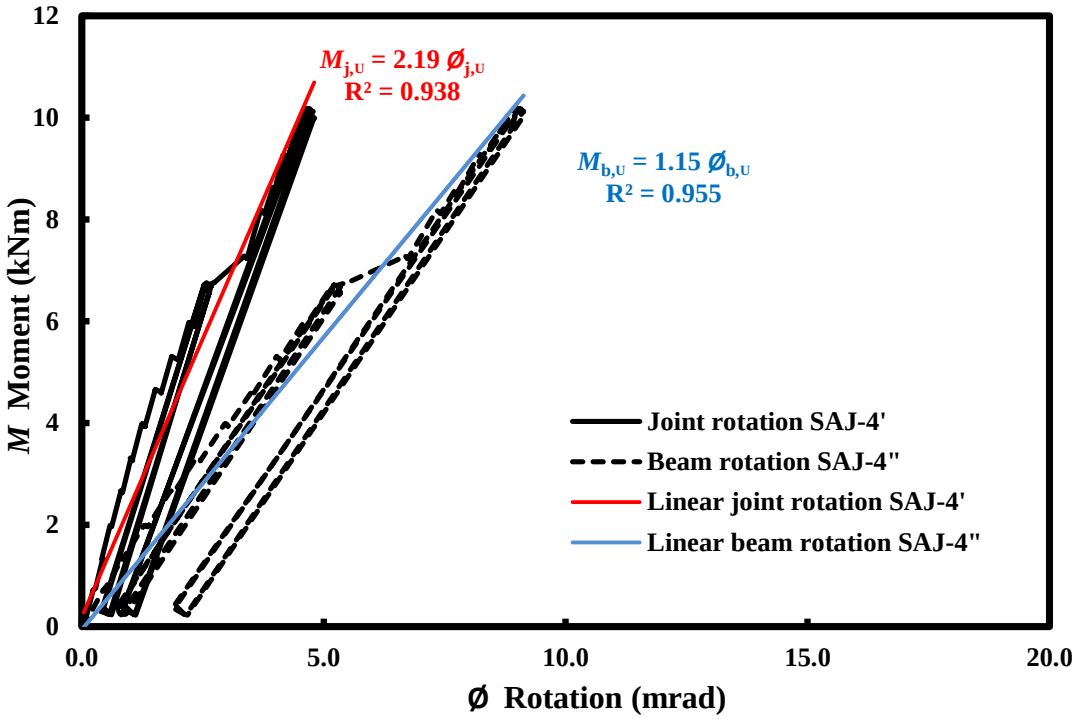

Figure 6.35. Cyclic *M*-Ø curves up to the design ULS moment for SAJ-4.

Figure 6.36 presents the moment-strain (*M*-ε) curves at the four connections labelled TLS, TRS, BLS and BRS. The positions of the four gauges are seen in Figure 6.22. It is noted that the *M*-ε curves for BLS and BRS coincide; they are the same. It is observed that the maximum bearing strain occurs at gauge TRS when *M* is 20.4 kNm. It is important to mention that, although, full bearing failure was observed at TRN and BRN the highest bearing strains were found at the TRS and BRS. The author cannot find a sound physical explanation why bearing failure is not associated with the highest measured bearing strains. From the TRS curve in Figure 6.36 its bearing strain, at *M* equals 20.4 kNm is 10300 με (or 1 %). Other maximum bearing strains recorded at TLS, BLS, and BRS are 3800 με, 5100 με and 5300 με, respectively.

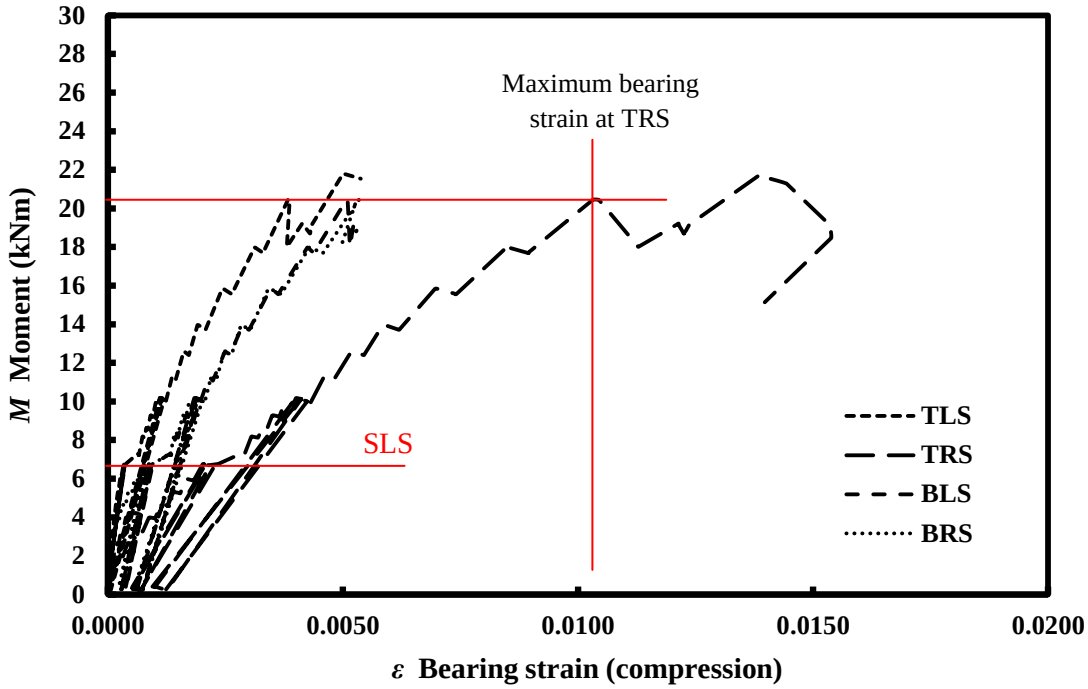

Figure 6.36. *M*-ε curves for SAJ-4.

Comparing the values of the bearing strain from gauges TLS, TRS, BLS and BRS for joints SAJ-4 (Figure 6.36) and SAJ-2 (Figure 6.32) it is found that, at the same *M*, the strains in SAJ-4 are about 3 to 6 times higher. This finding again indicates that the joint actions in SAJ-2 have effectively been transferred through the adhesively bonded connection.

The author believes that audible acoustic emissions (at about 16.5 kNm) might possibly be related to the initiation of bearing failure in the stud column walls contact. There are two reasons for this observation: Firstly, the stud's wall has a nominal thickness of 4.5 mm, which is 0.5 mm lower than for the beam's web. Because the same connection force is taken by both wall thicknesses failure happens in the stud's walls before the beam's webs. Secondly, there is a significant correlation between the value, about 16.5 kNm, which the audible acoustic emissions

were heard in the SAJ-4 testing and the dowel bearing strength that was obtained in a pilot study on the stud column dowel connection.

In 2011 the author conducted a series of tests, as a preliminary investigation, to determine the dowel bearing strengths of the stud column section. Details of specimens, test methodology and the test results are presented in Appendix A. From these test results the lowest failure load in the transverse direction of 26 kN can be taken as the bearing resistance of stud column in the Startlink frame connection (at the transverse orientation for the connection force). Using the joint geometry in Figure 6.11 this bearing resistance translates to a maximum joint moment, given by estimated to be 4 × 0.154 (m) × 26 (kN) = 16 kNm. The first number is for the four dowel connections, the second is the lever arm distance (given by 0.3074/2 m) from the centre of rotation, and the third number is for the lower bound connection force when failure is by bearing. This estimate of the joint moment for bearing correlation with failure has a high the M of 16.5 kNm at which (first) audible acoustic emissions were heard.

Another finding from testing joint SAJ-4 is the influence of using a structural adhesive to partially fill the voiding from the 2 mm gap between the joint members. This gap can be seen in Figure 6.10. It is observed that the presence of an amount of adhesive around the holes, and between the inner and outer surfaces of beam's webs and the stud walls, can change the connection location for bearing failure. By applying a liberal amount of adhesive, Figure 6.37(a) and 6.37(b) show that there can be an area of bonding around each hole perimeter. The minimum area has diameter of about 1.2 times the hole diameter (30 mm) and the maximum area has a diameter

of at least 2 times the hole diameter. It was found that, at dowel connections with the minimal bonding that the stud, experienced with its smaller wall thickness, bearing failure first. As seen in Figure 6.8(a) and 6.8(b) the beam web has a nominal thickness of 5 mm, whereas the stud wall has a nominal thickness of 4.5 mm. However, as discussed in process of the SAJ-4's failure, by applying the load to the joint, the failure was firstly initiated by dowel plug failure. The author believes that until the adhesive plug fails there is no deterioration in the dowel connections. It is obvious that once this 2 mm thick layer of the adhesive debonds from one of the members, it remains firmly attached to the another member. As a result one of the two walls will experience an effective increase in thickness, and thereby the FRP wall experiences a reduced mean bearing stress. Figures 6.37(a) and 6.37(b) show the South and North sides of SAJ-4 after dismantling, post testing, to inspect the failure.

Figure 6.37(a) shows that the connections at TRS and BRS in stud column had failed in bearing. It can be seen that around these two holes less adhesive had been applied. Consequently they had relatively a higher mean bearing stress than at connections TLS and TRS. No bearing failure is observed at the other six holes. On the North side, see Figure 6.37(b), the more severe stress field for bearing failure belongs to TRN and BRN in the beam's web. Again, this finding is because debonding failure changes the effective size of the bearing area. It can be seen that around the stud column holes there is a layer of bonding that has increased the connections bearing area.

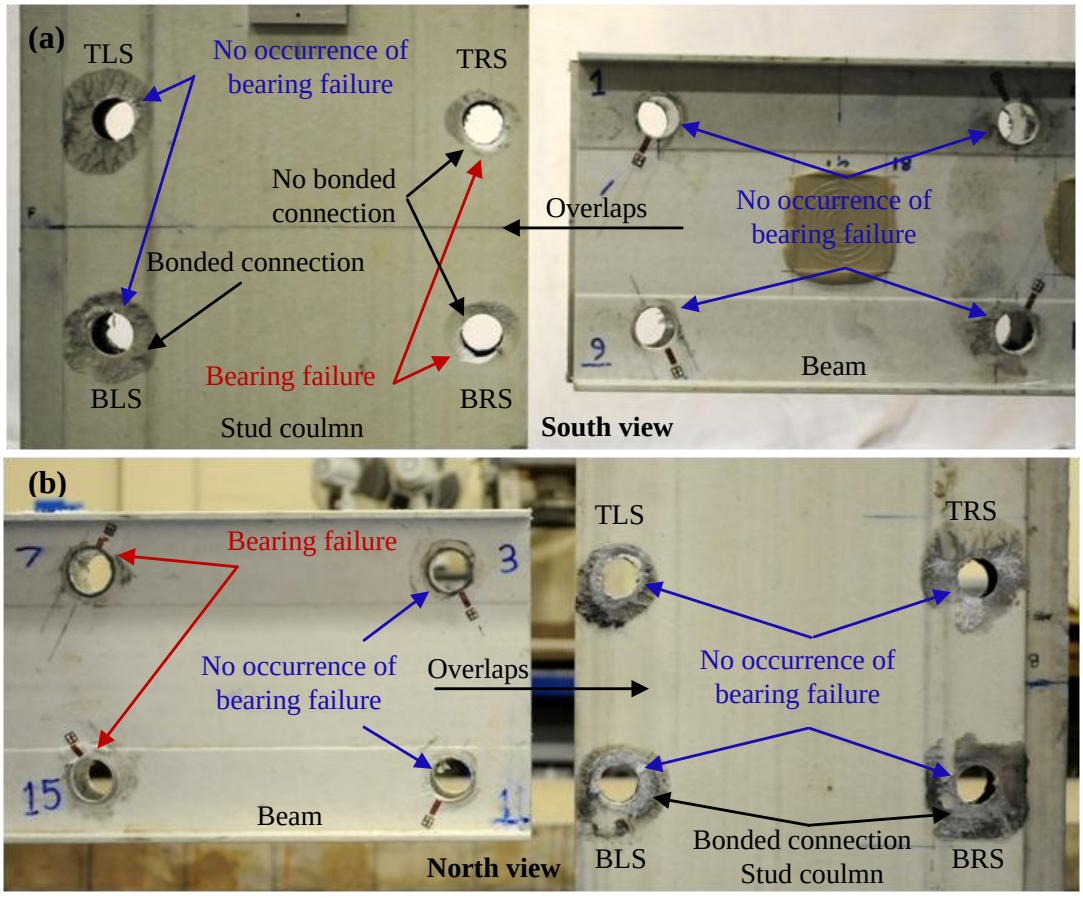

Figure 6.37. SAJ-4 debonding and bearing failures: (a) South view; (b) North view

As stated in section 6.2 the components and geometric configuration for joint SAJ-3 are the same for the SAJ-4. The differences are holes diameter tolerances and the precision of the positions for the hole centres in joint SAJ-3 (see Tables 6.4 and 6.5). The hole tolerances for beam member is in the range of 31.13 to 31.24 and in the column member is in the range of 31.11 to 31.86. In SAJ-3 the holes are not positioning at the exact and precise locations and subsequently the centre-to-centre holes distances are not the same. This imprecision is because the connection holes for SAJ-3 (and for all members for the Startlink demonstrator house) were drilled using a hand-held drill by an OCS plastics Ltd worker. The horizontal centre-to-centre holes distances for beam member in SAJ-3 are between 265.1 mm and 266.2

mm and vertical distances are between 154.2 mm to 155.2 mm. The equivalent variations for stud column member are 264.9 mm to 266.4 mm and 152.5 mm to 155.0 mm. These variations in the positions of the hole centres correspond with the tolerances that will exist in the fabrication of Startlink frame joints. Joint SAJ-3 is most representative of the details of the SLBS frame joints executed, on site, when the demonstrator house is built at Borne, Lincolnshire.

It is important to mention that the tolerances on hole positioning, hole diameter and dowel diameter will produce non-uniformed connection forces in the four dowel connections, and subsequently, non-constant localised stiffnesses. As a result it can be expected that there will be a premature bearing failure at one of four connections. Moreover, the effect of tolerances can cause a higher joint flexibility as the two members at one or more connections do not, initially, have full dowel contact. Joint SAJ-3 can possess 'pseudo' tight fitting connections.

Figures 6.38 and 6.39 show the ε-$\emptyset$ curves using the joint rotation $\emptyset_j$ for the SAJ-3 and SAJ-4. From the SAJ-3 curves plotted in Figure 6.38 it can be seen that, for connections TLS and BLS, they show a bilinear behaviour, whereas TRS and BRS the response stay linear. The initial linear part to the TLS and BLS curves ends at 11 mrad; for higher $\emptyset_j$ the 'bearing' strain increased at a higher rate. The author believed that for $\emptyset_j$ below 11 mrad these two dowels transfer their connection force through the adhesive bonding, which was introduced to fill the clearance hole voiding. For $\emptyset_j$ > 11 mrad the two dowels start to contact, directly, with the perimeters of the holes (in beam and column) and the increase in localised (bearing) stiffness explains why strain increased faster. It is observed that the change in

gradient of a ε-$\emptyset$ curve shows that the dowel made 'pseudo' tight fitting connection and, when started to contact FRP. A second finding is that adhesive bonding alone will not provide the same magnitude of stiffness opposing the dowel deformation as FRP material does. It is concluded that tolerances influencing joint assembly can lead to higher joint flexibility, even if voiding is removed by application of structural adhesive. The linear response of the ε-$\emptyset$ curves for TRS and BRS connections indicates that the dowel was making contact with FRP material from the beginning of the loading procedure.

Plotted in Figure 6.39 are the ε-$\emptyset$ results for the four connections in joint SAJ-4. It can be seen that the curves all show a fairly linear response. This was an expected finding because SAJ-4 has tight fitting dowels such that FRP on FRP contact at all eight contact surfaces was (virtually) guaranteed.

As Figure 6.27 shows the characteristics of the moment-rotation curves for SAJ-3 are similar to those for SAJ-4. As expected the main difference with SAJ-3 are a lower rotational stiffness and a lower failure moment because of the 'premature' bearing failure. M-$\emptyset$ curves in Figure 6.27 show that SAJ-3' and SAJ-3" remained linear to M is 10.1 kNm and 14.5 kNm, respectively. Both SAJ-3' and SAJ-3" curves then show non-linearity to 16.9 kNm, when final failure (testing ultimate failure) occurred. It can be seen that there is a falling branch response for further joint deformation.

Audible acoustic emissions could be just heard when M was 13.2 kNm. There was no visible sign of failure. It is believed that this is evidence for the start to debonding

of the adhesive connection around a hole. Louder acoustic emissions were heard when *M* reached 14.5 kNm, to signal the initiation of failure, first by bond fracture at connection TRN, followed by adhesive failures at BRN and TRS and then proceeded by bearing failure, in the same, at these three connections. Compared to SAJ-4, the bond fracture in specimen SAJ-3 was initiated at a lower joint moment. The reason for this result might be related to the variable quantity (a liberal amount) of adhesive which had been placed around the hole perimeters and which had ended-up, between the inner side of beam webs and stud walls. Testing ultimate failure occurred when *M* was 16.9 kNm as the joint lost its structural integrity.

Failure processes, in order, are shown in Figures 6.40(a) to 6.40(c). From photograph in Figure 6.40(a) bond fracture can be seen at TRN, whilst there is no any sign of this failure at BRN. Figure 6.40(b) shows the next stage of failure when bond fracture and bearing failure at BRN occurs simultaneously. Bearing failure at TRS is shown in Figure 6.40(c).

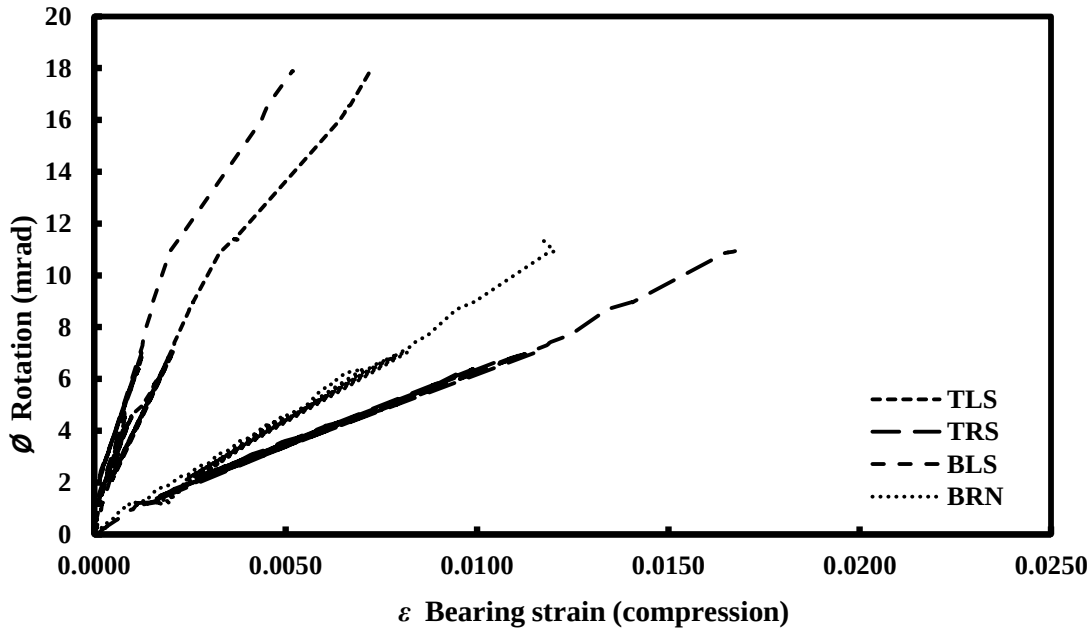

Figures 6.38. *ε*-*Ø* curves for the SAJ-3.

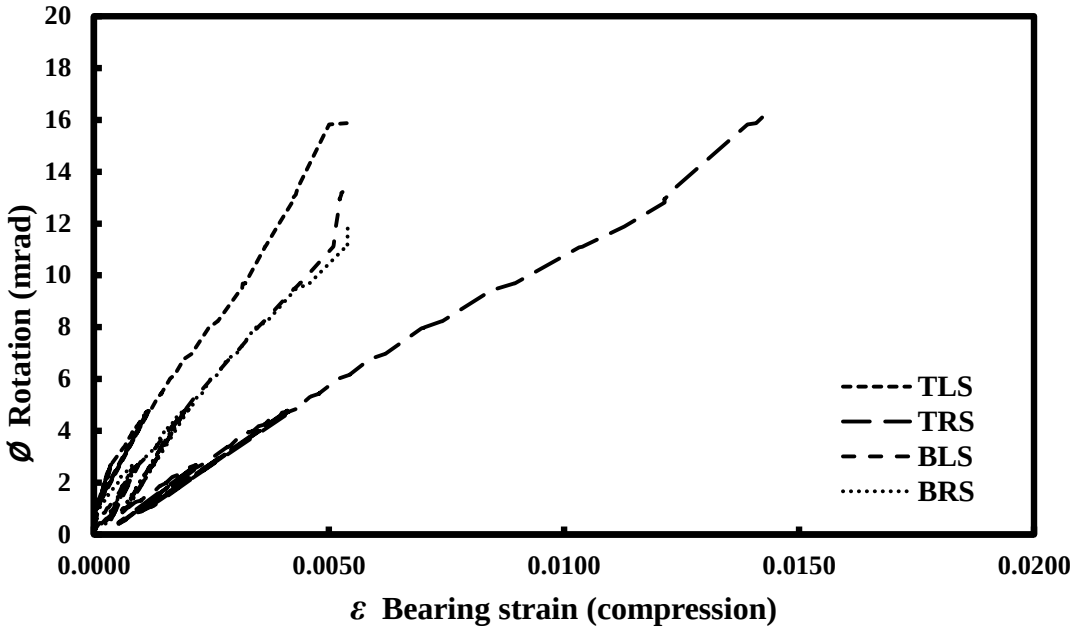

Figures 6.39. ε-$\emptyset$ curves for the SAJ-4.

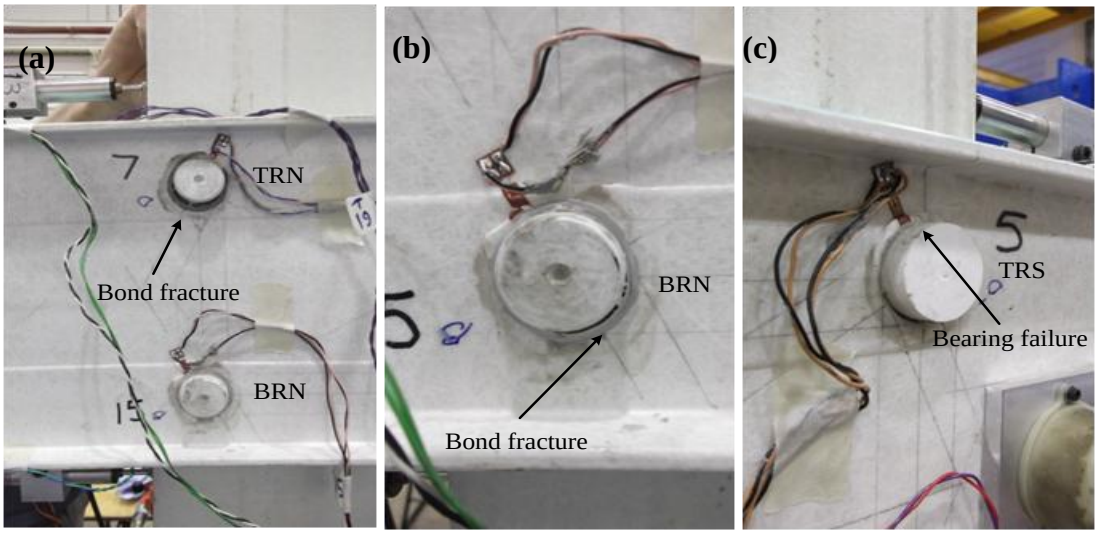

Figure 6.40. SAJ-3 failure mode: (a) bond fracture; (b) bond fracture and bearing failure; (c) bearing failure.

Figures 6.41(a) and 6.41(b) show the SAJ-3 connection from South side and North side, respectively, after dismantling the joint specimen to inspect failure at the holes. Figure 6.41(a) shows that connection TRS in beam member has bearing failure, whereas there is no failure on the stud column side. For bearing failure in the stud

the figure shows it is at BRS. No sign of bearing failure is seen at the other six holes. For the North side, the photograph in Figure 6.41(b) shows that at TRS and BRS there is bearing failure in both members.

From the distribution of hole failures in SAJ-4 and SAJ-3 (Figures 6.37 and 6.41), it can be seen that there are an anti-symmetric failure pattern for the LS and RS connections. At connections TLS and BLS there was no bond fracture or/and no bearing failure whereas, bearing failure does exist at TRS and BRS. The author has not found an acceptable physical explanation for this result of connections.

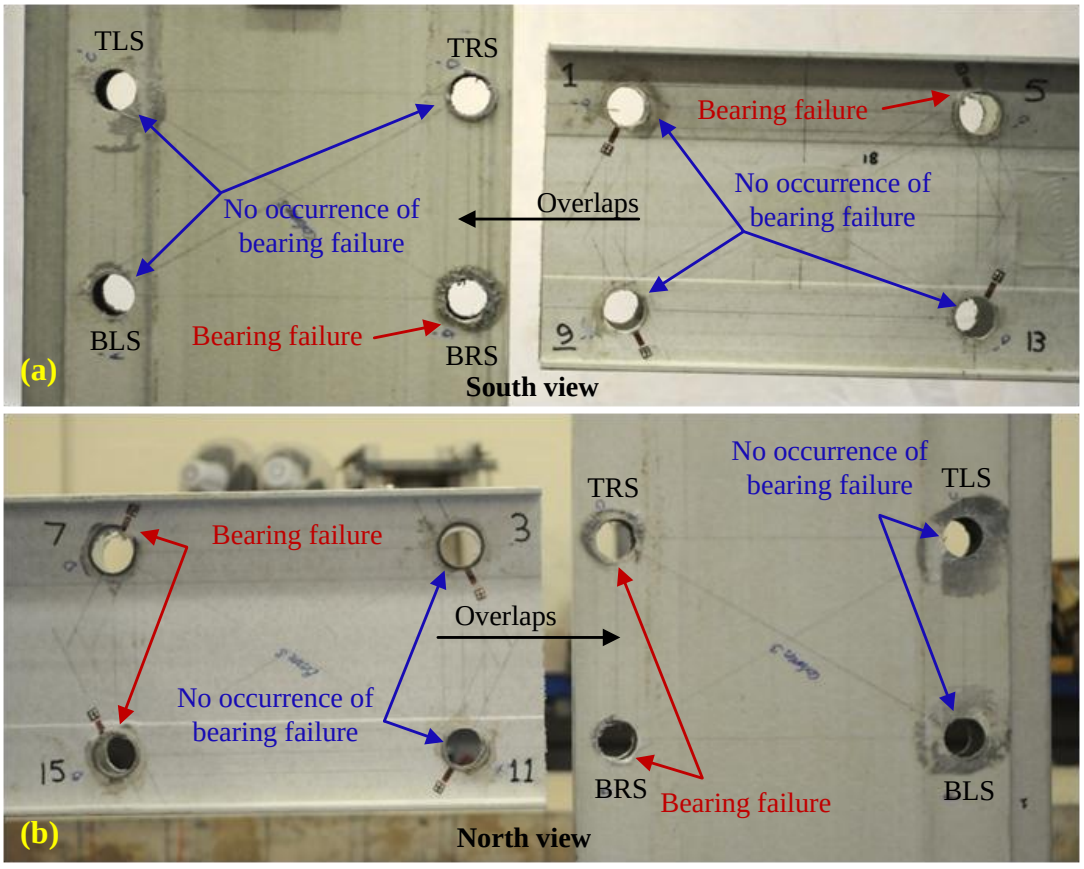

Figure 6.41. SAJ-3 bearing failures: (a) South view; (b) North view.

Figures 6.42 shows the unloading-reloading *M*-Ø curves for SAJ-3 up to M_s, for both $Ø_{j,s}$ and $Ø_{b,s}$. Figure 6.43 presents the same test results to M_U. For both curves a linear trend line, equation, and its R^2 value were obtained. From the curve fits in Figure 6.42 the SLS rotational stiffnesses is 1560 kNm/rad ($S_{j,s}$) and for the beam is 950 kNm/rad ($S_{b,s}$). From Figure 6.43, the rotational stiffnesses are 1480 kNm/rad ($S_{j,U}$) and 910 kNm/rad ($S_{b,U}$), respectively. Values for $Ø_{j,U}$, $Ø_{b,U}$, $S_{j,U}$ and $S_{b,U}$ will be used in Section 6.6 when the four SAJ joints have their stiffness classified. It was found that there is a negligible increase in $Ø_j$ and $Ø_b$ when SAJ-3 was unloaded and reloaded and so it is found that to M_U the joint's response remain elastic and without a reduction.

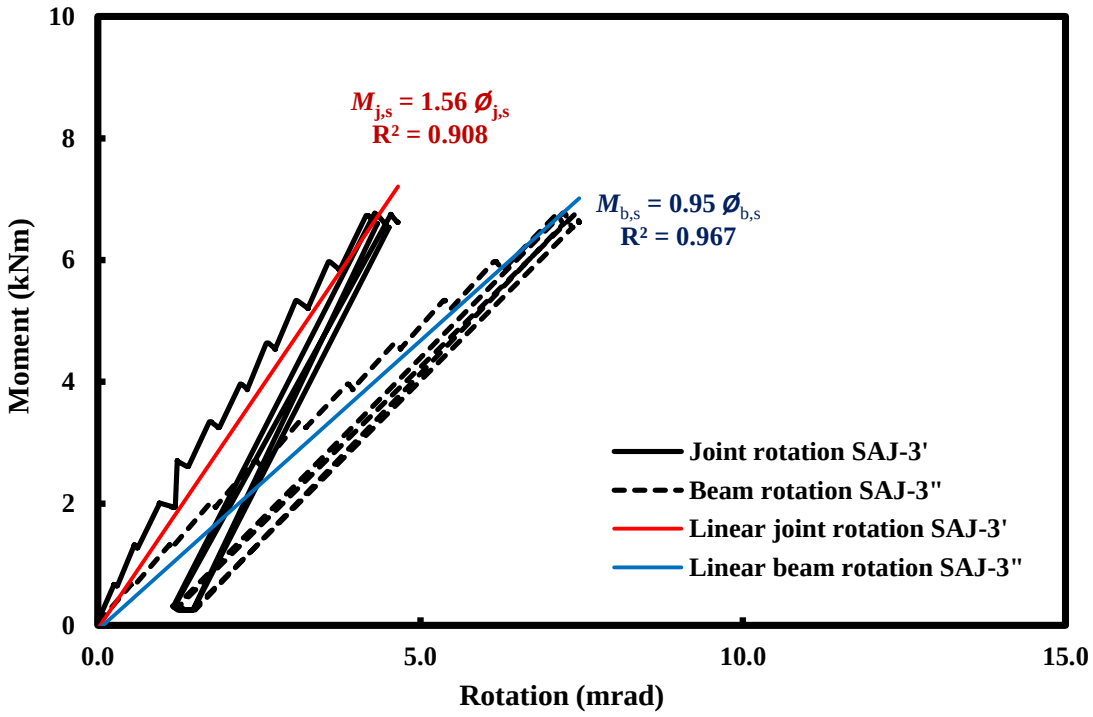

Figure 6.42. Cyclic *M*-Ø curves for SAJ-3 up to the design SLS moment of 6.8 kNm.

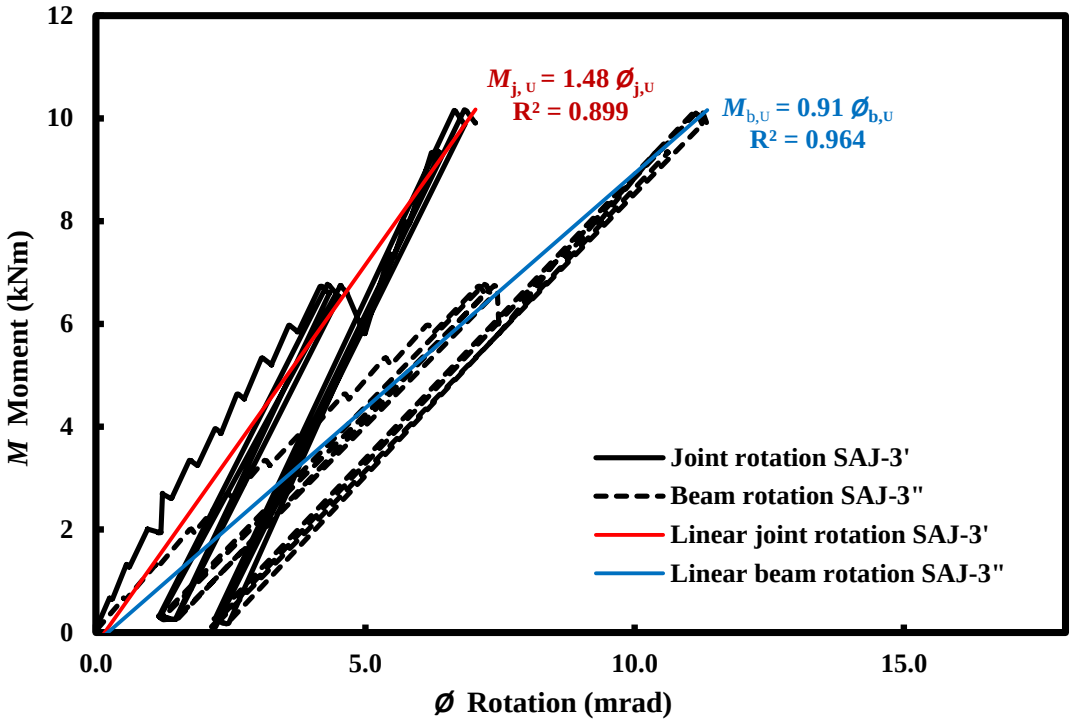

Figure 6.43. Cyclic *M*-Ø curves for SAJ-3up to the design ULS moment of 10.1 kNm.

Plotted in Figure 6.44 are the *M*-ε curves for SAJ-3 at the four of connections holes using strain gauges TLS, TRS, BLS and BRS. It was found that the maximum bearing failure occurred at connection TRS, when *M* is 14.5 kNm. As can be seen from Figure 6.44 the bearing strain at TRS position is 16000 με (or 1.6 %). Equivalent recorded bearing strains at TLS, BLS, and BRS are 6800 με, 2000 με and 12000 με, respectively.

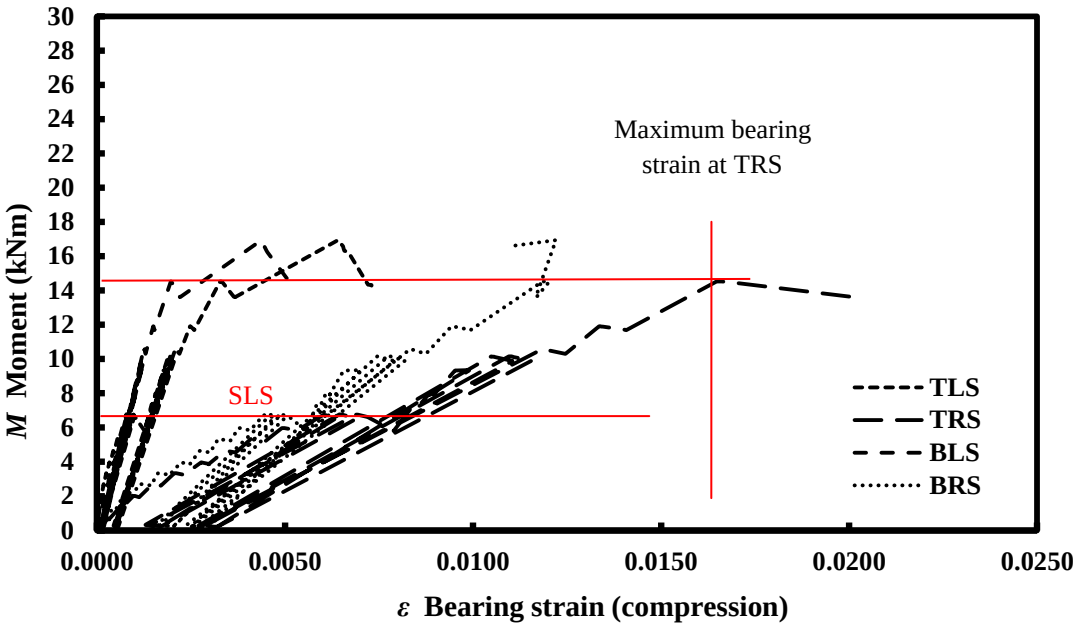

Figure 6.44. *M*-ε curves for SAJ-3.

Figure 6.45 present two *M*-Ø curves for SAJ'-1 and SAJ"-1. They were constructed using the results in Figure 6.25 to highlight the data to the two design load cases for M_s and M_u. SAJ-1 was fabricated with oversized clearance hole of 2-3 mm (in both members) and bonding to dowels to fill the voiding. Details of the SAJ-1 specimen are given in Section 6.2.

The *M*-Ø curves from SAJ-1 have very different characteristics to those from specimens SAJ-2 (see Figure 6.26), SAJ-3 (see Figure 6.27) and SAJ-4 (see Figure 6.28). The moment-rotation responses of SAJ-1' and SAJ-1" show the following three stages:

1. An initial linear behaviour;
2. Deviation from linearity when *M* is 3.4 kNm (this corresponds to only 0.5 M_s). There was continual progressive failure of the adhesive layers between dowels and members. The moment during this second stage stayed fairly constant, at 4

kNm (and as can be seen in Figure 6.45 *M* was reducing rapidly with time (5 minutes pre load step) due to 'creep-like' deformation). At the end of the secondary stage $\emptyset_j$ (SAJ-1') is 8.1 mrad and $\emptyset_b$ (SAJ"-1) is 12.2 mrad; the secant joint rotational stiffness is much lower than in the first stage.

3. During the third stage the joint became stiffer again and there was a rapid increase in *M* to 11.9 kNm, when ultimate failure occurred at a moment just above M_U 10.1 kNm. It is believed that this joint response is due to a change in stiffness when full contact is established between dowels and members. At the end of the third stage the maximum rotation for $\emptyset_j$ and $\emptyset_b$ are 16.1 mrad and 23.5 mad.

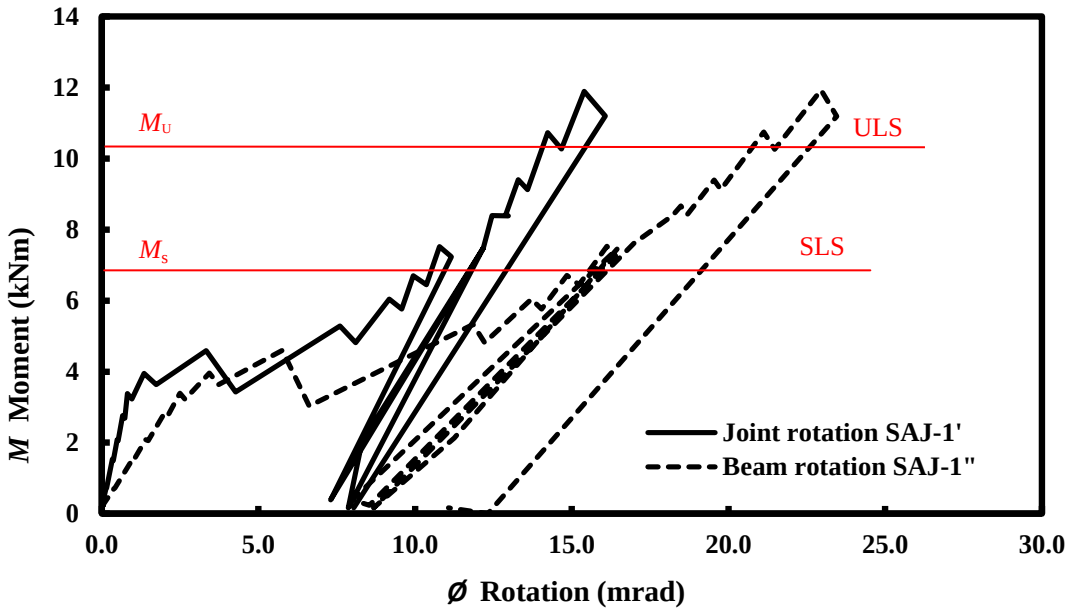

Figure 6.45. *M*-Ø curves for SAJ-1

Audible acoustic emissions were heard when *M* was 4.6 kNm. There was no visible sign of material failure. Initiation of irreversible damage was by bond fracture at TRS, TRN, BRS and BRN when *M* was 10.2 kNm. This was, simultaneously, signalled by the author hearing much louder acoustic emissions. Final failure (testing ultimate failure) in the form of excessive flange curling and web flexural

deformation on the North side of the beam was observed when M attained 11.9 kNm. The failure process of joint SAJ-1 is shown in Figures 6.46(a) and 6.46(b).

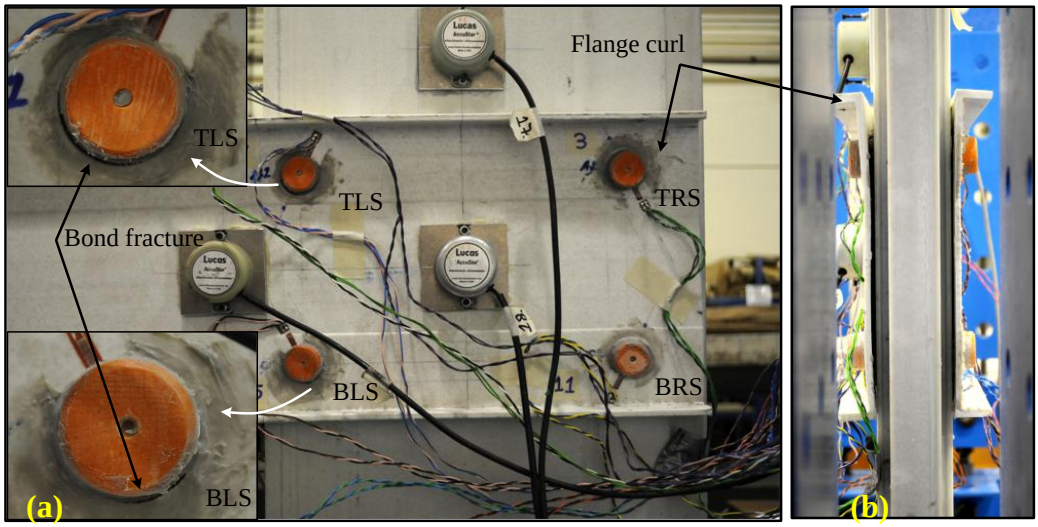

Figure 6.46. SAJ-1 failure mode: (a) bond fracture; (b) flange curl.

Figures 6.47 shows the unloading-reloading M-$\emptyset$ curves for joint SAJ-1 up to M_s for both $\emptyset_{j,s}$ and $\emptyset_{b,s}$. Figure 6.48 presents the same results up to M_u. For both curves a linear trend line, equation, and its R^2 value are obtained. From the curve fits in Figure 6.47 the SLS rotational stiffnesses is 410 kNm/rad ($S_{j,s}$) and for the beam is 330 kNm/rad ($S_{b,s}$). From Figure 6.48, the rotational stiffnesses are 530 kNm/rad ($S_{j,u}$) and 400 kNm/rad ($S_{b,u}$), respectively. Values for $\emptyset_{j,u}$, $\emptyset_{b,u}$, $S_{j,u}$ and $S_{b,u}$ will be used in Section 6.6 when rotational stiffness of joint SAJ-1 will be classified. It was found that there is permanent joint rotation when SAJ-1 was unloaded and reloaded to M_s. As seen in Figure 6.47 it is about 8 mrad for both both $\emptyset_j$ and $\emptyset_b$. The curves show the unloading-reloading joint response to be reasonably linear and to have, approximately, elastic behaviour during cyclic loading. No cyclic loading up to M_u was possible because joint SAJ-1 had failed.

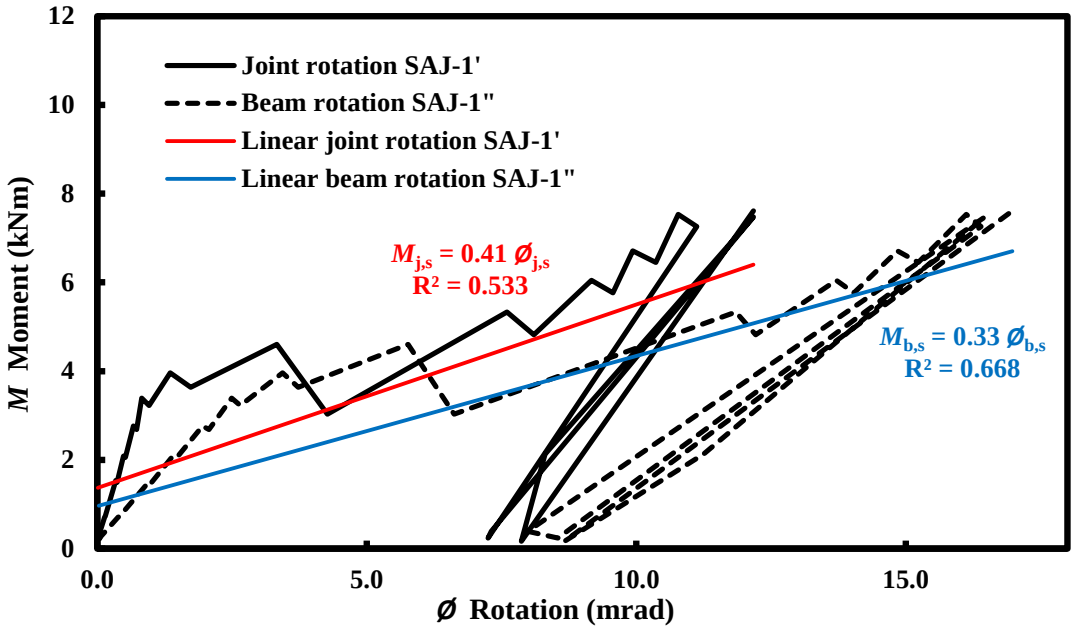

Figure 6.47. Cyclic *M*-Ø curves for SAJ-1 up to the design SLS moment of 6.8 kNm.

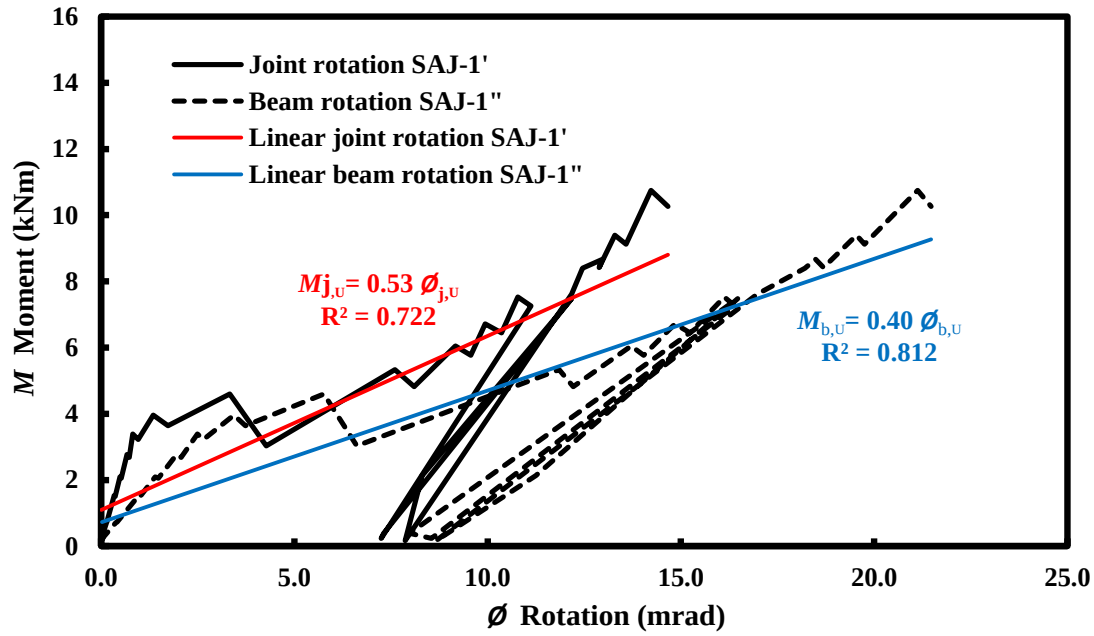

Figure 6.48. *M*-Ø curves for SAJ-1 up to the design ULS moment of 10.1 kNm.

6.6 SAJ Properties and Classification

Presented in Table 6.10 and 6.11 are measured joint properties from SAJ-1 to SAJ-4 using joint rotation Ø$_j$ and beam rotation Ø$_b$. They are presented in the order

matching the Startlink design requirements with regards to design/required joint resistance and 'rigid' rotational stiffness.

In the two tables column (1) gives the specimen label (with specimen number). Initial joint properties are given in columns (2) to (4), and are represented by initial moment ($M_{j,int}$), initial rotation ($\emptyset_{j,int}$) and initial (secant) stiffness ($S_{j,int} = M_{j,int} / \emptyset_{j,int}$). The initial values of $M_{j,int}$ and $\emptyset_{j,int}$ are from recorded data during the loading procedure over the M increments of 0.66 kNm to 1 kNm. The joint properties of $\emptyset_{j,s}$ and $S_{j,s}$ (the secant stiffness at SLS) with corresponding moment $M_{j,s}$ (6.8 kNm) are reported in columns (6) and (7) respectively. Similarly, $\emptyset_{j,u}$ and $S_{j,u}$ under ULS loading with corresponding moment $M_{j,u}$ (10.1 kNm) are given in columns (9) to (10). The values of $S_{j,s}$ and $S_{j,u}$ are the secant stiffnesses at the SLS and ULS, taken from curves plotted in Figures 6.30, 6.31, 6.35, 6.36, 6.42, 6.43, 6.47 and 6.48. Columns (5), (8) and (11) in Table 6.10 report values for $K_{j,int}$, $K_{j,s}$ and $K_{j,u}$. These non-dimensional stiffnesses are obtained by dividing the joint's rotational stiffness of $S_{j,ini}$, $S_{j,s}$ and $S_{j,u}$ by the flexural stiffness of beam (E_bI_b/L_b). Three beam parameters (E_b, I_b and L_b) were given in Section 6.1. The equivalent values for K_b are given in Table 6.11 on dividing the beam's rotational stiffness of $S_{b,ini}$, $S_{b,s}$ and $S_{b,u}$ by E_bI_b/L_b. Based on the design of the Startlink frame (Kendall, 2010), E_bI_b/L_b is 262 kNm. Reported in columns (12) and (13) are the maximum moment (M_{max}) and corresponding maximum rotation ($\emptyset_{max}$). These values are referred to the maximum M and maximum $\emptyset$ which the response of SAJ' and SAJ" curves stay linear. The last column (14) is used to list the moment for final testing ultimate failure (M_{fail}).

Table 6.10. SAJ′s properties from joint rotation $\emptyset_j$.

Specimen (1)	$M_{j,int}$ (kN m) (2)	$\emptyset_{j,int}$ (mrad) (3)	$S_{j,int} = M_{j,int} / \emptyset_{j,int}$ kN m/rad (4)	$K_{j,int}$ (5)	$\emptyset_{j,s}$ (mrad) (6)	$S_{j,s} = M_s / \emptyset_{j,s}$ kN m/rad (7)	$K_{j,s}$ (8)	$\emptyset_{j,U}$ (mrad) (9)	$S_{j,U} = M_U / \emptyset_{j,U}$ kN m/rad (10)	$K_{j,U}$ (11)	$M_{j,max}$ (kN m) (12)	$\emptyset_{j,max}$ (mrad) (13)	$M_{j,fail}$ (kN m) (14)
SAJ-2′	1.34	0.2	9000	34	0.4	15700	60	0.5	18700	71	29.1	1.5	29.1
SAJ-4′	1.33	0.5	2950	11	2.6	2650	10	4.7	2190	8	20.4	11.2	20.4
SAJ-3′	1.33	0.6	2300	9	4.2	1560	6	6.8	1480	6	10.2	6.7	16.9
SAJ-1′	1.45	0.3	4260	**16**	9.2	410	**2**	13.7	530	2	3.4	0.8	11.9

Table 6.11. SAJ″s properties from beam rotation $\emptyset_b$.

Specimen (1)	$M_{j,int}$ (kN m) (2)	$\emptyset_{b,int}$ (mrad) (3)	$S_{b,int} = M_{j,int} / \emptyset_{b,int}$ kN m/rad (4)	$K_{b,int}$ (5)	$\emptyset_{b,s}$ (mrad) (6)	$S_{b,s} = M_s / \emptyset_{b,s}$ kN m/rad (7)	$K_{b,s}$ (8)	$\emptyset_{b,U}$ (mrad) (9)	$S_{b,U} = M_U / \emptyset_{b,U}$ kN m/rad (10)	$K_{b,U}$ (11)	$M_{b,max}$ (kN m) (12)	$\emptyset_{b,max}$ (mrad) (13)	$M_{b,fail}$ (kN m) (14)
SAJ-2″	1.34	0.9	1490	6	4.4	1590	6	6.8	1560	6	24.1	17.0	29.1
SAJ-4″	1.33	0.9	1550	**6**	5.4	1300	5	9.1	1150	4	20.4	19.2	20.4
SAJ-3″	1.33	1.1	1110	5	7.1	950	4	11.2	910	3	14.5	16.1	16.9
SAJ-1″	1.45	1.0	1450	6	14.9	330	**1**	20.3	400	2	3.4	2.5	11.9

Notes: M_s is 6.8 kN m and M_U is 10.1 kN m.

From the M_{fail} results, given in column (14) of Table 6.10 or 6.11 it is found that testing ultimate moment for joints SAJ-2, SAJ-4, SAJ-3 and SAJ-1 is in excess of the ULS design moment (M_U) of 10.1 kNm. M_{fail} is 29.1 kNm, 20.4 kNm, 16.9 kNm, and 11.9 kNm, respectively.

Joint rotational stiffness results for SAJ-2' given in columns (4), (7) and (10) of Table 6.10 are 9000 kNm/rad for $S_{j,int}$, 15700 kNm/rad for $S_{j,s}$ and 18700 kNm/rad for $S_{j,U}$. The equivalent results for the beam rotational stiffness, given in Table 6.11, are 1490 kNm/rad for $S_{b,int}$, 1590 kNm/rad for $S_{b,s}$ and 1560 kN m/rad for $S_{b,U}$. Comparing the value of rotational stiffness for the joint and beam, it is found that the flexibility in the latter cases are about 6 times to 12 times higher than the former.

Reported values of $K_{j,int}$, $K_{j,s}$ and $K_{j,U}$ in columns 5, 8 and 11 in Table 6.10 for SAJ-2′ are 34, 60 and 71 respectively. The values of $K_{b,int}$, $K_{b,s}$ and $K_{b,U}$ for SAJ-2", given in Table 6.11, show a constant value of 6.

According to clauses 5.2.2 in BS EN 1993-1-8:2005 for stiffness classification of steel joints, a frame joint is classified rigid if $K \geq 25$, pinned if $K \leq 0.5$ and semirigid when falling in range given by $0.5 < K < 25$ (see Section 6.1).

For classification of SAJ-2, the joint is found to be rigid, as K_j at initial, SLS and ULS is > 25. For joints SAJ-4, SAJ-3 and SAJ-1 the initial, SLS and ULS K_j in Table 6.10 are in the range of 16 down to 2. The equivalent results for K_b, in the Table 6.11, give a range of 6 down to 1. Appling the classification process introduced in Section 6.1 shows that these rotational stiffnesses are for a semi-rigid joint. None of

these three joint details offers a Startlink frame joint with adequate rotational stiffness to satisfy the design assumption of 'rigid' joint.

The rotational stiffness of SAJ-1 indicates that this joint's response is akin a pin and is far removed from the clamped condition that had been assumed by Kendall (2010) when he designed the SLBS portal frame. Although the strength measured from the single joint test is similar to that required to satisfy M_U the rotational stiffness of SAJ-1 is too far low at M_s of 6.8 kNm.

Figure 6.49 shows the stiffness classification of the SAJs joints at SLS using the form of figure shown in Figure 6.7. The stiffnesses for the four joints have been taken from Tables 6.10 and 6.11. In the figure the classification boundaries for rigid (zone 1), semirigid (zone 2) and pinned (zone 3) joints are shown by the solid and dashed lines. In Figure 6.49 the rotational stiffnesses of $S_{j,s}$ and $S_{b,s}$ (at 6.8 kNm), from measured $\emptyset_{j,s}$ and $\emptyset_{b,s}$ values are plotted.

From Figure 6.49 it can be seen that joints SAJ-2 and SAJ-4 have the highest joint stiffness. Rotational stiffness for joint SAJ-4 informs that even with presence of the tight fit dowel connections (for SAJ-4) and without having additional bonded connection (for SAJ-2) a rigid rotational stiffness in the Startlink frame joint is not achievable. It is also the use of structural adhesive on the site for having the additional bonded connection between overlapping surfaces of the members in SAJ-2 is a formidable task, specially, in wet condition. These finding indicates that to have rigid behaviour in the Startlink portal frame, when SLBS housing goes into production, the application of a bracing system should be considered.

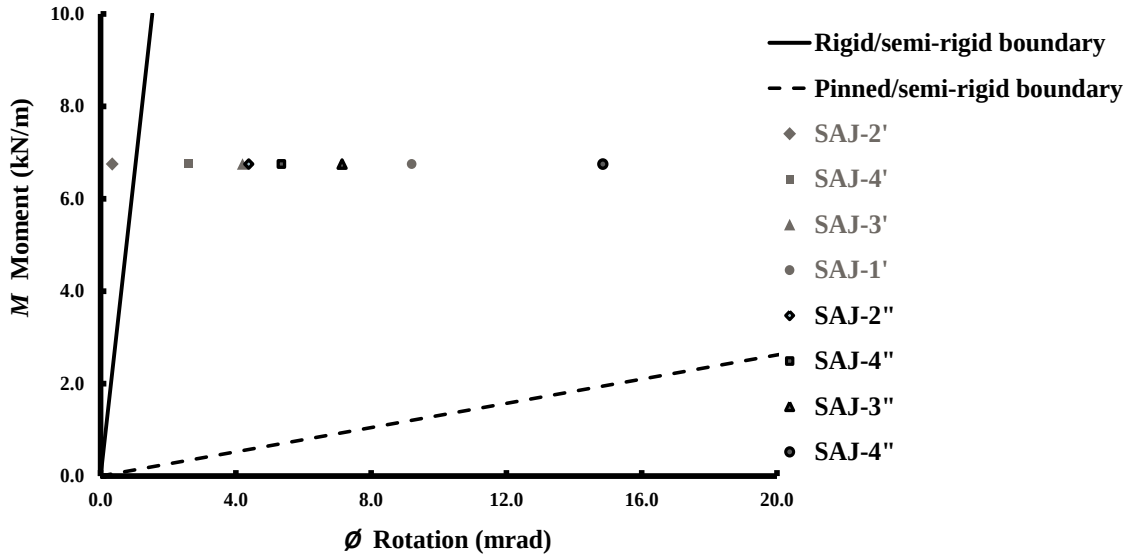

Figure 6.49. Classification of the SAJ joints stiffness by *M*-Ø zones at SLS loading.

6.7Concluding remarks

A series of four physical tests have been conducted under static load to provide indicative test results on the moment-rotation characteristics and determine the mode(s) of failure of practical Startlink frame joints, having FRP dowel connections, between the floor beam and stud column. The results are used to establish of the joint detailing, have adequate rotational stiffness and resistance to meet the design requirements. Using the test results an evaluation is made on the performance of joints in the Startlink portal frames with regards to design/required joint resistance and 'rigid' rotational stiffness. Individual specimens were either with or without hole clearance and one specimen (with hole clearance) had adhesive bonding between common surfaces of the members. Perimeter of connections holes and dowels were coated with a structural adhesive before engaging the members to provide continuity in the presence of hole clearance.

The following are salient results that can be used to develop an overall understanding of the unbraced Startlink frame (Figures 6.1 to 6.4) with regard to its overall stiffness and structural performance when FRP dowelling is a method of connection.

- The joint moment at failure is in excess of 10.1 kNm, which is the ULS moment given by multiplying by 1.5 the SLS design moment of 6.8 kNm, for the most severe load case.

- According to BS EN 1993-1-8:2005 the frame joint with a 2 mm thick bond connection between overlapping surfaces of the members gave a moment-rotation response that classifies secant rotational stiffness as rigid and the rest of three joints as semi-rigid.

- The order of four Sub-Assembly Joints (SAJs), in trying to satisfy the Startlink design requirements of stiffness and resistance are:

  [SAJ-2]- this joint had 2-3 mm hole clearance (in both bean and column members) and a 2 mm thick bond connection between overlapping surfaces of the members.

  [SAJ-4]- this joint had tight fit dowel connections and the holes were positioning at the exact and precise locations.

  [SAJ-3]- this joint had ‘pseudo’ tight fit dowel connections, as holes were not positioning at the exact and precise locations (centre-to-centre holes distances were not constant too).

  [SAJ-1]- this joint had 2-3 mm hole clearance in both joint members.

- The *M-Ø* curve for joint SAJ-2 was found to be linear to 29.1 kNm, which is three times higher than the ULS design moment. It was observed that joint failure was related to geometry and method of connections, and not because PFRP material strength. Measurements of bearing strain at the dowel connections indicated that loading was effectively transferred through the bonded connection joining beam webs to column outer walls.

- Characteristics of *M-Ø* curves for joint SAJ-4 and SAJ-3 were similar when the maximum moment was attained, but the latter joint showed lower rotational stiffness than the former. The *M-Ø* responses remained linear to *M* of 20.4 kNm (SAJ-4) and 10.1 kNm (SAJ-3). The failure modes for the SAJ-3 were bond fracture at dowel connections, followed by bearing failure. For SAJ-4 the failure processes were bond fracture at dowel connections, then connection bearing failure, followed by top flange curl and excessive web flexural deformation.

- It is important to mention that the presence of tolerances on hole positioning in SAJ-3 produced non-uniformed connection forces in the four dowel connections and, subsequently, non-constant localised stiffness opposing the dowel bearing forces. As a result there was a premature bearing failure in the joint. Moreover, the tolerances on hole positioning allowed there to be a higher joint flexibility as joint members did not have full contact at all four dowels.

- Testing of joint SAJ-1 showed that this detailing cannot provide the required rotational stiffness. It was found that its response was akin to a pinned joint. It can be concluded that the application of structural adhesive to pack-out clearance hole voiding cannot provide adequate strength/stiffness when transferring the

connection forces from dowel into members. In other words the existence of hole clearance will increase the flexibility of a SLBS joint.

- Rotational stiffnesses at the SLS design member for joints SAJ-2, SAJ-4, SAJ-3 and SAJ-1 suggest that, even with presence of tight fit dowel connections in SAJ-4, the ‘rigid’ rotational stiffness is not achievable. It is also the use of structural adhesive on the site for having the additional bonded connection between overlapping surfaces of the members in SAJ-2 is a formidable task, specially, in wet condition. These findings indicate that to ensure the Startlink house does not have maximum lateral displacement exceeding the SLS limit the structural system requires vertical bracing.

Chapter 7

Concluding Remarks and Further Work

The following concluding remarks can be drawn from the work presented in this thesis for two experimental investigations with Pultruded Fibre Reinforced Polymer (PFRP) material. One study is for the determination of material pin-bearing strength and the second study is for the characterisation of dowel connections and a frame joint using the 2012 Startlink lightweight building system for the Startlink house.

7.1 Determination of Pin-bearing Strengths for Bolted Connections

The following remarks are from the research presented in Chapters 2, 3 and 4:

(1) To calculate a safe design strength (using Equation (2.1)) the new pin-bearing strength test results show that it is essential for the determination of a characteristic strength to take account of the strength reduction due to hole clearance, and for the much larger material thicknesses and bigger bolt sizes found in practice. The new results, importantly, show that existing standard test methods (e.g., ASTM D953-02, ASTM D 5961-05, BS EN 13706-2:2002) are likely to give a non-conservative (too high) measurement because they specify a single specified pin diameter of 6.35 mm and there is no requirement for a clearance hole. It has been established that existing standard test methods require a size of tension specimen that is too big to prepare with pultruded structural shapes, such as the 203×203×9.53 mm wide flange used in

the test programme. As a consequence of this severe limitation an alternative test method with a smaller coupon size is needed should all the required pin-bearing strengths be quantified.

(2) A loading fixture and test method (having no lateral restraint from tightening the nut and bolt) developed at the University of Warwick was successfully used and it has the potential to become the standard test method for the determination of pin-bearing strength of FRP materials in construction.

(3) To account for all possible influences on lowering the bearing strength, by the end of a PFRP structure's service life, it is recommended that the pin-bearing strength should be used in design calculations for the resistance of bolted connections.

(4) Evaluated are mean and characteristic values for pin-bearing strengths at the six material orientations of 0, 5, 10, 20, 45 and 90^{o} to the direction of pultrusion. At each orientation testing involved the four steel pin diameters of 9.7, 12.2, 18.8 and 25.4 mm (giving pin diameter-to- material thickness ratios of 1.1 to 2.8). Because it reduces strength the clearance hole was a minimum of 2.1 mm. Characteristic strength values were determined in accordance with Eurocode 0, allowing for the acceptable assumption that coefficients of variations are not greater than 10%. It was found that strength decreases with an increase in the pin diameter-to-material thickness ratio. It was also found that the minimum characteristic values of (97 N/mm^2) are obtained with the largest bolt diameter of 25.4 mm. Based on the minimum characteristic strengths for the web material a decrease of 40-50% in pin-bearing strength can be expected by increasing the bolt diameter from 9.7 mm to the 25.4 mm. It is observed that the longitudinal and transverse strengths at 120 and 97

N/mm^2, respectively, cannot be associated with the maximum (pin) bearing strengths of 207 N/mm^2 (LW) and 126 N/mm^2 (CW), respectively, given in the Creative Pultrusion Inc. design manual (Anonymous, 2012a).

(5) Assessing the mean values it is found that there is a trivial reduction in strength with orientation from 0 to 5^o and that, at the highest pin diameter-to-material thickness ratios, there is a tendency for their means to coincide. This finding does not contradict the proposed design guidance in an American pre-standard (that is expected to be a standard by the end of 2013) to use the 0^o characteristic value for orientations between 0^o and 5^o and the 90^o value for all other orientations (i.e. > 5^o to 90^o).

(6) It is shown that the variation of pin-bearing strength with material orientation cannot be predicted by the curve generated by the formula known as the Hankinson equation, which requires only the 0 and 90^o values to be known. To establish a curve fit to the variation with orientation might require a polynomial of order six. This order would not be suitable for a formula to be found in a design standard.

To simulate what could occur when bolted connections in pultruded structures are exposed to weather over their service life, specimens were subjected to hot-wet conditioning and the characteristic strengths for three material orientations at 0, 45 and 90° have been determined. The comparisons with equivalent strength test results of non-aged specimens obtained at room temperature were quantified. Knowledge of this strength property, taking account of any reduction over the service lives of structures, is required when using Equation (2.1) to calculate bearing strength in designing bolted connections. The following remarks are from the research on the

effect of hot-wet aging on pin-bearing strength:

(1) Comparing characteristic strengths from hot-wet (in water at 40^{o}C for 3000 hours) aged material with those from non-aged material, obtained using the same test matrix, showed that the pin-bearing strength reduced by 20 to 30% following the environmental conditioning. It is important to note that the hot-wet aging is for an unknown number of service years. It was found that characteristic values determined with the largest (25.4 mm) pin size do not fit in statistically with those obtained using the three smaller diameters. By ignoring results for the largest pin, the mean reduction is highest, at nearly 30%, for the 0^{o} material (when the unidirectional roving reinforcement layers govern), and lower, at about 20% for the 45^{o} and 90^{o} material orientations.

(2) The lowest characteristic strengths for the three material orientations of 0^{o}, 45^{o} and 90^{o} were obtained with the largest pin of 25.4 mm diameter. For the 0^{o} orientation this strength is found to be 91 N/mm^{2}. It is 67 N/mm^{2} when the web material is oriented at 90^{o}. Comparing the two orthogonal strengths of 206 N/mm^{2} and 124 N/mm^{2} from Creative Pultrusions Inc. with the lowest characteristic non-aged strengths, it is found that the strengths for the longitudinal (LW) and transverse (CW) orientations have reduced by 56% and 46%. These reductions are about four and three times higher than the 15% reduction recommended by Creative Pultrusions Inc. (refer to Table 6.1 in Anonymous (2012a)). The American pre-standard (Anonymous, 2012d) allows a reduction (adjustment) factor of 0.7 to adjust the strength loss for the purpose of structural design when using polyester material at 40C^{o} and moisture conditioning. Based on this adjustment factor, it can be seen that the strengths of 91 N/mm^{2} and 67 N/mm^{2} are about 14% and 24% higher than that

permitted by the American pre-standard. It is important to mention that the 0.7 factor is for the residual strength that must exist after the materials have been exposed to moisture and 40 C^o temprature which can be obtained by using the American LRFD pre-standard are for sustained end-used condition of structural products after being used in moisture and temperature over the structures service lives. In Part 3 to the European standard EN 13706 Table 1 reports, again, for non-aged material, the required minimum pin-bearing strengths. It is observed from the aged strengths reported herein that the 0^o and 90^o minimums of 150 and 70 N/mm^2 are not met after the web material had been subjected to the hot-wet aging. The strength loss is likely to have been higher still, had strength testing itself been carried out at the evaluated temperature of 40^oC. It is therefore imperative that the determination of pin-bearing strength is carried out with test conditions that allow for the worse probable reduction that could be realized at the end of the service life of a pultruded structure with bolted connections.

(3) The strength loss, at about 30% for 0^o and 20% for 45^o and 90^o orientations, for characteristic values with pin diameters between 9.7 and 18.8 mm is a constant percentage of the non-aged strength. This indicates that costly testing could be limited to a relatively low number of batches with the outcome that pultruders and others can more readily establish the characteristic pin-bearing strengths required for the design of bolted connections.

7.2 Characterisation of dowel connections and a joint in the SLBS

For the second study, the characterisation by testing of dowel connections and portal frame joints is specific to the bespoke geometries and assemblies in the Startlink

house that is constructed using the SLBS. This second experimental investigation includes two series of tests. The first is a series of static coupon-sized tests that were conducted to determine the minimum resistance of PFRP closed shapes dowel connections similar to those used in the Startlink house. These results were used to verify the structural engineering design calculations. The following remarks are from this research presented in Chapter 5:

(1) Based on a pragmatic analysis of the test results for the 'damage' characteristic strength for a tube and for a square closed (off-the-shelf) PFRP shape used to fabricate dowel connections it is found that the shear resistance of PFRP dowelling is a function of the load configuration and how the load is transferred into the dowel section.

(2) It was observed that the ratio of the cross-section areas of the square and tube shapes at 3.3:1 is not proportional to their shear resistance ratio, which depending on test configration is found to vary between 37:1 to 1:1.8.

The second series of sub-assembly tests, with different geometrical configurations, was used to determine the moment-rotation characteristics of joint details for the portal frame in the SLBS house. The following remarks are from the research presented in Chapter 6:

(1) Four individual beam-to-column external frame joints with dowel connections, and with and without adhesively bonded connections, have been statically loaded to evaluate the performance of joints in the Startlink portal frames with regard to design/required joint resistance and 'rigid' rotational stiffness. It was found that the moment at failure was in excess of minimum 18 % (for the worst case)

of the design (Ultimate Limit State) ULS moment and therefore the four joints had adequate strength against the design ULS moment.

(2) According to BS EN 1993-1-8:2005 the frame joint with a bonded connection between overlapping surfaces of the beam and column members gave a moment-rotation response that classifies the secant rotational stiffness as rigid. The other three joints in the experimental study have initial stiffnesses that are classified as semi-rigid.

(3) For the joint with the bond connection between overlapping member surfaces, it was found that loading was effectively transferred through the bonded connection and joint failure was related to the geometry and methods of connection, and not because of PFRP material strength or member stiffness. Failure modes for the joint with tight fitted dowel connections (the holes were positioned at exact and precise locations) were bond fracture at dowel connections, followed by bearing failure in the column shape. For the joint with 'pseudo' tight fitted dowel connections (the holes were not positioned at exact and precise locations and also centre-to-centre holes distances were not constant) the failure processes were bond fracture at dowel connections, then connection bearing failure, followed by top flange curl and excessive web flexural deformation.

(4) It was found that the application of structural adhesive to pack-out clearance hole voiding (for the single frame joint that had 2-3 mm hole clearances) cannot provide adequate stiffness and the moment-rotation response of the joint was close to that classified as a pinned joint. In other words, when relatively big clearance holes are present the joint's rotational stiffness is going to be too low, and this structural limitation cannot be overcome simply by the liberal use of adhesive bonding.

(5) Measured joint rotational stiffnesses at the moment for Serviceability Limit State (SLS) design suggests that, even with the presence of tight fitting dowel connections, the 'rigid' condition used to design the Startlink house frame is not achievable. It is noteworthy that the use of adhesive on site to provide the necessary bonded connection for a 'rigid' joint could reduce both the speed of execution and quality, especially if construction is during wet/cold/hot weather. These findings indicate that to guarantee that the Startlink house does not have a maximum (roof level) lateral displacement exceeding the SLS limit its structural system should include effective vertical bracing.

7.3 Further Work

In order to build upon the findings of this thesis, further research is suggested to deal with the following issues:

(1) Experimental data presented in Chapter 2, 3 and 4 of this thesis shows that the pin-bearing strength reduces by increasing hole clearance. Yuan *et al*. (1996) conducted tests to show that by increasing hole clearance up to 50% of pin diameter (12.7 mm) the bearing strength was still reducing. For pin-bearing test results reported in this thesis the available drill bits meant the clearance sizes, as a percentage of pin diameter, were 20, 21, 11 and 10 for the bolt (pin) diameters of 9.7, 12.2, 18.8 and 25.4 mm. It is therefore likely that measurements for the two smaller bolt sizes are relatively lower than what has been measured for the two bigger bolt sizes. This observation suggests that to establish a trend between pin-bearing strength and the bolt diameter to material thickness ratio, testing should be performed with a clearance size that is set at a constant percentage (say 10%) of the

pin diameter, for all bolt sizes. The trend of the strength reduction, for all six orientations might be modelled linearly, but confirmation will require more test results (with a minimum of 10 nominally identical specimens per batch).

(2) By aging the specimens in water at a constant temperature of 40^{o}C for 3000 hours, and conducting pin-bearing strength tests for three different orientations from 0° to 90° at ambient temperature conditioning, the strength reduced by 20 to 30% of its non-aged characteristic value. The strength loss is likely to have been higher still, had strength testing itself been carried out at the evaluated temperature of 40^{o}C. It is therefore imperative that the determination of pin-bearing strength is carried out with test conditions that allow for the worse probable reduction that could be realized at the end of the service life of the PFRP structure. Also additional research is required to find out why characteristic strengths with the largest pin of 25.4 mm diameter do not follow the orientation reduction.

Appendix A

Determination of the Dowel Bearing Strengths of the Stud-Column Section

B. Zafari and J.T. Mottram

School of Engineering, University of Warwick (UW)

Date: 22nd August 2011

The purpose of this report, which is principally factual, is to present the longitudinal (0^o) and transverse (90^o) bearing strengths for the stud column section using the same dowel connection as for the Startlink House.

EXEL Composites UK provided Warwick University (WU) with 150 mm lengths of the stud column section (Figure 1) and 15 lengths (210 mm) of a 28 mm diameter mine bolt pultruded product. The FRP bolt is black in colour. At the time of writing this factual report WU does not have the material specification of the stud column or mine bolt. The average diameter of the smoothed surface bolt is 27.6 mm. Using a CNC machine, in the workshop of the School of Engineering, 27.8 mm diameter holes were drilled at the centre of the two 'box' sections in the stud column. These are labelled as holes A and B in Figure 1. The precision of the hole drilling meant that, on inserting the dowel length (mine bolt), there is a tight fit between the dowel and stud column. To make the dowel rotate in the hole it is necessary to give the rod a good firm hand twist.

Figure 1 shows the cross-sectional shape of the stud column and location of the two holes A and B. Hole A is for the side of the stud column that on the inside of the house. The external side of the stud column has the hole labelled B. On the cross-

section drawing the four walls (with the holes drilled through) are labelled (1 to 4) and their thicknesses are measured a three positions (t_1, t_2 and t_3) using a 0.01 mm micrometer gauge. For the left and right sides of stud column the results of the thickness measurements are given in columns (2) to (4) and (6) to (8), respectively, of Table 1. Columns (5) and (9) in the table give the mean thicknesses from the three measurements and the last column, (10), lists the bearing thickness for strength calculation, which is the sum of the two mean wall values. Alternate row entries are for holes A and B. From Table 1 it is seen that the mean thicknesses of hole A are A1 from 3.93 to 3.98 mm and A2 from 5.04 to 5.22 mm, while hole B has B3 from 4.12 to 4.15 mm and B4 from 4.97 to 5.09 mm. From column 10 the two holes possess a bearing thickness in the range 8.98 to 9.18 mm, giving a mean from the five A and five B holes of 9.12 mm (with CV of 8%). Further evaluation will show that the holes A and B have slightly different mean bearing thicknesses at 9.10 ad 9.14 mm, respectively.

The test arrangement, using a 100 kN Testometric testing machine, for determination of longitudinal bearing strength is shown in Figure 2. To apply load there is, on the two sides of the stud column, equal lengths of a ‘yellow’ box section (50 x 38 mm). These sections have a hole of 28 mm diameter at a distance from the shortest free end that enables the bearing force to be applied to its maximum, and this required a stroke increase of up to 3 mm. A ‘black’ dowel of 201 mm length passes through the stud columns and the two ‘yellow’ box sections. The bearing resistance of the two loading ‘yellow’ boxes is greater than that of the stud column (the weak link is the stud column). During testing it was observed that longitudinal cracking (at the corners) did occur in the ‘yellow’ box sections, and because this would be heard as

acoustic emission it has not been possible, with the test arrangement used in Figure 2, to determine the damage load for the onset of bearing failure.

In Figure 3 the stud column section shows surface damage that is for the usual bearing failure with through-thickness delamination in the vicinity of the bearing surface of the hole. Note that for the longitudinal specimens the free end distance is about three times the dowel diameter and that this proximity has not affected the measured maximum bearing strength.

It was necessary to conduct the testing for the transverse (90^o) orientation strength by cutting-off the two box sections and having a solid block of steel (of a same width as the stud column section) to subject the compression load into the specimen. This test arrangment is shown in Figure 4 and typical surface failure patterns are seen in Figure 5. Because the distance from the centre of the hole to the edge of the specimen is about one dowell diameter and there is stiffness (and strength) from the presence of the side wall to the stud column (and, addiitonally, from the rigid steel loading pad) the mode of failure can be a combination of bearing (through-thickness delamination) and crushing in front of the bearing surface.

Ten nominally identical specimens for the two orientations were tested. Except for a roughness appearing on the surface of the mine bolt there was no other form of damage to the dowels.

Test results are given in Tables 2 and 3. Table 2 gives the maximum loads, which can be higher than the damage loads when the testing first indicates, by acoustic emission, some form of material failure (not necessarily at a hole). In determining

the maximum bearing stress the bearing area is taken to be the sum of the two wall thicknesses (column (10) in Table 1) times the 27.6 mm diameter of the dowel. The statistical analysis in Table 3 of the 10 specimens (assuming holes A and B are the same, which they might not be) show that the coefficient of variation (CV) is about 10% (this is usual) and that the characterstic longitudinal (0^o) and transverse (90^o) strengths are 180 and 100 N/mm^2 (MPa), respectively. In terms of maximum dowel force these equate to the Table 2 maximum load entries of 46.6 and 26.6 kN, respectively.

Assuming that the lowest transverse value of 26 kN can be taken as the bearing resistance (at the unknown orientation for the connection force when the Startlink portal frame is subjected to the worse ulitmate limit state load case) we can use the design calculation sheets from David Kendall (Optima Projects Ltd.) to estimate the maximum moment, when the mode of failure is bearing. There is a possibility that the moment resistance for a different mode of failure is lower, and this can be established by testing sub-assembly joint specimens.

Using the geometry in Figure 6 the maximum moment is estimated to be 4 x 0.15 x 26 = 15.6 kNm. The first number is for the four dowels in the joint, the second is the lever arm distance (= 0.3/2 m) from the centre of rotation, and the third number is for the lower bound bearing failure load for the connection force (at each dowel). It is assumed that the connection force at a dowel acts perpendicular to the line going through the centre of the group of dowels and centre of its hole. This estimate of moment resistance (= 15.6/6.9) is over two times greater than required by the design calculations (see 100302 Startlink portal frame calcs.pdf), which has an overall

factor of safety (for ulimate limit state) of 2.25. Note that the moment resistance will be slighly lowered because the design calculations show there is a shear force (5.1 kN) and an axial force (3.4 kN) acting through the joint. It can be observed from Figure 6 that David Kendall had decided on a FRP dowel of 30 mm diameter. Interestingly, the value of the bearing transverse strength in the design calculations (pg 13) is 100 N/mm^2 (MPa); the same as the characterisitc value reported in Table 3.

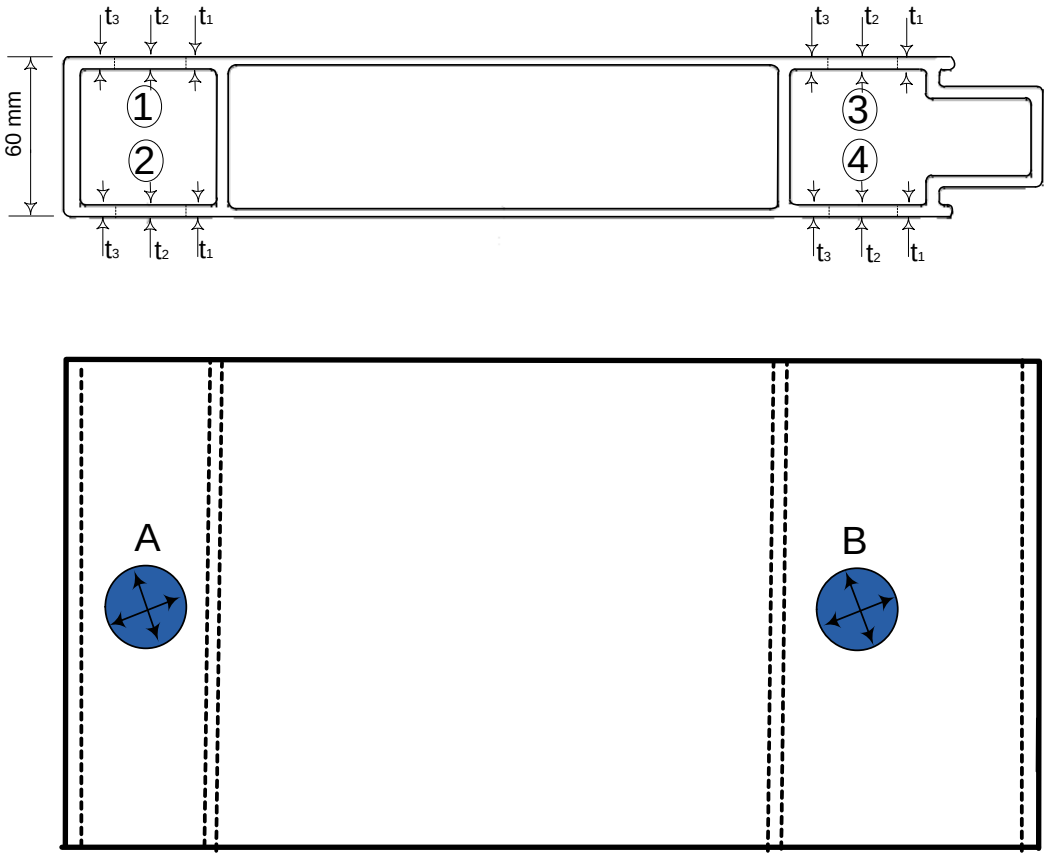

Figure 1. Stud column specimen with locactions for measurement of wall thicknesses.

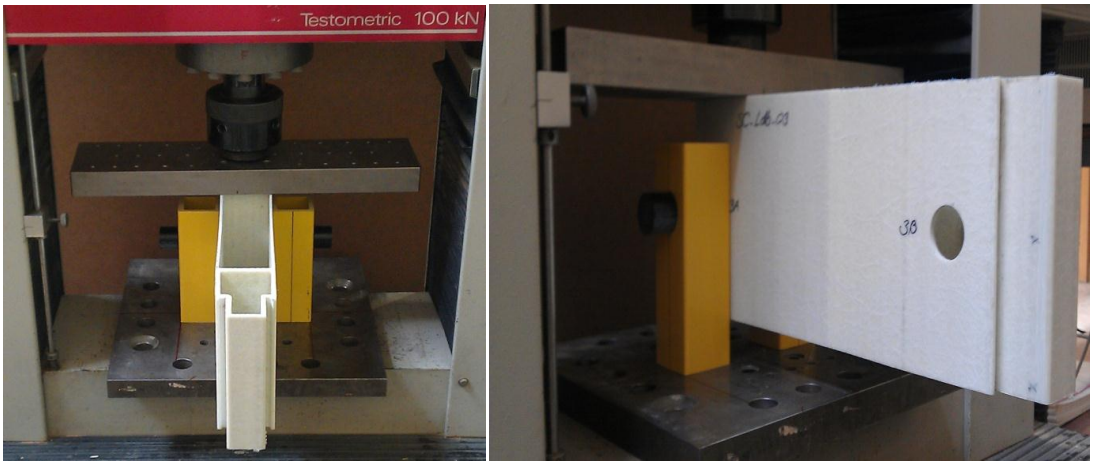

Figure 2. **W**arwick **U**niversity specimen **WU-sc-Ldb**-3A for **L**ongitudinal **d**owel **b**earing strength.

Figure 3. Bearing mode of failure of stud-column section in specimens WU-sc-Ldb-2A and WU-sc-Ldb-2B.

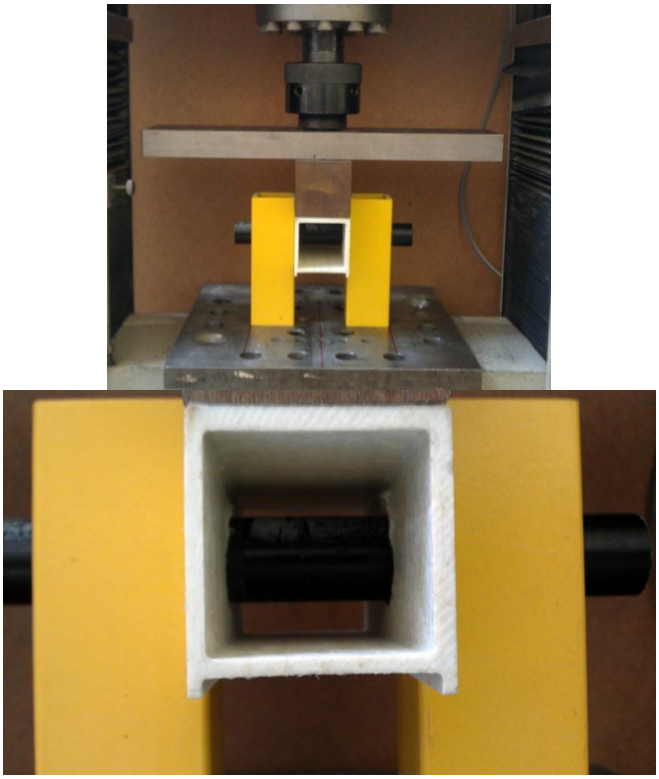

Figure 4. **W**arwick **U**niversity specimens of **s**tud-**c**olumn section for **Transverse** **d**owel **b**earing strength. The right side photo for specimen **WU-sc-Tdb**-1A shows internal permanent deformation after bearing failure.

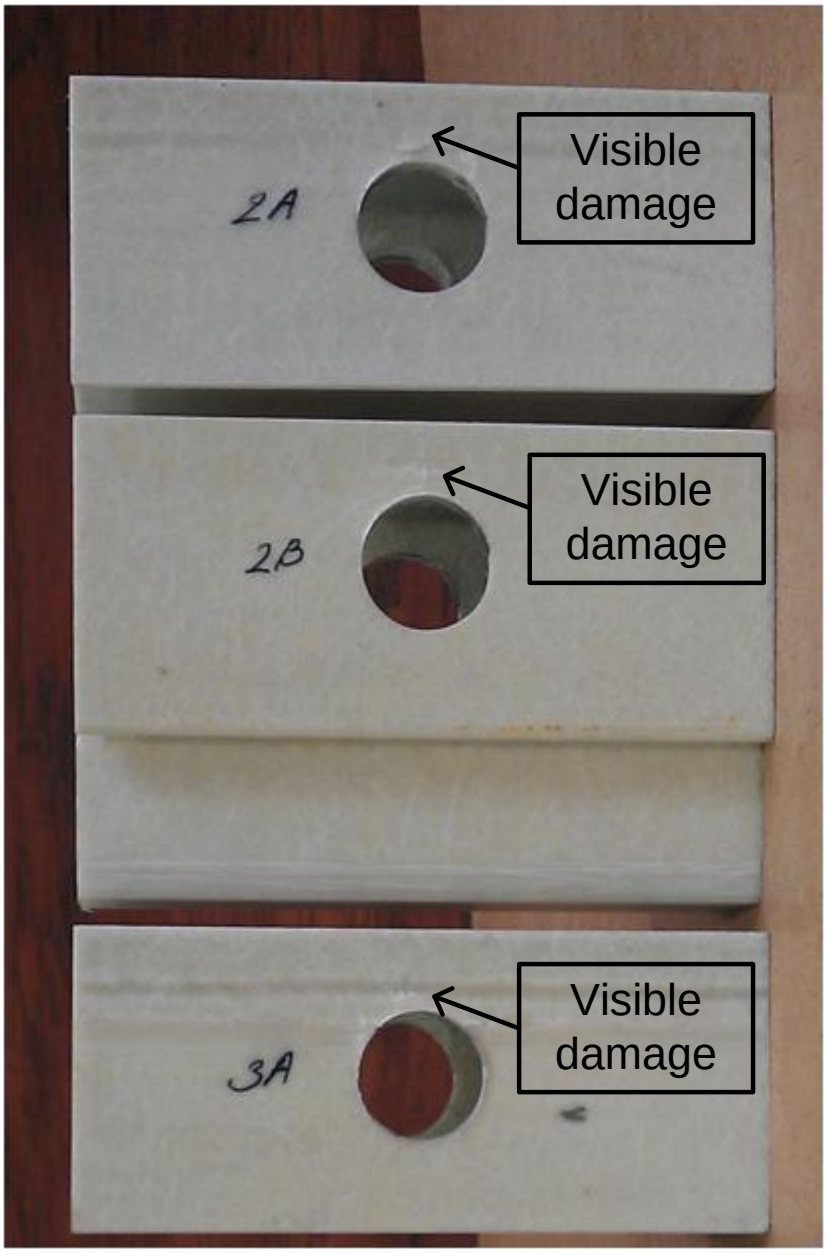

Figure 5. Bearing mode of failure (not necessarily the classical bearing failure owing to material crushing) of stud column section from specimens WU-sc-Tdb-3A, WU-sc-Tdb-2B and WU-sc-Tdb-2A.

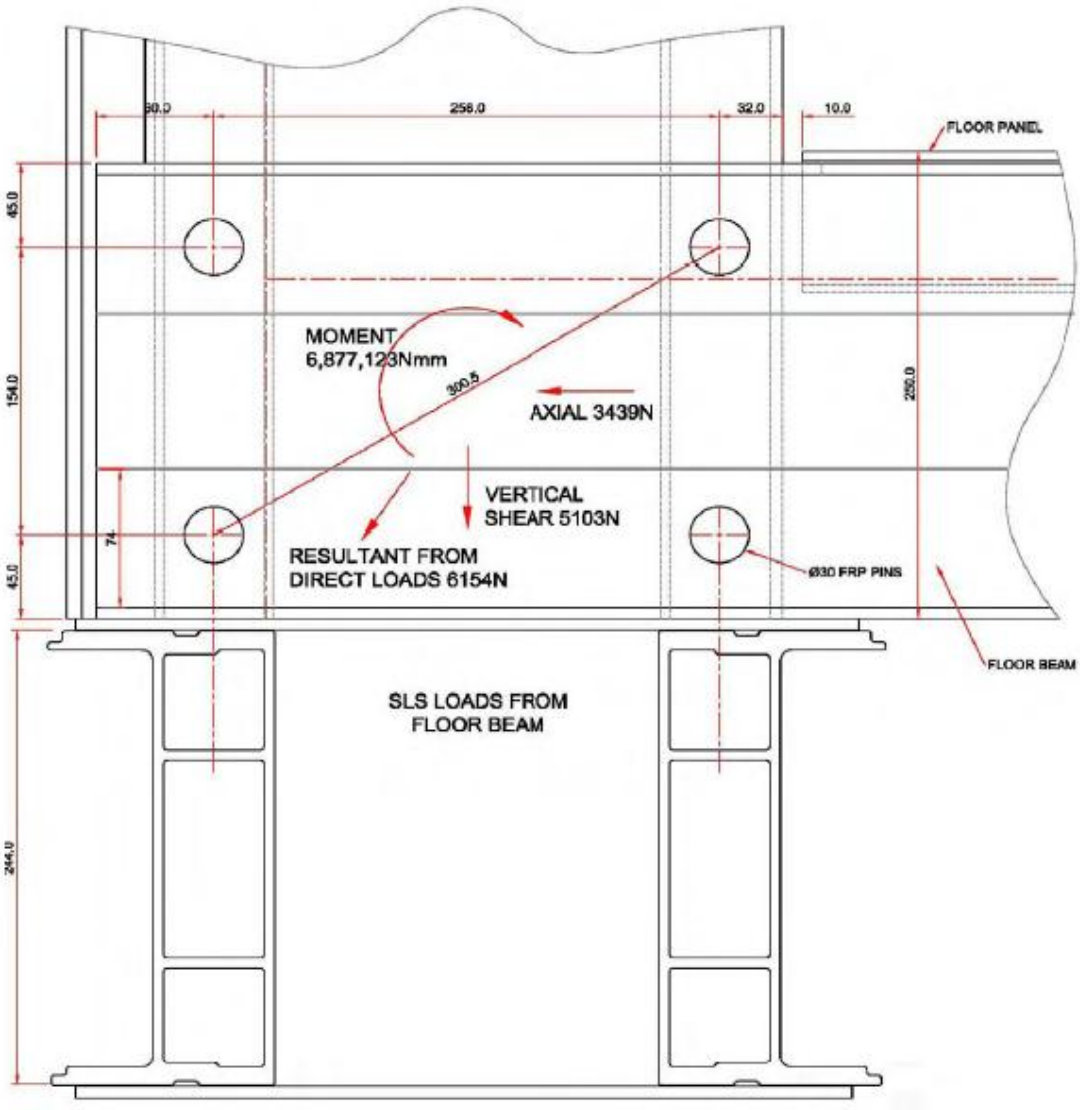

Figure 6. Reproduction of joint detailing and joint actions from Startlink portal frame calculations by David Kendall (2010).

Table 1. Measurements of wall thickness of stud column section and total thickness for bearing at holes A and B.

Wall thicknesses (mm)									
Specimen label	Left-side walls (A1 or B3)			Average thickness left-side	Right-side walls (A2 or B4)			Average thickness right-side	Total wall thickness for bearing area
	t_1	t_2	t_3	(mm)	t_1	t_2	t_3	(mm)	(mm)
(1)	(2)	(3)	(4)	(5) = ((2)+(3)+(4))/3	(6)	(7)	(8)	(9) = (6)+(7)+(8))/3	(10) = ((5) + (9))/2
WU-sc-Ldb-01A	4.02	3.90	3.87	**3.93**	5.22	5.21	5.29	**5.24**	**9.17**
WU-sc-Ldb-01B	4.11	4.15	4.10	**4.12**	5.02	4.97	4.92	**4.97**	**9.09**
WU-sc-Ldb-02A	3.99	4.01	3.88	**3.96**	5.19	5.18	5.29	**5.22**	**9.18**
WU-sc-Ldb-02B	4.08	4.18	4.07	**4.11**	5.01	5.00	4.96	**4.99**	**9.10**
WU-sc-Ldb-03A	4.08	4.04	4.01	**4.04**	5.05	5.09	5.06	**5.07**	**9.11**
WU-sc-Ldb-03B	4.12	4.18	4.14	**4.15**	5.08	4.96	5.01	**5.02**	**9.16**
WU-sc-Ldb-04A	4.05	3.98	3.91	**3.98**	5.06	5.10	5.12	**5.09**	**9.07**
WU-sc-Ldb-04B	4.18	4.17	4.10	**4.15**	5.06	5.10	5.12	**5.09**	**9.24**
WU-sc-Ldb-05A	3.95	3.91	3.94	**3.93**	5.10	5.10	4.93	**5.04**	**8.98**
WU-sc-Ldb-05B	4.10	4.14	4.18	**4.14**	5.05	4.93	4.93	**4.97**	**9.11**
Average									**9.12 mm**
Standard Deviation									**0.07 mm**
Coefficient of Variation									**7.8%**

Table 2. Measured maximum bearing loads from the 20 longtidunal and transverse test specimens.

Longitudinal (0^o) specimen label	Maximum load (kN)	Transverse (90^o) specimen label	Maximum Load (kN)
WU-sc-Ldb-1A	57.2	WU-sc-Tdb-1A	30.0
WU-sc-Ldb-1B	65.9	WU-sc-Tdb-1B	32.9
WU-sc-Ldb-2A	47.6	WU-sc-Tdb-2A	31.0
WU-sc-Ldb-2B	63.7	WU-sc-Tdb-2B	30.0
WU-sc-Ldb-3A	54.1	WU-sc-Tdb-3A	29.2
WU-sc-Ldb-3B	63.1	WU-sc-Tdb-3B	36.0
WU-sc-Ldb-4A	56.3	WU-sc-Tdb-4A	31.9
WU-sc-Ldb-4B	65.7	WU-sc-Tdb-4B	35.3
WU-sc-Ldb-5A	46.6	WU-sc-Tdb-5A	26.6
WU-sc-Ldb-5B	57.1	WU-sc-Tdb-5B	30.1

Note: Bold font is used to highlight the lowest resistance in each batch of ten specimens.

Table 3. Maximum failure loads for compression loading of Startlink stud-column section.

Specimen label	Bearing strength (MPa)	Specimen label	Bearing strength (MPa)
(1)	(2)	(3)	(4)
Longitudinal (0°)		Transverse (90°)	
WU-sc-Ldb-1A	225	WU-sc-Tdb-1A	124
WU-sc-Ldb-1B	262	WU-sc-Tdb-1B	131
WU-sc-Ldb-2A	187	WU-sc-Tdb-2A	124
WU-sc-Ldb-2B	253	WU-sc-Tdb-2B	120
WU-sc-Ldb-3A	215	WU-sc-Tdb-3A	116
WU-sc-Ldb-3B	249	WU-sc-Tdb-3B	142
WU-sc-Ldb-4A	224	WU-sc-Tdb-4A	127
WU-sc-Ldb-4B	257	WU-sc-Tdb-4B	139
WU-sc-Ldb-5A	187	WU-sc-Tdb-5A	105
WU-sc-Ldb-5B	226	WU-sc-Tdb-5B	120
Mean	229	Mean	125
SD	26.9	SD	10.9
CV %	11.8	CV %	8.7
Characteristic value[1]	182	Characteristic value[1]	106

Note:

1. Characteristic = mean - 1.72SD.

References

Anonymous. (2007). ACMA Develops design standard for civil engineers. *Reinforced Plastics*, **51**, (9), 12.

Anonymous. (2008). *Guide for the design and construction of structures made of FRP pultruded elements*, Advisory Committee on Technical Recommendations for Construction, National Research of Italy, CNR-DT 2005/2007, Rome, CNR October 2008. http://www.cnr.it/documenti/norme/IstruzioniCNR_DT205_2007_eng.pdf

Anonymous. (2012a). *The new and improved Pultrex® pultrusion design manual (Imperial version)*, Creative Pultrusions, Inc., Alum Bank, PA. (www.creativepultrusions.com/rd.html) (August 30, 2012).

Anonymous. (2012b). *Strongwell design manual*, Strongwell, Bristol, Va. (www.strongwell.com/) (August 30, 2012).

Anonymous. (2012c). *Fiberline design manual for structural profiles in composite materials*, Fiberline Composites A/S, Kolding, Denmark, 1st Ed. 1995, updated 2nd Edition 2001.

Anonymous (2012d). *New pre-standard for pultruded FRP composites funded thru ACMA means increased applications*, American Composites Manufacturers Association (ACMA) press release. //www.acmanet.org/pressreleases/2011/011711.html (August 31, 2012)

Anonymous. (2012e). Pultrex Ltd., Century House, Colchester, Essex. (www.pultrex.com/production-machinery/pultrusion/pultrusion-process/) (September 20, 2012).

Apicella, A., Migliaresi, C., Nicolais, L., Iaccarino, L., & Roccotelli, S. (1983). The water ageing of unsaturated polyester-based composites: influence of resin chemical structure. *Composites*, **14**(4), 387-392.

ASCE (1995). '*Standard for Load and Resistance Factor Design (LRFD) for Engineered Wood Construction,'*AF&PA/ASCE.16-95, American Society of Civil Engineers, Reston, VA.

Ascione, F., Feo, L., & Maceri, F. (2009). An experimental investigation on the bearing failure load of glass fibre/epoxy laminates. *Composites Part B: Engineering*, **40**(3), 197-205.

ASTM D 953–02 (2002). *Standard Test Method for Bearing Strength of Plastics*. American Society for Testing and Materials International, West Conshohocken, PA.

ASTM D 5961-05 (2005). *Standard Test Method for Bearing Response of Polymer Matrix Composite Laminates*. American Society for Testing and Materials International, West Conshohocken, PA.

ASTM D 7290-06 (2006). *Standard Practice for Evaluating Material Property Characteristic Values for Polymeric Composites for Civil Engineering Structural Applications*. American Society for Testing and Materials International, West Conshohocken, PA.

ASTM D 5764-97a (Reapproved 2007). *Standard Test Method for Evaluating Dowel-Bearing Strength of Wood and Wood-Based Products*. American Society for Testing and Materials International, West Conshohocken, PA.

ASTM D695-08 (2008). *Standard test method for compressive properties of rigid plastics*, ASTM International, West Conshohocken, PA.

Bakis, C., Bank, L. C., Brown, V., Cosenza, E., Davalos, J. F., Lesko, J. J., Machida A., Rizkalla S. H. & Triantafillou, T. C. (2002). Fiber-reinforced polymer composites for construction-state-of-the-art review. *Journal of Composites for Construction*,**6**(2), 73-87.

Bank L. C. (2006). *Composites for Construction: Structural Design with FRP Materials*, Wiley, New Jersey, USA.

Bank L. C., Gentry T. R., Thompson B. J. & Russell J. S. (2003). 'A model specification for FRP composites for civil engineering structures,' *Const. Build. Mater.*, 17, 2003, 405-437.

Bank, L. C., Gentry, T. R., & Barkatt, A. (1995). Accelerated test methods to determine the long-term behavior of FRP composite structures: environmental effects. *Journal of Reinforced Plastics and Composites*, **14**(6), 559-587.

Barker, K. (2004). Review of housing supply. *Final Report–Recommendations*. The Office of the Deputy Prime Minster, London, UK.

Beddows, J., Purnell, P., & Mottram, J. T. (2002). Application of GRC accelerated ageing rationales to pultruded structural GRP. *FRC 2002: 9 th International Fibre Reinforced Composites*, 215-221.

Bradley, W. L., & Grant, T. S. (1995). The effect of the moisture absorption on the interfacial strength of polymeric matrix composites. *Journal of materials science*, **30**(21), 5537-5542.

BS EN 1990:2002. Basis *of structural design*. British Standards Institution, United Kingdom.

BS EN ISO 2578:1999 (BS 2782-1: method 135: 1993). '*Plastics – Determination of timetemperature mlimits after prolong exposure to heat'*. British Standard Institute, United Kingdom.

BS 476: Part 2 (1987). *Fire Tests on Building Materials and Structures. Methods for Determination of the Fire Resistance of Load Bearing Elements of Construction*. BSI, Milton Keynes, UK.

BS 6399-2: 1997. *Loading for buildings. Code of practice for wind loads*. British Standard Institution, United Kingdom.

BS EN 1990:2002. Basis *of structural design*. British Standards Institution, United Kingdom.

BS EN 13706-2:2002. *Reinforced plastic composites - Specification for pultruded profiles - Part 2: Methods of test and general requirements*. British Standards Institution, United Kingdom.

Camanho, P. P., & Matthews, F. L. (1997). Stress analysis and strength prediction of mechanically fastened joints in FRP: a review. *Composites Part A: Applied Science and Manufacturing*, **28**(6), 529-547.

Chateauminois, A., Chabert, B., Soulier, J. P., & Vincent, L. (2004). Dynamic mechanical analysis of epoxy composites plasticized by water: artifact and reality. *Polymer composites*, **16**(4), 288-296.

Chin, J. W., Nguyen, T., & Aouadl, K. (1997). Effects of environmental exposure on fiber-reinforced plastic (FRP) materials used in construction. *Journal of Composites Technology and Research*, **19**, 205-213.

Clarke, J. L. (1996). *Structural design of polymer composites: Eurocomp design code and background document*. Taylor & Francis.

Code for Sustainable Homes: Technical Guide (2007). Department of Communities and Local Government, London.

Cooper, C., & Turvey, G. J. (1995). Effects of joint geometry and bolt torque on the structural performance of single bolt tension joints in pultruded GRP sheet material. *Composite Structures*, **32**(1), 217-226.

D'Alessandro, R. G. (2010). Characteristic values of mechanical properties of wide-flange pultruded FRF beams. MS, PDFMSc Thesis, University of Wisconsin-Madison, USA.

Daniel, R. A. (2003). Environmental considerations to structural material selection for a bridge. In *Proceedings of the Ewopean Bridge Engineering Conference" Lightweight Bridge Decks", Rotterdam the Netherlands.*

DCLG. (2006). *Code for sustainable homes*. Department of Communities and Local Government, United Kingdom. http://www.planningportal.gov.uk/uploads/code_for_sust_homes.pdf (August 31, 2012)

Evernden, M. C. & Mottram, J. T. (2012). 'A case for houses to be constructed of fibre reinforced polymer components'. *Construction materials*, 165, (2012), 3-13.

Gates, P., Darby, A., Ibell, T. & Evernden M. (2011). 'An FRP durability study: mechanical testing of panels from the Severn Crossing Visitors' Centre', *Proceeding of the 5th International Conference on Advanced Composites in Construction (ACIC 2011)*, Coventry, Net Composites, Chesterfield, pp. 277-288.

Gentry, T. R., Bank, L. C., Barkatt, A., & Prian, L. (1998). Accelerated test methods to determine the long-term behavior of composite highway structures subject to environmental loading. *Journal of composites technology & research*, **20**(1), 38-50.

Ghorbel, I., & Valentin, D. (2004). Hydrothermal effects on the physico-chemical properties of pure and glass fiber reinforced polyester and vinylester resins. *Polymer composites*, **14**(4), 324-334.

Gibb, A. & Goodier, C. (2005). 'The value of UK Market for offsite, Build off site, London.

Godwin, E. W., & Matthews, F. L. (1980). A review of the strength of joints in fibre-reinforced plastics: Part 1. Mechanically fastened joints. *Composites*,**11**(3), 155-160.

Gulvanessian, H. Galgaro, J-A & Holický, M. (2002). *Designers' guide to EN 1990 Eurocode: Basic of structural design*, Thomas Telford, London.

Hankinson, R. L. (1921). *Investigation of crushing strength of spruce at varying angles of grain. Air Service Information Circular,* **3** *(259)* (No. 130). Material Section Report.

Hassan, N. K., Mohamedien, M. A., & Rizkalla, S. H. (1996). Finite element analysis of bolted connections for PFRP composites. *Composites Part B: Engineering*, *27*(3), 339-349.

Head, P. R. (1994). Cost effective advanced composite structures designed for life in the infrastructure. In *Proc., 22nd British Plastic Federation Composites Congress* (pp. 59-73). London: British Plastic Federation.

Head, P. R. (1995). Composite materials for bridges and structures. In *Proc., 1st Israeli Workshop on Composite Materials for Civil Engineering Construction*(pp. 136-144). Technion, Israel: National Building Research Institute.

Hollaway, L. (1993). '*Polymer composites for civil and structural engineering*,' Blackie Academic & Prof., London.

Hollaway, L., & Head, P. R. (2001). *Advanced polymer composites and polymers in the civil infrastructure*. Elsevier., Oxford, UK.

Homes for future: more affordable, more sustainable- Housing Green Paper (2007). *Communities and local Government publications*, wetherby.

Hutchinson, J. & Hartley, J. (2011). 'STARTLINK Lightweight Building System – Wholly Polymeric Structures'. *Proceeding of the 5th International Conference on Advanced Composites in Construction (ACIC 2011)*, Coventry, Net Composites, Chesterfield, pp. 355-363.

Ireman, T. (1998). Three-dimensional stress analysis of bolted single-lap composite joints. *Composite structures*, **43(**3), 195-216.

Johnson, M. & Matthews, F. L. (1979). 'Determination of safety factors for use when designing bolted joints in GRP,' *Composites*; **10** (2): 155-160.

Kaiser, H. J. (1945). '*Prefabricated Plastic Houses'*. Henry J. Kaiser Company – Housing Division, California, USA, Technical report.

Karbhari, V. M. (Ed.). (2007). *Durability of composites for civil structural applications*. Woodhead Publishing in materials. Cambridge, Woodhead.

Karbhari, V. M., Chin, J. W., Hunston, D., Benmokrane, B., Juska, T., Morgan, R., Lesko, J. J., Sorathia, U. & Reynaud, D. (2003). Durability gap analysis for fiber-reinforced polymer composites in civil infrastructure. *Journal of Composites for Construction*, **7**(3), 238-247.

Zhang, J. S., Karbhari, V. M., Wu, L., & Reynaud, D. (2003). Field exposure based durability assessment of FRP column wrap systems. *Composites Part B: Engineering*, *34*(1), 41-50.

Katz, A., Berman, N., & Bank, L. C. (1999). Effect of high temperature on bond strength of FRP rebars. *Journal of Composites for Construction*, **3**(2), 73-81.

Kellogg, K. G., Kallmeyer, A. R., Chinnam, R. B., & Dutta, P. K. (1999). Influence of moisture and low temperature on notched izod impact toughness in a pultruded reinforced composite. In *Proc., 9th Int. Offshore and Polar Engineering Conf* (Vol. 4, pp. 270-275).

Kendall, D.(2010).'*FRP structural calculations*,' Report OP-036-R1 to Exel Composites for the Startlink Project, 21st September 2010, pp 71.

Kennedy, J. B. & Neville, A. M. (1986). 'Basic Statistical Methods for Engineers and Scientists', 3rd Ed., Harper & Row, New York & London.

Kim, D. H. (1995). 'Composite structures for civil and architectural engineering', London; New York: E & FN Spon.

Kodur, V. K. R., Bisby, L. A., & Green, M. F. (2007). Preliminary guidance for the design of FRP-strengthened concrete members exposed to fire. *Journal of Fire Protection Engineering*, **17**(1), 5-26.

Lane, A. (2002). 'An Experimental Investigation of Buckling Mode Interaction in PFRP Columns', title is PhD thesis, University of Warwick, UK.

Leggatt, A. (1984). *GRP and buildings: a design guide for architects and engineers*. Butterworths, UK.

Liao, K., Schultheisz, C. R., & Hunston, D. L. (1999). Effects of environmental aging on the properties of pultruded GFRP. *Composites Part B: Engineering*,**30**(5), 485-493.

Liao, K., Schultheisz, C. R., Hunston, D. L., & Brinson, L. C. (1998). Long-term durability of fiber-reinforced polymer-matrix composite materials for infrastructure applications: A review. *Journal of advanced materials*, **30**(4), 3-40.

McCarthy, M. A., McCarthy, C. T., Lawlor, V. P., & Stanley, W. F. (2005). Three-dimensional finite element analysis of single-bolt, single-lap composite bolted joints: part I—model development and validation. *Composite Structures*,**71**(2), 140-158.

Mosallam, A. S. (2003). Chapter 45 - Composites in construction,' Material Selection Handbook, Kutz (Ed.), John Wiley Publishing Co., NY, pp. 53.

Mottram, J. T. (2004). Friction and Load Transfer in Bolted Joints of Pultruded Fibre Reinforced Polymer Section, presented at the *2nd International Conference on FRP Composites in Civil Engineering*, Adelaide, Australia.

Mottram, J. T. (2009a). Design guidance for bolted connections in structures of pultruded shapes: gaps in knowledge. In *Proceedings of the 17th International*

Conference on Composite Materials (ICCM17) (No. Paper A1: 6, pp. 1-10). IOM Communications Ltd..

Mottram, J. T. (2009b). 'Determination of pin-bearing strength for the design of bolted connections with standard Pultruded profiles', *Proceedings of the 4th International Conference on Advanced Composites in Construction (ACIC)*, Edinburgh, 483-495.

Mottram, J. T. & Turvey, G. J., (Eds.) (1998). *State-of-the-art review on design, testing, analysis and application of polymeric composite connections*, Polymeric Composite Structures Working Group 7, COST C1 Project on Behaviour of Civil Engineering Structural Connections, DG XII, European Commission, Office for Official Publications of the European Communities, Brussels & Luxembourg, p. 99.

Mottram, J. T., & Turvey, G. J. (2003). Physical test data for the appraisal of design procedures for bolted joints in pultruded FRP structural shapes and systems. *Progress in Structural Engineering and Materials*, *5*(4), 195-222.

Mottram, J. T., & Zheng, Y. (1999). Further tests of beam-to-column connections for pultruded frames: flange-cleated. *Journal of Composites for Construction*, **3** (3), 108-116.

NA to BS EN 1993-1-1:2005. *UK National Annex to Eurocode 3: Design of steel structures Part 1-1: General rules and rules for buildings,* British Standards Institution, UnitedKingdom.

Nishizaki, I., & Meiarashi, S. (2002). Long-term deterioration of GFRP in water and moist environment. *Journal of composites for construction*, *6*(1), 21-27.

Pan, W., Gibb, A. G., & Dainty, A. R. (2005). Houseproud [Practices and strategies of leading UK housebuilders on Offsite-MMC]. *PAN*, McClelland Publishing, Manchester, UK, spring edition, pp. 20–22.

Parkyn, B. (Ed.). (1970). *Glass Reinforced Plastics'*, Butterworth & Co. Publishers Ltd., Norwich, UK.

Phifer, S. P., Verghese, K. N. E., & Lesko, J. J. (2000). Remaining strength of hygrothermally aged pultruded vinylester E-glass composites. In *Proc., 3rd Int. Conf. on Advanced Composite Materials in Bridges and Structures* (pp. 29-36).

POST. (2003). Modern Methods of House-building, Parliamentary Office of Science and Technology, Postnote No. 209. See http://www.parliament.uk/documents/post/postpn209.pdf (accessed 21/08/2012).

Prian, L., & Barkatt, A. (1999). Degradation mechanism of fiber-reinforced plastics and its implications to prediction of long-term behavior. *Journal of materials science*, **34**(16), 3977-3989.

Rogatzki, P. (2007). Building the EcoHouse^{TM}. *The Structural Engineer* **85** (20), 14–17.

Robert, M., Wang, P., Cousin, P., & Benmokrane, B. (2010). Temperature as an accelerating factor for long-term durability testing of FRPs: Should there be any

limitations?. *Journal of Composites for Construction*, **14**(4), 361-367.

Rosner, C. N., & Rizkalla, S. H. (1995). Bolted connections for fiber-reinforced composite structural members: experimental program. *Journal of Materials in civil Engineering*, **7**(4), 223-231.

Schutte, C. L. (1994). Environmental durability of glass-fiber composites.*Materials Science and Engineering: R: Reports*, **13**(7), 265-323.

Singleton, M. (2004). 'Startlink system of pultruded GRP profiles for structural systems', International Patent Application No. PCT/GB2004/003832, 2004.

Singleton, M. & Hutchinson, J. (2007). 'STARTLINK composite housing', unpublished paper. (www2.warwick.ac.uk/fac/ sci/eng/staff/jtm/acic07_paper_startlink.pdf.) (30 August 2012)

Sridharan, S., Zureick, A. H., & Muzzy, J. D. (1998). Effect of hot-wet environments on E-glass/vinylester composites. *In Proceedings of the 56th Annual Technical Conference of the Society of Plastics Engineers*, 2255-2259.

Stanfield, K. (2006). Working together to face the low carbon economy. *The Structural Engineer* **84** (9): 17–20.

STARTLINK – Lightweight Building System (2009). Project Ref: TP No TP/11LIB/6/I/AM082F. *Components and materials for Low Impact Building.* Exel Composites UK.

Turvey, G. J. (1998). Single-bolt tension joint tests on pultruded GRP plate—effects of tension direction relative to pultrusion direction. *Composite structures*,**42**(4), 341-351.

Turvey, G. J. (2000). Bolted connections in PFRP structures. *Progress in Structural Engineering and Materials*, **2**(2), 146-156.

Turvey, G. J., & Wang, P. (2007). Failure of pultruded GRP single-bolt tension joints under hot–wet conditions. *Composite structures*, **77**(4), 514-520.

Technology Strategy Board, Low Impact Buildings Platform Gathers Pace. *Innovation & Research*, Issue No. 78, 29th August 2012.http://www.innovationandresearchfocus.org.uk/articles/html/issue_78/buildings_innovation_platform.asp

Technology Strategy Board, Low Impact Buildings. 29th August 2012. http://www.innovateuk.org/ourstrategy/innovationplatforms/lowimpactbuilding.ashx

Van Den Abeele, K., Carmeliet, J., & Van De Velde, K. (2001). Inferring the degradation of pultruded composites from dynamic nonlinear resonance measurements. *Polymer composites*, *22*(4), 555-567.

Vangrimde, B., & Boukhili, R. (2003). Descriptive relationships between bearing response and macroscopic damage in GRP bolted joints. *Composites Part B: Engineering*, **34**(7), 593-605.

Wang, H. S., Hung, C. L., & Chang, F. K. (1996). Bearing failure of bolted composite joints. Part I: experimental characterization. *Journal of Composite Materials*, **30**(12), 1284-1313.